School of Electrical Engineering and Computing

Modelling and Control of a Novel Single Phase Generator Based on a Three Phase Cage Rotor Induction Machine

Diana Aroshanie Hikkaduwa Liyanage

This thesis is presented for the Degree of
Doctor of Philosophy
of
Curtin University

September 2015

Declaration

To the best of my knowledge and belief this thesis contains no material previously published by any other person except where due acknowledgment has been made.

This thesis contains no material which has been accepted for the award of any other degree or diploma in any university.

Signature: …….

Date: ……...

ABSTRACT

This thesis develops the mathematical modelling and the closed loop control of a single-phase induction generator based on a three-phase cage rotor machine suitable for renewable energy conversion. In this generator topology, one of the three windings is used as the control winding for real and reactive power control, and the other two windings are connected in series to form the output winding. Since the steady-state model of this generator system has not been reported earlier, a mathematical model, equivalent circuit, and comprehensive steady-state analysis are developed for the uncontrolled system before designing the feedback control system.

Due to the larger percentage of errors produced by existing dynamic models in comparison to the values obtained in experiments, the improved dynamic model of this generator configuration is developed, taking into consideration the effect of core losses and the non-linearity of the magnetizing inductance in the saturated region which have been ignored in previous studies. The dynamic equivalent circuit is developed for the existing and the improved mathematical models, which has not been reported earlier. Moreover, a comprehensive dynamic analysis of the generator due to the sudden variation in each operational parameter is presented.

In order to supply a constant voltage and a constant frequency at the output winding, the control system proposed in this thesis automatically adjusts the external AC supply of the control winding voltage and frequency. A bi-directional DC-AC inverter connected at the control winding terminals facilitates such control of voltage and frequency. Depending on the direction of active power flow, the Energy Storage System (ESS) connected at the dc-side of the bi-directional inverter charges or discharges to maintain the active power balance of the generator system. Once the ESS is fully charged, excess power is diverted to a dump resistive load connected in parallel with the ESS. Thus, this generator is capable of producing constant voltage and frequency at the output, regardless of the fluctuations in both load demand and renewable energy sources such as wind and hydro. The unregulated turbine used in this generator system eliminates the need for an expensive speed governor.

Dynamic and steady-state behaviour of the unregulated generator system is studied using the Matlab simulation results. The accuracies of the developed models are

verified by the laboratory experiments performed on a 3 kW induction generator driven by a variable speed drive. The performance of the regulated generator system is studied using the simulation results obtained by Matlab Simulink. In this analysis, the real-time wind turbine characteristics curves are used to study the influence of different types of prime movers and wind conditions on the performance of the generator. The simulation results show the excellent capability of the proposed control system to regulate output voltage and frequency at the rated values.

ACKNOWLEDGEMENTS

I would like to express my special appreciation and thanks to my supervisor Dr Sumedha Rajakaruna for his excellent guidance, motivation, patience and understanding during the entire period of this research program. His advice on both my research and career is priceless. I could not imagine having a better supervisor for my PhD study.

I would like to thank the other thesis committee members - Professor Arindam Ghosh, Professor Chemmangot Nayar - and all my previous supervisors for their efforts and contribution to my research program.

My special thanks go to all the administrative staff in the Department of Electrical and Computer Engineering at Curtin University for their support on numerous occasions. Mr Zibby Cielma, Mr Russ Wilkinson, Mr Mark Fowler and all the other technical staff deserve sincere thanks for their support and commitment during the laboratory work undertaken for this research program.

The financial support offered by the Australian Postgraduate Award (APA) scholarship during the study period is highly appreciated. Additionally, I would like to thank Ms Sok Bewley in the Graduate Research School at Curtin University for her support during times of hardship.

I would like to acknowledge the contribution of my friends in the Department of Electrical and Computer Engineering, especially during the candidacy of my research program. I have really enjoyed working with them and thank all of them for being wonderful friends.

Special thanks goes to Ms Bruna Pomella for her professional editing services and time spent on proofreading this thesis.

Finally, I would like to thank my mother and my loving husband for their continuous support and understanding during the last five years of the research. Patience shown by my little daughter Sanuki during my studies will never be forgotten. The encouragement and support given by all other family members and friends both in Sri Lanka and Australia are greatly appreciated.

LIST OF PUBLICATIONS

Journal Papers

- **Diana Liyanage**, S. Rajakaruna, “Dynamic Analysis of a Novel Single-Phase Induction Generator using an Improved Machine Model", IEEE Transactions on Energy Conversion, 2015, under review (TEC-00138-2015.R2 is to be submitted).

Conference Papers

- **Diana Liyanage**, S. Rajakaruna, "An Improved Dynamic Model for a Single-Phase Generator based on Three-Phase Cage Rotor Induction Machine", in Conf. Rec. IEEE Conf. on Power Electronics and Drive Systems (PEDS), Sydney, 2015, pp. 934-939.
- **Diana Liyanage**, S. Rajakaruna, "Steady-state Analysis of a Novel Single Phase Induction Generator for Renewable Energy Conversion", in Conf. Rec. IEEE Conf. on Power Engineering (AUPEC), Perth, 2014, pp. 1-6.
- **Diana Liyanage**, S. Rajakaruna, “Transient analysis of a single-phase variable speed cage induction generator with active excitation control”, in Conf. Rec. IEEE Conf. on Power Engineering (AUPEC), Tasmania, 2013, pp. 1-6.
- Lucas Zieland, Sumedha Rajakaruna, **Diana Liyanage**, “Modelling and performance assessment of large scale solar photovoltaic plants in rural Australia”, in Conf. Rec. IEEE Conf. on Power Engineering (AUPEC), Tasmania, 2013, pp. 1-6.
- **D. Liyanage** , S. Rajakaruna, “Performance evaluation and cost-benefit analysis of a large solar PV installation at a mine site in Western Australia”, in Conf. Rec. IEEE Conf. on PES Innovative Smart Grid Technologies Asia (ISGT), Perth, 2011, pp. 1-8.

LIST OF SYMBOLS

A_T	- Swept area of wind turbine, m^2
B	- Friction coefficient of the turbine, N.m.s
C	- Chord length of wind turbine blade, m
C_o	- Fixed capacitance, F
C_p	- Power coefficient of wind turbine
C_T	- Torque coefficient of wind turbine
$d-q$	- d-axis and q-axis in arbitrary reference frame
f	- Frequency of output voltage, Hz
g	- Acceleration of gravity, m/s^2
h	- Head of hydro turbine, m
i_c	- Current through the fixed capacitance C_o, A
i_{core}	- Current through the core loss resistance, A
i_{c1}, i_{c2}	- Currents through the core loss resistances in α–axis and β–axis respectively, A
i_{m1}, i_{me}	- Current through the magnetizing reactance in α–axis, A
i_{m2}, i_{mo}	- Current through the magnetizing inductance in β–axis, A
i_{mse}, i_{mso}	- Stator currents through the mutual inductance in α–axis and β–axis respectively, A
$i_{mr\alpha}, i_{mr\beta}$	- Rotor currents through the mutual inductance in α–axis and β–axis respectively, A
i_o	- Current through the consumer load, A
i_r	- Rotor current in standard machine, A

i_{rated}	- Rated current of the machine, A
i_{ra}, i_{rb}, i_{rc}	- Rotor currents in phase a, b and c respectively, A
$i_{r\alpha}, i_{r\beta}$	- Rotor currents in phase α and β respectively, A
i_s	- Stator current in standard machine, A
i_{sa}, i_{sb}, i_{sc}	- Stator currents in phase a, b and c respectively, A
$\boldsymbol{i_{sa}, i_{sb}, i_{sc}}$	- Current vectors in stator phase a, b and c respectively
i_{se}, i_e	- Stator currents in phase α, A
i_{so}	- Stator currents in phase β, A
$\boldsymbol{i_{se}, i_{so}}$	- Current vectors in stator phase α and β respectively
J	- Moment of inertia of the turbine, kg.m^2
K_p, K_i	- Proportional and integral gains of PI controller respectively
L_{lr}	- Rotor leakage inductance referred to the stator in standard machine, H
L_{ls}	- Stator leakage inductance in standard machine, H
L_{m1}	- Mutual inductance in α-axis, H
L_{m2}	- Mutual inductance in β-axis, H
L_{mr}	- Rotor mutual inductance in standard machine, H
L_{ms}	- Stator mutual inductance in standard machine, H
L_{rs}	- Mutual inductance between rotor and stator, H
L_{sr}	- Mutual inductance between stator and rotor, H
L_o	- Consumer load inductance, H
m	- Negative gradient of the torque-speed characteristics of wind turbine

N	- Turns ratio of the step-up transformer
N_b	- Number of blades of wind turbine
N_m	- Winding ratio of the machine
P_m	- Mechanical power, W
P_{out}, P_o	- Real power in output winding, W
$P_{r,loss}$	- Resistive losses of the machine, W
$P_{r,loss\_\alpha}$	- Resistive losses of the machine in α-axis, W
$P_{r,loss\_\beta}$	- Resistive losses of the machine in β-axis, W
P_{se}, P_{ex}, P_e	- Real power in excitation control winding, W
P_T	- Turbine mechanical power, W
pu	- Per unit value
Q_{se}, Q_e	- Reactive power in excitation control winding, VAr
Q_{so}	- Reactive power in output winding, VAr
R_c	- Core loss resistance, Ω
R_o	- Consumer load resistance, Ω
R_r, r_r	- Rotor winding resistance referred to the stator of standard machine, Ω
R_s, r_s	- Stator winding resistance of standard machine, Ω
T_e	-Electromagnetic torque, Nm
T_T	-Turbine torque, Nm
V_{m1}, V_{m2}	- Voltages across the magnetizing reactance in α–axis and β-axis respectively, V
V_r	- Rotor voltage in standard machine, V

V_{rated} - Rated voltage of the machine, V

V_s - Stator voltage in standard machine, V

V_{sa}, V_{sb}, V_{sc} - Stator voltages in phase a, b and c respectively, V

$\boldsymbol{V_{sa}, V_{sb}, V_{sc}}$ - Voltage vectors in stator phase a, b and c respectively

V_{se}, V_e - Stator voltages in phase α, V

V_{so}, V_o - Stator voltages in phase β, V

$\boldsymbol{V_{se}, V_{so}}$ - Voltage vectors in stator phase α and β respectively

V_w - Wind speed, m/s

σ - Turbine rotor solidity

η - Efficiency

ρ - Density of water, kg/ m^3

q - Flow rate of water, m^3/s

ρ_a - Density of air, kg/m^3

λ - Flux linkage of the windings, Wb-turns

ψ - Magnetic flux of the machine, Wb

ψ_r - Magnetic flux in the rotor, Wb

ψ_s - Magnetic flux in the stator, Wb

ψ_m - Mutual flux of the machine, Wb

ψ_{mr} - Mutual flux in the rotor, Wb

ψ_{ms} - Mutual flux in the stator, Wb

$\psi_{msa}, \psi_{msb}, \psi_{msc}$ - Mutual flux in stator phase a, b and c respectively, Wb

ψ_{lr} - Leakage flux in the rotor, Wb

ψ_{ls} - Leakage flux in the stator, Wb

$\psi_{lsa}, \psi_{lsb}, \psi_{lsc}$	- Leakage flux in stator phase a, b and c respectively, Wb
ψ_{se}, ψ_{so}	- Flux in excitation control and output winding respectively, Wb
δ	- Phase of current in excitation control winding w.r.t. that of voltage in same winding, rad
ω_1	- Frequency of output voltage, rad/s
ω_c	- Cut-off frequency, rad/s
ω_m	- Angular rotor speed, mechanical, rad/s
ω_r	- Angular rotor speed, electrical rad/s
ω_t	- Angular speed of turbine, rad/s

TABLE OF CONTENTS

LIST OF FIGURES

LIST OF TABLES

CHAPTER 1- INTRODUCTION

1.1 Background

Australia has an abundant and a rich diversity of energy resources distributed across the country. The non-renewable energy resources such as coal, gas and uranium are expected to last for many more decades. However, in order to reduce the global warming and environmental impacts caused due to the use of non-renewable energy sources, renewable energy resources such as wind, hydro, solar, wave and bio energy are focused to supply the growing energy demand in the country. Wind is a vast potential renewable energy source in the world. It is the fastest growing renewable energy resource which is expected to continue until 2030. Some of the best wind resources in the world are located in the coastal regions of western, south-western, southern and south-eastern Australia. Depending on the requirement, the availability of the renewable energy source and the economical factors, the wind energy generation plants are operated as grid-connected or off-grid power stations.

The purpose of this thesis is to design and control of a small-scale wind or hydro energy generation plant suitable for both grid-connected and off-grid operation. This power generation system consists of the following major components.

- A small-scale three-phase induction machine
- Bi-directional DC-AC inverter
- Battery energy storage system
- Wind/ Hydro turbine
- Load Circuit
- Control system

Since the modern electronic equipments are more sensitive to the variations and disturbances of the electric power, reliability and quality of the electricity supply determines the fitness of the power generation scheme. Especially, in off-grid operation, the electricity generation using wind power depends on the fluctuations of the wind speed and the load demand. In order to supply a constant voltage and

sinusoidal waveform with the desired frequency, the energy storage system and the control system capable of maintaining the desired output under different conditions are needed to design.

The research was carried out over a period of five years with both theoretical and experimental analyses. Problem definitions, mathematical calculations and system modelling were developed as the theoretical analysis and implementation of theoretical model in the real world was executed as the experimental analysis.

Using the existing theories in Electrical/ Electronic Engineering, the mathematical model of each component in the energy generation system was theoretically developed. The developed model was simulated in Matlab/ Matlab Simulink to obtain the theoretical results of the generator system. This model was verified using the experimental results obtained on laboratory experimental setup.

From the starting point of this research a numerous number of literature related to the thesis was collected. The search engines provided by Curtin Library were heavily utilized to find out the journal papers, proceedings, textbooks, conference papers and online articles related to the each section of this thesis. However, only a selected number of references are listed in the Bibliography of the thesis. Each of the references is described in detail in the literature review in Chapter 2.

Some of the technical works related to the main body of the thesis are presented as appendices. Appendix A-H is given at the end of the thesis.

1.2 System Overview

This thesis focuses on the modeling and control of a single-phase induction generator based on a three-phase squirrel cage rotor machine suitable for renewable energy generation such as wind or micro-hydro plants located in remote areas. In this generator topology shown in the schematic diagram in Fig.1.2.1, two windings of the three-phase machine are connected in a series as the output winding, and the remaining third winding is used as an isolated control winding to regulate the voltage and frequency at the output winding using a bidirectional DC-AC inverter with battery energy storage system (ESS) at the DC side. The terminals of the output winding are connected to the consumer load. A fixed capacitor is also usually connected in parallel with the consumer load at the output terminals to supplement

the reactive power requirement of the generator. It reduces the inverter current rating by supplying a portion of the required reactive power locally. It also helps to improve the balance of the currents among three phases.

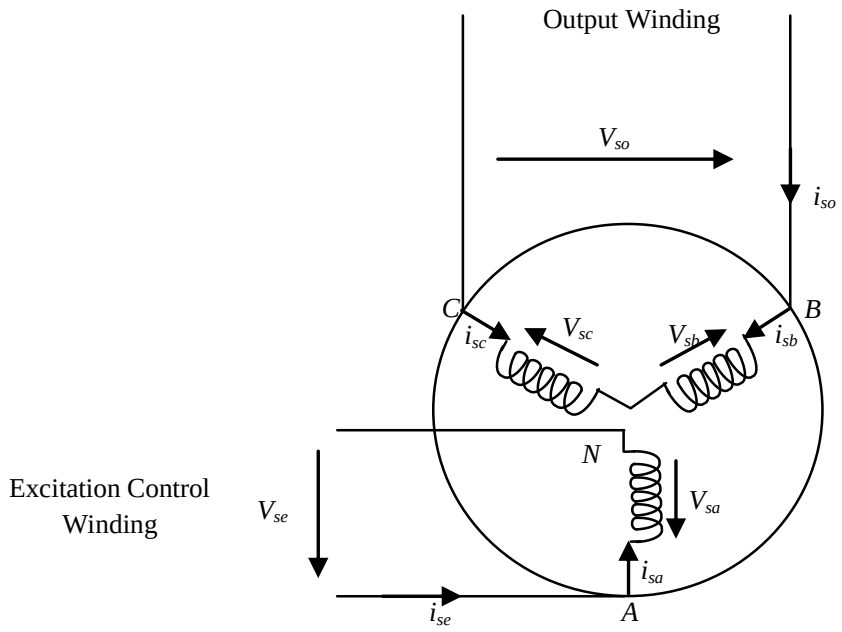

Fig. 1.2.1. Schematic diagram of the winding connection of single-phase Induction Generator

In terms of power, the control winding supplies the deficit of reactive power requirement of the machine and is therefore referred to in this thesis as the *excitation control winding*. However, the same winding is also used to supply or absorb the real power required to balance the real power in the system under varying consumer load demands and the varying renewable energy source coupled to the shaft of the machine. The battery energy storage on the DC side of the inverter stores the excess electricity generation of the machine during periods of high renewable energy availability, and supplies the deficit energy requirement during other periods where renewable energy generation is less than what is demanded by the load. Therefore, the output voltage and frequency can be regulated at their rated values despite the changes in renewable energy availability and load demand. Hence, the system is capable of capturing the maximum energy from the renewable energy source.

1.3 Significance of the Research and Research Motivation

The developed single-phase induction generator can be employed in a small-scale energy generation scheme. Since it is capable of generating constant voltage, constant frequency output regardless of the fluctuations of available renewable energy source and load demand, it is an ideal candidate for the small-scale renewable energy applications such as wind power plant. The knowledge of its theoretical behaviour is important before employing in the real world. Therefore, developing the mathematical models of the single-phase induction generator both in transient and steady states are significant not only to analyse its behaviour, but also to control the generation system under different situations. Once the theoretical models are experimentally verified using laboratory experimental results, this generator system can be utilized in many renewable energy generation schemes with no uncertainties.

An incomplete set of dynamic equations of the single-phase induction generator is reported in the literature. However, a large percentage error can be identified when comparing the experimental and simulation results given in the literature. Considering the importance of this system in renewable energy generation, improving the accuracy of the existing dynamic model is highly required. This motivates the researcher to seek the comprehensive dynamic model presented in Chapter 3. Furthermore, the steady-state model and the control system in synchronous reference frame were developed to study the performance of the regulated energy generation system.

1.4 Objectives of the Research

In order to achieve and analyze the predicted results, the following objectives were examined in this thesis.

- In order to study the dynamic behavior of the generator:
    i. Develop an improved dynamic model in stationary αβ reference frame that takes into account the core loss resistance and the non-linearity of magnetizing reactance in the saturated region.
    ii. Develop a dynamic equivalent circuit in α-axis and β-axis.
    iii. Analyze the dynamic behavior of the generator following sudden change(s) in operational parameters such as load, fixed capacitance,

rotor speed and excitation control voltage.

- In order to study the steady-state behavior of the generator:
    i. Develop a steady-state model in stationary αβ reference frame.
    ii. Obtain the steady-state equivalent circuit in α-axis and β-axis.
    iii. Develop computational techniques to calculate the system variables in steady-state for a given set of operational parameters.
    iv. Develop computational techniques to calculate operational parameters in order to achieve a balance between current and voltage in the generator system.
    v. Analyze the steady-state behavior of the generator under different load demands, fixed capacitance, rotor speed and excitation control voltage.
- Develop a dynamic model in synchronous reference frame in order to design the control system of the generator.
- Design a control system that meets the following requirements.
    i. Supply a constant voltage and a constant frequency at the output by controlling the voltage and the frequency of the excitation control winding.
    ii. Isolate the ESS and the bi-directional converter from the generator system when the ESS is fully discharged.
    iii. Dissipate the excess energy as heat through a variable resistor connected in parallel with the battery energy storage when the ESS is fully charged.
- Design the ESS to supply the rated output power of the generator for three days continuous in situations where the renewable energy source is not capable of supplying the load demand.
- Design a bi-directional converter to transfer both active and reactive power between the ESS and the generator.
- Design a model of Wind Turbine Characteristics which is capable of providing the rated power of the generator at a wind speed of 10 m/s.
- In order to verify both the transient and the steady-state models developed in this thesis, compare the computer simulation results with the experimental

results obtained using a small-scale induction generator system assembled in the laboratory.

- Simulate the steady-state model of the generator system including the unregulated wind turbine using Matlab Simulink in order to study the performance of the proposed regulated system.

1.5 Organization of the Thesis

This thesis is arranged in the following Chapters.

Chapter 1 (this Chapter) introduces and briefly describes the research work and presents the objectives of this research. The research work undertaken in order to achieve these objectives is explored in detail in the subsequent chapters.

Chapter 2 presents a survey of the literature pertaining to the generation of electricity using renewable energy sources such as wind and hydro; the role of the single-phase induction generators in electricity generation in remote areas; the single-phase operation of three-phase induction machines; the methods of developing the mathematical models of the generator; the designing of bi-directional power converters and energy storage systems, the wind turbine characteristics and their operations and the control systems. One of the main focuses of this work is the modelling and analysis of the single-phase induction generator in both transient and steady-states. The literature survey was carried out with the aim of discovering the types of connections that are available for generating single-phase output using a three-phase induction machine, and the methods used to develop mathematical models. Furthermore, due to the large discrepancy between the experimental results and the computer simulation results obtained from the already-developed dynamic model of this generator configuration, the literature survey was carried out in order to discover a means of improving the accuracy of the existing dynamic model. All the references given in this chapter are directly connected with the content of this thesis and highly relevant to this research work.

Chapter 3 of the thesis presents the rationale for this research and the existing dynamic model of this generator configuration. The large percentage error identified when comparing the experimental and simulation results given in the literature motivated the researcher to seek a comprehensive dynamic model described in the

first part of Chapter 3. Starting from the fundamental flux equations of a three-phase induction generator, the dynamic equations of a single-phase generator in stationary 'abc' reference frame were developed to take into account the core loss resistance and the non-linearity of the magnetizing reactance in the saturated region. In order to avoid the complexity of dealing with a multi-phase system, the model developed in the stationary 'abc' reference frame was transformed into a stationary 'αβ' reference frame. Furthermore, the equivalent circuit of the comprehensive dynamic model in the α-axis and β-axis comprising the generator, the prime mover, excitation capacitors and the consumer loads is given in this chapter. In the second part of Chapter 3, the steady-state model in a stationary αβ reference frame and the steady-state equivalent circuit in α–axis and β-axis are presented.

In this thesis, load, fixed capacitance and rotor speed are considered as the operating parameters of the generator system. Chapter 4 presents the computational techniques developed to calculate the system variables in steady-state for a given set of operating parameters in two different scenarios. In the first scenario, the rotor speed is considered to be fixed and known whereas in the second scenario, the rotor speed is considered as a load-dependent variable. The computational methods used to calculate the system variables for both the scenarios are described in detail. Furthermore, in the latter part of Chapter 4, the computational techniques for calculating the operational range of the operating parameters are presented.

The study of the dynamic performance of the induction generator driven by an unregulated wind turbine is developed in Chapter 5. First, the computer simulation results obtained from the existing dynamic model and the comprehensive dynamic model in the stationary 'αβ' reference frame are compared with the corresponding experimental results obtained from the laboratory experiment conducted to verify the improved accuracy of the comprehensive dynamic model compared with the existing dynamic model. Secondly, a procedure to determine the dynamic behaviour of the generator for a given operating parameter is developed. Then, the dynamic behaviour of the generator due to sudden variation in each operating parameter is studied separately. The variable step Runge-Kutta technique is used to compute the dynamic performance using Matlab software. The results obtained from computer simulations are experimentally verified.

Chapter 6 presents a detailed analysis of the steady-state behaviour of the induction generator driven by an unregulated wind turbine. Studies are conducted to investigate the effects of changes to the consumer load, the excitation capacitance and the speed of the prime mover. The developed dynamic model was simulated in Matlab simulink. The results of the simulation are experimentally verified.

Chapter 7 describes the control system proposed by this thesis to regulate the voltage and the frequency at output winding under different load demand and fluctuations in a renewable energy source. The mathematical model of the single-phase generator in synchronous reference frame is developed in order to design the proposed control system. The selection of a suitable ESS and its capacity are discussed in this chapter. In addition, the design procedure of the bi-directional converter is explained. In order to study the performance of the generator with the real-time wind turbine characteristics, a model of a wind turbine suitable for small-scale wind energy generation systems is developed. The performance of the combined system is studied using Matlab Simulink.

Chapter 8 summarizes the main contributions of this thesis and presents the conclusions.

CHAPTER 2- REVIEW OF LITERATURE

The excessive and inefficient use of conventional energy sources such as oil, natural gas and coal has become a global concern due to the rapid depletion of fossil fuels, increasing demand for energy, global warming and climate change [1]. Governments worldwide are focusing on power generation using renewable energy sources such as wind, solar, biomass, geothermal and hydro due to their sustainability, efficiency, cost-effectiveness and reliability for long-term operation [2-10]. Renewable energy is used in four different areas: electricity generation, water/space heating, motor fuels and rural (off-grid) energy services [11-16].

Wind and hydro power make a significant contribution to the generation of electricity in some countries [17-23]. Mostly, the small scale wind turbine and the micro-hydro generate decentralized power for cooperative or individual consumption at the local generation point. It implements the concept of stand-alone operation of the energy conversion system (ECS) [24-25]. In order to capture maximum power available from wind and hydro, it is not practicable for the prime mover operate at a constant speed [26-27]. In the past, it has been found that variable speed turbines are capable of capturing more effective power than do fixed speed turbines with similar capacity [28-30]. In order to track the maximum power, a variable speed generator is employed. Of the two types of variable speed generators, variable speed induction generator is more popular due to its advantages: it is smaller and less expensive; it is rugged and brushless; it does not need a separate DC source; maintenance is easy, and it has self- protection against severe overloads and short circuits compared to the variable speed synchronous generators with the same power ratings [31-37].

2.1 Operation of Three-Phase Induction Machine as a Single-Phase Generator

Most of the renewable energy sources available in abundance are located in remote areas where the three-phase electricity supply may not be available. [38-42]. Therefore, in these areas, the variable speed, single-phase induction generators are the most suitable for the generation of electricity using renewable energy sources. However, for power ratings above 3 kW, there is an increasing tendency to use

standard three-phase induction generators to generate single-phase output because they are less heavy, smaller in size, cheaper, incur less power loss, are more efficient, easy to maintain and readily available as a means for comparison with the single-phase induction machines with the same power ratings [43-47]. In the past decades, extensive work has been done by many researchers on the design and analysis of single-phase electricity generation using three-phase induction machines [44, 48-55]. As an approach to supply power to a single-phase load on a three-phase self-excited induction generator, Bhattacharya, J.L. *et al.* [48] introduced the C-2C connection where the capacitance across one phase is twice that across the second phase, and there is no capacitance across the third phase. The single-phase load is connected in parallel with the single capacitance. Al-Bahrani A.H. *et al.* [49] discuss a method of supplying a single-phase output using a three-phase isolated self-excited star or delta-connected induction generator employing a single excitation capacitor. Tadashi Fukami *et al.* [51] introduced a method of connecting three capacitors in series and parallel with the stator winding of a squirrel cage three-phase induction machine in order to supply an electric power to a single-phase load. Chan T.F. *et al.* [44] introduced Steinmetz connections which are capable of supplying single-phase power using three-phase induction motors with a single capacitor connected across the lagging phase. Chan T.F. *et al.* [52] present an enhanced method of Steinmetz connections to provide a single-phase power with reduced voltage regulation and increased power output. In this connection, the excitation capacitance is connected across the lagging phase, whereas the compensation capacitor is connected in series with the single-phase load across the reference phase. Madawala *et al.* [55] has recently introduced a configuration with two windings in series and one isolated winding as an alternative (TSCAOI configuration). It is a more attractive method since it facilitates incorporating a controllable source in the isolated winding to produce a constant voltage and a constant frequency at the output terminals regardless of the fluctuations in available renewable energy.

2.2 Energy Storage in Renewable Energy System

The variable speed turbines face technical challenges in producing continuous electrical output since they extract the maximum available power from the renewable energy source. Thus, the output of the generator fluctuates because excess energy is generated during periods of high renewable energy availability, and there is a deficit

of energy during other periods when the availability of renewable energy is less than what is demanded by the load [56-57]. In order to become a more reliable ECS, the output power needs to be smoothed and constant at the consumer point or the grid point [58-60]. Hence, there is the need for a properly designed energy management system which is capable of fulfilling the consumer demand at all times [61-67]. Electrical energy can be stored in many forms such as electrochemical energy, thermal energy, mechanical energy, electrostatic energy, etc [66]. Since capital investment is required for the installation of an energy management system, it is important to design a particular system that takes several factors into consideration [68]. Thus, in addition to energy storage capability, variation of the load, historical data of the renewable energy fluctuations in a selected area, specific details of the ESS, data specific to the inverter are crucial factors to be considered when designing an energy management system [69-71]. The most common forms of renewable ESS are rechargeable batteries, thermal energy storage, flywheels, cryogenic energy storage and superconducting magnetic energy storage [72-82]. The most common types of rechargeable batteries are lead-acid, lithium-ion, nickel-cadmium (NiCd) and nickel-metal hydride (NiMH) [77, 80]. The initial cost of rechargeable batteries is higher. However, they can be recharged at a lower cost and used for several years. Compared to all other ESS, flywheels have the longer lifetime and can be used with little or no maintenance for several years.

The evaluation of the Ampere-hour capacity of a battery energy storage system (BESS) is a more crucial factor for the load levelling for several hours during extremely low availability of the renewable energy source [83]. After determining the required capacity of the system, the most economical and effective ESS can be selected. The function of ESS has to be carefully controlled by a control circuit. At the depth of discharge of the batteries the BESS is isolated from the generator system to avoid the damage that may be caused to the batteries if fully discharged. This controlling is essential to protect batteries from cell reversal since a number of batteries are connected in series to make the ESS. In order to prevent the batteries from overcharging, the redundant power is dissipated as heat through a variable resistor connected in parallel to the BESS [83-90]. If required, the dissipated heat may be used for other purposes such as water heating and steam making.

2.3 Control Issues and Techniques

Single-phase, full-bridge inverters with insulated-gate bipolar transistor (IGBT) and diodes are capable of acting as bi-directional converters [91-93]. The same sinusoidal Pulse width modulation (PWM) controller is used to generate switching signals for the IGBT gates in both inverter and rectifier.

Basically, an ECS is controlled using two controlling methods: voltage control and current control. In a stand-alone operation, the voltage control method is preferable to the current control method [94]. Proportional Integral (PI), Proportional Integral Derivative (PID) controllers or Fuzzy logic controllers can be used for the satisfactory operation of the control system [95-98]. In between the two common classes of control systems; i.e. open loop and closed loop control systems, the second system is employed in the case of linear feedback systems, in order to regulate a particular variable at a desired value. The Nyquist plots can be used to determine the stability of the chosen gain parameters of the closed loop transfer function [99].

2.4 TSCAOI Configuration Novel Single-Phase Induction Generator

This topology is shown in the schematic diagram in Fig. 2.4.1.

Phases ‘b’ and ‘c’ of the three-phase machine are connected in series as the output winding and its terminals are connected to the consumer load. The remaining third winding of phase ‘a’ is used as the isolated control winding to regulate the output of the generator. The renewable energy source is coupled to the shaft of the machine.

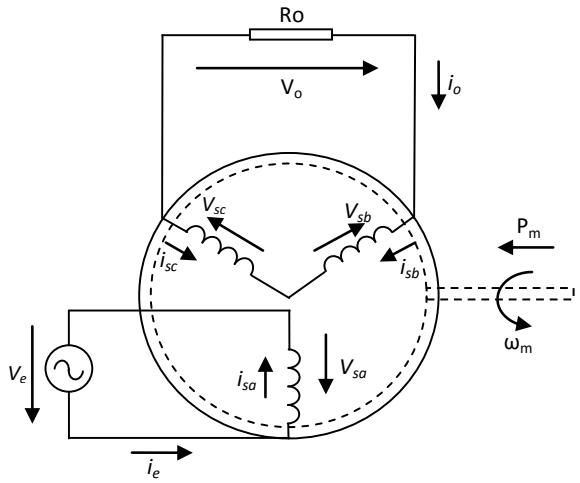

Fig. 2.4.1. Schematic diagram of the TSCAOI configuration

In the TSCAOI configuration, the output voltage and the frequency are controlled by isolated winding using a battery energy storage system (ESS) connected at the DC side of a bidirectional converter. From the point of view of power, the control winding is used to supply or absorb the real power required to balance the real power in the system under varying consumer load demand and the varying renewable energy source. The battery energy storage on the DC side of the inverter stores the excess electricity generation of the machine during periods of high renewable energy availability, and supplies the energy requirements during other periods of deficit when renewable energy generation is less than what is demanded by the load. Therefore, the output voltage and frequency can be regulated at their rated values despite the changes in renewable energy availability and load demand. Therefore, the system is capable of capturing the maximum energy from the renewable energy source. However, the same winding is also used for supplying the deficit of reactive power requirement of the machine and is therefore referred to in this thesis as the *excitation control winding*. A fixed capacitor is usually connected in parallel at the output terminals to supplement the reactive power requirement of the generator. It reduces the inverter current rating by supplying a portion of the required reactive power locally. It also helps to improve the balance of the currents among three phases. The schematic diagram of this renewable energy generation system is shown in Fig. 2.4.2.

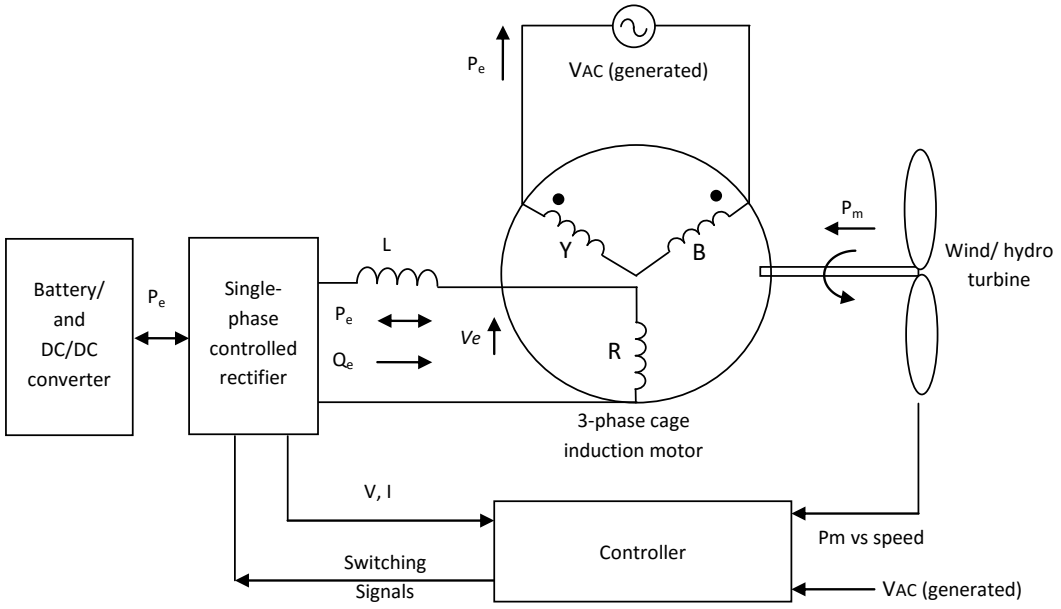

Fig. 2.4.2. The schematic diagram of this renewable energy generation system

Unlike the conventional wind ECSs, a reversible converter is used at the excitation control winding in this ECS [55]. This converter is capable of working as a DC/AC inverter as well as an AC/DC rectifier. The inverter circuit is active during reactive power requirement for the excitation process of the generator and the deficit energy requirement when the availability of the renewable source is low. The excess energy generated during the period of high availability of renewable energy source is transferred to the ESS through the rectifier circuit. Thus, the reversible converter is one of the most important components of this generator system.

In order to derive the dynamic model of the proposed generator system, the stator phase 'a' is considered as the reference phase and rotor phase 'a' is considered as φ_r degree inclined to the reference phase.

The stator and rotor voltages of a standard three-phase squirrel cage induction machine in an "abc" reference frame can be represented by the following equations [55].

$$\left[v_{s,abc}\right] = [R_s]\left[i_{s,abc}\right] + \ p\left\{[L_s]\left[i_{s,abc}\right]\right\} + p\left\{[L_{sr}]\left[i_{r,abc}\right]\right\} \tag{2.4.1}$$

where p is the differential operator and

$$\left[v_{s,abc}\right] = \begin{bmatrix} v_{sa} \\ v_{sb} \\ v_{sc} \end{bmatrix} \ , \ \left[i_{s,abc}\right] = \begin{bmatrix} i_{sa} \\ i_{sb} \\ i_{sc} \end{bmatrix}$$

$$[R_s] = \begin{bmatrix} r_s & 0 & 0 \\ 0 & r_s & 0 \\ 0 & 0 & r_s \end{bmatrix}$$

$$[L_s] = \begin{bmatrix} (L_{ls} + L_{ms}) & -L_{ms}/2 & -L_{ms}/2 \\ -L_{ms}/2 & (L_{ls} + L_{ms}) & -L_{ms}/2 \\ -L_{ms}/2 & -L_{ms}/2 & (L_{ls} + L_{ms}) \end{bmatrix}$$

$$[L_{sr}] = L_{ms}\begin{bmatrix} \cos(\varphi_r) & \cos\left(\varphi_r + \frac{2\pi}{3}\right) & \cos\left(\varphi_r - \frac{2\pi}{3}\right) \\ \cos\left(\varphi_r - \frac{2\pi}{3}\right) & \cos(\varphi_r) & \cos\left(\varphi_r + \frac{2\pi}{3}\right) \\ \cos\left(\varphi_r + \frac{2\pi}{3}\right) & \cos\left(\varphi_r - \frac{2\pi}{3}\right) & \cos(\varphi_r) \end{bmatrix}$$

$$\left[v_{r,abc}\right] = [R_r]\left[i_{r,abc}\right] + \ p\left\{[L_{sr}]^T\left[i_{s,abc}\right]\right\} + p\left\{[L_r]\left[i_{r,abc}\right]\right\} \tag{2.4.2}$$

where $[i_{r,abc}] = \begin{bmatrix} i_{ra} \\ i_{rb} \\ i_{rc} \end{bmatrix}$, $[v_{r,abc}] = \begin{bmatrix} v_{ra} \\ v_{rb} \\ v_{rc} \end{bmatrix}$ = 0 for cage rotor machines.

$$[R_r] = \begin{bmatrix} r_r & 0 & 0 \\ 0 & r_r & 0 \\ 0 & 0 & r_r \end{bmatrix}, [L_r] = \begin{bmatrix} (L_{lr} + L_{mr}) & -L_{mr}/2 & -L_{mr}/2 \\ -L_{mr}/2 & (L_{lr} + L_{mr}) & -L_{mr}/2 \\ -L_{mr}/2 & -L_{mr}/2 & (L_{lr} + L_{mr}) \end{bmatrix}$$

According to the winding connection of the proposed configuration, the voltages and the currents in the output and excitation control windings can be given by [55]

$$[v_{s,eo}] = [Q][v_{s,abc}] \tag{2.4.3}$$

$$[i_{s,eo}] = [Q][i_{s,abc}] \tag{2.4.4}$$

where $[v_{s,eo}] = \begin{bmatrix} v_{se} \\ v_{so} \end{bmatrix}$, $[i_{s,eo}] = \begin{bmatrix} i_{se} \\ i_{so} \end{bmatrix}$

$$[Q] = \begin{bmatrix} 1 & 0 & 0 \\ 0 & 1 & -1 \end{bmatrix} \quad , \quad [Q]^{-1} = [Q]^T$$

In order to avoid the complexity of dealing with multi-phase system, three-phases of the rotor are transformed into a "*αβ*" frame using the transformation in (2.4.5) assuming that the "*α*" axis of the "*αβ*" frame is aligned with the phase "a" of the stator windings, as shown in Fig. 2.4.3 [55].

$$[K_r] = \frac{2}{3} \begin{bmatrix} \cos(\varphi_r) & \cos\left(\varphi_r + \frac{2\pi}{3}\right) & \cos\left(\varphi_r - \frac{2\pi}{3}\right) \\ \sin(\varphi_r) & \sin\left(\varphi_r + \frac{2\pi}{3}\right) & \sin\left(\varphi_r - \frac{2\pi}{3}\right) \end{bmatrix} \tag{2.4.5}$$

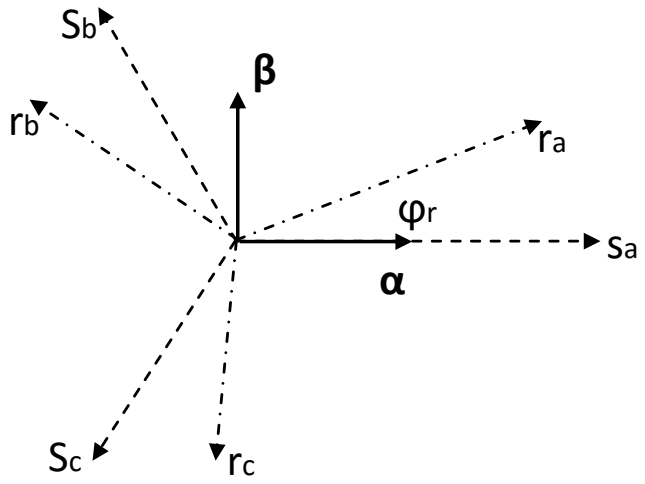

Fig. 2.4.3. Stator and rotor with respect to the "*αβ*" reference frame

The phases of excitation control winding and output winding denoted as ‘e’ and ‘o’ respectively form the ‘eo’ frame. ‘e’ and ‘o’ in the ‘eo’ frame correspond to ‘α’ and ‘β’ in the ‘αβ’ frame respectively. When the rotor parameters in the “abc” frame are transformed into “αβ” frame, the stator and rotor voltages in “eo” and “$\alpha\beta$” frames can be defined as (2.4.6) and (2.4.7) respectively.

$$\left[v_{s,eo}\right] = [Q][R_s][Q]^{-1}\left[i_{s,eo}\right] + [Q]p\left\{[L_s][Q]^{-1}\left[i_{s,eo}\right]\right\} + [Q]p\left\{[L_{sr}][K_r]^{-1}\left[i_{r,\alpha\beta}\right]\right\} \tag{2.4.6}$$

$$\left[v_{r,\alpha\beta}\right] = [K_r][R_r][K_r]^{-1}\left[i_{r,\alpha\beta}\right] + [K_r]p\left\{[L_{sr}]^T[Q]^{-1}\left[i_{s,eo}\right]\right\} + [K_r]p\left\{[L_r][K_r]^{-1}\left[i_{r,\alpha\beta}\right]\right\} \tag{2.4.7}$$

After lengthy manipulations with appropriate substitutions, (2.4.6) and (2.4.7) can be rewritten in the following form [55]:

$$\left[v_{s,eo}\right] = r_s\begin{bmatrix}1 & 0\\ 0 & 2\end{bmatrix}\left[i_{s,eo}\right] + \begin{bmatrix}L_{ls}+L_{ms} & 0\\ 0 & 2L_{ls}+3L_{ms}\end{bmatrix}p\left[i_{s,eo}\right] + \frac{3}{2}L_{ms}\begin{bmatrix}1 & 0\\ 0 & \sqrt{3}\end{bmatrix}p\left[i_{r,\alpha\beta}\right] \tag{2.4.8}$$

$$0 = L_{ms}\omega_r\begin{bmatrix}0 & \sqrt{3}\\ -1 & 0\end{bmatrix}\left[i_{s,eo}\right] + L_{ms}\begin{bmatrix}1 & 0\\ 0 & \sqrt{3}\end{bmatrix}p\left[i_{s,eo}\right]r_r\left[i_{r,\alpha\beta}\right] +$$

$$\left(L_{lr}+\frac{3}{2}L_{ms}\right)\omega_r\begin{bmatrix}0 & 1\\ -1 & 0\end{bmatrix}\left[i_{r,\alpha\beta}\right] + \left(L_{lr}+\frac{3}{2}L_{ms}\right)p\left[i_{r,\alpha\beta}\right] \tag{2.4.9}$$

In order to derive the mathematical model, the elements of the machine current vector are chosen as the state variables. The state space model of the single-phase generator can be represented as shown in (2.4.10).

$$p[i] = [A][i] + [B][v] \tag{2.4.10}$$

where $[i] = [i_{se} \quad i_{so} \quad i_{r\alpha} \quad i_{r\beta}]^T$, $[v] = \left[v_{s,eo}\right] = [v_{se} \quad v_{so}]^T$

$$[A] = \begin{bmatrix} -\frac{r_s L_{rr}}{D_1} & \frac{2{L_M}^2\omega_r}{\sqrt{3}D_1} & \frac{L_M r_r}{D_1} & \frac{L_M L_{rr}\omega_r}{D_1} \\ -\frac{{L_M}^2\omega_r}{\sqrt{3}D} & -\frac{r_s L_{rr}}{D} & -\frac{\sqrt{3}L_M L_{rr}\omega_r}{2D} & \frac{\sqrt{3}L_M r_r}{2D} \\ \frac{2r_s L_M}{3D} & -\frac{2L_M\left(L_{ls}+\frac{2}{3}L_M\right)\omega_r}{\sqrt{3}D} & -\frac{r_r\left(L_{ls}+\frac{2}{3}L_M\right)}{D} & -\frac{L_{rr}\left(L_{ls}+\frac{2}{3}L_M\right)\omega_r}{D} \\ \frac{2L_M L_{ss}\omega_r}{3D} & \frac{2r_s L_M}{\sqrt{3}D} & \frac{L_{ss}L_{rr}\omega_r}{D} & -\frac{L_{ss}r_r}{D} \end{bmatrix}$$

$$[B] = \begin{bmatrix} \frac{L_{rr}}{D_1} & 0 \\ 0 & \frac{L_{rr}}{2D} \\ -\frac{2L_M}{3D} & 0 \\ 0 & -\frac{L_M}{\sqrt{3}D} \end{bmatrix}$$

$$L_M = \frac{3}{2}L_{ms} \quad , \quad L_{ss} = L_{ls} + L_M \quad , \quad L_{rr} = L_{lr} + L_M$$

$$D = \left(L_{ss}L_{rr} - {L_M}^2\right)$$

$$D_1 = L_{ls}L_{rr} + \frac{2}{3}L_{lr}L_M$$

The electromagnetic torque of the machine can be derived from [55]

$$T_e = \frac{P}{2}\left[i_{s,abc}\right]\frac{\partial}{\partial\varphi_r}\left\{[L_{sr}]\left[i_{r,abc}\right]\right\} \tag{2.4.11}$$

When the in "abc" quantities in (2.4.11) are transformed into the "eo" and "$\alpha\beta$" frames, the electromagnetic torque can be re-written as

$$T_e = \frac{P}{2}L_M\left(\sqrt{3}i_{so}i_{r\alpha} - i_{se}i_{r\beta}\right) \tag{2.4.12}$$

The relation between the electrical and the mechanical components of the machine can be presented using the equation of the motion of the generator and is given by

$$p\omega_r = \frac{P}{2}\frac{1}{J}(T_T - T_e) \tag{2.4.13}$$

2.5 Turbine Models Used in Renewable Energy Generation

This generator topology is suitable mainly for renewable energy generation in wind and hydro power plants. In the wind power generation industry, two different designs of wind turbines are being used for electricity generation: the horizontal axis and the vertical axis. Vertical axis wind turbines (VAWT) such as Darrieus, Savonius, Giromill and Cycloturbine, are capable of capturing wind from different directions without using the yaw mechanism. It is quiet and maintenance is easy since the electrical components are installed at ground level [100-102]. They are more suitable for small-scale, distributed wind generation plants in urban environments. The main disadvantage of VAWT is the difficulty of designing a stall control at high wind speed to prevent over speed and over voltage when a permanent magnet synchronous generator is used [103-104]. Horizontal axis wind turbines (HAWT) are capable of

aerodynamic control at high wind speed in order to limit the speed and the voltage [105-107]. However, these types of wind turbines are commonly used in the large-scale wind farms located in an open topography such as a sea coast or plain where there is a consistent wind flow throughout the year [107]. In terms of the speed of the prime mover, the wind turbines can be classified into two categories: constant speed wind turbines (CSWT) and variable speed wind turbines (VSWT). CSWTs are aerodynamically less efficient than VSWTs. VSWTs extract more energy from wind since they can operate at the optimum rotor speed, thus increasing energy extraction by 20-30% than do the CSWTs. The advantage of the CSWTs is the simplicity of their stall control system [108].

The tip-speed ratio (TSR) of a wind turbine is the ratio between the tangential speed of the tip of a blade and the actual speed of the wind. The TSR is highly related to the efficiency of the wind turbine by optimizing the number of blades to be used. The relationship between TSR and the number of blades used is given by (2.5.1) [109].

$$TSR_{opt} = \frac{4\pi}{N_b} \tag{2.5.1}$$

The performance of the wind turbine is affected by the solidity of the rotor which depends on the number of blades used as in (2.5.2) [110].

$$\sigma = \frac{N_b C}{r} \tag{2.5.2}$$

The power that can be extracted from the available wind source depends on the power coefficient of the wind turbine [111]. The power coefficient is a higher-order function of the TSR and varies with different wind speeds. However, the theoretical maximum power coefficient has been defined by Betz in 1926 and is equal to 16/27 =0.59 [109].

Hydro turbines are categorized mainly into two groups: impulse turbines and reaction turbines [112]. The type of turbine selected for the hydro power plant depends mainly on the height of the standing water (the head). In addition, the efficiency and the cost are crucial since the cost of the hydro energy is competing with the conventional energy sources. In impulse turbines, the turbine runners are pushed and move due to the velocity of a water jet. These types of hydro turbines are used mostly in high head, low flow applications [112]. Pelton wheels and cross-flow

turbines are two different types of the impulse turbines. Due to the combined action of pressure and water movement, the reaction turbine converts the kinetic energy into electricity [113-114]. This hydro turbine is suitable for low or medium head applications. Propeller turbines, Francis turbines and kinetic energy turbines are examples of reaction turbines. . The power extracted by the hydro turbine P from the water stream can be given by (2.5.3) [115].

$$P = \eta.\rho.g.h.q \tag{2.5.3}$$

2.6 Modelling Issues of Induction Generator

Knowledge of the performance of the induction generator during both transient and steady-states is essential before it is utilized in an electricity generation scheme. An extensive work on transient and steady-state analysis of the induction generators has been reported in the literature [116-130]. Olorunfemi Ojo *et al.* [116] discuss transient analysis on a self-excited single-phase induction generator in d-q reference frame. Quinonez-Varela. G. et al. [121] analyses the transient conditions in abc reference frame. Transient analyses of the single-phase operations of three-phase induction machines are discussed in Murthy S.S. *et al.* [131], Mahato S. N. *et al.* [132], Shidhar L. *et al.* [133] and Liyanage D. [134]. Al-Bahrani A. H. et al. [49], Chan T.F. *et al.* [52-54] and Fukami T. *et al.* [51] discuss the steady-state performance analysis of the different arrangements of a three-phase induction generator employed to supply for the single-phase load. In some of the analyses, performance of the generator is discussed based on the assumption of linear magnetizing reactance. However, some analyses are based on the non-linear magnetizing reactance.

Magnetizing inductance plays a vital role in the dynamic analysis of induction generators. In the unsaturated region, the magnetizing reactance X_m is the ratio of air gap voltage V_g and magnetizing current I_m which is almost a constant, whereas in the saturated region this ratio decreases with the increasing magnetizing current. Therefore, it is important to identify the saturated magnetizing reactance for more accurate analysis [135-137]. In order to define a mathematical equation for the measured magnetizing characteristics of an induction machine, different approaches have been discussed in the literature. In Murthy S.S. *et al.* [138] and Devabhaktuni S. *et al.* [139], the non-linear region of the magnetizing characteristic curve is divided

into a few linear parts and each part is denoted by a linear equation to represent the saturation effect. In Murthy S.S. *et al.* [47, 140], the variation under the saturated region has been defined by an approximated linear curve. Seyoum D. *et al.* [137], Sandeep V. *et al.* [141] and Debta B. K. e*t al.* [142] have discussed a higher order curve fitting method to approximate the non-linear region of magnetizing characteristic curve. Rajakaruna S. *et al.* [128] presented a more interesting method to approximate the linear and non-linear regions of the magnetizing characteristics curve using two separate equations. This method matches most of the magnetizing characteristics very accurately. For convenience, the core loss resistance of an electrical machine has usually been neglected in most of the analyses [143]. However, consideration of the effect of core loss resistance on the dynamic behaviour of the induction machine has proved the increased accuracy of the analysis [144].

2.7 Summary

The increasing demand for renewable energy sources such as wind and hydro in electricity generation in the world has been discussed in the first part of this chapter. The role of induction generators in off-grid and grid connected energy generation schemes and the existing models of single-phase operation of three-phase induction generators are discussed in detail. A survey of the literature pertaining to the energy storage systems, the wind turbines used in renewable energy generation plants and the control techniques and issues are presented in this chapter. Furthermore, the existing dynamic model of the novel single-phase generator based on a three- phase induction machine has been presented. Due to the large discrepancy between the experimental and the computer simulation results reported in the literature, a comprehensive dynamic model which can improve the accuracy of theoretical results will be developed in the next Chapter.

CHAPTER 3- SYSTEM MODELLING

In order to analyse the dynamic behaviour of the single-phase operation of a three-phase induction generator, an incomplete set of equations has been presented in [55] by neglecting the effect of core loss resistance and the non-linear nature of the magnetizing reactance in the saturated region. The first objective of this thesis is to develop the dynamic mathematical model and the per-phase equivalent circuit of the single-phase induction generator that takes into consideration both the effect of core losses and the non-linearity of the magnetizing inductance in the saturated region. However, due to the following reasons, the dynamic equations given in [55] are not adequate for developing the comprehensive model.

- Equation (2.4.9) presents the voltage equations of rotor in stationary αβ reference frame. However, the highlighted segment of (2.4.9) is not meaningful in a voltage equation.

$$0 = L_{ms}\omega_r \begin{bmatrix} 0 & \sqrt{3} \\ -1 & 0 \end{bmatrix} [i_{s,eo}] + L_{ms} \begin{bmatrix} 1 & 0 \\ 0 & \sqrt{3} \end{bmatrix} p[i_{s,eo}] r_r [i_{r,\alpha\beta}] + \left(L_{lr} + \frac{3}{2}L_{ms}\right)$$

$$\omega_r \begin{bmatrix} 0 & 1 \\ -1 & 0 \end{bmatrix} [i_{r,\alpha\beta}] + \left(L_{lr} + \frac{3}{2}L_{ms}\right) p[i_{r,\alpha\beta}]$$

- When the state space model defined in (2.4.10) is simulated in Matlab software to reproduce the results presented in [55] with the same operating conditions, it is noted that the obtained outputs do not replicate the results in the literature. All the tests performed using the given state space model produce unstable outputs.
- Some matrix conversions are unclear. Each component of the model has to be simple and unequivocal.
- The model of the consumer load and the fixed excitation capacitor has not been presented.

In order to avoid the above identified errors of the existing model, in order for the model presented in this thesis to be more comprehensive and accurate; the dynamic

equations of the single-phase induction generator are developed by starting from the flux linkage of the windings of the standard three-phase induction machine.

3.1 Dynamic Model in Stationary αβ Reference Frame

The flux linkage can be defined as a product of the number of turns in a loop and the magnetic flux through the same loop as in (3.1.1).

$$\lambda = N\,\psi \tag{3.1.1}$$

By Faraday's law of induction, the electro motive force (emf) generated in the loop is given by (3.1.2)

$$e = N\frac{d}{dt}\psi \tag{3.1.2}$$

Thus, stator and rotor voltages in each phase of a standard three-phase machine can be presented by (3.1.3) and (3.1.4) respectively.

$$V_s = R_s i_s + \frac{d}{dt}\psi_s \tag{3.1.3}$$

$$V_r = R_r i_r + \frac{d}{dt}\psi_r \tag{3.1.4}$$

where ψ_s and ψ_r can be defined as (3.1.5) and (3.1.6) respectively.

$$\psi_s = \psi_{ls} + \psi_{ms} = L_{ls} i_s + M_s i_{m1} \tag{3.1.5}$$

$$\psi_r = \psi_{lr} + \psi_{mr} = L_{lr} i_r + M_r i_{m2} \tag{3.1.6}$$

M_s and M_r are the inductive parameters of stator and rotor respectively. By ignoring the core loss resistance of the machine, currents through the air -gap i.e. i_{m1} and i_{m2} can be defined as (3.1.7).

$$i_{m1} = i_{m2} = (i_s + i_r) \tag{3.1.7}$$

If the slip of the machine is given as 's', the per-phase voltage equations for stator and rotor windings of a standard three-phase induction machine can be represented by the equivalent circuit in Fig. 3.1.1. M_s and M_r are same and denoted by L_m in Fig. 3.1.1. Assuming the stator phase 'a' is as the reference phase and rotor phase 'a' is φ_r degree inclined to the reference phase, the magnetizing air-gap fluxes of stator and rotor of a three-phase induction machine can be defined as (3.1.8) and (3.1.9) respectively.

$$\psi_{ms} = L_{ms}\begin{bmatrix} 1 & \cos\left(\frac{2\pi}{3}\right) & \cos\left(-\frac{2\pi}{3}\right) \\ \cos\left(-\frac{2\pi}{3}\right) & 1 & \cos\left(\frac{2\pi}{3}\right) \\ \cos\left(\frac{2\pi}{3}\right) & \cos\left(-\frac{2\pi}{3}\right) & 1 \end{bmatrix}\begin{bmatrix} i_{sa} \\ i_{sb} \\ i_{sc} \end{bmatrix} + L_{sr}\begin{bmatrix} \cos\varphi_r & \cos(\varphi_r + \frac{2\pi}{3}) & \cos(\varphi_r - \frac{2\pi}{3}) \\ \cos(\varphi_r - \frac{2\pi}{3}) & \cos\varphi_r & \cos(\varphi_r + \frac{2\pi}{3}) \\ \cos(\varphi_r + \frac{2\pi}{3}) & \cos(\varphi_r - \frac{2\pi}{3}) & \cos\varphi_r \end{bmatrix}\begin{bmatrix} i_{ra} \\ i_{rb} \\ i_{rc} \end{bmatrix} \quad (3.1.8)$$

$$\psi_{mr} = L_{rs}\begin{bmatrix} \cos\varphi_r & \cos(\varphi_r - \frac{2\pi}{3}) & \cos(\varphi_r + \frac{2\pi}{3}) \\ \cos(\varphi_r + \frac{2\pi}{3}) & \cos\varphi_r & \cos(\varphi_r - \frac{2\pi}{3}) \\ \cos(\varphi_r - \frac{2\pi}{3}) & \cos(\varphi_r + \frac{2\pi}{3}) & \cos\varphi_r \end{bmatrix}\begin{bmatrix} i_{sa} \\ i_{sb} \\ i_{sc} \end{bmatrix} + L_{mr}\begin{bmatrix} 1 & \cos\left(\frac{2\pi}{3}\right) & \cos\left(-\frac{2\pi}{3}\right) \\ \cos\left(-\frac{2\pi}{3}\right) & 1 & \cos\left(\frac{2\pi}{3}\right) \\ \cos\left(\frac{2\pi}{3}\right) & \cos\left(-\frac{2\pi}{3}\right) & 1 \end{bmatrix}\begin{bmatrix} i_{ra} \\ i_{rb} \\ i_{rc} \end{bmatrix} \quad (3.1.9)$$

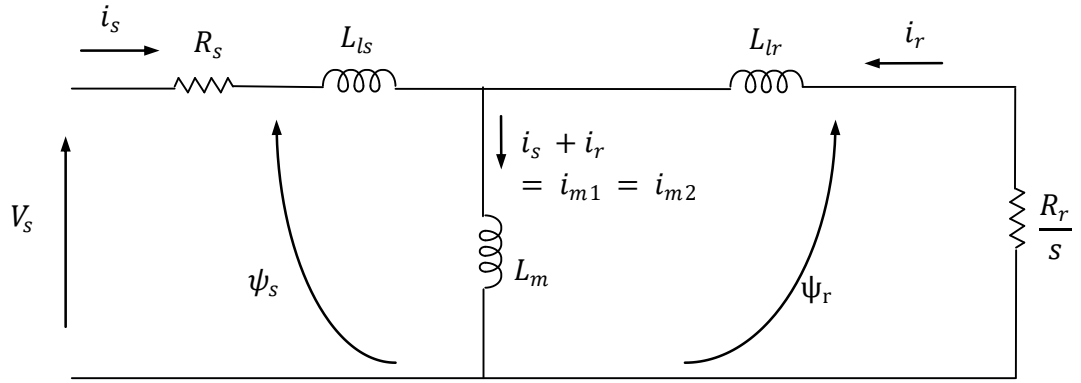

Fig. 3.1.1. Equivalent circuit of three-phase induction machine

Using (3.1.3)-(3.1.6) and (3.1.8)-(3.1.9), the voltage in each phase of stator and rotor in a stationary ‘abc’ reference frame can be presented by (3.1.10).

$$\begin{bmatrix} v_{sa} \\ v_{sb} \\ v_{sc} \\ v_{ra} \\ v_{rb} \\ v_{rc} \end{bmatrix} = \begin{bmatrix} R_s & 0 & 0 & -\omega_r L_{sr}\sin(\varphi_r) & -\omega_r L_{sr}\sin\left(\varphi_r+\frac{2\pi}{3}\right) & -\omega_r L_{sr}\sin\left(\varphi_r-\frac{2\pi}{3}\right) \\ 0 & R_s & 0 & -\omega_r L_{sr}\sin\left(\varphi_r-\frac{2\pi}{3}\right) & -\omega_r L_{sr}\sin(\varphi_r) & -\omega_r L_{sr}\sin\left(\varphi_r+\frac{2\pi}{3}\right) \\ 0 & 0 & R_s & -\omega_r L_{sr}\sin\left(\varphi_r+\frac{2\pi}{3}\right) & -\omega_r L_{sr}\sin\left(\varphi_r-\frac{2\pi}{3}\right) & -\omega_r L_{sr}\sin(\varphi_r) \\ -\omega_r L_{rs}\sin(\varphi_r) & -\omega_r L_{rs}\sin\left(\varphi_r-\frac{2\pi}{3}\right) & -\omega_r L_{rs}\sin\left(\varphi_r+\frac{2\pi}{3}\right) & R_r & 0 & 0 \\ -\omega_r L_{rs}\sin\left(\varphi_r+\frac{2\pi}{3}\right) & -\omega_r L_{rs}\sin(\varphi_r) & -\omega_r L_{rs}\sin\left(\varphi_r-\frac{2\pi}{3}\right) & 0 & R_r & 0 \\ -\omega_r L_{rs}\sin\left(\varphi_r-\frac{2\pi}{3}\right) & -\omega_r L_{rs}\sin\left(\varphi_r+\frac{2\pi}{3}\right) & -\omega_r L_{rs}\sin(\varphi_r) & 0 & 0 & R_r \end{bmatrix} \begin{bmatrix} i_{sa} \\ i_{sb} \\ i_{sc} \\ i_{ra} \\ i_{rb} \\ i_{rc} \end{bmatrix}$$

$$+ \begin{bmatrix} (L_{ls}+L_{ms}) & -\frac{1}{2}L_{ms} & -\frac{1}{2}L_{ms} & L_{sr}\cos(\varphi_r) & L_{sr}\cos\left(\varphi_r+\frac{2\pi}{3}\right) & L_{sr}\cos\left(\varphi_r-\frac{2\pi}{3}\right) \\ -\frac{1}{2}L_{ms} & (L_{ls}+L_{ms}) & -\frac{1}{2}L_{ms} & L_{sr}\cos\left(\varphi_r-\frac{2\pi}{3}\right) & L_{sr}\cos(\varphi_r) & L_{sr}\cos\left(\varphi_r+\frac{2\pi}{3}\right) \\ -\frac{1}{2}L_{ms} & -\frac{1}{2}L_{ms} & (L_{ls}+L_{ms}) & L_{sr}\cos\left(\varphi_r+\frac{2\pi}{3}\right) & L_{sr}\cos\left(\varphi_r-\frac{2\pi}{3}\right) & L_{sr}\cos(\varphi_r) \\ L_{rs}\cos(\varphi_r) & L_{rs}\cos\left(\varphi_r-\frac{2\pi}{3}\right) & L_{rs}\cos\left(\varphi_r+\frac{2\pi}{3}\right) & (L_{lr}+L_{mr}) & -\frac{1}{2}L_{mr} & -\frac{1}{2}L_{mr} \\ L_{rs}\cos\left(\varphi_r+\frac{2\pi}{3}\right) & L_{rs}\cos(\varphi_r) & L_{rs}\cos\left(\varphi_r-\frac{2\pi}{3}\right) & -\frac{1}{2}L_{mr} & (L_{lr}+L_{mr}) & -\frac{1}{2}L_{mr} \\ L_{rs}\cos\left(\varphi_r-\frac{2\pi}{3}\right) & L_{rs}\cos\left(\varphi_r+\frac{2\pi}{3}\right) & L_{rs}\cos(\varphi_r) & -\frac{1}{2}L_{mr} & -\frac{1}{2}L_{mr} & (L_{lr}+L_{mr}) \end{bmatrix} \frac{d}{dt} \begin{bmatrix} i_{sa} \\ i_{sb} \\ i_{sc} \\ i_{ra} \\ i_{rb} \\ i_{rc} \end{bmatrix} \quad (3.1.10)$$

According to the standard notations of electrical circuits, the current in the output winding of the single-phase generator proposed in [55] is equal to the winding current in the stator phase ‘b’ and the negative value of that in the stator phase ‘c’. The output voltage is equal to the voltage difference of phase ‘b’ and ‘c’ windings. The winding current and voltage in stator phase ‘a’ are the same as the current and voltage in the excitation control winding respectively. This is illustrated in the schematic diagram in Fig. 2.4.1.

$$i_{so} = i_{sb} = -i_{sc} \quad (3.1.11)$$

$$i_{se} = i_{sa} \quad (3.1.12)$$

$$V_{so} = V_{sb} - V_{sc} \tag{3.1.13}$$

$$V_{se} = V_{sa} \tag{3.1.14}$$

Using (3.1.11) and (3.1.12), the voltage equations in (3.1.10) can be re-written as (3.1.15).

$$\begin{bmatrix} v_{sa} \\ v_{sb} \\ v_{sc} \\ v_{ra} \\ v_{rb} \\ v_{rc} \end{bmatrix} = \begin{bmatrix} R_s & 0 & -\omega_r L_{sr}\sin(\varphi_r) & -\omega_r L_{sr}\sin\left(\varphi_r + \frac{2\pi}{3}\right) & -\omega_r L_{sr}\sin\left(\varphi_r - \frac{2\pi}{3}\right) \\ 0 & R_s & -\omega_r L_{sr}\sin\left(\varphi_r - \frac{2\pi}{3}\right) & -\omega_r L_{sr}\sin(\varphi_r) & -\omega_r L_{sr}\sin\left(\varphi_r + \frac{2\pi}{3}\right) \\ 0 & -R_s & -\omega_r L_{sr}\sin\left(\varphi_r + \frac{2\pi}{3}\right) & -\omega_r L_{sr}\sin\left(\varphi_r - \frac{2\pi}{3}\right) & -\omega_r L_{sr}\sin(\varphi_r) \\ -\omega_r L_{rs}\sin(\varphi_r) & \sqrt{3}\omega_r L_{rs}\cos\varphi_r & R_r & 0 & 0 \\ -\omega_r L_{rs}\sin\left(\varphi_r + \frac{2\pi}{3}\right) & \sqrt{3}\omega_r L_{rs}\cos\left(\varphi_r + \frac{2\pi}{3}\right) & 0 & R_r & 0 \\ -\omega_r L_{rs}\sin\left(\varphi_r - \frac{2\pi}{3}\right) & \sqrt{3}\omega_r L_{rs}\cos\left(\varphi_r - \frac{2\pi}{3}\right) & 0 & 0 & R_r \end{bmatrix} \begin{bmatrix} i_{se} \\ i_{so} \\ i_{ra} \\ i_{rb} \\ i_{rc} \end{bmatrix}$$

$$+ \begin{bmatrix} (L_{ls} + L_{ms}) & 0 & L_{sr}\cos(\varphi_r) & L_{sr}\cos\left(\varphi_r + \frac{2\pi}{3}\right) & L_{sr}\cos\left(\varphi_r - \frac{2\pi}{3}\right) \\ -\frac{1}{2}L_{ms} & \left(L_{ls} + \frac{3}{2}L_{ms}\right) & L_{sr}\cos\left(\varphi_r - \frac{2\pi}{3}\right) & L_{sr}\cos(\varphi_r) & L_{sr}\cos\left(\varphi_r + \frac{2\pi}{3}\right) \\ -\frac{1}{2}L_{ms} & -\left(L_{ls} + \frac{3}{2}L_{ms}\right) & L_{sr}\cos\left(\varphi_r + \frac{2\pi}{3}\right) & L_{sr}\cos\left(\varphi_r - \frac{2\pi}{3}\right) & L_{sr}\cos(\varphi_r) \\ L_{rs}\cos(\varphi_r) & \sqrt{3}L_{rs}\sin\varphi_r & (L_{lr} + L_{mr}) & -\frac{1}{2}L_{mr} & -\frac{1}{2}L_{mr} \\ L_{rs}\cos\left(\varphi_r + \frac{2\pi}{3}\right) & \sqrt{3}L_{rs}\sin\left(\varphi_r + \frac{2\pi}{3}\right) & -\frac{1}{2}L_{mr} & (L_{lr} + L_{mr}) & -\frac{1}{2}L_{mr} \\ L_{rs}\cos\left(\varphi_r - \frac{2\pi}{3}\right) & \sqrt{3}L_{rs}\sin\left(\varphi_r - \frac{2\pi}{3}\right) & -\frac{1}{2}L_{mr} & -\frac{1}{2}L_{mr} & (L_{lr} + L_{mr}) \end{bmatrix} \frac{d}{dt}\begin{bmatrix} i_{se} \\ i_{so} \\ i_{ra} \\ i_{rb} \\ i_{rc} \end{bmatrix} \tag{3.1.15}$$

Using the equations of output voltage and excitation control voltage defined in (3.1.13) and (3.1.14) respectively, and assuming that the rotor voltage in each phase of a cage rotor machine is zero, six equations presented in (3.1.15) can be reduced to five equations as in (3.1.16).

$$\begin{bmatrix} v_{se} \\ v_{so} \\ 0 \\ 0 \\ 0 \end{bmatrix} = \begin{bmatrix} R_s & 0 & -\omega_r L_{sr}\sin(\varphi_r) & -\omega_r L_{sr}\sin\left(\varphi_r+\frac{2\pi}{3}\right) & -\omega_r L_{sr}\sin\left(\varphi_r-\frac{2\pi}{3}\right) \\ 0 & 2R_s & \sqrt{3}\omega_r L_{sr}\cos\varphi_r & \sqrt{3}\omega_r L_{sr}\cos\left(\varphi_r+\frac{2\pi}{3}\right) & \sqrt{3}\omega_r L_{sr}\cos\left(\varphi_r-\frac{2\pi}{3}\right) \\ -\omega_r L_{rs}\sin(\varphi_r) & \sqrt{3}\omega_r L_{rs}\cos\varphi_r & R_r & 0 & 0 \\ -\omega_r L_{rs}\sin\left(\varphi_r+\frac{2\pi}{3}\right) & \sqrt{3}\omega_r L_{rs}\cos\left(\varphi_r+\frac{2\pi}{3}\right) & 0 & R_r & 0 \\ -\omega_r L_{rs}\sin\left(\varphi_r-\frac{2\pi}{3}\right) & \sqrt{3}\omega_r L_{rs}\cos\left(\varphi_r-\frac{2\pi}{3}\right) & 0 & 0 & R_r \end{bmatrix} \begin{bmatrix} i_{se} \\ i_{so} \\ i_{ra} \\ i_{rb} \\ i_{rc} \end{bmatrix}$$

$$+ \begin{bmatrix} (L_{ls}+L_{ms}) & 0 & L_{sr}\cos(\varphi_r) & L_{sr}\cos\left(\varphi_r+\frac{2\pi}{3}\right) & L_{sr}\cos\left(\varphi_r-\frac{2\pi}{3}\right) \\ 0 & 2\left(L_{ls}+\frac{3}{2}L_{ms}\right) & \sqrt{3}L_{sr}\sin\varphi_r & \sqrt{3}L_{sr}\sin\left(\varphi_r+\frac{2\pi}{3}\right) & \sqrt{3}L_{sr}\sin\left(\varphi_r-\frac{2\pi}{3}\right) \\ L_{rs}\cos(\varphi_r) & \sqrt{3}L_{rs}\sin\varphi_r & (L_{lr}+L_{mr}) & -\frac{1}{2}L_{mr} & -\frac{1}{2}L_{mr} \\ L_{rs}\cos\left(\varphi_r+\frac{2\pi}{3}\right) & \sqrt{3}L_{rs}\sin\left(\varphi_r+\frac{2\pi}{3}\right) & -\frac{1}{2}L_{mr} & (L_{lr}+L_{mr}) & -\frac{1}{2}L_{mr} \\ L_{rs}\cos\left(\varphi_r-\frac{2\pi}{3}\right) & \sqrt{3}L_{rs}\sin\left(\varphi_r-\frac{2\pi}{3}\right) & -\frac{1}{2}L_{mr} & -\frac{1}{2}L_{mr} & (L_{lr}+L_{mr}) \end{bmatrix} \frac{d}{dt}\begin{bmatrix} i_{se} \\ i_{so} \\ i_{ra} \\ i_{rb} \\ i_{rc} \end{bmatrix} \quad (3.1.16)$$

In this equation, the stator parameters are in the ‘eo’ frame and the rotor parameters are in the ‘abc’ frame. To avoid the complexity of dealing with this multi-phase system, three-phases of the rotor are transformed into two phases. If the phase of excitation control winding in the ‘eo’ frame is aligned with the α-axis of the ‘αβ’ frame, the phase of output winding will be aligned on the β-axis as they are perpendicular to each other. This transformation is shown in Fig. 3.1.2.

Using the Park transformation, the rotor components in phases a, b and c in ‘abc’ frame can be transformed into ‘αβ’ frame as in (3.1.17).

$$\begin{bmatrix} u_{r\alpha} \\ u_{r\beta} \end{bmatrix} = \left(\frac{2}{3}\right) \begin{bmatrix} \cos\varphi_r & \cos\left(\varphi_r + \left(\frac{2\pi}{3}\right)\right) & \cos\left(\varphi_r - \left(\frac{2\pi}{3}\right)\right) \\ \sin\varphi_r & \sin\left(\varphi_r + \left(\frac{2\pi}{3}\right)\right) & \sin\left(\varphi_r - \left(\frac{2\pi}{3}\right)\right) \end{bmatrix} \begin{bmatrix} u_{ra} \\ u_{rb} \\ u_{rc} \end{bmatrix} \tag{3.1.17}$$

Using the inverse of (3.1.17), the rotor components in the ‘abc’ frame can be defined in terms of ‘αβ’ components as in (3.1.18).

$$\begin{bmatrix} u_{ra} \\ u_{rb} \\ u_{rc} \end{bmatrix} = \begin{bmatrix} \cos\varphi_r & \sin\varphi_r \\ \cos\left(\varphi_r + \left(\frac{2\pi}{3}\right)\right) & \sin\left(\varphi_r + \left(\frac{2\pi}{3}\right)\right) \\ \cos\left(\varphi_r - \left(\frac{2\pi}{3}\right)\right) & \sin\left(\varphi_r - \left(\frac{2\pi}{3}\right)\right) \end{bmatrix} \begin{bmatrix} u_{r\alpha} \\ u_{r\beta} \end{bmatrix} \tag{3.1.18}$$

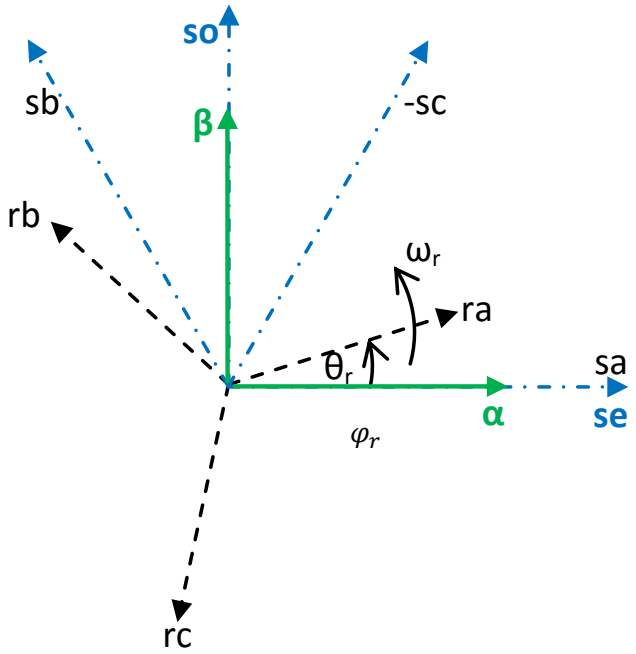

Fig. 3.1.2. αβ transformation of rotor phases a, b and c

Assuming the machine stator to rotor turns ratio is as 1:1 for the simplicity, L_{ms}, L_{sr}, L_{rs} and L_{mr} are considered to be equal to L_{ms}. From (3.1.16), the stator and rotor voltages can be defined as (3.1.19) and (3.1.20) respectively.

$$\begin{bmatrix} V_{se} \\ V_{so} \end{bmatrix} = \begin{bmatrix} R_s & 0 \\ 0 & 2R_s \end{bmatrix} \begin{bmatrix} i_{se} \\ i_{so} \end{bmatrix} + \omega_r L_{ms} \begin{bmatrix} -\sin\varphi_r & -\sin(\varphi_r + 2\pi/3) & -\sin(\varphi_r - 2\pi/3) \\ \sqrt{3}\cos\varphi_r & \sqrt{3}\cos(\varphi_r + 2\pi/3) & \sqrt{3}\cos(\varphi_r - 2\pi/3) \end{bmatrix} \begin{bmatrix} i_{ra} \\ i_{rb} \\ i_{rc} \end{bmatrix}$$

$$+ \begin{bmatrix} (L_{ls} + L_{ms}) & 0 \\ 0 & 2\left(L_{ls} + \frac{3}{2}L_{ms}\right) \end{bmatrix} \frac{d}{dt} \begin{bmatrix} i_{se} \\ i_{so} \end{bmatrix} +$$

$$L_{ms} \begin{bmatrix} \cos\varphi_r & \cos(\varphi_r + 2\pi/3) & \cos(\varphi_r - 2\pi/3) \\ \sqrt{3}\sin\varphi_r & \sqrt{3}\sin(\varphi_r + 2\pi/3) & \sqrt{3}\sin(\varphi_r - 2\pi/3) \end{bmatrix} \frac{d}{dt} \begin{bmatrix} i_{ra} \\ i_{rb} \\ i_{rc} \end{bmatrix} \quad (3.1.19)$$

$$\begin{bmatrix} 0 \\ 0 \\ 0 \end{bmatrix} = \begin{bmatrix} R_r & 0 & 0 \\ 0 & R_r & 0 \\ 0 & 0 & R_r \end{bmatrix} \begin{bmatrix} i_{ra} \\ i_{rb} \\ i_{rc} \end{bmatrix} + \omega_r L_{ms} \begin{bmatrix} -\sin\varphi_r & \sqrt{3}\cos\varphi_r \\ -\sin(\varphi_r + 2\pi/3) & \sqrt{3}\cos(\varphi_r + 2\pi/3) \\ -\sin(\varphi_r - 2\pi/3) & \sqrt{3}\cos(\varphi_r - 2\pi/3) \end{bmatrix} \begin{bmatrix} i_{se} \\ i_{so} \end{bmatrix}$$

$$+ \begin{bmatrix} (L_{lr} + L_{mr}) & -\frac{1}{2}L_{mr} & -\frac{1}{2}L_{mr} \\ -\frac{1}{2}L_{mr} & (L_{lr} + L_{mr}) & -\frac{1}{2}L_{mr} \\ -\frac{1}{2}L_{mr} & -\frac{1}{2}L_{mr} & (L_{lr} + L_{mr}) \end{bmatrix} \frac{d}{dt} \begin{bmatrix} i_{ra} \\ i_{rb} \\ i_{rc} \end{bmatrix} +$$

$$L_{ms} \begin{bmatrix} \cos\varphi_r & \sqrt{3}\sin\varphi_r \\ \cos(\varphi_r + 2\pi/3) & \sqrt{3}\sin(\varphi_r + 2\pi/3) \\ \cos(\varphi_r - 2\pi/3) & \sqrt{3}\sin(\varphi_r + 2\pi/3) \end{bmatrix} \frac{d}{dt} \begin{bmatrix} i_{se} \\ i_{so} \end{bmatrix} \quad (3.1.20)$$

After substituting for rotor components from (3.1.17) – (3.1.18) and lengthy mathematical work-out given in Appendix A, the stator and rotor voltages in stationary 'αβ' reference frame can be presented as (3.1.21) and (3.1.22) respectively.

$$\begin{bmatrix} V_{se} \\ V_{so} \end{bmatrix} =$$

$$\begin{bmatrix} R_s & 0 \\ 0 & 2R_s \end{bmatrix} \begin{bmatrix} i_{se} \\ i_{so} \end{bmatrix} + \begin{bmatrix} (L_{ls} + L_{ms}) & 0 \\ 0 & 2\left(L_{ls} + \frac{3}{2}L_{ms}\right) \end{bmatrix} \frac{d}{dt} \begin{bmatrix} i_{se} \\ i_{so} \end{bmatrix} + \frac{3}{2}L_{ms} \begin{bmatrix} 1 & 0 \\ 0 & \sqrt{3} \end{bmatrix} \frac{d}{dt} \begin{bmatrix} i_{r\alpha} \\ r_{r\beta} \end{bmatrix} \quad (3.1.21)$$

$$\begin{bmatrix} 0 \\ 0 \end{bmatrix} =$$

$$\omega_r L_{ms} \begin{bmatrix} 0 & \sqrt{3} \\ -1 & 0 \end{bmatrix} \begin{bmatrix} i_{se} \\ i_{so} \end{bmatrix} + L_{ms} \begin{bmatrix} 1 & 0 \\ 0 & \sqrt{3} \end{bmatrix} \frac{d}{dt} \begin{bmatrix} i_{se} \\ i_{so} \end{bmatrix} + \begin{bmatrix} R_r & 0 \\ 0 & R_r \end{bmatrix} \begin{bmatrix} i_{r\alpha} \\ r_{r\beta} \end{bmatrix} + \omega_r \left(L_{lr} + \frac{3}{2}L_{ms}\right) \begin{bmatrix} 0 & 1 \\ -1 & 0 \end{bmatrix} \begin{bmatrix} i_{r\alpha} \\ r_{r\beta} \end{bmatrix} +$$

$$\left(L_{lr} + \frac{3}{2}L_{ms}\right) \begin{bmatrix} 1 & 0 \\ 0 & 1 \end{bmatrix} \frac{d}{dt} \begin{bmatrix} i_{r\alpha} \\ r_{r\beta} \end{bmatrix} \quad (3.1.22)$$

The error identified in (2.4.9) has been corrected in the above equation. The highlighted part in (3.1.22) shows that it is a sum of the voltage across the rotor

resistance and the mutual induction instead of the product of these two components as given in (2.4.9).

In order to discover the errors that persist in the state space model given in (2.4.10), the same approach given in [55] is used to develop the state space model described below. The voltage equations of stator and rotor given in (3.1.21) and (3.1.22) is combined to form one matrix as in (3.1.23).

$$\begin{bmatrix} V_{se} \\ V_{so} \\ 0 \\ 0 \end{bmatrix} = \begin{bmatrix} R_s & 0 & 0 & 0 \\ 0 & 2R_s & 0 & 0 \\ 0 & \sqrt{3}L_{ms}\omega_r & R_r & \omega_r\left(L_{lr}+\frac{3L_{ms}}{2}\right) \\ -L_{ms}\omega_r & 0 & -\omega_r\left(L_{lr}+\frac{3L_{ms}}{2}\right) & R_r \end{bmatrix} \begin{bmatrix} i_{se} \\ i_{so} \\ i_{r\alpha} \\ i_{r\beta} \end{bmatrix}$$

$$+ \begin{bmatrix} (L_{ls}+L_{ms}) & 0 & \frac{3L_{ms}}{2} & 0 \\ 0 & (2L_{ls}+3L_{ms}) & 0 & \frac{3\sqrt{3}L_{ms}}{2} \\ L_{ms} & 0 & \left(L_{lr}+\frac{3L_{ms}}{2}\right) & 0 \\ 0 & \sqrt{3}L_{ms} & 0 & \left(L_{lr}+\frac{3L_{ms}}{2}\right) \end{bmatrix} \frac{d}{dt} \begin{bmatrix} i_{se} \\ i_{so} \\ i_{r\alpha} \\ i_{r\beta} \end{bmatrix} \tag{3.1.23}$$

After substituting for inductive components in (3.1.23), it can be simplified as (3.1.24).

$$\begin{bmatrix} V_{se} \\ V_{so} \\ 0 \\ 0 \end{bmatrix} =$$

$$\begin{bmatrix} R_s & 0 & 0 & 0 \\ 0 & 2R_s & 0 & 0 \\ 0 & 2L_m\omega_r/\sqrt{3} & R_r & \omega_r L_{rr} \\ -2L_m\omega_r/3 & 0 & -\omega_r L_{rr} & R_r \end{bmatrix} \begin{bmatrix} i_{se} \\ i_{so} \\ i_{r\alpha} \\ i_{r\beta} \end{bmatrix} + \begin{bmatrix} (L_{ls}+2L_m/3) & 0 & L_m & 0 \\ 0 & 2L_{ss} & 0 & \sqrt{3}L_m \\ 2L_m/3 & 0 & L_{rr} & 0 \\ 0 & 2L_m/\sqrt{3} & 0 & L_{rr} \end{bmatrix} \frac{d}{dt} \begin{bmatrix} i_{se} \\ i_{so} \\ i_{r\alpha} \\ i_{r\beta} \end{bmatrix}$$

(3.1.24)

where $L_m = \frac{3}{2}L_{ms}$, $L_{ss} = L_{ls} + \frac{3}{2}L_{ms}$ and $L_{rr} = L_{lr} + \frac{3}{2}L_{ms}$

After choosing the elements of the current vector as the state variables and the lengthy calculations given in Appendix A, the simplified state space model can be presented as (3.1.25) where $D = L_{ss}L_{rr} - {L_m}^2$ and $D_1 = L_{ls}L_{rr} + \frac{2}{3}L_{lr}L_m$.

$$\frac{d}{dt}\begin{bmatrix} i_{se} \\ i_{so} \\ i_{r\alpha} \\ i_{r\beta} \end{bmatrix} = \begin{bmatrix} \left(\frac{L_{rr}}{D_1}\right) & 0 & \left(\frac{-L_m}{D_1}\right) & 0 \\ 0 & \left(\frac{L_{rr}}{2D}\right) & 0 & \left(\frac{-\sqrt{3}L_m}{2D}\right) \\ \left(\frac{-2L_m}{3D_1}\right) & 0 & \left(\frac{L_{ls}+\frac{2}{3}L_m}{D_1}\right) & 0 \\ 0 & \left(\frac{-L_m}{\sqrt{3}D}\right) & 0 & \left(\frac{L_{ss}}{D}\right) \end{bmatrix} \begin{bmatrix} V_{se} \\ V_{so} \\ 0 \\ 0 \end{bmatrix}$$

$$+ \begin{bmatrix} \left(\frac{-L_{rr}R_s}{D_1}\right) & \left(\frac{2{L_m}^2\omega_r}{\sqrt{3}D_1}\right) & \left(\frac{L_mR_r}{D_1}\right) & \left(\frac{L_m\omega_rL_{rr}}{D_1}\right) \\ \left(\frac{-{L_m}^2\omega_r}{\sqrt{3}D}\right) & \left(\frac{-L_{rr}R_s}{D}\right) & \left(\frac{-\sqrt{3}L_m\omega_rL_{rr}}{2D}\right) & \left(\frac{\sqrt{3}L_mR_r}{2D}\right) \\ \left(\frac{2L_mR_s}{3D_1}\right) & \left(\frac{-2L_m\omega_r(L_{ls}+2L_m/3)}{\sqrt{3}D_1}\right) & \left(\frac{-(L_{ls}+2L_m/3)R_r}{D_1}\right) & \left(\frac{-L_{rr}\omega_r(L_{ls}+2L_m/3)}{D_1}\right) \\ \left(\frac{2L_{ss}L_m\omega_r}{3D}\right) & \left(\frac{2L_mR_s}{\sqrt{3}D}\right) & \left(\frac{L_{ss}\omega_rL_{rr}}{D}\right) & \left(\frac{-L_{ss}R_r}{D}\right) \end{bmatrix} \begin{bmatrix} i_{se} \\ i_{so} \\ i_{r\alpha} \\ i_{r\beta} \end{bmatrix} \quad (3.1.25)$$

The comparison of the state space models developed in this thesis and [55] shows that the denominator of the each element in the third row of the both matrices A and B, are different from each other. The term D in the denominator in [55] has been replaced by the term D_1 in this thesis. In order to determine the accuracy of the model given in (3.1.25), some tests are carried out and the simulation results are compared with the experimental results. Due to the satisfactory agreement between those two results, (3.1.25) is considered as the accurate state space model of the newly developed single-phase induction generator. The dynamic equations formed for this state space model are used for future developments presented in this thesis.

The development of an equivalent circuit is important to gain a better understanding of the single-phase operation of a three-phase induction generator which has not been reported yet in the literature. In order to develop the equivalent circuit of the single-phase induction generator, the derived dynamic equations are arranged to form a circuit diagram as described in the next section.

3.2 Dynamic Equivalent Circuit in Stationary αβ Reference Frame

Stator and rotor voltages defined in (3.1.21) and (3.1.22) can be re-written as (3.2.1) - (3.2.4).

$$V_{se} = R_s i_{se} + L_{ls}\frac{d}{dt}i_{se} + L_{ms}\left(\frac{d}{dt}i_{se} + \frac{3}{2}\frac{d}{dt}i_{r\alpha}\right) \quad (3.2.1)$$

$$V_{so} = 2R_s i_{so} + 2L_{ls}\frac{d}{dt}i_{so} + 3L_{ms}\left(\frac{d}{dt}i_{so} + \frac{\sqrt{3}}{2}\frac{d}{dt}i_{r\beta}\right) \quad (3.2.2)$$

$$0 = L_{ms}\left(\frac{d}{dt}i_{se} + \frac{3}{2}\frac{d}{dt}i_{r\alpha}\right) + \sqrt{3}L_{ms}\omega_r i_{so} + \left(L_{lr} + \left(\frac{3}{2}\right)L_{ms}\right)\omega_r i_{r\beta} + R_r i_{r\alpha} + L_{lr}\frac{d}{dt}i_{r\alpha} \quad (3.2.3)$$

$$0 = \sqrt{3}L_{ms}\left(\frac{d}{dt}i_{so} + \frac{\sqrt{3}}{2}\frac{d}{dt}i_{r\beta}\right) - L_{ms}\omega_r i_{se} - \left(L_{lr} + \left(\frac{3}{2}\right)L_{ms}\right)\omega_r i_{r\alpha} + R_r i_{r\beta} + L_{lr}\frac{d}{dt}i_{r\beta} \quad (3.2.4)$$

Equations (3.2.1) and (3.2.3) represent the stator and the rotor voltages in the α-axis respectively. In both the equations, the air-gap voltage is given by $L_{ms}\left(\frac{d}{dt}i_{se} + \frac{3}{2}\frac{d}{dt}i_{r\alpha}\right)$. Similarly (3.2.2) and (3.2.4) represent the stator and the rotor voltages in β-axis respectively. The air-gap voltage of the stator winding is equal to $3L_{ms}\left(\frac{d}{dt}i_{so} + \frac{\sqrt{3}}{2}\frac{d}{dt}i_{r\beta}\right)$. However, the air-gap voltage in the rotor winding is equal to $1/\sqrt{3}$ times that of the stator winding. In order to form the same air-gap in both the windings, (3.2.4) is multiplied by $\sqrt{3}$ and given by (3.2.5).

$$0 = 3L_{ms}\left(\frac{d}{dt}i_{so} + \frac{\sqrt{3}}{2}\frac{d}{dt}i_{r\beta}\right) - \sqrt{3}L_{ms}\omega_r i_{se} - \sqrt{3}\left(L_{lr} + \left(\frac{3}{2}\right)L_{ms}\right)\omega_r i_{r\alpha} + \sqrt{3}R_r i_{r\beta} + \sqrt{3}L_{lr}\frac{d}{dt}i_{r\beta} \quad (3.2.5)$$

After substituting $i_{r\alpha} = (2/3)\, i_{r\alpha}{}'$ and $i_{r\beta} = (2/\sqrt{3})\, i_{r\beta}{}'$ in (3.2.1)-(3.2.3) and (3.2.5), they can be re-written as in (3.2.6)-(3.2.9).

$$V_{se} = R_s i_{se} + L_{ls}\frac{d}{dt}i_{se} + L_{ms}\frac{d}{dt}(i_{se} + i_{r\alpha'}) \quad (3.2.6)$$

$$V_{so} = 2R_s i_{so} + 2L_{ls}\frac{d}{dt}i_{so} + 3L_{ms}\frac{d}{dt}\left(i_{so} + i_{r\beta'}\right) \quad (3.2.7)$$

$$0 = L_{ms}\frac{d}{dt}(i_{se} + i_{r\alpha'}) + \sqrt{3}L_{ms}\omega_r\left(i_{so} + i_{r\beta'}\right) + \frac{2}{\sqrt{3}}L_{lr}\omega_r i_{r\beta'} + \frac{2}{3}R_r i_{r\alpha'} + \frac{2}{3}L_{lr}\frac{d}{dt}i_{r\alpha'} \quad (3.2.8)$$

$$0 = 3L_{ms}\frac{d}{dt}\left(i_{so} + i_{r\beta'}\right) - \sqrt{3}L_{ms}\omega_r(i_{se} + i_{r\alpha'}) - \frac{2}{\sqrt{3}}L_{lr}\omega_r i_{r\alpha'} + 2R_r i_{r\beta'} + 2L_{lr}\frac{d}{dt}i_{r\beta'} \quad (3.2.9)$$

Equation (3.2.6) together with (3.2.8) represents the stator and rotor voltages in the α-axis with the same air-gap voltage of $L_{ms}\frac{d}{dt}\left(i_{se} + i_{r\alpha'}\right)$. Similarly, (3.2.7) and (3.2.9) represent the stator and rotor voltages in β-axis with the same air-gap voltage of $3L_{ms}\frac{d}{dt}\left(i_{so} + i_{r\beta'}\right)$. Therefore, the rotor quantities can be referred to the stator across the air-gap voltage. Since the frequencies of the stator and rotor components

are the same in the stationary ‘αβ’ frame, the rotor elements can be referred to the stator with its own frequency. The equivalent circuit resulting from (3.2.6)-(3.2.9) is shown in Fig. 3.2.1.

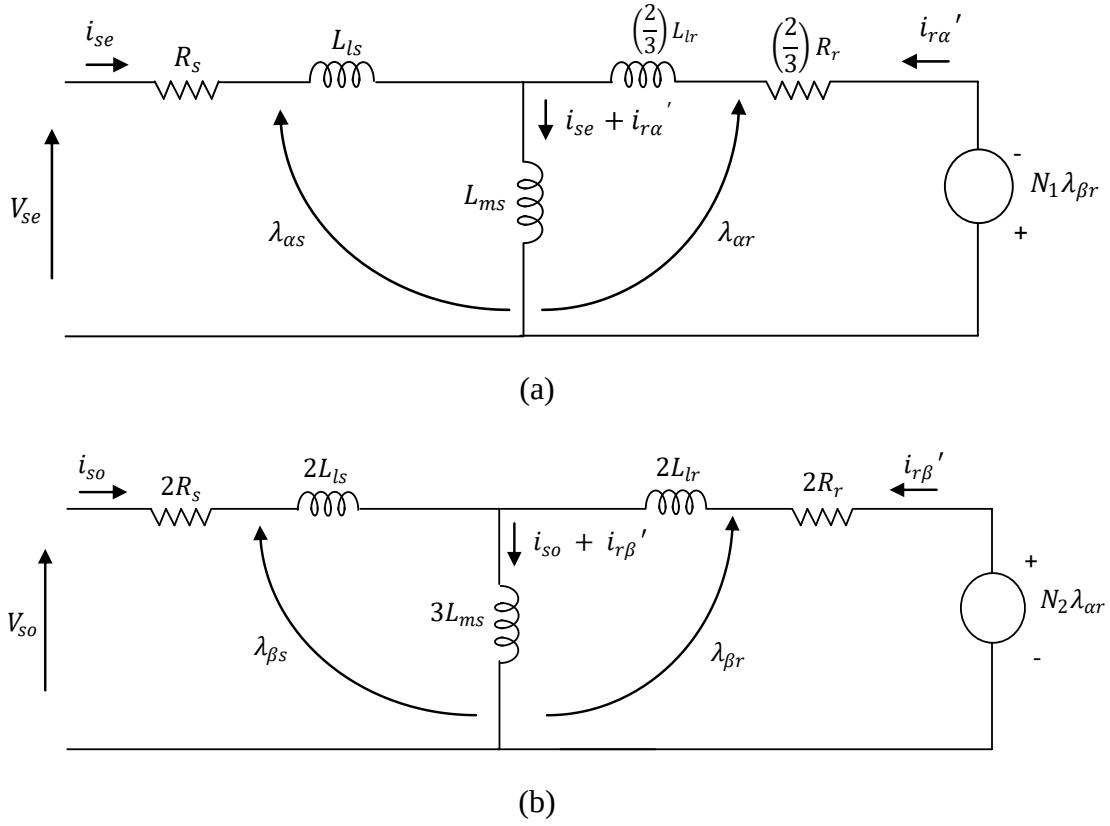

Fig. 3.2.1. Equivalent circuit of single-phase generator (a) α-axis (b) β-axis

where;

$$\lambda_{\beta r} = \left(3L_{ms}\left(i_{so} + i'_{r\beta}\right) + 2L_{lr}i'_{r\beta}\right)\omega_r \tag{3.2.10}$$

$$\lambda_{\alpha r} = \left(L_{ms}(i_{se} + i_{r\alpha}{}') + \left(\frac{2}{3}\right)L_{lr}i_{r\alpha}{}'\right)\omega_r \tag{3.2.11}$$

$$N_2 = \frac{1}{N_1} = \sqrt{3} \tag{3.2.12}$$

In phase ‘α’, the resistance and the leakage inductance of the stator is the same as per phase resistance and leakage inductance of a standard three-phase machine. Resistance and leakage inductance of the rotor and mutual inductance are 2/3 of the corresponding per phase values of a standard three-phase machine. However, voltages across the resistors and inductors remain the same since the rotor current is multiplied by 3/2. In phase ‘β’ where two stator windings are connected in series to form one winding, all the resistive and inductive components are twice those of standard per phase values.

In the above figure, the magnetizing characteristic of the machine is represented by a linear inductance. However, due to the single-phase operation of the three-phase induction machine, it is important to consider the non-linear effect of magnetizing inductance in the saturated region. Therefore, the magnetizing inductance must be represented by a non-linear inductance matching the non-linear region of the measured magnetizing characteristic. Also, it is important to include the core losses for accurate modelling of the induction generator. In this thesis, core losses are modelled by constant resistors which are parallel to the mutual inductances of each phase of the machine. The core loss resistance of phase 'α' is considered as R_c and that of phase 'β' is considered to be twice that of R_c. Thus, the comprehensive dynamic model and the equivalent circuit of the single-phase induction generator are developed in the next section to take into account both magnetic saturation and core losses which is not reported in the literature.

3.3 Comprehensive Dynamic Model and Equivalent Circuit in Stationary 'αβ' Reference Frame

When the core resistance is connected in parallel with the magnetizing inductance of each phase, currents through the magnetizing inductance i.e. i_{m1} and i_{m2} defined in (3.1.7) can be modified as (3.3.1).

$$i_{m1} = i_{m2} = (i_s + i_r) - i_{core} = i_{ms} + i_{mr} \tag{3.3.1}$$

Thus, using (3.1.8) and (3.1.9), the magnetizing air-gap fluxes of stator and rotor of a three-phase induction machine can be defined as (3.3.2) and (3.3.3) respectively.

$$\psi_{ms} = L_{ms}\begin{bmatrix} 1 & \cos\left(\frac{2\pi}{3}\right) & \cos\left(-\frac{2\pi}{3}\right) \\ \cos\left(-\frac{2\pi}{3}\right) & 1 & \cos\left(\frac{2\pi}{3}\right) \\ \cos\left(\frac{2\pi}{3}\right) & \cos\left(-\frac{2\pi}{3}\right) & 1 \end{bmatrix}\begin{bmatrix} i_{msa} \\ i_{msb} \\ i_{msc} \end{bmatrix} + L_{sr}\begin{bmatrix} \cos\varphi_r & \cos(\varphi_r + \frac{2\pi}{3}) & \cos(\varphi_r - \frac{2\pi}{3}) \\ \cos(\varphi_r - \frac{2\pi}{3}) & \cos\varphi_r & \cos(\varphi_r + \frac{2\pi}{3}) \\ \cos(\varphi_r + \frac{2\pi}{3}) & \cos(\varphi_r - \frac{2\pi}{3}) & \cos\varphi_r \end{bmatrix}\begin{bmatrix} i_{mra} \\ i_{mrb} \\ i_{mrc} \end{bmatrix} \tag{3.3.2}$$

$$\psi_{mr} = L_{rs}\begin{bmatrix} \cos\varphi_r & \cos(\varphi_r - \frac{2\pi}{3}) & \cos(\varphi_r + \frac{2\pi}{3}) \\ \cos(\varphi_r + \frac{2\pi}{3}) & \cos\varphi_r & \cos(\varphi_r - \frac{2\pi}{3}) \\ \cos(\varphi_r - \frac{2\pi}{3}) & \cos(\varphi_r + \frac{2\pi}{3}) & \cos\varphi_r \end{bmatrix}\begin{bmatrix} i_{msa} \\ i_{msb} \\ i_{msc} \end{bmatrix} + L_{mr}\begin{bmatrix} 1 & \cos\left(\frac{2\pi}{3}\right) & \cos\left(-\frac{2\pi}{3}\right) \\ \cos\left(-\frac{2\pi}{3}\right) & 1 & \cos\left(\frac{2\pi}{3}\right) \\ \cos\left(\frac{2\pi}{3}\right) & \cos\left(-\frac{2\pi}{3}\right) & 1 \end{bmatrix}\begin{bmatrix} i_{mra} \\ i_{mrb} \\ i_{mrc} \end{bmatrix} \tag{3.3.3}$$

Since the ratio of machine stator to rotor turns is considered as 1:1, L_{ms}, L_{sr}, L_{rs} and L_{mr} are equal and considered as L_{ms} for simplicity. As the magnetizing characteristics are non-linear in nature, in order to find out L_{ms} of the induction machine used for the experimental verification, the magnetizing air-gap flux was plotted against the magnetizing current and these results are approximated using separate equations as discussed in Appendix B. [128].

After following all the steps described from (3.1.10) to (3.1.20), the stator and rotor voltages of the comprehensive model which had taken into account the core loss resistance and magnetic saturation in the stationary 'αβ' reference frame can be given by (3.3.4) and (3.3.5) respectively.

$$\begin{bmatrix} V_{se} \\ V_{so} \end{bmatrix} = R_s \begin{bmatrix} 1 & 0 \\ 0 & 2 \end{bmatrix} \begin{bmatrix} i_{se} \\ i_{so} \end{bmatrix} + L_{ls} \begin{bmatrix} 1 & 0 \\ 0 & 2 \end{bmatrix} \frac{d}{dt} \begin{bmatrix} i_{se} \\ i_{so} \end{bmatrix} + L_{ms} \begin{bmatrix} 1 & 0 \\ 0 & 3 \end{bmatrix} \frac{d}{dt} \begin{bmatrix} i_{mse} \\ i_{mso} \end{bmatrix} + L_{ms} \begin{bmatrix} \frac{3}{2} & 0 \\ 0 & \frac{3\sqrt{3}}{2} \end{bmatrix} \frac{d}{dt} \begin{bmatrix} i_{mr\alpha} \\ i_{mr\beta} \end{bmatrix} \tag{3.3.4}$$

$$\begin{bmatrix} 0 \\ 0 \end{bmatrix} =$$

$$R_r \begin{bmatrix} i_{r\alpha} \\ i_{r\beta} \end{bmatrix} + L_{lr} \frac{d}{dt} \begin{bmatrix} i_{r\alpha} \\ i_{r\beta} \end{bmatrix} + \omega_r L_{lr} \begin{bmatrix} 0 & 1 \\ -1 & 0 \end{bmatrix} \begin{bmatrix} i_{r\alpha} \\ i_{r\beta} \end{bmatrix} + \frac{3}{2} L_{ms} \frac{d}{dt} \begin{bmatrix} i_{mr\alpha} \\ i_{mr\beta} \end{bmatrix} + \frac{3}{2} \omega_r L_{ms} \begin{bmatrix} 0 & 1 \\ -1 & 0 \end{bmatrix} \begin{bmatrix} i_{mr\alpha} \\ i_{mr\beta} \end{bmatrix} +$$

$$L_{ms} \begin{bmatrix} 1 & 0 \\ 0 & \sqrt{3} \end{bmatrix} \frac{d}{dt} \begin{bmatrix} i_{mse} \\ i_{mso} \end{bmatrix} + \omega_r L_{ms} \begin{bmatrix} 0 & \sqrt{3} \\ -1 & 0 \end{bmatrix} \begin{bmatrix} i_{mse} \\ i_{mso} \end{bmatrix} \tag{3.3.5}$$

By multiplying the second row of (20) by $\sqrt{3}$ and substituting $i_{r\alpha} = (2/3)\, i_{r\alpha}{}'$, $i_{mr\alpha} = (2/3)\, i_{mr\alpha}{}'$, $i_{r\beta} = (2/\sqrt{3})\, i_{r\beta}{}'$ and $i_{mr\beta} = (2/\sqrt{3})\, i_{mr\beta}{}'$ in (3.3.4)-(3.3.5), they can be re-written as in (3.3.6)-(3.3.7).

$$\begin{bmatrix} V_{se} \\ V_{so} \end{bmatrix} = R_s \begin{bmatrix} 1 & 0 \\ 0 & 2 \end{bmatrix} \begin{bmatrix} i_{se} \\ i_{so} \end{bmatrix} + L_{ls} \begin{bmatrix} 1 & 0 \\ 0 & 2 \end{bmatrix} \frac{d}{dt} \begin{bmatrix} i_{se} \\ i_{so} \end{bmatrix} + L_{ms} \begin{bmatrix} 1 & 0 \\ 0 & 3 \end{bmatrix} \frac{d}{dt} \begin{bmatrix} i_{me} \\ i_{mo} \end{bmatrix} \tag{3.3.6}$$

$$\begin{bmatrix} 0 \\ 0 \end{bmatrix} =$$

$$R_r \begin{bmatrix} \frac{2}{3} & 0 \\ 0 & 2 \end{bmatrix} \begin{bmatrix} i_{r\alpha}{}' \\ i_{r\beta}{}' \end{bmatrix} + L_{lr} \begin{bmatrix} \frac{2}{3} & 0 \\ 0 & 2 \end{bmatrix} \frac{d}{dt} \begin{bmatrix} i_{r\alpha}{}' \\ i_{r\beta}{}' \end{bmatrix} + L_{ms} \begin{bmatrix} 1 & 0 \\ 0 & 3 \end{bmatrix} \frac{d}{dt} \begin{bmatrix} i_{me} \\ i_{mo} \end{bmatrix} +$$

$$\frac{2}{\sqrt{3}} \omega_r L_{lr} \begin{bmatrix} 0 & 1 \\ -1 & 0 \end{bmatrix} \begin{bmatrix} i_{r\alpha}{}' \\ i_{r\beta}{}' \end{bmatrix} + \sqrt{3} \omega_r L_{ms} \begin{bmatrix} 0 & 1 \\ -1 & 0 \end{bmatrix} \begin{bmatrix} i_{me} \\ i_{mo} \end{bmatrix} \tag{3.3.7}$$

where; $i_{me} = i_{mse} + i_{mr\alpha}{}'$ and $i_{mo} = i_{mso} + i_{mr\beta}{}'$

Replacing the mutual inductance of α-axis i.e. L_{ms} by L_{m1} and the mutual inductance of the β-axis i.e. $3L_{ms}$ by L_{m2}, (21) and (23) can be re-written as (3.3.8)-(3.3.11).

$$V_{se} = R_s i_{se} + L_{ls} \frac{d}{dt} i_{se} + L_{m1} \frac{d}{dt} i_{me} \tag{3.3.8}$$

$$V_{so} = 2R_s i_{so} + 2L_{ls}\frac{d}{dt}i_{so} + L_{m2}\frac{d}{dt}i_{mo} \tag{3.3.9}$$

$$0 = \frac{2}{3}R_r i_{r\alpha}{}' + \frac{2}{3}L_{lr}\frac{d}{dt}i_{r\alpha}{}' + L_{m1}\frac{d}{dt}i_{me} + \frac{1}{\sqrt{3}}\omega_r\left(2L_{lr}i_{r\beta}{}' + L_{m2}i_{mo}\right) \tag{3.3.10}$$

$$0 = 2R_r i_{r\beta}{}' + 2L_{lr}\frac{d}{dt}i_{r\beta}{}' + L_{m2}\frac{d}{dt}i_{mo} - \sqrt{3}\omega_r\left(\frac{2}{3}L_{lr}i_{r\alpha}{}' + L_{m1}i_{me}\right) \tag{3.3.11}$$

Air-gap voltages in the α-axis and β-axis can be given by (3.3.12)-(3.3.13) respectively.

$$V_{m1} = L_{m1}\frac{d}{dt}i_{me} = R_c\, i_{c1} \tag{3.3.12}$$

$$V_{m2} = L_{m2}\frac{d}{dt}i_{mo} = 2R_c\, i_{c2} \tag{3.3.13}$$

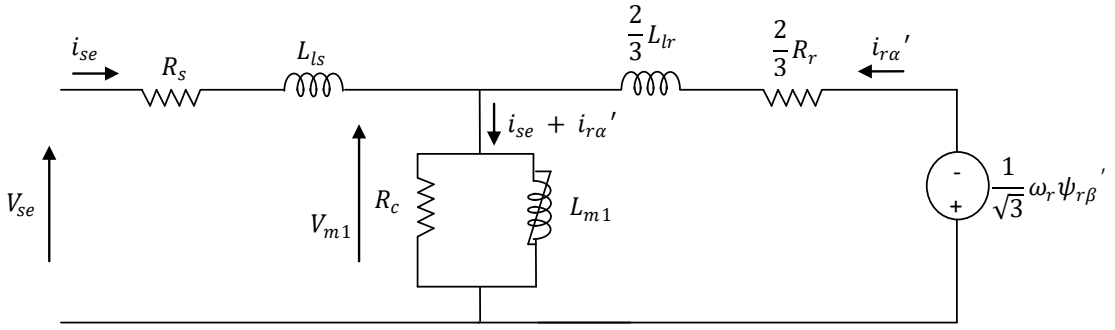

(a)

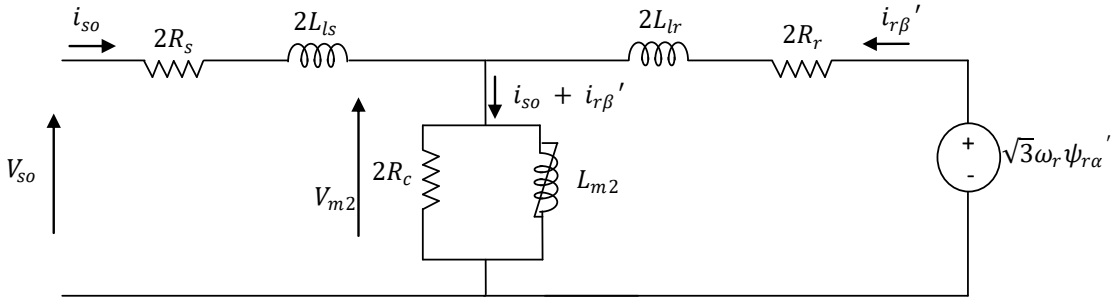

(b)

Fig. 3.3.1. Comprehensive dynamic equivalent circuit of single-phase generator (a) α-axis (b) β-axis

From (3.3.1), (3.3.12) and (3.3.13), the currents through the air-gap in α-axis and β-axis can be defined as (3.3.14)-(3.3.15) respectively.

$$i_{me} = i_{se} + i_{r\alpha}^{'} - \frac{L_{m1}}{R_c}\frac{d}{dt}i_{me} \tag{3.3.14}$$

$$i_{mo} = i_{so} + i_{r\beta}^{'} - \frac{L_{m2}}{2R_c}\frac{d}{dt}i_{mo} \quad (3.3.15)$$

The schematic diagram of the comprehensive equivalent circuit in the α-axis and β-axis resulting from (3.3.8)-(3.3.11) and (3.3.14)-(3.3.15) is illustrated in Fig. 3.3.1.

where

$$\psi_{\beta r}{}' = \left(2L_{lr}i_{r\beta}{}' + L_{m2}i_{mo}\right) \quad (3.3.16)$$

$$\psi_{\alpha r}{}' = \left(\frac{2}{3}L_{lr}i_{r\alpha}{}' + L_{m1}i_{me}\right) \quad (3.3.17)$$

3.4 The Load and the Excitation Capacitors

Since this single-phase induction generator is operated as a stand-alone generator to supply electricity for an isolated community, the most common uses of electricity may be for lighting and heating. Therefore, the consumer load can be considered as a single series RL load with a lagging power close to unity. For the simulations performed to demonstrate the operation of ECS, a series RL load is connected as the consumer load at the output winding. However, for the dynamic and steady-state analysis presented in this thesis, a single resistive load is used for reasons of practicality in laboratory experiments.

The fixed excitation capacitor connected in parallel with the consumer load is considered as an ideal capacitor. The electrical circuit of the model of load and excitation capacitor is illustrated in Fig. 3.4.1.

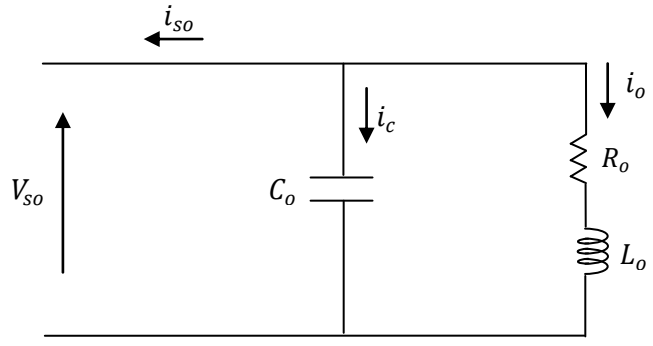

Fig. 3.4.1. The equivalent circuit of the consumer load and the fixed excitation capacitor

The voltage across RL load is the sum of voltage across the resistive load Ro and the inductive load Lo and can be defined as

$$V_{so} = R_o i_o + L_o \frac{d}{dt} i_o \tag{3.4.1}$$

The current through the fixed capacitor Co can be defined as the product of the capacitance and the time derivative of the output voltage.

$$i_c = C_o \frac{d}{dt} V_{so} \tag{3.4.2}$$

The addition of i_o and i_c is equal to the negative value of the single-phase output current i_{so} which can be defined as (3.4.3).

$$i_{so} = -(i_c + i_o) \tag{3.4.3}$$

In the case of ideal resistive load, the current through the load can be given as

$$i_o = \frac{V_{so}}{R_o} \tag{3.4.4}$$

Using (3.4.2)-(3.4.4), the relationship of output winding voltage and current can be given by (3.4.5).

$$i_{so} = -(C_o \frac{d}{dt} V_{so} + \frac{V_{so}}{R_o}) \tag{3.4.5}$$

3.5 The Electromagnetic Torque

The instantaneous electromagnetic torque of an electrical machine in terms of vector quantities can be defined as

$$T_e = \left(\frac{P}{2}\right) \frac{3}{2} \, imag \, (\boldsymbol{\psi}_s{}^* . \boldsymbol{i}_s) \tag{3.5.1}$$

Using (3.1.5), the space vector of the linked fluxes is the sum of the space vectors of leakage fluxes and magnetizing fluxes in the air-gap of the machine.

$$\boldsymbol{\psi}_s = \boldsymbol{\psi}_{ls} + \boldsymbol{\psi}_{ms} \tag{3.5.2}$$

Considering the stator phase ‘a’ of a three-phase electrical machine is as the real axis, the instantaneous leakage fluxes in three phases can be given in terms of vector quantities as (3.5.3)-(3.5.5).

$$\boldsymbol{\psi_{lsa}} = \psi_{lsa} \tag{3.5.3}$$

$$\boldsymbol{\psi_{lsb}} = \left(-\frac{1}{2} + j \frac{\sqrt{3}}{2}\right) . \psi_{lsb} \tag{3.5.4}$$

$$\boldsymbol{\psi_{lsc}} = \left(-\frac{1}{2} - j\,\frac{\sqrt{3}}{2}\right).\psi_{lsc} \tag{3.5.5}$$

The space vector of the leakage fluxes is equal to 2/3 of the sum of the above three vectors as given by (3.5.6).

$$\boldsymbol{\psi_{ls}} = \frac{2}{3}\left(\psi_{lsa} + \left(-\frac{1}{2} + j\,\frac{\sqrt{3}}{2}\right).\psi_{lsb} + \left(-\frac{1}{2} - j\,\frac{\sqrt{3}}{2}\right).\psi_{lsc}\right) \tag{3.5.6}$$

Similarly, the space vector of the magnetizing fluxes can be given as (3.5.7).

$$\boldsymbol{\psi_{ms}} = \frac{2}{3}\left(\psi_{msa} + \left(-\frac{1}{2} + j\,\frac{\sqrt{3}}{2}\right).\psi_{msb} + \left(-\frac{1}{2} - j\,\frac{\sqrt{3}}{2}\right).\psi_{msc}\right) \tag{3.5.7}$$

As the instantaneous current through the leakage inductance is equal to the stator current in each phase, the current vector related to the leakage fluxes can be defined by (3.5.8).

$$\boldsymbol{i_{ls}} = \frac{2}{3}\left(i_{sa} + \left(-\frac{1}{2} + j\,\frac{\sqrt{3}}{2}\right).i_{sb} + \left(-\frac{1}{2} - j\,\frac{\sqrt{3}}{2}\right).i_{sc}\right) \tag{3.5.8}$$

However, due to the core loss resistance connected in parallel with the magnetizing inductance, the instantaneous stator current through the magnetizing inductance is reduced by the current through the core loss resistance. Assuming that the total current through the core loss resistance is equal to the current supplied by the stator, the related current vector of the magnetizing fluxes can be given as (3.5.9).

$$\boldsymbol{i_{ms}} = \frac{2}{3}\left(i_{sa} + \left(-\frac{1}{2} + j\,\frac{\sqrt{3}}{2}\right).i_{sb} + \left(-\frac{1}{2} - j\,\frac{\sqrt{3}}{2}\right).i_{sc}\right) - \frac{2}{3}\left(i_{ca} + \left(-\frac{1}{2} + j\,\frac{\sqrt{3}}{2}\right).i_{cb} + \left(-\frac{1}{2} - j\,\frac{\sqrt{3}}{2}\right).i_{cc}\right) \tag{3.5.9}$$

In order to determine the space vectors of currents of the single-phase induction generator, i_{sa}, i_{sb} and i_{sc} are substituted by (3.1.8) and (3.1.7) respectively. The resulting vectors are given by (3.5.10) and (3.5.11).

$$\boldsymbol{i_{ls}} = \frac{2}{3}\left(i_{se} + \left(-\frac{1}{2} + j\,\frac{\sqrt{3}}{2}\right).i_{so} - \left(-\frac{1}{2} - j\,\frac{\sqrt{3}}{2}\right).i_{so}\right) \tag{3.5.10}$$

$$\boldsymbol{i_{ms}} = \frac{2}{3}\left(i_{se} + \left(-\frac{1}{2} + j\,\frac{\sqrt{3}}{2}\right).i_{so} - \left(-\frac{1}{2} - j\,\frac{\sqrt{3}}{2}\right).i_{so}\right) - \frac{2}{3}\left(i_{c1} + \left(-\frac{1}{2} + j\,\frac{\sqrt{3}}{2}\right).i_{c2} - \left(-\frac{1}{2} - j\,\frac{\sqrt{3}}{2}\right).i_{c2}\right) \tag{3.5.11}$$

In terms of real and imaginary components, the electromagnetic torque can be given by (3.5.12) as discussed in the Appendix A.

$$T_e = \left(\frac{P}{2}\right)\frac{3}{2}\left(\left(\boldsymbol{\psi_{lsR}}\boldsymbol{i_{lsI}} - \boldsymbol{\psi_{lsI}}\boldsymbol{i_{lsR}}\right) + \left(\boldsymbol{\psi_{msR}}\boldsymbol{i_{msI}} - \boldsymbol{\psi_{msI}}\boldsymbol{i_{msR}}\right)\right) \tag{3.5.12}$$

Real and imaginary components of current vector in (3.5.10) can be given by (3.5.13) and (3.5.14) respectively.

$$\boldsymbol{i}_{lsR} = \frac{2}{3} i_{se} \tag{3.5.13}$$

$$\boldsymbol{i}_{lsI} = \frac{2}{\sqrt{3}} i_{so} \tag{3.5.14}$$

Similarly, real and imaginary current components of (3.5.11) can be given as (3.5.15) and (3.5.16) respectively.

$$\boldsymbol{i}_{msR} = \frac{2}{3}(i_{se} - i_{c1}) \tag{3.5.15}$$

$$\boldsymbol{i}_{msI} = \frac{2}{\sqrt{3}}(i_{so} - i_{c2}) \tag{3.5.16}$$

When the complex equation in (3.5.6) represents the leakage flux vector is separated into real and imaginary components $\boldsymbol{\psi}_{lsR}$ and $\boldsymbol{\psi}_{lsI}$ can be defined as (3.5.17) and (3.5.18) respectively.

$$\boldsymbol{\psi}_{lsR} = \frac{2}{3}\left(\psi_{lsa} - \frac{1}{2}\psi_{lsb} - \frac{1}{2}\psi_{lsc}\right) \tag{3.5.17}$$

$$\boldsymbol{\psi}_{lsI} = \frac{2}{3}\left(\frac{\sqrt{3}}{2}\,\psi_{lsb} - \frac{\sqrt{3}}{2}\psi_{lsc}\right) \tag{3.5.18}$$

Similarly, the real and imaginary components of mutual flux vector in (3.5.7) can be given by (3.5.19) and (3.5.20) respectively.

$$\boldsymbol{\psi}_{msR} = \frac{2}{3}\left(\psi_{msa} - \frac{1}{2}\psi_{msb} - \frac{1}{2}\psi_{msc}\right) \tag{3.5.19}$$

$$\boldsymbol{\psi}_{msI} = \frac{2}{3}\left(\frac{\sqrt{3}}{2}\,\psi_{msb} - \frac{\sqrt{3}}{2}\psi_{msc}\right) \tag{3.5.20}$$

When the three phase quantities of rotor currents are transformed into two phases using the Park transformation and appropriate substitutions, three fluxes of the phases a, b and c of the stator given in (3.1.4) can be re-written as (3.5.21).

$$\begin{bmatrix}\psi_{sa}\\ \psi_{sb}\\ \psi_{sc}\end{bmatrix} = L_{ls}\begin{bmatrix}1 & 0\\ 0 & 1\\ 0 & -1\end{bmatrix}\begin{bmatrix}i_{se}\\ i_{so}\end{bmatrix} + \begin{bmatrix}L_{m1} & 0\\ -\frac{1}{2}L_{m1} & \frac{1}{2}L_{m2}\\ -\frac{1}{2}L_{m1} & -\frac{1}{2}L_{m2}\end{bmatrix}\left\{\begin{bmatrix}i_{se}\\ i_{so}\end{bmatrix} + \begin{bmatrix}i_{r\alpha}{}'\\ r_{r\beta}{}'\end{bmatrix} - \begin{bmatrix}i_{c1}\\ i_{c2}\end{bmatrix}\right\} \tag{3.5.21}$$

Thus, leakage and mutual fluxes can be written as (3.5.22) and (3.5.23) respectively.

$$\begin{bmatrix}\psi_{lsa}\\ \psi_{lsb}\\ \psi_{lsc}\end{bmatrix} = L_{ls}\begin{bmatrix}1 & 0\\ 0 & 1\\ 0 & -1\end{bmatrix}\begin{bmatrix}i_{se}\\ i_{so}\end{bmatrix} \tag{3.5.22}$$

$$\begin{bmatrix}\psi_{msa}\\ \psi_{msb}\\ \psi_{msc}\end{bmatrix} = \begin{bmatrix}L_{m1} & 0\\ -\frac{1}{2}L_{m1} & \frac{1}{2}L_{m2}\\ -\frac{1}{2}L_{m1} & -\frac{1}{2}L_{m2}\end{bmatrix}\left\{\begin{bmatrix}i_{se}\\ i_{so}\end{bmatrix} + \begin{bmatrix}i_{r\alpha}{}'\\ r_{r\beta}{}'\end{bmatrix} - \begin{bmatrix}i_{c1}\\ i_{c2}\end{bmatrix}\right\} \tag{3.5.23}$$

Using (3.5.13)-(3.5.20) and (3.5.22) - (3.5.23) and matrix calculations given in Appendix A, instantaneous electromagnetic torque given in (3.5.12) can be represented by four quantities of currents as

$$T_e = \left(\frac{P}{2}\right)\sqrt{3}\left(L_{m1}(i_{mo} - i_{r\beta}{}')i_{me} - \frac{1}{3}L_{m2}(i_{me} - i_{r\alpha}{}')i_{mo}\right) \quad (3.5.24)$$

3.6 The Wind Turbine

In the simulations carried out to study the operation of the ECS, an unregulated wind turbine is employed as the prime mover. It is assumed that during the operation of the ECS, the wind flow is constant for a given wind speed. Therefore, the transients are not expected due to changes in turbine input conditions. However, the effect of changing the turbine input can be studied as a change in a system parameter. Since, in this ECS, the prime mover is not regulated by the system, it will extract the maximum power available in the wind at a certain point. The power extracted by a wind turbine from the wind is determined by the power coefficient of the turbine which is a function of TSR and represented by a higher order polynomial. The relationship between the output power of the turbine and the power coefficient can be given by (3.6.1) [145].

$$P_T = \frac{1}{2}\rho_a A_T {V_w}^3 C_p \quad (3.6.1)$$

The torque of the wind turbine can be obtained by dividing the turbine output power by the angular speed of the turbine. Thus, the turbine torque can be given as

$$T_T = \frac{1}{2}\rho_a A_T {V_w}^2 R_T C_T \quad (3.6.2)$$

where $C_T = \frac{C_p}{TSR}$ (3.6.3)

In order to extract the maximum power available in the wind, the turbine should be operated at the peak of the power-speed characteristic curve. However, most of the wind turbines are operated after the peak region where the slope of the curve is negative. When a gear ratio is applied in between the turbine and the rotor, the torque-speed characteristics of the wind turbine for different wind speeds can be shown in Fig. 3.6.1 [145].

In a characteristic torque-speed curve, the region after the optimal torque point can be approximated by a straight line with a negative slope. In order to make the

analysis easier, the approximated line is used as the torque of the wind turbine in this thesis.

Therefore, the torque for a given speed of the rotor can be determined by

$$T_T = m\omega_r + C \tag{3.6.4}$$

If the negative slope m and any point on the straight line represents the torque-speed characteristics of the rotor is known, the torque at any given speed can be calculated by

$$T_T = T_0 + m(\omega_r - \omega_{r0}) \tag{3.6.5}$$

where T_0 and ω_{r0} are the coordinates of the any known point on the straight line.

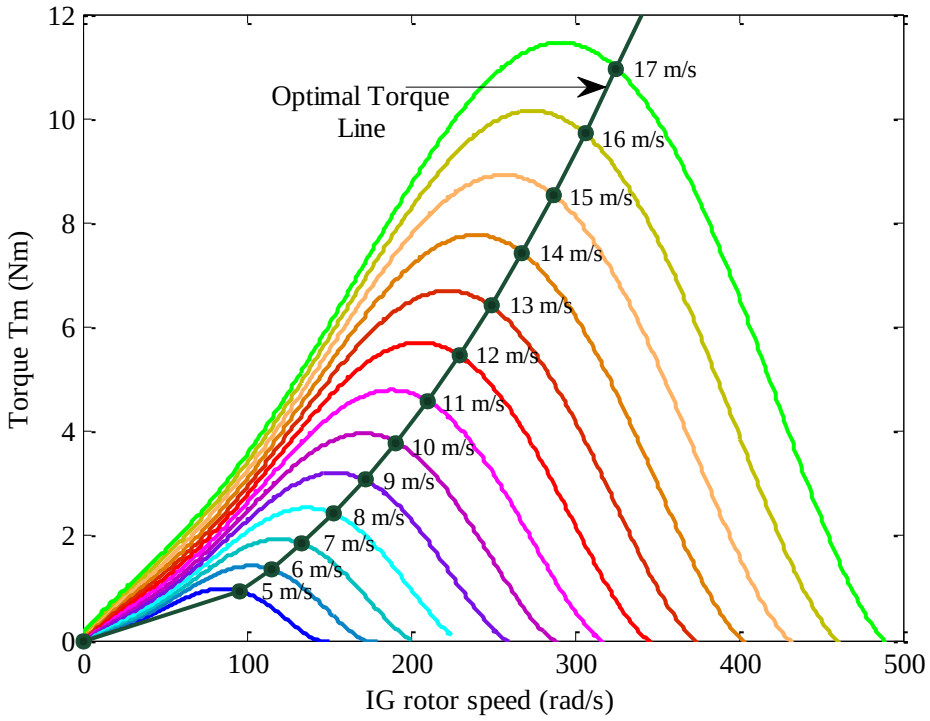

Fig. 3.6.1. Torque-speed characteristics of a wind turbine

Since all the dynamic equations derived for the single-phase generator are based on the conventional notations of a standard three-phase induction motor, the equation of motion is also defined assuming the electrical machine is operating as a motor. Thus, the equation of the motion of the induction machine can be given by

$$T_e = T_m + J\frac{d}{dt}\omega_m + B\omega_m \tag{3.6.6}$$

Using (3.5.24) and (3.6.5), the equation of motion of electrical machine can be given as (3.6.7).

$$0 = T_0 + m(\omega_r - \omega_{r0}) + \left(\frac{2}{P}\right) J \frac{d}{dt}\omega_r + \left(\frac{2}{P}\right) B\omega_r - \left(\frac{P}{2}\right)\sqrt{3}\left(L_{m1}(i_{mo} - i_{r\beta}{}')i_{me} - \frac{1}{3}L_{m2}(i_{me} - i_{r\alpha}{}')i_{mo}\right) \quad (3.6.7)$$

3.7 The Model of the Combined System

By combining the dynamic equations derived for each component of the ECS in preceding sections, (3.3.8) together with (3.3.9) - (3.3.11), (3.3.14) - (3.3.15), (3.4.1)-(3.4.3) and (3.6.7) describes the comprehensive dynamic model of the single-phase induction generator employed a three-phase cage rotor machine. Considering $\begin{bmatrix} i_{se} & i_{so} & i_{r\alpha}{}' & i_{r\beta}{}' & i_{me} & i_{mo} & V_{so} & i_o \end{bmatrix}^T$ is as the state vector, the state space model can be given as

$$\frac{d}{dt}[X] = A[X] + B[U] \quad (3.7.1)$$

where $A = -inv(A_2).A_1$ and $B = inv(A_2).A_1$, A_2 and U are defined as below.

$$A_1 = \begin{bmatrix} R_s & 0 & 0 & 0 & 0 & 0 & 0 & 0 \\ 0 & 2R_s & 0 & 0 & 0 & 0 & -1 & 0 \\ 0 & 0 & (2/3)R_r & \left(2/\sqrt{3}\right)L_{lr}\omega_r & 0 & (1/\sqrt{3})\,L_{m2}\omega_r & 0 & 0 \\ 0 & 0 & -\left(2/\sqrt{3}\right)L_{lr}\omega_r & 2R_r & \sqrt{3}L_{m1}\omega_r & 0 & 0 & 0 \\ 1 & 0 & 1 & 0 & -1 & 0 & 0 & 0 \\ 0 & 1 & 0 & 1 & 0 & -1 & 0 & 0 \\ 0 & 1 & 0 & 0 & 0 & 0 & 0 & 1 \\ 0 & 0 & 0 & 0 & 0 & 0 & 1 & -Ro \end{bmatrix}$$

$$A_2 = \begin{bmatrix} L_{ls} & 0 & 0 & 0 & L_{m1} & 0 & 0 & 0 \\ 0 & 2L_{ls} & 0 & 0 & 0 & L_{m2} & 0 & 0 \\ 0 & 0 & (2/3)L_{lr} & 0 & L_{m1} & 0 & 0 & 0 \\ 0 & 0 & 0 & 2L_{lr} & 0 & L_{m2} & 0 & 0 \\ 0 & 0 & 0 & 0 & -L_{m1}/R_c & 0 & 0 & 0 \\ 0 & 0 & 0 & 0 & 0 & -L_{m2}/(2R_c) & 0 & 0 \\ 0 & 0 & 0 & 0 & 0 & 0 & C_o & 0 \\ 0 & 0 & 0 & 0 & 0 & 0 & 0 & -L_o \end{bmatrix}$$

$$U = [V_{se} \quad 0 \quad 0 \quad 0 \quad 0 \quad 0 \quad 0 \quad 0]^T$$

There are only eight variables to be determined using the given eight equations. Using (3.6.7), the speed of the rotor can be determined. Thus, (3.7.1) and (3.6.7) are solved together to determine the system performance under any given operating condition. This newly proposed model is used for all the future developments presented in this thesis.

3.8 The Steady-state Model and Equivalent Circuit in Stationary αβ Reference Frame

The dynamic equations derived in the preceding section can be used to predict the system performance both in the transient and the steady-states. However, steady-state results can be obtained after an initial transient period. This becomes inconvenient for the specific purpose of steady-state analysis. Therefore, using (3.3.8)-(3.3.15), (3.4.1) and (3.4.2) the steady-state model where the resulting state variables are constant is derived to avoid this inconvenience. Since the dynamic model is derived in a stationary reference frame, the harmonic balance technique is applied to the above equations in order to derive the steady-state model [146-147].

Differential equations given by (3.3.8)-(3.3.15), (3.4.1) and (3.4.5) can be re-written as (3.8.1)-(3.8.10).

$$\frac{d}{dt}\psi_{se} = V_{se} - R_s i_{se} \tag{3.8.1}$$

$$\frac{d}{dt}\psi_{so} = V_{so} - 2R_s i_{so} \tag{3.8.2}$$

$$\frac{d}{dt}\psi_{\alpha r}{}' = -\frac{2}{3}R_r i_{r\alpha}{}' - \frac{1}{\sqrt{3}}\omega_r \psi_{\beta r}{}' \tag{3.8.3}$$

$$\frac{d}{dt}\psi_{\beta r}{}' = -2R_r i_{r\beta}{}' + \sqrt{3}\omega_r \psi_{r\alpha}{}' \tag{3.8.4}$$

$$\frac{d}{dt} i_{me} = \frac{V_{m1}}{L_{m1}} = \frac{R_c}{L_{m1}}\, i_{c1} \tag{3.8.5}$$

$$\frac{d}{dt} i_{mo} = \frac{V_{m2}}{L_{m2}} = \frac{2R_c}{L_{m2}}\, i_{c2} \tag{3.8.6}$$

$$\frac{d}{dt} i_{me} = \frac{R_c}{L_{m1}}(i_{se} + i_{r\alpha}' - i_{me}) \tag{3.8.7}$$

$$\frac{d}{dt} i_{mo} = \frac{2R_c}{L_{m2}}\left(i_{so} + i_{r\beta}' - i_{mo}\right) \tag{3.8.8}$$

$$\frac{d}{dt} i_o = \frac{1}{L_o}(V_{so} - R_o i_o) \tag{3.8.9}$$

$$\frac{d}{dt}V_{so} = \frac{1}{C_o}i_c \tag{3.8.10}$$

where;

$$\psi_{se} = L_{ls}i_{se} + L_{m1}i_{me} \tag{3.8.11}$$

$$\psi_{so} = 2L_{ls}i_{so} + L_{m2}i_{mo} \tag{3.8.12}$$

Considering the angular speed of generated voltage at the inverter output is ω_1, the state variables in (3.8.1)-(3.8.10) are multiplied by $e^{-j\omega_1 t}$and then added to the right hand-side of the (3.8.1)-(3.8.10) respectively. The resulting equations can be given by (3.3.13)-(3.3.22).

$$\frac{d}{dt}\psi_{se} = V_{se} - R_s i_{se} - j\omega_1\psi_{se} \tag{3.8.13}$$

$$\frac{d}{dt}\psi_{so} = V_{so} - 2R_s i_{so} - j\omega_1\psi_{so} \tag{3.8.14}$$

$$\frac{d}{dt}\psi_{\alpha r}{}' = -\frac{2}{3}R_r i_{r\alpha}{}' - \frac{1}{\sqrt{3}}\omega_r\psi_{\beta r}{}' - j\omega_1\psi_{\alpha r}{}' \tag{3.8.15}$$

$$\frac{d}{dt}\psi_{\beta r}{}' = -2R_r i_{r\beta}{}' + \sqrt{3}\omega_r\psi_{r\alpha}{}' - j\omega_1\psi_{\beta r}{}' \tag{3.8.16}$$

$$\frac{d}{dt}i_{me} = \frac{V_{m1}}{L_{m1}} = \frac{R_c}{L_{m1}}\, i_{c1} - j\omega_1 i_{me} \tag{3.8.17}$$

$$\frac{d}{dt}i_{mo} = \frac{V_{m2}}{L_{m2}} = \frac{2R_c}{L_{m2}}\, i_{c2} - j\omega_1 i_{mo} \tag{3.8.18}$$

$$\frac{d}{dt}i_{me} = \frac{R_c}{L_{m1}}(i_{se} + i_{r\alpha}' - \, i_{me}) - j\omega_1 i_{me} \tag{3.8.19}$$

$$\frac{d}{dt}i_{mo} = \frac{2R_c}{L_{m2}}\left(i_{so} + i_{r\beta}' - i_{mo}\right) - j\omega_1 i_{mo} \tag{3.8.20}$$

$$\frac{d}{dt}i_o = \frac{1}{L_o}(V_{so} - R_o i_o) - j\omega_1 i_o \tag{3.8.21}$$

$$\frac{d}{dt}V_{so} = \frac{1}{C_o}i_c - j\omega_1\, V_{so} \tag{3.8.22}$$

At the steady-state, the time derivatives of the state variables in the differential equations become zero. Therefore, the steady-state equations resulting from equations (3.8.13) to (3.8.22) can be written as (3.8.23) to (3.8.32).

$$V_{se} = R_s i_{se} + j\omega_1(L_{ls}i_{se} + L_{m1}i_{me}) \tag{3.8.23}$$

$$V_{so} = 2R_s i_{so} + j\omega_1(2L_{ls}i_{so} + L_{m2}i_{mo}) \tag{3.8.24}$$

$$0 = \frac{2}{3}R_r i_{r\alpha}{}' + j\omega_1\left(\frac{2}{3}L_{lr}i_{r\alpha}{}' + L_{m1}i_{me}\right) + \frac{1}{\sqrt{3}}\omega_r\psi_{\beta r}{}' \tag{3.8.25}$$

$$0 = 2R_r i_{r\beta}{}' + j\omega_1\left(2L_{lr} i_{r\beta}{}' + L_{m2} i_{mo}\right) - \sqrt{3}\omega_r \psi_{r\alpha}{}' \tag{3.8.26}$$

$$V_{m1} = j\omega_1 L_{m1} i_{me} = R_c\, i_{c1} \tag{3.8.27}$$

$$V_{m2} = j\omega_1 L_{m2} i_{mo} = 2R_c\, i_{c2} \tag{3.8.28}$$

$$i_{me} = (i_{se} + i'_{r\alpha}) - \frac{j\omega_1 L_{m1} i_{me}}{R_c} \tag{3.8.29}$$

$$i_{mo} = \left(i_{so} + i'_{r\beta}\right) - \frac{j\omega_1 L_{m2} i_{mo}}{2R_c} \tag{3.8.30}$$

$$V_{so} = R_o i_o + j\omega_1 L_o i_o \tag{3.8.31}$$

$$i_c = j\omega_1 C_o V_{so} \tag{3.8.32}$$

Steady-state equations together with the algebraic equations (3.4.3) and (3.4.4) describe the steady-state behaviour of the single-phase induction generator. The resulting equivalent circuit in stationary α-axis and β-axis is illustrated in Fig. 3.8.1.

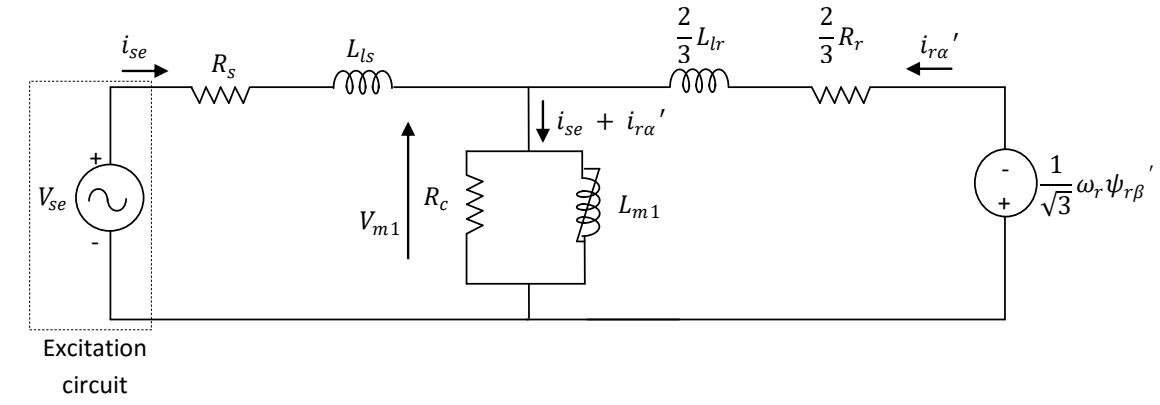

(a)

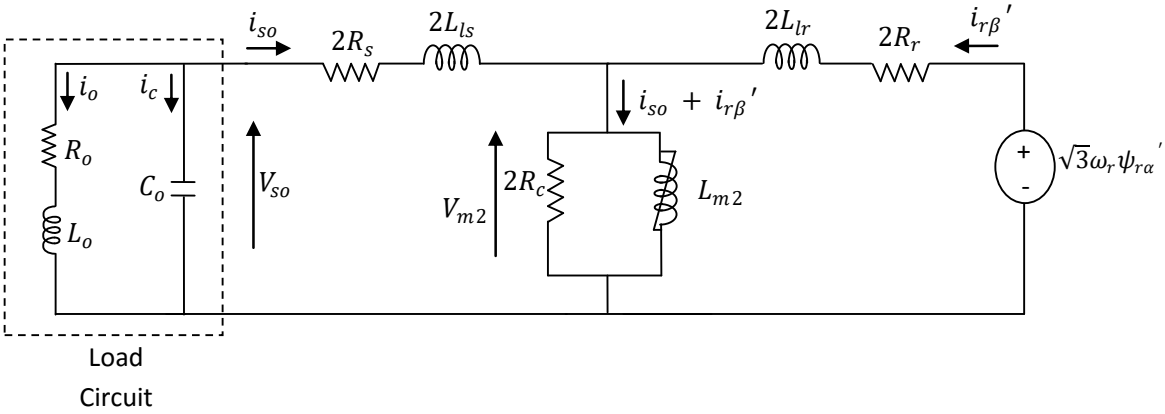

(b)

Fig. 3.8.1 Steady-state equivalent circuit of single-phase generator (a) α-axis (b) β-axis

CHAPTER 4- COMPUTATIONAL TECHNIQUES FOR STEADY-STATE

4.1 Introduction

The steady-state model of the single-phase induction generator has not been reported in the existing literature. Therefore, the study of the system performance of this generator configuration in steady-state has never been discussed. One of the main objectives of this research program is to study the system performance in steady-state for a given set of operating parameters. In order to do so, it is essential to develop a computational technique which can be used to calculate the values of system variables in steady-state for a given set of operating parameters. This computational technique should capable of calculating the values of system variables using the derived steady-state equations of the single-phase induction generator presented in the preceding chapter.

In the first part of this calculation procedure, fixed capacitance, consumer load and rotor speed are considered as the given operating parameters. The voltage of the output winding is considered as a known system variable since it is the desired voltage of the generator. Using the developed steady-state equations, other system variables are defined as a function of output voltage for a given set of operating parameters. Once the output voltage is selected, all the system variables can be calculated using the derived expressions. This computational technique is based on the developed steady-state equivalent circuit of the single-phase induction generator in the α–axis and β–axis presented in Section 3.8. As discussed in Section 3.1, the excitation control and the output windings of the generator can be represented by α–axis and β–axis respectively. Thus, adding the excitation circuit to the α–axis and the load circuit to the β-axis, the steady-state equivalent circuit of the single-phase generator is shown in Fig. 4.1.1. In the calculations, the non-linear nature of the magnetizing characteristics of both the windings in the saturated region is taken into account to increase the accuracy of the theoretical results. Although the speed of the

prime mover depends on the generator load, in these calculations, the speed of the rotor is considered as a given operating parameter.

In order to consider the effects of the prime mover on the generator performance, the torque-speed characteristics of the prime mover are included in the equations described in the second part of the calculation procedure. Similar to the previous section, the magnetic saturation is taken into account to increase the accuracy of the simulated results.

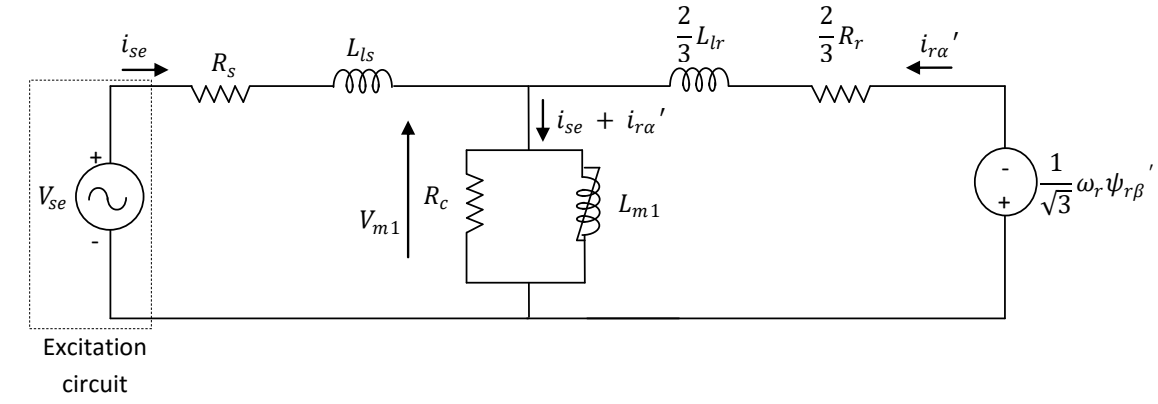

(a)

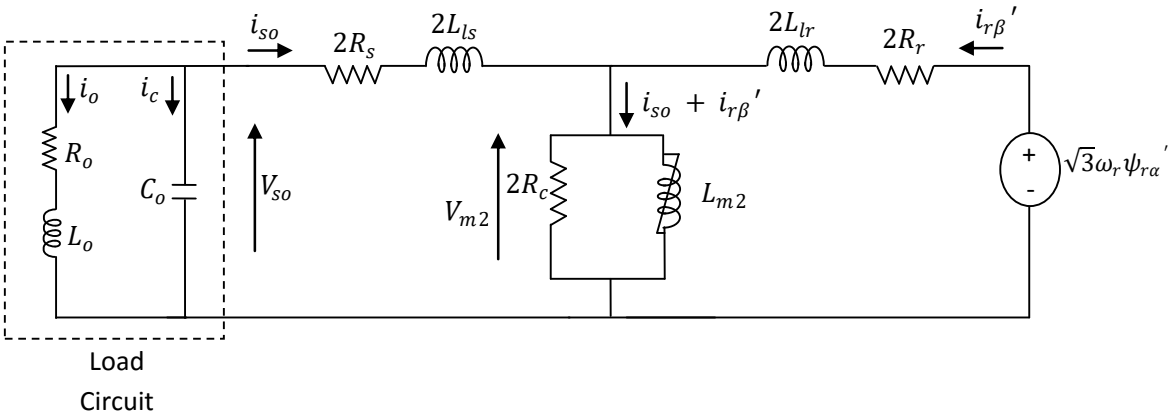

(b)

Fig. 4.1.1 Steady-state equivalent circuit of single-phase generator (a) α-axis (b) β-axis

Finally, a method is developed to calculate the operating parameters required to obtain a given system performance using the steady-state equivalent circuit of the single phase induction generator in α–axis and β–axis. Similar to the previous sections, these operating parameters are dependent on the output winding voltage. When the desired voltage of the output winding is specified, the fixed capacitance,

the consumer load, and the rotor speed can be calculated for a given power factor of the load.

4.2 Computation of system variables for given rotor speed

Since the operating parameters are connected to the output winding of the induction generator, the computational process is started from the equivalent circuit in the β-axis. Using the steady-state equations presented in section 3.8, the system variables in steady-state can be calculated for a given set of operating parameters using the fourteen steps described below.

Step 1:

Considering the current balance in (3.4.3), the equivalent resistance and inductance of the load circuit shown by the broken lines in Fig. 4.1.1 (b) can be given by (4.2.1) and (4.2.2) respectively.

$$R_{eq} = \frac{-{X_c}^2 R_o}{\left({R_o}^2+(X_o-X_c)^2\right)} \tag{4.2.1}$$

$$X_{eq} = \frac{X_c\left({R_o}^2+X_o(X_o-X_c)\right)}{\left({R_o}^2+(X_o-X_c)^2\right)} \tag{4.2.2}$$

where X_o and X_c are defined as below.

$$X_o = \omega_1 L_o \tag{4.2.3}$$

$$X_c = \frac{1}{\omega_1 C_o} \tag{4.2.4}$$

Thus the output winding current can be expressed in terms of the equivalent resistance and inductance as (4.2.5).

$$i_{so} = \left(\frac{1}{R_{eq}+jX_{eq}}\right) V_{so} \tag{4.2.5}$$

Step 2:

By substituting for $j\omega_1 L_{m2} i_{mo}$ in (3.8.24) from (3.8.28), output winding voltage can be re-written as,

$$V_{so} = (2R_s + j2\omega_1 L_{ls}) i_{so} + V_{m2} \tag{4.2.6}$$

In order to calculate the magnetizing voltage V_{m2} in output winding for the given set of operating parameters, the calculated output winding current in (4.2.5) can be substituted in (4.2.6). The resulting magnetizing voltage can be given by (4.2.7).

$$V_{m2} = \left(\mu_{eqt} + j\gamma_{eqt}\right)V_{so} \tag{4.2.7}$$

where the unitless variables μ_{eqt} and γ_{eqt} of (4.2.7) can be given as,

$$\mu_{eqt} = 1 - \frac{2(R_s R_{eq} + \omega_1 L_{ls} X_{eq})}{\left({R_{eq}}^2 + {X_{eq}}^2\right)} \tag{4.2.8}$$

$$\gamma_{eqt} = \frac{2\left(R_s X_{eq} - \omega_1 L_{ls} R_{eq}\right)}{\left({R_{eq}}^2 + {X_{eq}}^2\right)} \tag{4.2.9}$$

Thus, the magnitude of the magnetizing voltage in β–axis can be written as,

$$|V_{m2}| = \sqrt{{\mu_{eqt}}^2 + {\gamma_{eqt}}^2}|V_{so}| \tag{4.2.10}$$

Step 3:

Using the magnetizing characteristics curve, the magnetizing inductance L_m can be expressed as the ratio of magnetizing flux ψ_m and magnetizing current i_m as

$$L_m = \frac{\psi_m}{i_m} \tag{4.2.11}$$

Using the per unit steady-state relation, the magnetizing flux is the ratio of magnetizing voltage V_m and the angular frequency of the magnetizing current ω_1 as given in (4.2.12):

$$\psi_m = \frac{V_m}{\omega_1} \tag{4.2.12}$$

The magnetizing inductance is given by (4.2.13):

$$L_m = \frac{V_m}{\omega_1 i_m} \tag{4.2.13}$$

The magnetizing characteristic of the machine has been approximated by three separate equations as discussed in the Appendix B. In the first linear region, the magnetizing inductance is independent of the magnetizing current and can be given as a constant. In the second linear region and the saturated region, the magnetizing currents of the machine can be approximated by (4.2.14) and (4.2.15) respectively.

$$i_m = \frac{1}{K_l}(\psi_m + C) \tag{4.2.14}$$

$$i_m = i_{mo1} + \frac{1}{b}\tan\left(b\left(\frac{1}{K_l}(\psi_m + C) - i_{mo1}\right)\right) \tag{4.2.15}$$

where K_l , i_{mo1} , b and C are constants used to obtain the best approximated curve for the measured magnetizing characteristics of the machine. Thus, from (4.2.12) and (4.2.13), the magnetizing inductance for the two different regions can be given by (4.2.16) and (4.2.17) respectively:

$$L_m = \frac{K_l V_m}{\omega_1(\psi_m + C)} \tag{4.2.16}$$

$$L_m = \frac{V_m}{\omega_1\left[i_{mo1} + \frac{1}{b}\tan\left(b\left(\frac{1}{K_l}(\psi_m + C) - i_{mo1}\right)\right)\right]} \tag{4.2.17}$$

Since magnetizing voltage of the output winding V_{m2} is calculated from (4.2.10), the magnetizing inductance in β-axis L_{m2} can be obtained by substituting for the constant of the above equations as given in the Appendix B.

Step 4:

Substituting for $\omega_1 L_{m2} = X_{m2}$ and the calculated value of V_{m2} from (4.2.7) in (3.8.28), currents through the core loss resistance and mutual inductance can be calculated as

$$i_{c2} = \frac{\left(\mu_{eqt} + j\gamma_{eqt}\right)}{2R_c} V_{so} \tag{4.2.18}$$

$$i_{mo} = \frac{\left(\mu_{eqt} + j\gamma_{eqt}\right)}{jX_{m2}} V_{so} \tag{4.2.19}$$

Substituting the calculated system variables i_{so} , i_{c2} and i_{mo} and (3.8.28) in the current balance equation in (3.8.30) , rotor current in β–axis, $i_{r\beta}{}'$ can be calculated as (4.2.20):

$$i_{r\beta}{}' = \left(\mu_{eq1} + j\gamma_{eq1}\right)V_{so} \tag{4.2.20}$$

where variables μ_{eq1} and inductance γ_{eq1} with unit $1/\Omega$ as given as

$$\mu_{eq1} = \frac{\mu_{eqt}}{2R_c} + \frac{\gamma_{eqt}}{X_{m2}} - \frac{R_{eq}}{\left(R_{eq}{}^2 + X_{eq}{}^2\right)} \tag{4.2.21}$$

$$\gamma_{eq1} = \frac{\gamma_{eqt}}{2R_c} - \frac{\mu_{eqt}}{X_{m2}} + \frac{X_{eq}}{\left({R_{eq}}^2 + {X_{eq}}^2\right)} \tag{4.2.22}$$

Step 5:

Thus, from (3.3.17), (3.8.26) - (3.8.28), the rotor current in α-axis ${i_{r\alpha}}'$ can be expressed as a function of the magnetizing voltage in excitation control winding V_{m1} as (4.2.23).

$${i_{r\alpha}}' = \left(\frac{\sqrt{3}}{2L_{lr}\omega_r}\left(V_{m2} + 2(R_r + j\omega_1 L_{lr}){i_{r\beta}}'\right) - \frac{3V_{m1}}{j\omega_1 2L_{lr}}\right) \tag{4.2.23}$$

Substituting for $\omega_1 L_{m1} i_{me}$, $L_{m2} i_{mo}$ and ${\psi_{\beta r}}'$ in (3.8.25) from (3.8.27), (3.8.28) and (3.3.16) respectively, the rotor voltage in the α-axis can be re-written as

$$0 = \frac{2}{3}(R_r + j\omega_1 L_{lr}){i_{r\alpha}}' + V_{m1} + \frac{1}{\sqrt{3}}\omega_r\left(2L_{lr}{i_{r\beta}}' + \frac{V_{m2}}{j\omega_1}\right) \tag{4.2.24}$$

Substituting from (4.2.23) in (4.2.24) and after a lengthy manipulation, it leads to a single equation with only one unknownV_{m1}. V_{m1} can be calculated by (4.2.25):

$$V_{m1} = \left(R_{eq1} + jX_{eq1}\right){i_{r\beta}}' + \left(K_{eq1} + jK_{eq2}\right)V_{m2} \tag{4.2.25}$$

where the equivalent components are defined as

$$R_{eq1} = \left(\frac{-4{\omega_1}^2 L_{lr}}{\sqrt{3}\omega_r}\right) \tag{4.2.26}$$

$$X_{eq1} = \left(\frac{2\omega_1\left({R_r}^2 + {L_{lr}}^2({\omega_r}^2 - {\omega_1}^2)\right)}{\sqrt{3}\omega_r R_r}\right) \tag{4.2.27}$$

$$K_{eq1} = \left(\frac{L_{lr}({\omega_r}^2 - {\omega_1}^2)}{\sqrt{3}\omega_r R_r}\right) \tag{4.2.28}$$

$$K_{eq2} = \left(\frac{\omega_1}{\sqrt{3}\omega_r}\right) \tag{4.2.29}$$

Substituting for ${i_{r\beta}}'$ and V_{m2} in (4.2.25) from (4.2.20) and (4.2.7) respectively, the magnetizing voltage in α–axis can be expressed as a function of output voltage as

$$V_{m1} = \left(\mu_{eq2} + j\gamma_{eq2}\right)V_{so} \tag{4.2.30}$$

where variables μ_{eq2} and γ_{eq2} are defined as

$$\mu_{eq2} = \left(R_{eq1}\mu_{eq1} - X_{eq1}\gamma_{eq1}\right) + \left(K_{eq1}\mu_{eqt} - K_{eq2}\gamma_{eqt}\right) \tag{4.2.31}$$

$$\gamma_{eq2} = \left(\mu_{eq1}X_{eq1} + R_{eq1}\gamma_{eq1}\right) + \left(\mu_{eqt}K_{eq2} + \gamma_{eqt}K_{eq1}\right) \tag{4.2.32}$$

Thus, the magnitude of the magnetizing voltage in α–axis can be calculated by (4.2.33):

$$|V_{m1}| = \sqrt{{\mu_{eq2}}^2 + {\gamma_{eq2}}^2}\ |V_{so}| \tag{4.2.33}$$

Using (4.2.16) and (4.2.17) and the appropriate substitutions described in Appendix B, the magnetizing inductance in excitation control winding L_{m1} can be determined.

Step 6:

Using (3.8.27) and substituting for $\omega_1 L_{m1} = X_{m1}$, currents through the core loss resistance and mutual inductance in α-axis can be calculated by (4.2.34) and (4.2.35) respectively:

$$i_{c1} = \frac{(\mu_{eq2} + j\gamma_{eq2})}{R_c} V_{so} \tag{4.2.34}$$

$$i_{me} = \frac{(\mu_{eq2} + j\gamma_{eq2})}{jX_{m1}} V_{so} \tag{4.2.35}$$

Step 7:

Substituting for ${i_{r\beta}}'$, V_{m2} and V_{m1} from (4.2.20) , (4.2.7) and (4.2.30) respectively in (4.2.23), the rotor current in α–axis can be calculated by

$${i_{r\alpha}}' = (\mu_{eq3} + j\gamma_{eq3}) V_{so} \tag{4.2.36}$$

where variables μ_{eq3} and γ_{eq3} are given by (4.2.37) and (4.2.38) respectively:

$$\mu_{eq3} = \frac{\sqrt{3}}{L_{lr}} \left(\frac{(R_r \mu_{eq1} - \omega_1 L_{lr} \gamma_{eq1})}{\omega_r} + \frac{\mu_{eqt}}{2\omega_r} - \frac{\sqrt{3}\gamma_{eq2}}{2\omega_1} \right) \tag{4.2.37}$$

$$\gamma_{eq3} = \frac{\sqrt{3}}{L_{lr}} \left(\frac{(\omega_1 L_{lr} \mu_{eq1} + R_r \gamma_{eq1})}{\omega_r} + \frac{\gamma_{eqt}}{2\omega_r} + \frac{\sqrt{3}\mu_{eq2}}{2\omega_1} \right) \tag{4.2.38}$$

Step 8:

Using the current balance equation in (3.8.29), stator current in the excitation control winding i_{se} can be calculated by (4.2.39):

$$i_{se} = (\mu_{eq4} + j\gamma_{eq4}) V_{so} \tag{4.2.39}$$

where the variables of the equation are given as

$$\mu_{eq4} = \frac{\gamma_{eq2}}{X_{m1}} + \frac{\mu_{eq2}}{R_c} - \mu_{eq3} \tag{4.2.40}$$

$$\gamma_{eq4} = \frac{\gamma_{eq2}}{R_c} - \frac{\mu_{eq2}}{X_{m1}} - \gamma_{eq3} \tag{4.2.41}$$

Step 9:

As the last step in the calculation of generator variables, the excitation control voltage V_{se} can be calculated using (3.8.23):

$$V_{se} = \left(\mu_{eq5} + j\gamma_{eq5}\right)V_{so} \tag{4.2.42}$$

The variables of the equation are defined as

$$\mu_{eq5} = \left(\mu_{eq2} + R_s\mu_{eq4} - \omega_1 L_{ls}\gamma_{eq4}\right) \tag{4.2.43}$$

$$\gamma_{eq5} = \left(\gamma_{eq2} + \omega_1 L_{ls}\mu_{eq4} + R_s\gamma_{eq4}\right) \tag{4.2.44}$$

Step 10:

Using steps 1-9, generator variables have been defined in terms of output voltage for a given set of operating parameters. In this step, the resistive losses of the generator are calculated. The resistive losses due to the stator, rotor and core loss resistances in α-axis and β-axis can be expressed by (4.2.45)-(4.2.50):

$${i_{so}}^2 . 2R_s = \frac{2R_s}{\left({R_{eq}}^2 + {X_{eq}}^2\right)}{V_{so}}^2 \tag{4.2.45}$$

$${i_{c2}}^2 . 2R_c = \frac{{\mu_{eqt}}^2 + {\gamma_{eqt}}^2}{2R_c}{V_{so}}^2 \tag{4.2.46}$$

$${i_{r\beta}}'^2 . 2R_r = 2R_r\left({\mu_{eq1}}^2 + {\gamma_{eq1}}^2\right){V_{so}}^2 \tag{4.2.47}$$

$${i_{r\alpha}}'^2 . \frac{2}{3}R_r = \frac{2}{3}R_r\left({\mu_{eq3}}^2 + {\gamma_{eq3}}^2\right){V_{so}}^2 \tag{4.2.48}$$

$${i_{c1}}^2 . R_c = \frac{\left({\mu_{eq2}}^2 + {\gamma_{eq2}}^2\right)}{R_c}{V_{so}}^2 \tag{4.2.49}$$

$${i_{se}}^2 . R_s = R_s\left({\mu_{eq4}}^2 + {\gamma_{eq4}}^2\right){V_{so}}^2 \tag{4.2.50}$$

Therefore, the total resistive losses can be given by (4.2.51):

$$P_{r,loss} = {i_{so}}^2.2R_s + {i_{c2}}^2.2R_c + {i_{r\beta}}^{'2}.2R_r + {i_{r\alpha}}^{'2}.\frac{2}{3}R_r + {i_{c1}}^2.R_c + {i_{se}}^2.R_s \quad (4.2.51)$$

In order to simplify this expression, it can be re-written as

$$P_{r,loss} = K_{r,loss}.{V_{so}}^2 \quad (4.2.52)$$

where constant $K_{r,loss}$ is defined by,

$$K_{r,loss} = \frac{2R_s}{({R_{eq}}^2+{X_{eq}}^2)} + \frac{{\mu_{eqt}}^2+{\gamma_{eqt}}^2}{2R_c} + 2R_r\left({\mu_{eq1}}^2 + {\gamma_{eq1}}^2\right) + \frac{2}{3}R_r\left({\mu_{eq3}}^2 + {\gamma_{eq3}}^2\right) + \frac{({\mu_{eq2}}^2+{\gamma_{eq2}}^2)}{R_c} + R_s\left({\mu_{eq4}}^2 + {\gamma_{eq4}}^2\right) \quad (4.2.53)$$

Step 11:

The active power consumption at the output winding can be given as

$$P_{out} = {i_{so}}^2.R_{eq} \quad (4.2.54)$$

From (4.2.1) and (4.2.5), output power can be expressed in terms of output voltage as

$$P_{out} = -\frac{1}{\left({R_{eq}}^2+{X_{eq}}^2\right)}.\frac{{X_c}^2R_o}{({R_o}^2+(X_o-X_c)^2)}{V_{so}}^2 \quad (4.2.55)$$

Step 12:

The active power stored through the excitation control winding is given by

$$P_{ex} = V_{se}.i_{se}.PF_{se} \quad (4.2.56)$$

where PF_{se} is the power factor of the excitation control winding.

Substituting for i_{se} and V_{se} in (4.2.56) from (4.2.39) and (4.2.42) respectively:

$$P_{ex} = \left(\sqrt{{\mu_{eq5}}^2 + {\gamma_{eq5}}^2}\right).\left(\sqrt{{\mu_{eq4}}^2 + {\gamma_{eq4}}^2}\right).PF_{se}.{V_{so}}^2 \quad (4.2.57)$$

Step 13:

Considering a small-scale wind turbine as the prime mover, the input mechanical power of the generator can be given as

$$P_m = \left(T_0 + m(\omega_r - \omega_{r0})\right)\omega_r \quad (4.2.58)$$

where the parameters of the equation are as given in the Appendix C.

Step 14:

The active power balance is considered as the last step of the computational procedure.

If the input mechanical power is greater than what is required at the output and the resistive losses, the additional power is stored in the ESS through the excitation control winding. This can be written as

$$P_m = P_{out} + P_{ex} + P_{r,loss} \tag{4.2.59}$$

If the input mechanical power is not sufficient to supply the consumer demand, the deficit active power is supplied by ESS. This can be expressed by

$$P_m + P_{ex} = P_{out} + P_{r,loss} \tag{4.2.60}$$

The equations above have been derived based on the assumption that the rotor speed ω_r is known. However, a computational technique needs to be developed to calculate the values of system variables for a given set of operating parameters when the rotor speed depends on the consumer load. This procedure is discussed in the next section.

4.3 Computation of system variables for load-dependant rotor speed

The steps from 1 to 4 in the computational techniques described in section 4.2 are independent of the rotor speed ω_r. Thus, in steady-state, the system variables in the β-axis do not depend on the rotor speed. However, the system variables in the α-axis depend on the speed of the prime mover. Therefore, the computational methods used to calculate the system variables in steady-state, described in steps 5 to 9 in section 4.2 are re-arranged as steps 1 to 5 in the first part of this section.

Step 1:

As described in step 5 in section 4.2, the magnetizing voltage in α-axis can be written as

$$V_{m1} = \left(R_{eq1} + jX_{eq1}\right) i_{r\beta}{}' + \left(K_{eq1} + jK_{eq2}\right) V_{m2} \tag{4.3.1}$$

where the equivalent components are defined as

$$R_{eq1} = \left(\frac{-4{\omega_1}^2 L_{lr}}{\sqrt{3}}\right)\frac{1}{\omega_r} \tag{4.3.2}$$

$$X_{eq1} = \left(\frac{2\omega_1 {L_{lr}}^2}{\sqrt{3}R_r}\right)\omega_r + \left(\frac{2\omega_1 R_r}{\sqrt{3}} - \frac{2{L_{lr}}^2{\omega_1}^3}{\sqrt{3}R_r}\right)\frac{1}{\omega_r} \tag{4.3.3}$$

$$K_{eq1} = \left(\frac{L_{lr}}{\sqrt{3}R_r}\right)\omega_r - \left(\frac{L_{lr}{\omega_1}^2}{\sqrt{3}R_r}\right)\frac{1}{\omega_r} \tag{4.3.4}$$

$$K_{eq2} = \left(\frac{\omega_1}{\sqrt{3}}\right)\frac{1}{\omega_r} \tag{4.3.5}$$

Substituting for ${i_{r\beta}}'$ and V_{m2} in (4.3.1) from (4.2.20) and (4.2.7) respectively, the magnetizing voltage in the α–axis can be expressed as a function of output voltage and rotor speed as

$$V_{m1} = \left(\left(\frac{K_1}{\omega_r} + K_2\omega_r\right) + j\left(\frac{K_3}{\omega_r} + K_4\omega_r\right)\right)V_{so} \tag{4.3.6}$$

where constants K_1 , K_2 , K_3 and K_4 are defined as

$$K_1 = \left(\frac{-4{\omega_1}^2 L_{lr}}{\sqrt{3}}\right)\mu_{eq1} - \left(\frac{2\omega_1 R_r}{\sqrt{3}} - \frac{2{L_{lr}}^2{\omega_1}^3}{\sqrt{3}R_r}\right)\gamma_{eq1} - \left(\frac{L_{lr}{\omega_1}^2}{\sqrt{3}R_r}\right)\mu_{eqt} - \left(\frac{\omega_1}{\sqrt{3}}\right)\gamma_{eqt} \tag{4.3.7}$$

$$K_2 = \left(\frac{L_{lr}}{\sqrt{3}R_r}\right)\mu_{eqt} - \left(\frac{2\omega_1 {L_{lr}}^2}{\sqrt{3}R_r}\right)\gamma_{eq1} \tag{4.3.8}$$

$$K_3 = \left(\frac{2\omega_1 R_r}{\sqrt{3}} - \frac{2{L_{lr}}^2{\omega_1}^3}{\sqrt{3}R_r}\right)\mu_{eq1} + \left(\frac{-4{\omega_1}^2 L_{lr}}{\sqrt{3}}\right)\gamma_{eq1} + \left(\frac{\omega_1}{\sqrt{3}}\right)\mu_{eqt} - \left(\frac{L_{lr}{\omega_1}^2}{\sqrt{3}R_r}\right)\gamma_{eqt} \tag{4.3.9}$$

$$K_4 = \left(\frac{2\omega_1 {L_{lr}}^2}{\sqrt{3}R_r}\right)\mu_{eq1} + \left(\frac{L_{lr}}{\sqrt{3}R_r}\right)\gamma_{eqt} \tag{4.3.10}$$

Since the magnetizing voltage is dependent on the rotor speed ω_r which is not yet calculated, the magnetizing inductance cannot be determined using the magnetizing characteristics curve. However, in (3.3.9), the magnetizing inductance in the β-axis L_{m2} is equal to $3L_{ms}$. Similarly from (3.3.8), the magnetizing inductance in the α-axis L_{m1} is equal to L_{ms}. Therefore L_{m1} can be approximated as one third of L_{m2}.

$$L_{m1} \approx \frac{1}{3}L_{m2} \tag{4.3.11}$$

Step 2:

Using (3.8.27) and substituting for $\omega_1 L_{m1} = X_{m1}$, currents through the core loss resistance and mutual inductance in the α-axis can be calculated by (4.3.12) and (4.3.13) respectively.

$$i_{c1} = \left(\frac{1}{R_c}\left(\frac{K_1}{\omega_r} + K_2\omega_r\right) + j\frac{1}{R_c}\left(\frac{K_3}{\omega_r} + K_4\omega_r\right)\right)V_{so} \quad (4.3.12)$$

$$i_{me} = \left(\frac{1}{X_{m1}}\left(\frac{K_3}{\omega_r} + K_4\omega_r\right) - j\frac{1}{X_{m1}}\left(\frac{K_1}{\omega_r} + K_2\omega_r\right)\right)V_{so} \quad (4.3.13)$$

Step 3:

Substituting for $i_{r\beta}{}'$, V_{m2} and V_{m1} from (4.2.20) and (4.2.7) and (4.3.6) respectively in (4.2.23), the rotor current in α–axis can be calculated by

$$i_{r\alpha}{}' = \left(\left(\frac{K_5}{\omega_r} + K_6\omega_r\right) + j\left(\frac{K_7}{\omega_r} + K_8\omega_r\right)\right)V_{so} \quad (4.3.14)$$

where constants K_5 , K_6 , K_7 and K_8 are given in (4.3.15) - (4.3.18) respectively.

$$K_5 = \frac{\sqrt{3}}{L_{lr}}\left(R_r\mu_{eq1} - \omega_1 L_{lr}\,\gamma_{eq1} + \frac{\mu_{eqt}}{2}\right) - \left(\frac{3}{2\omega_1 L_{lr}}\right)K_3 \quad (4.3.15)$$

$$K_6 = -\left(\frac{3}{2\omega_1 L_{lr}}\right)K_4 \quad (4.3.16)$$

$$K_7 = \frac{\sqrt{3}}{L_{lr}}\left(\omega_1 L_{lr}\mu_{eq1} + R_r\gamma_{eq1} + \frac{\gamma_{eqt}}{2}\right) + \left(\frac{3}{2\omega_1 L_{lr}}\right)K_1 \quad (4.3.17)$$

$$K_8 = \left(\frac{3}{2\omega_1 L_{lr}}\right)K_2 \quad (4.3.18)$$

Step 4:

Using the current balance equation in (3.8.29), stator current in the excitation control winding i_{se} can be calculated by (4.3.19).

$$i_{se} = \left(\left(\frac{K_9}{\omega_r} + K_{10}\omega_r\right) + j\left(\frac{K_{11}}{\omega_r} + K_{12}\omega_r\right)\right)V_{so} \quad (4.3.19)$$

where the constants of the equation K_9 , K_{10} , K_{11} and K_{12} are given as

$$K_9 = \frac{K_3}{X_{m1}} + \frac{K_1}{R_c} - K_5 \quad (4.3.20)$$

$$K_{10} = \frac{K_4}{X_{m1}} + \frac{K_2}{R_c} - K_6 \quad (4.3.21)$$

$$K_{11} = -\frac{K_1}{X_{m1}} + \frac{K_3}{R_c} - K_7 \quad (4.3.22)$$

$$K_{12} = -\frac{K_2}{X_{m1}} + \frac{K_4}{R_c} - K_8 \tag{4.3.23}$$

Step 5:

As the last step of calculating generator variables, the excitation control voltage V_{se} can be calculated using (3.8.23).

$$V_{se} = \left(\left(\frac{K_{13}}{\omega_r} + K_{14}\omega_r\right) + j\left(\frac{K_{15}}{\omega_r} + K_{16}\omega_r\right)\right)V_{so} \tag{4.3.24}$$

The constants of the equation are defined as

$$K_{13} = (K_1 + R_s K_9 - \omega_1 L_{ls} K_{11}) \tag{4.3.25}$$

$$K_{14} = (K_2 + R_s K_{10} - \omega_1 L_{ls} K_{12}) \tag{4.3.26}$$

$$K_{15} = (K_3 + R_s K_{11} + \omega_1 L_{ls} K_9) \tag{4.3.27}$$

$$K_{16} = (K_4 + R_s K_{12} + \omega_1 L_{ls} K_{10}) \tag{4.3.28}$$

All the system variables in the α-axis are defined in terms of output winding voltage and rotor speed. Thus, for a specified output winding voltage, any system variable can be calculated if the rotor speed is known. Steps 6 to 9 present the computational procedure that can be used to calculate the rotor speed.

Step 6:

In this step, the resistive losses of the generator are calculated. The resistive losses in the β-axis can be given as the sum of (4.2.45) – (4.2.47) as

$$P_{r,loss\_\beta} = \left[\left(\frac{2R_s}{{R_{eq}}^2 + {X_{eq}}^2}\right) + \left(\frac{{\mu_{eqt}}^2 + {\gamma_{eqt}}^2}{2R_c}\right) + \left(2R_r\left({\mu_{eq1}}^2 + {\gamma_{eq1}}^2\right)\right)\right]{V_{so}}^2 \tag{4.3.29}$$

Substituting the values of each parameter, the resistive losses in β–axis can be calculated as an integer.

However, the resistive losses in the α-axis depend on the speed of the rotor. The resistive losses due to the stator, rotor and core loss resistances in the α-axis can be given by (4.3.30)-(4.3.32) respectively.

$${i_{se}}^2 . R_s = R_s\left(\left(\frac{K_9}{\omega_r} + K_{10}\omega_r\right)^2 + \left(\frac{K_{11}}{\omega_r} + K_{12}\omega_r\right)^2\right){V_{so}}^2 \tag{4.3.30}$$

$$i_{r\alpha}{}'^2 . \frac{2}{3} R_r = \frac{2}{3} R_r \left(\left(\frac{K_5}{\omega_r} + K_6 \omega_r \right)^2 + \left(\frac{K_7}{\omega_r} + K_8 \omega_r \right)^2 \right) {V_{so}}^2 \quad (4.3.31)$$

$$i_{c1}{}^2 . R_c = \frac{1}{R_c} \left(\left(\frac{K_1}{\omega_r} + K_2 \omega_r \right)^2 + \left(\frac{K_3}{\omega_r} + K_4 \omega_r \right)^2 \right) {V_{so}}^2 \quad (4.3.32)$$

Therefore, the total resistive losses in the α-axis can be given by (4.3.33):

$$P_{r,loss\_\alpha} = K_{r,loss\_\alpha} . {V_{so}}^2 \quad (4.3.33)$$

where $K_{r,loss\_\alpha}$ is a rotor speed dependant variable which can be expressed as

$$K_{r,loss\_\alpha} = R_s \left(\left(\frac{K_9}{\omega_r} + K_{10} \omega_r \right)^2 + \left(\frac{K_{11}}{\omega_r} + K_{12} \omega_r \right)^2 \right) + \frac{2}{3} R_r \left(\left(\frac{K_5}{\omega_r} + K_6 \omega_r \right)^2 + \left(\frac{K_7}{\omega_r} + K_8 \omega_r \right)^2 \right) + \frac{1}{R_c} \left(\left(\frac{K_1}{\omega_r} + K_2 \omega_r \right)^2 + \left(\frac{K_3}{\omega_r} + K_4 \omega_r \right)^2 \right) \quad (4.3.34)$$

Equation (4.3.34) can be further simplified as

$$K_{r,loss\_\alpha} = \frac{C_1}{{\omega_r}^2} + C_2 {\omega_r}^2 + C_3 \quad (4.3.35)$$

where constants C_1 , C_2 and C_3 are defined as

$$C_1 = R_s ({K_9}^2 + {K_{11}}^2) + \frac{2}{3} R_r ({K_5}^2 + {K_7}^2) + \frac{1}{R_c} ({K_1}^2 + {K_3}^2) \quad (4.3.36)$$

$$C_2 = R_s ({K_{10}}^2 + {K_{12}}^2) + \frac{2}{3} R_r ({K_6}^2 + {K_8}^2) + \frac{1}{R_c} ({K_2}^2 + {K_4}^2) \quad (4.3.37)$$

$$C_3 = 2R_s (K_9 K_{10} + K_{11} K_{12}) + \frac{4}{3} R_r (K_5 K_6 + K_7 K_8) + \frac{2}{R_c} (K_1 K_2 + K_3 K_4) \quad (4.3.38)$$

Step 7:

Using (4.2.55), the real power generation at the output winding can be given as

$$P_{out} = - \frac{1}{\left({R_{eq}}^2 + {X_{eq}}^2 \right)} \cdot \frac{{X_c}^2 R_o}{\left({R_o}^2 + (X_o - X_c)^2 \right)} {V_{so}}^2 \quad (4.3.39)$$

For a specified output voltage, the real power at output winding can be calculated by substituting the values of given operating parameters.

Step 8:

The active power absorb by the excitation control winding is given by

$$P_{ex} = Re\left(V_{se} . {i_{se}}^* \right) \quad (4.3.40)$$

Substituting for V_{se} and i_{se} from (4.3.24) and (4.3.19) respectively in (4.3.40), the real power in excitation control winding can be expressed as a function of rotor speed as in (4.3.41):

$$P_{ex} = \left(\frac{C_4}{{\omega_r}^2} + C_5{\omega_r}^2 + C_6\right){V_{so}}^2 \tag{4.3.41}$$

where constants can be defined as

$$C_4 = K_9K_{13} + K_{11}K_{15} \tag{4.3.42}$$

$$C_5 = K_{10}K_{14} + K_{12}K_{16} \tag{4.3.43}$$

$$C_6 = K_{10}K_{13} + K_9K_{14} + K_{12}K_{15} + K_{11}K_{16} \tag{4.3.44}$$

Step 9:

In order to achieve the real power balance in the system, the input mechanical power can be equal to the sum of the real power at both excitation control and output windings and the resistive losses of the machine. Thus, substituting from (4.2.58), (4.3.29), (4.3.33), (4.3.39) and (4.3.41) in (4.2.59), the real power balance equation of the generator system can be given by a quartic equation as,

$${\omega_r}^4 + D_3{\omega_r}^3 + D_2{\omega_r}^2 + D_0 = 0 \tag{4.3.45}$$

where the constants are defined as follows:

$$D_3 = [(m\omega_{r0} - T_0)/(P/2)]/\left[(C_5 - C_2){V_{so}}^2 - (m/(P/2)^2)\right] \tag{4.3.46}$$

$$D_2 = \left[(C_6 - C_3){V_{so}}^2 + P_{out} - P_{r,loss\_\beta}\right]/\left[(C_5 - C_2){V_{so}}^2 - (m/(P/2)^2)\right] \tag{4.3.47}$$

$$D_0 = \left[(C_4 - C_1){V_{so}}^2\right]/\left[(C_5 - C_2){V_{so}}^2 - (m/(P/2)^2)\right] \tag{4.3.48}$$

Solving (4.3.45), the rotor speed can be obtained by

$$\omega_r = -\frac{D_3}{4} + \frac{1}{2}\left(\pm_s\sqrt{2u} \pm_d \sqrt{-\left(2u + 2\left(D_2 - \frac{3{D_3}^2}{8}\right) \pm_s \frac{\sqrt{2}\left(-\frac{D_2D_3}{2} + \frac{{D_3}^3}{8}\right)}{\sqrt{u}}\right)}\right) \tag{4.3.49}$$

where $\pm_s$ and $\pm_d$denote either + or -. At $\pm_s$ the sign should be same. u is a root of the cubic equation in (4.3.50).

$$8u^3 + 8\left(D_2 - \frac{3{D_3}^2}{8}\right)u^2 + 2\left(D_2 - \frac{3{D_3}^2}{8}\right)^2 u - 8\left(D_0 + \frac{D_2{D_3}^2}{16} - \frac{3{D_3}^4}{256}\right)u - \left(-\frac{D_2D_3}{2} + \frac{{D_3}^3}{8}\right)^2 = 0 \tag{4.3.50}$$

Of the four possible solutions, the results with the complex values can be ignored as the rotor speed of a real generator should be an integer. Also, the solution with the

negative sign is not meaningful. Therefore, the solution with a positive integer can be selected as the rotor speed of the induction generator.

Using the computational techniques presented in this section, all the system variables including the rotor speed can be calculated. The simulation results obtained using both the techniques are compared with the corresponding experimental results and are presented in Chapter 6 together with the steady-state analysis of the single-phase generator system.

4.4 Computation of operating parameters

The computational techniques to calculate the values of system variables in steady-state for a given set of operating parameters were discussed in the preceding sections. However, as a pre-requisite, the operational range of the operating parameters should be determined for the safety of the generator system. Therefore, it is necessary to calculate the minimum values of the operating parameters required to generate the desired voltage at the output winding. A computational method to compute these operating parameters is important not only for the steady-state analysis, but also for designing and operating a practical renewable energy generation scheme. Such a method is not presented in the literature. The computational method described in this section is based on the steady-state equations of the single-phase induction generator presented in section 3.8. The operating parameters, i.e. load resistance, load inductance, fixed capacitance, rotor speed and power factor at the excitation control winding are calculated in order to achieve the phase balancing of the generator system.

Similar to (3.5.3)-(3.5.5), considering the stator phase ‘a’ of a three-phase electrical machine as the real axis, the instantaneous voltages in three phases can be given in terms of vector quantities as

$$\boldsymbol{V_{sa}} = V_{sa} \tag{4.4.1}$$

$$\boldsymbol{V_{sb}} = \left(-\frac{1}{2} + j\,\frac{\sqrt{3}}{2}\right).V_{sb} \tag{4.4.2}$$

$$\boldsymbol{V_{sc}} = \left(-\frac{1}{2} - j\,\frac{\sqrt{3}}{2}\right).V_{sc} \tag{4.4.3}$$

Using (3.1.13) and (3.1.14), instantaneous voltages in single-phase arrangement of three-phase induction generator can be given as

$$\boldsymbol{V_{se}} = V_{sa} \tag{4.4.4}$$

$$\boldsymbol{V_{so}} = -\frac{1}{2}(V_{sb} - V_{sc}) + j\,\frac{\sqrt{3}}{2}(V_{sb} + V_{sc}) \tag{4.4.5}$$

Since the voltages in each phase of a balanced three-phase machine are equal in magnitude, (4.4.4) and (4.4.5) can be re-written as

$$\boldsymbol{V_{se}} = V \tag{4.4.6}$$

$$\boldsymbol{V_{so}} = j\sqrt{3}\,\mathrm{V} \tag{4.4.7}$$

Thus, the magnitude of voltages in excitation control winding and output winding can be obtained by (4.4.8) and (4.4.9) respectively.

$$|\boldsymbol{V_{se}}| = V \tag{4.4.8}$$

$$|\boldsymbol{V_{so}}| = \sqrt{3}\,\mathrm{V} \tag{4.4.9}$$

Similar to (4.4.1) – (4.4.3), the instantaneous currents in a standard three-phase induction machine can be written in vector quantities as

$$\boldsymbol{i_{sa}} = i_{sa} \tag{4.4.10}$$

$$\boldsymbol{i_{sb}} = \left(-\frac{1}{2} + j\,\frac{\sqrt{3}}{2}\right).i_{sb} \tag{4.4.11}$$

$$\boldsymbol{i_{sc}} = \left(-\frac{1}{2} - j\,\frac{\sqrt{3}}{2}\right).i_{sc} \tag{4.4.12}$$

Using (3.1.12) and (3.1.11), the instantaneous currents in excitation control and output windings of single-phase induction machine can be written as (4.4.13) and (4.4.14) respectively:

$$\boldsymbol{i_{se}} = i_{sa} \tag{4.4.13}$$

$$\boldsymbol{i_{so}} = \frac{1}{2}\left[\left(-\frac{1}{2} + j\,\frac{\sqrt{3}}{2}\right).i_{sb} - \left(-\frac{1}{2} - j\,\frac{\sqrt{3}}{2}\right).i_{sc}\right] \tag{4.4.14}$$

Considering the magnitude of the current in each phase of three-phase machine is as I, (4.4.13) and (4.4.14) can be re-written as

$$\boldsymbol{i_{se}} = I \tag{4.4.15}$$

$$\boldsymbol{i_{so}} = j\,\frac{\sqrt{3}}{2}I \tag{4.4.16}$$

Thus, the magnitude of the currents in each phase of single-phase machine can be obtained by

$$|\boldsymbol{i_{se}}| = I \tag{4.4.17}$$

$$|\boldsymbol{i_{so}}| = \frac{\sqrt{3}}{2} I \tag{4.4.18}$$

The desired voltage at the output is equal to the rated voltage V_{rated} of the three-phase machine. In order to achieve the voltage balance in the single-phase induction generator, the excitation control winding voltage can be calculated as $V_{rated}/\sqrt{3}$ using (4.4.8) and (4.4.9). The fixed capacitance connected at the output winding supplements the reactive power requirement of the generator in order to keep the excitation control winding current below the rated value of the machine. Therefore, the maximum current in the excitation control winding should be the rated current of the machine which is given as i_{rated}. Thus, in a balanced system, the magnitude of the current in output winding can be calculated using (4.4.17) and (4.4.18) as

$$|\boldsymbol{i_{so}}| = \frac{\sqrt{3}}{2} i_{rated} \tag{4.4.19}$$

In the first part of this section, the computational procedure is described for a unity power factor load i.e. ideal resistive load. In the second part of this section, the calculations are extended for an RL load with a known power factor. The calculation procedure is described in the twelve steps below.

Step 1:

Fig. 4.4.1 shows the equivalent circuit of single-phase generator in the α-axis and β-axis with an ideal resistive load. Since the operating parameters of the load circuit connected to the β-axis are unknown, the computational procedure is started from the α-axis.

The magnitudes of current and voltage in excitation control winding are given as i_{rated} and $V_{rated}/\sqrt{3}$ respectively. The excitation control voltage is considered as the reference phase and the excitation control winding current is considered to be lagging the reference phase by angle δ.

To simplify the calculations, the magnetizing voltage in α-axis is approximated to the excitation control voltage.

$$|V_{m1}| \approx |V_{se}| \tag{4.4.20}$$

Substituting the given parameters in the Appendix B in (4.2.16) and (4.2.17), the magnetizing inductance in α-axis L_{m1} can be calculated. From (3.3.8), the

magnetizing inductance in α-axis L_{m1} is equal to L_{ms}. Similar to (3.3.7), the magnetizing inductance in β-axis L_{m2} is equal $3L_{ms}$. Therefore, L_{m2} can be approximated as three times the L_{m1}.

Step 2:

The current in the excitation control winding i_{se} can be defined as

$$i_{se} = |i_{se}|\angle(-\delta) \tag{4.4.21}$$

In the complex form, it can be re-written as

$$i_{se} = i_{seR} + ji_{seI} = |i_{se}|(\cos\delta - j\sin\delta) \tag{4.4.22}$$

Substituting for $j\omega_1 L_{m1} i_{me}$ in (3.8.23) from (3.8.27), the magnetizing voltage in α-axis can be written as

$$V_{m1} = V_{m1R} + jV_{m1I} \tag{4.4.23}$$

where subscript R and I denote the real and imaginary components respectively. The values of V_{m1R} and V_{m1I} can be given by

$$V_{m1R} = (V_{se} - R_s i_{seR} + \omega_1 L_{ls} i_{seI}) \tag{4.4.24}$$

$$V_{m1I} = -(R_s i_{seI} + \omega_1 L_{ls} i_{seR}) \tag{4.4.25}$$

Since angle δ is unknown, the magnetizing voltage in the α-axis can be written as a function of δ as

$$V_{m1} = f(\delta) \tag{4.4.26}$$

Step 3:

As shown in Fig. 4.4.1(a) the magnetizing current in the α-axis is defined as i_{me}. Using (3.8.27) and substituting for $\omega_1 L_{m1} = X_{m1}$, i_{me} can be given as

$$i_{me} = i_{meR} + ji_{meI} \tag{4.4.27}$$

where the real and imaginary components of (4.4.27) can be given as

$$i_{meR} = \frac{V_{m1I}}{X_{m1}} \tag{4.4.28}$$

$$i_{meI} = \frac{-V_{m1R}}{X_{m1}} \tag{4.4.29}$$

From the above definitions, the magnetizing current in α-axis can be written as a function of δ.

$$i_{me} = f(\delta) \tag{4.4.30}$$

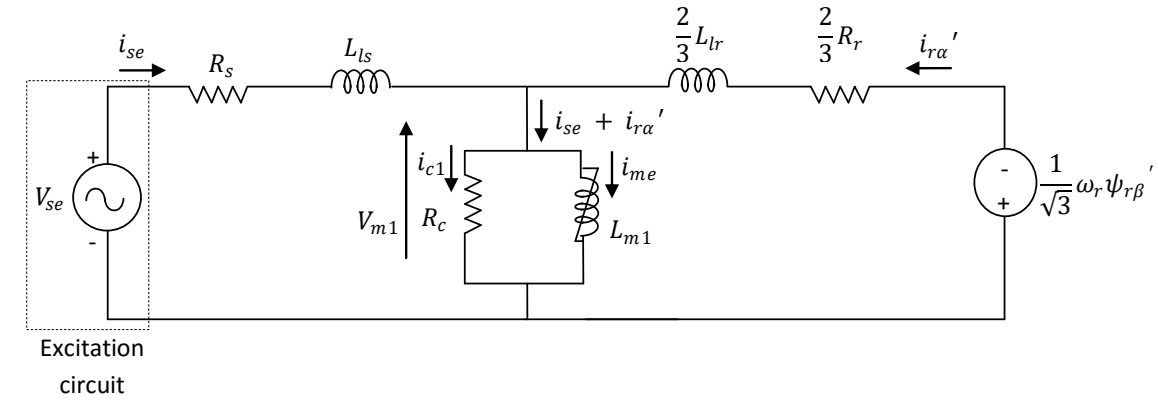

(a)

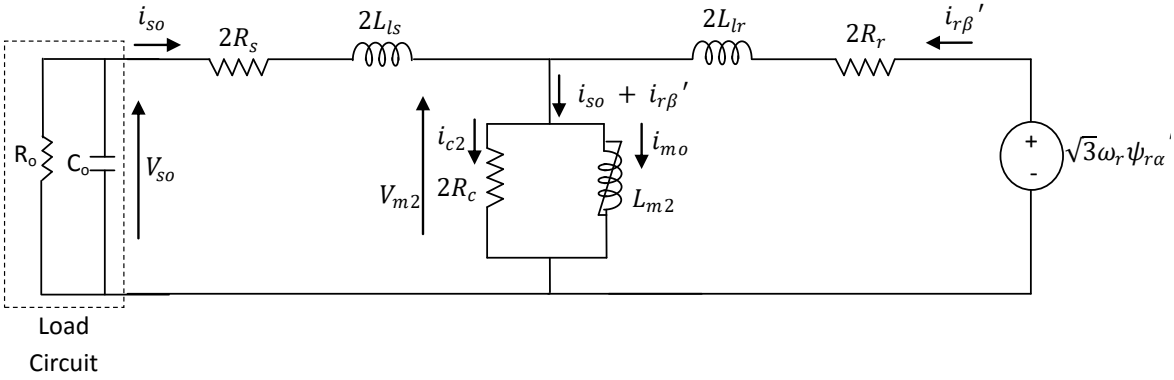

(b)

Fig. 4.4.1 Steady-state equivalent circuit of single-phase generator (a) α-axis (b) β-axis with ideal resistive load

Similarly, using (3.8.27), the current through the core loss resistance can be written in the complex form as

$$i_{c1} = i_{c1R} + j i_{c1I} \tag{4.4.31}$$

where i_{c1R} and i_{c1I} can be defined as

$$i_{c1R} = \frac{V_{m1R}}{R_c} \tag{4.4.32}$$

$$i_{c1I} = \frac{V_{m1I}}{R_c} \tag{4.4.33}$$

The current that flows through the core loss resistance is dependent on the angle δ. Thus, it can be re-written as

$$i_{c1} = f(\delta) \tag{4.4.34}$$

Step 4:

Using the current balance equation in (3.8.29), the rotor current in the α-axis can be given as

$$i_{r\alpha}{}' = i_{r\alpha R}{}' + j i_{r\alpha I}{}' \tag{4.4.35}$$

where real and imaginary components of rotor current can be given by two separate equations as

$$i_{r\alpha R}{}' = (i_{meR} + i_{c1R} - i_{seR}) \tag{4.4.36}$$

$$i_{r\alpha I}{}' = (i_{meI} + i_{c1I} - i_{seI}) \tag{4.4.37}$$

Similar to the other current components in the α-axis, the rotor current is also a function of δ.

$$i_{r\alpha}' = f(\delta) \tag{4.4.38}$$

Step 5:

Using (3.8.25), (3.3.16), (3.8.27) and (3.8.28), the rotor current in β-axis $i_{r\beta}{}'$ can be written as a function of δ, ω_r and V_{m2}.

$$i_{r\beta}{}' = -\frac{\sqrt{3}}{2\omega_r L_{lr}}\left(\frac{2}{3}(R_r + j\omega_1 L_{lr}) i_{r\alpha}{}' + V_{m1} + \frac{1}{\sqrt{3}}\omega_r \frac{V_{m2}}{j\omega_1}\right) \tag{4.4.39}$$

$$i_{r\beta}{}' = f(\delta, \omega_r, V_{m2}) \tag{4.4.40}$$

Substituting from (3.3.17), (3.8.27) and (3.8.28) in (3.8.26), the rotor voltage in the β-axis can be re-written as

$$0 = 2(R_r + j\omega_1 L_{lr}) i_{r\beta}{}' + V_{m2} - \omega_r \left(\frac{2}{\sqrt{3}} L_{lr} i_{r\alpha}{}' + \sqrt{3}\frac{V_{m1}}{j\omega_1}\right) \tag{4.4.41}$$

Using (4.4.39), substituting for $i_{r\beta}{}'$ in (4.4.41), the magnetizing voltage in the β-axis V_{m2} can be given in the complex form as

$$V_{m2} = V_{m2R} + jV_{m2I} \tag{4.4.42}$$

where real and imaginary components are defined by

$$V_{m2R} = \frac{2\omega_1}{\sqrt{3}\omega_r R_r}\left(\left({R_r}^2 - {\omega_1}^2{L_{lr}}^2\right){i_{r\alpha I}}' + 2\omega_1 L_{lr} R_r {i_{r\alpha R}}'\right) + \frac{2\omega_1\omega_r {L_{lr}}^2}{\sqrt{3}R_r}{i_{r\alpha I}}' + \frac{\sqrt{3}\omega_1}{\omega_r R_r}(R_r V_{m1I} + \omega_1 L_{lr} V_{m1R}) - \frac{\sqrt{3}\omega_r L_{lr}}{R_r} V_{m1R} \tag{4.4.43}$$

$$V_{m2I} = \frac{2\omega_1}{\sqrt{3}\omega_r R_r}\left(2\omega_1 L_{lr} R_r {i_{r\alpha I}}' - \left({R_r}^2 - {\omega_1}^2{L_{lr}}^2\right){i_{r\alpha R}}'\right) - \frac{2\omega_1\omega_r {L_{lr}}^2}{\sqrt{3}R_r}{i_{r\alpha R}}' + \frac{\sqrt{3}\omega_1}{\omega_r R_r}(\omega_1 L_{lr} V_{m1I} - R_r V_{m1R}) - \frac{\sqrt{3}\omega_r L_{lr}}{R_r} V_{m1I} \tag{4.4.44}$$

The magnetizing voltage in β-axis if depend on both angle δ and the rotor speed ω_r.

$$V_{m2} = f(\delta, \omega_r) \tag{4.4.45}$$

Step 6:

Substituting for ${i_{r\alpha}}'$, V_{m1} and V_{m2} from (4.4.35), (4.4.23) and (4.4.42) respectively in (4.4.39), the rotor current in β-axis ${i_{r\beta}}'$ can be written as a function of angle δ and rotor speed ω_r.

$${i_{r\beta}}' = {i_{r\beta R}}' + j{i_{r\beta I}}' \tag{4.4.46}$$

where the real and imaginary components can be defined as

$${i_{r\beta R}}' = -\frac{\sqrt{3}}{2\omega_r L_{lr}}\left(\frac{2}{3}\left(R_r {i_{r\alpha R}}' - \omega_1 L_{lr} {i_{r\alpha I}}'\right) + V_{m1R} + \frac{\omega_r}{\sqrt{3}\omega_1} V_{m2I}\right) \tag{4.4.47}$$

$${i_{r\beta I}}' = -\frac{\sqrt{3}}{2\omega_r L_{lr}}\left(\frac{2}{3}\left(\omega_1 L_{lr} {i_{r\alpha R}}' + R_r {i_{r\alpha I}}'\right) + V_{m1I} - \frac{\omega_r}{\sqrt{3}\omega_1} V_{m2R}\right) \tag{4.4.48}$$

$${i_{r\beta}}' = f(\delta, \omega_r) \tag{4.4.49}$$

Step 7:

The magnetizing current in the β-axis is defined as i_{mo} as shown in Fig. 4.4.1(b). Substituting for $\omega_1 L_{m2} = X_{m2}$ in (3.8.28), i_{mo} can be given as

$$i_{mo} = i_{moR} + j i_{moI} \tag{4.4.50}$$

where i_{moR} and i_{moI} are given by

$$i_{moR} = \frac{V_{m2I}}{X_{m2}} \tag{4.4.51}$$

$$i_{moI} = \frac{-V_{m2R}}{X_{m2}} \tag{4.4.52}$$

Both real and imaginary components in (4.4.49) depend on the angle δ and rotor speed ω_r. Therefore, magnetizing current can be written as

$$i_{mo} = f(\delta, \omega_r) \tag{4.4.53}$$

Similarly, using (3.8.28), the current through the core resistance i_{c2} can be given as

$$i_{c2} = i_{c2R} + j i_{c2I} \tag{4.4.54}$$

where i_{c2R} and i_{c2I} are defined as,

$$i_{c2R} = \frac{V_{m2R}}{2R_c} \tag{4.4.55}$$

$$i_{c2I} = \frac{V_{m2I}}{2R_c} \tag{4.4.56}$$

The current through the core resistance i_{c2} is a function of angle δ and rotor speed ω_r and can be given by

$$i_{c2} = f(\delta, \omega_r) \tag{4.4.57}$$

Step 8:

Using the current balance in (3.8.30), output winding current i_{so} can be given by

$$i_{so} = i_{soR} + j i_{soI} \tag{4.4.58}$$

where its real and imaginary components are defined as

$$i_{soR} = \left(i_{moR} + i_{c2R} - i'_{r\beta R}\right) \tag{4.4.59}$$

$$i_{soI} = \left(i_{moI} + i_{c2I} - i'_{r\beta I}\right) \tag{4.4.60}$$

The same as other system variables in the β-axis, the output winding current is also a function of angle δ and rotor speed ω_r as written as

$$i_{so} = f(\delta, \omega_r) \tag{4.4.61}$$

Step 9:

Substituting for i_{so} and $j\omega_1 L_{m2} i_{mo}$ from (4.4.58), (3.8.28) and (4.4.42) in (3.8.24), the output winding voltage V_{so} can be calculated as

$$V_{so} = V_{soR} + j V_{soI} \tag{4.4.62}$$

where real and imaginary components are given by

$$V_{soR} = 2(R_s i_{soR} - \omega_1 L_{ls} i_{soI}) + V_{m2R} \quad (4.4.63)$$

$$V_{soI} = 2(\omega_1 L_{ls} i_{soR} + R_s i_{soI}) + V_{m2I} \quad (4.4.64)$$

Output winding voltage is also depend on the angle δ and rotor speed ω_r as given in

$$V_{so} = f(\delta, \omega_r) \quad (4.4.65)$$

Step 10:

Since the magnitude of output winding current is equal to $\frac{\sqrt{3}}{2} i_{rated}$, using (4.4.58), output winding current can be written in the forms of

$$i_{so} = \sqrt{{i_{soR}}^2 + {i_{soI}}^2} = \frac{\sqrt{3}}{2} i_{rated} \quad (4.4.66)$$

which depends on both angle δ and rotor speed ω_r.

Similarly, using (4.4.62), the magnitude of output winding voltage can be calculated as a function of angle δ and rotor speed ω_r and equal to the rated voltage as in (4.4.67).

$$V_{rated} = \sqrt{{V_{soR}}^2 + {V_{soI}}^2} \quad (4.4.67)$$

Both the equations in (4.4.66) and (4.4.67) depend on the magnitude of i_{se} , V_{se}, δ and ω_r. However, the magnitudes i_{se} and $V_{se}$are known. Therefore, the only unknowns in both the equations are δ and ω_r. Solving these two equations simultaneously, rotor speed ω_r and the angle of excitation control winding current δ w.r.t. the reference phase can be calculated.

Step 11:

Substituting the calculated values of δ and ω_r in (4.4.58) and (4.4.62), i_{so} and V_{so} can be determined.

Then the active and the reactive power at the output winding can be calculated by (4.4.68) and (4.4.69) respectively.

$$P_{out} = Re[V_{so}.{i_{so}}^{*}] \quad (4.4.68)$$

$$Q_{out} = Im[V_{so}.{i_{so}}^{*}] \quad (4.4.69)$$

where superscript *, Re and Im denote the conjugate of output winding current, real component and imaginary component respectively.

When a unity power factor load is connected, the total active power is consumed by the resistive load R_o and the total reactive power is supplied by the fixed capacitance C_o. Since the load and the fixed capacitance are connected in parallel, the voltage across each element is equal to output winding voltage V_{so}. Therefore, load resistance and fixed capacitance can be calculated by (4.4.70) and (4.4.71) respectively:

$$R_o = \frac{{V_{so}}^2}{P_{out}} \quad (4.4.70)$$

$$C_o = \frac{Q_{out}}{\omega {V_{so}}^2} \quad (4.4.71)$$

Step 12:

In this step, the computational technique to calculate the load and the capacitance is described when a series-connected RL load is operated at the output, instead of the unity power factor load. Rotor speed and frequency of the generator variables are considered unchanged as before. In order to ensure that the impedance seen by the generator remains unchanged, the fixed capacitance and the load impedance is changed with the load power factor. If the magnitude of load impedance and load power factor are given as Z and ϕ respectively, the resistive and inductive components of the load i.e. R_l and X_l can be written as (4.4.72) and (4.4.73) respectively.

$$R_l = Z.\phi \quad (4.4.72)$$

$$X_l = Z.\sqrt{1-\phi^2} \quad (4.4.73)$$

Substituting R_l and X_l for $R_o$and X_o in (4.2.1) and (4.2.2), the new equivalent resistance and inductance of the load circuit shown by the broken lines in Fig. 4.1.1 (b) can be re-written as (4.4.74) and (4.4.75) respectively:

$$R_{eq\_new} = \frac{-{X_{c1}}^2 Z.\phi}{\left(Z^2.\phi^2 + \left(Z.\sqrt{1-\phi^2} - X_{c1}\right)^2\right)} \tag{4.4.74}$$

$$X_{eq\_new} = \frac{X_{c1}\left(Z^2.\phi^2 + Z.\sqrt{1-\phi^2}\left(Z.\sqrt{1-\phi^2} - X_{c1}\right)\right)}{\left(Z^2.\phi^2 + \left(Z.\sqrt{1-\phi^2} - X_{c1}\right)^2\right)} \tag{4.4.75}$$

where X_{c1} is the new reactance of the fixed capacitor.

When the unity power factor load is connected, the equivalent resistive and inductive components can be defined as (4.4.76) and (4.4.77) using (4.2.1) and (4.2.2) respectively:

$$R_{eq\_unity} = \frac{-{X_c}^2 R_o}{\left({R_o}^2 + {X_o}^2\right)} \tag{4.4.76}$$

$$X_{eq\_unity} = \frac{X_c {R_o}^2}{\left({R_o}^2 + {X_o}^2\right)} \tag{4.4.77}$$

In both situations, the impedance seen by the generator remains unchanged; the equivalent resistive and inductive components in two different situations are equal to each other as given by,

$$R_{eq\_new} = R_{eq\_unity} \tag{4.4.78}$$

$$X_{eq\_new} = X_{eq\_unity} \tag{4.4.79}$$

The only unknowns in these two equations are Z and X_{c1}. Therefore, by solving these two equations simultaneously, C_{o1}, R_l and L_l can be determined.

$$C_{o1} = C_o + \frac{1}{\omega_1 R_o}\frac{\sqrt{1-\phi^2}}{\phi} \tag{4.4.80}$$

$$R_l = \phi^2 R_o \tag{4.4.81}$$

$$L_l = \frac{\phi\sqrt{1-\phi^2}}{\omega_1} R_o \tag{4.4.82}$$

where C_{o1} is the new value of the fixed capacitance.

4.5 Chapter Conclusions

Using the techniques described in the preceding sections, the system variables for a given set of operating parameters can be calculated when the rotor speed is given as either a constant or a load-dependant. Using the method presented in the last section, the operating parameters can be calculated in order to obtain the phase balancing of the generator system. Thus, the operating range of fixed capacitance, load resistance and inductance, rotor speed can be estimated before operating the three-phase induction machine as a single-phase generator.

In the first part of the steady-state analysis, the operating ranges of the operational parameters have been presented. Then, the system variables have been calculated for a given set of operating parameters. All these results are verified by the experiments carried out on the laboratory experimental set-up.

CHAPTER 5- MODEL VERIFICATION AND SYSTEM PERFORMANCE IN TRANSIENT-STATE

5.1 Introduction

In order to verify the errors identified in the dynamic equations given in the literature, the simulation results obtained from the existing model were compared with those from the model developed in Chapter 3. Since the effects of core losses and magnetic saturation have been ignored in the existing model, the dynamic model given in (3.1.25), based on the same assumption, was used for this comparison. In order to compare the simulation results with the experimental results presented in the literature, the same machine parameters as those in the literature were used for both models, simulated in Matlab software. The current, voltage and rotor speed obtained from both models are presented in the next section of this chapter.

The verification of the comprehensive model developed in the preceding chapter was made by performing the experiments on a laboratory experimental set-up. A 400 V, 50 Hz, 3 kW, 4-pole small squirrel cage three-phase induction machine was assembled as the single-phase generator using the equipment available in the laboratory and the generator shaft was coupled to similar three-phase induction motor driven by a variable speed drive (VSD) to emulate the renewable energy source such as a wind turbine. Induction machine parameters obtained by DC test, blocked rotor test and no load tests are given in Appendix B. A capacitor and a resistive load are connected in parallel at the output winding of the generator. At the excitation control winding, a single-phase auto transformer is connected to replace the bi-directional DC-AC inverter. It is energized by the utility grid. By changing the ac voltage supplied by the auto transformer, the excitation control winding voltage is adjusted. Similarly, by changing the speed of the VSD, the desired speed of the rotor is selected. Because of the lower ratings of the three-phase induction generator, the rotor speed is maintained below the rated value. The experimental setup used for the

verification of comprehensive dynamic model of the single-phase generator is shown in Fig. 5.1.1.

The state space vector and the equation of motion developed for the comprehensive dynamic model of the single-phase generator were simulated in Matlab and the dynamic performance was computed using the variable step Runge-Kutta technique. The flow chart of the simulation process is given in Appendix D.

The knowledge of transient-performance of the unregulated single-phase generator is important before utilizing it in the renewable energy generation schemes which is not discussed in the literature. Using the comprehensive dynamic model developed in the previous chapter, the transient-performance of the unregulated generator system was theoretically studied and the results were experimentally verified.

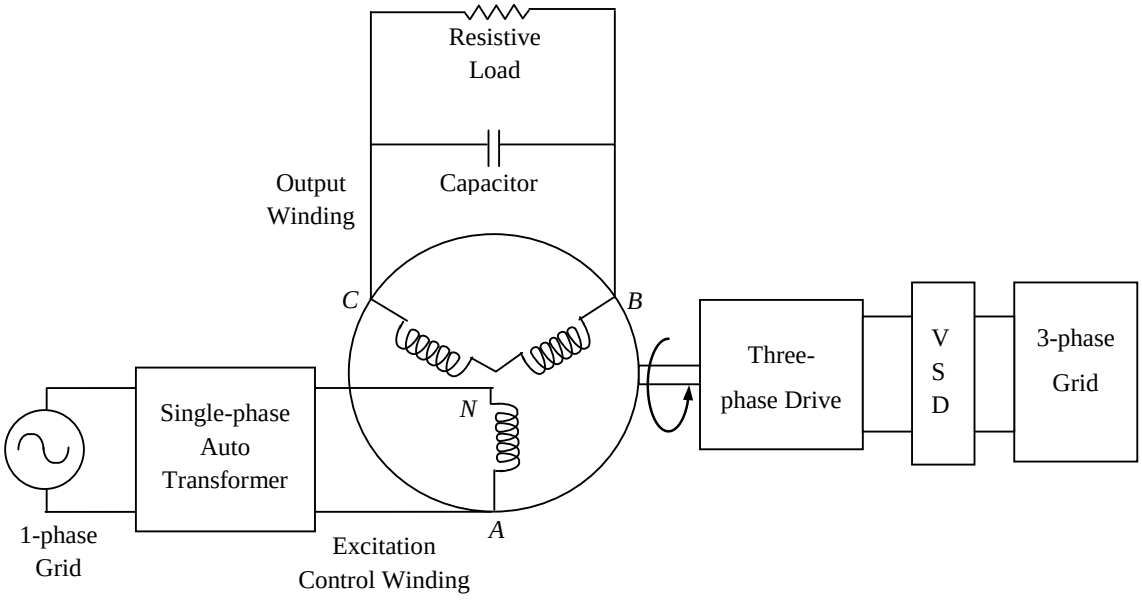

Fig. 5.1.1 Experimental setup used for dynamic mathematical model verification

5.2 Verification of Identified Errors in the Literature

The study was performed to supply active power of 750 W to a resistive load at the output winding. In order to generate 230 V/ 50 Hz at the output, both the existing model and the improved model were simulated in Matlab and operated under the same conditions. An AC voltage of 146 V/ 50 Hz was supplied from the excitation control winding at the rotor speed of 1560 rpm. A fixed capacitance of 30 µF was connected in parallel with the consumer load to supply the balance of the reactive

power requirement during the excitation. Due to the lack of information provided in the literature, the following assumptions have been made to obtain the simulation results in both models.

- The model of load and excitation capacitor was considered as (3.4.5).
- During the generator mode of operation of the single-phase induction machine, the torque of the turbine was considered as a negative constant value.
- Due to the error persists in the Matlab program, the equation of motion was corrected to $p\omega_r = \frac{P}{2}\frac{1}{J}\left(T_e - T_p\right)$

Currents and voltages in both excitation control and output windings and rotor speeds obtained from both models are shown below.

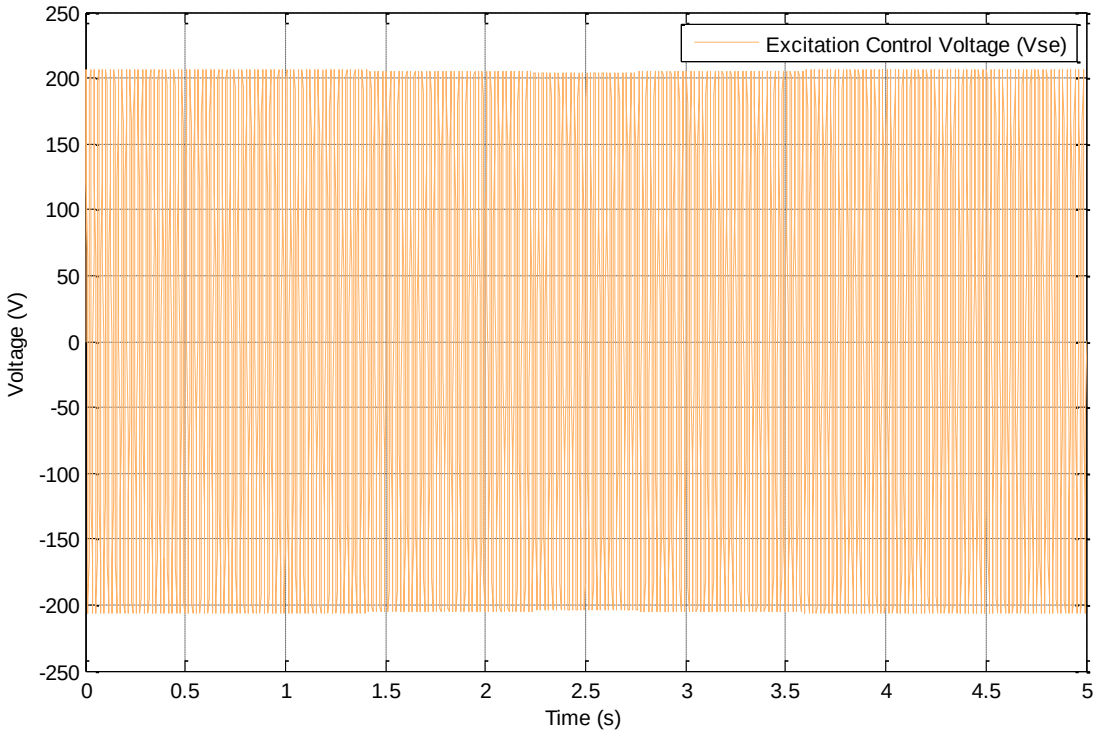

Fig. 5.2.1. Excitation control winding voltage

When the same excitation control winding voltage shown in Fig 5.2.1 was applied with the same mechanical torque for both existing and improved models, the simulation results obtained for excitation control current, output winding voltage, output winding current and rotor speed are those shown in Figs. 5.2.2 - 5.2.5 respectively. Part (a) of each figure shows the results obtained from the existing model whereas part (b) shows the results obtained from the improved model.

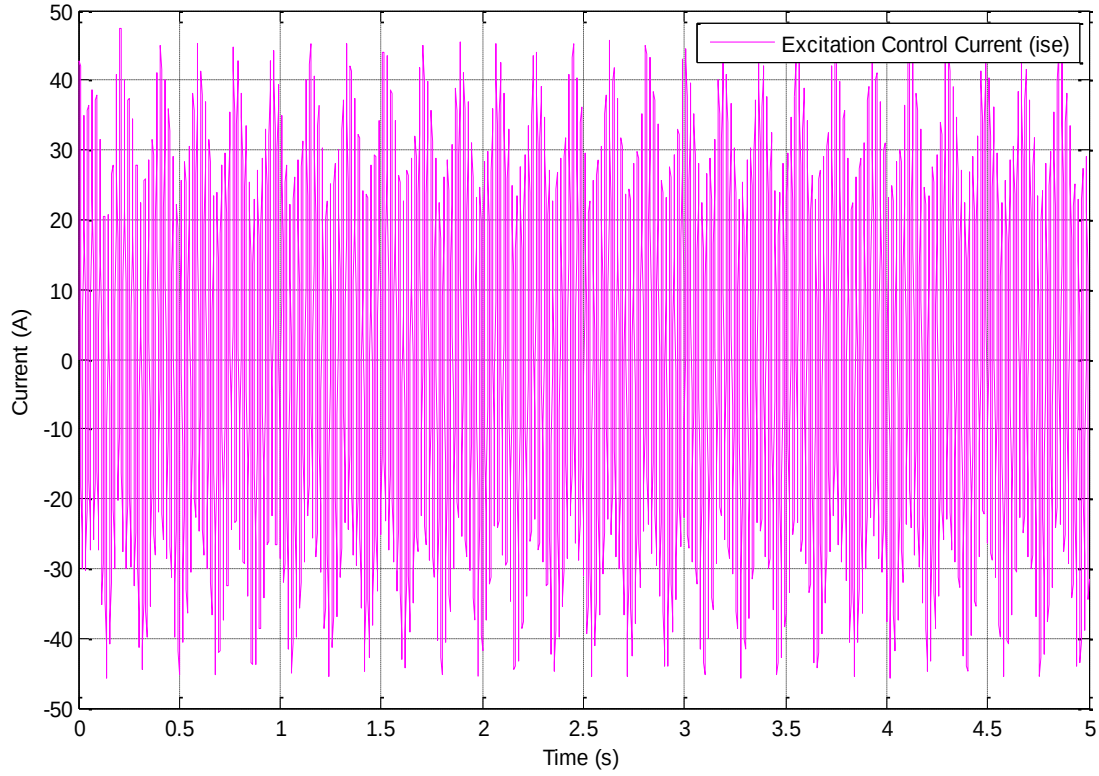

(a)

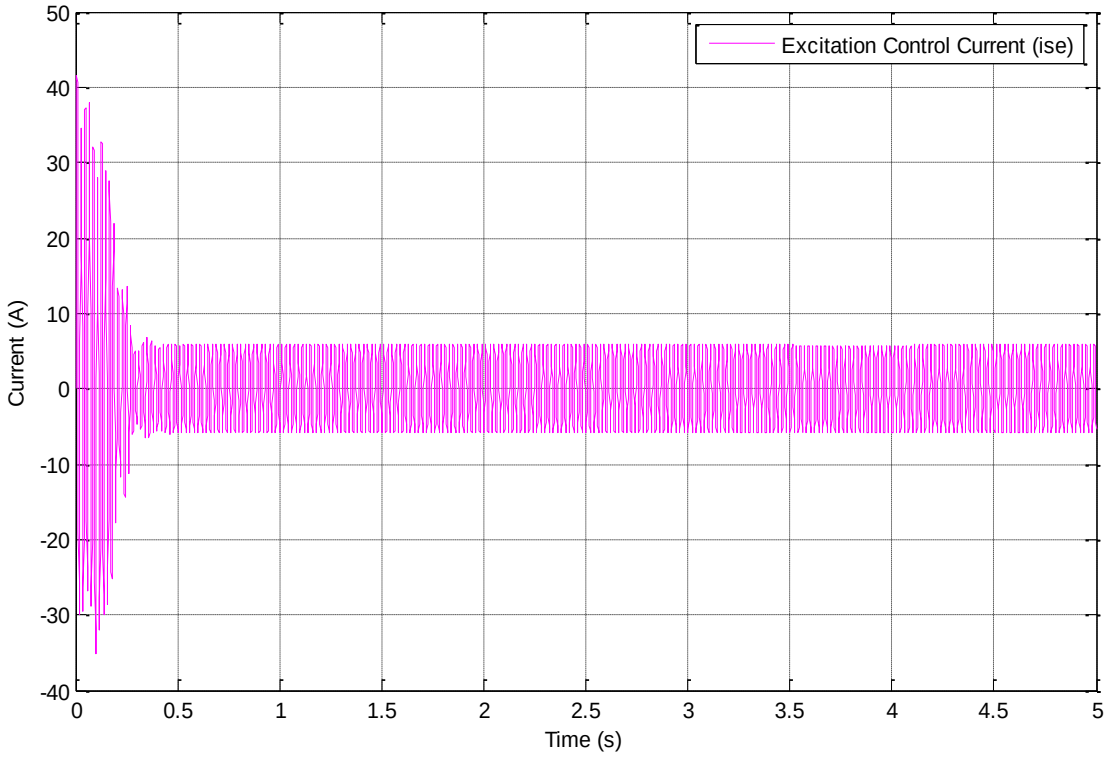

(b)

Fig. 5.2.2. Excitation control current (a) Existing model (b) Improved model

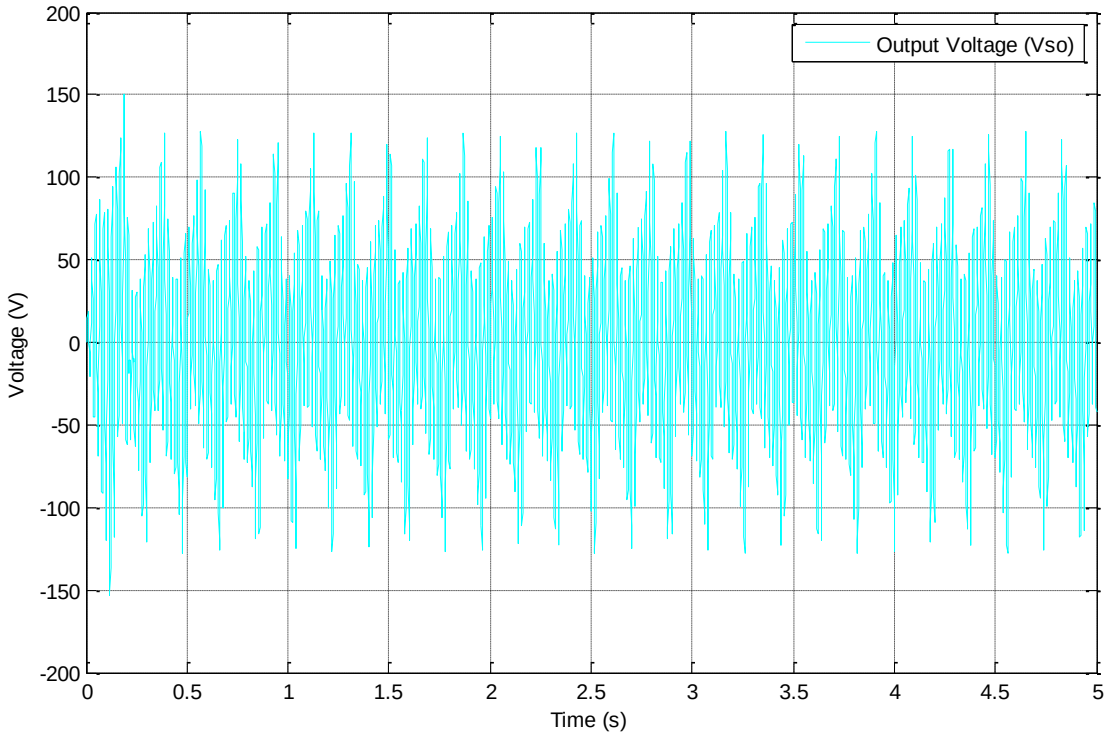

(a)

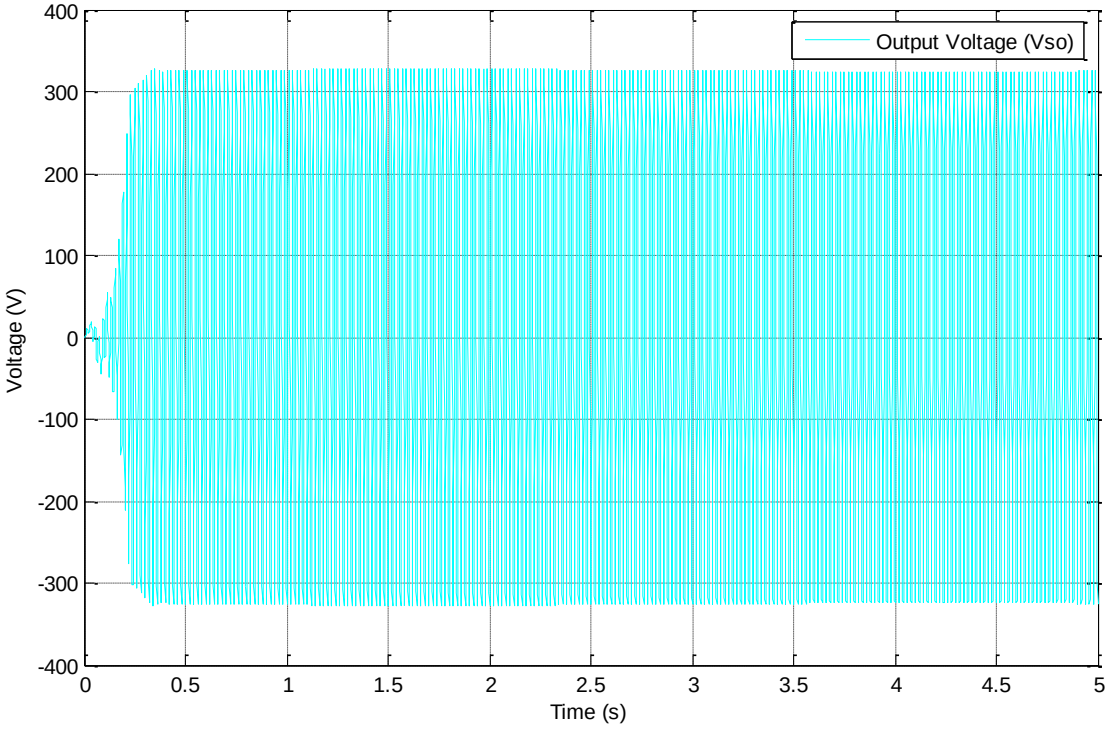

(b)

Fig. 5.2.3. Output winding voltage (a) Existing model (b) Improved model

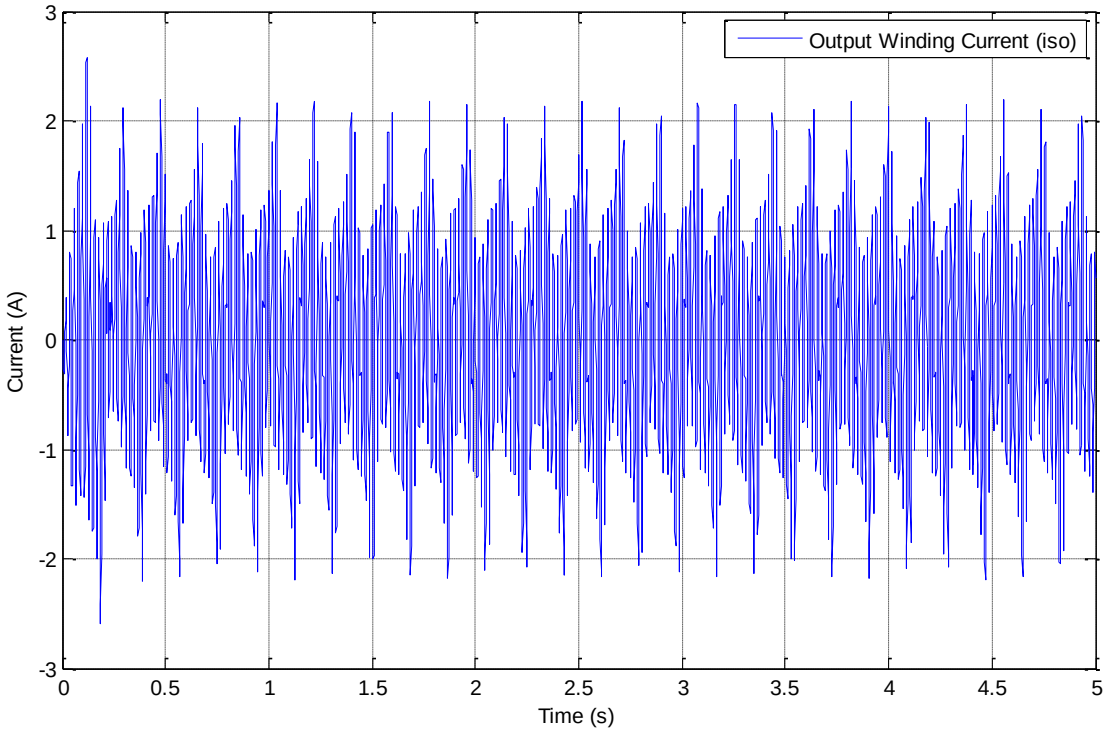

(a)

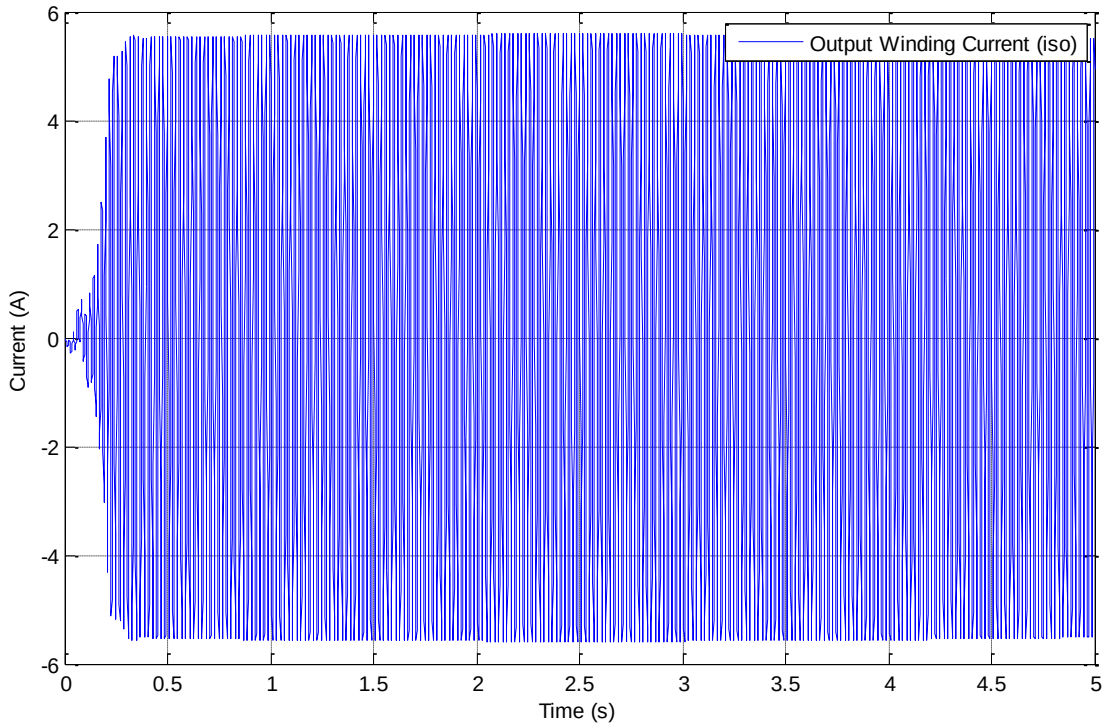

(b)

Fig. 5.2.4. Output winding current (a) Existing model (b) Improved model

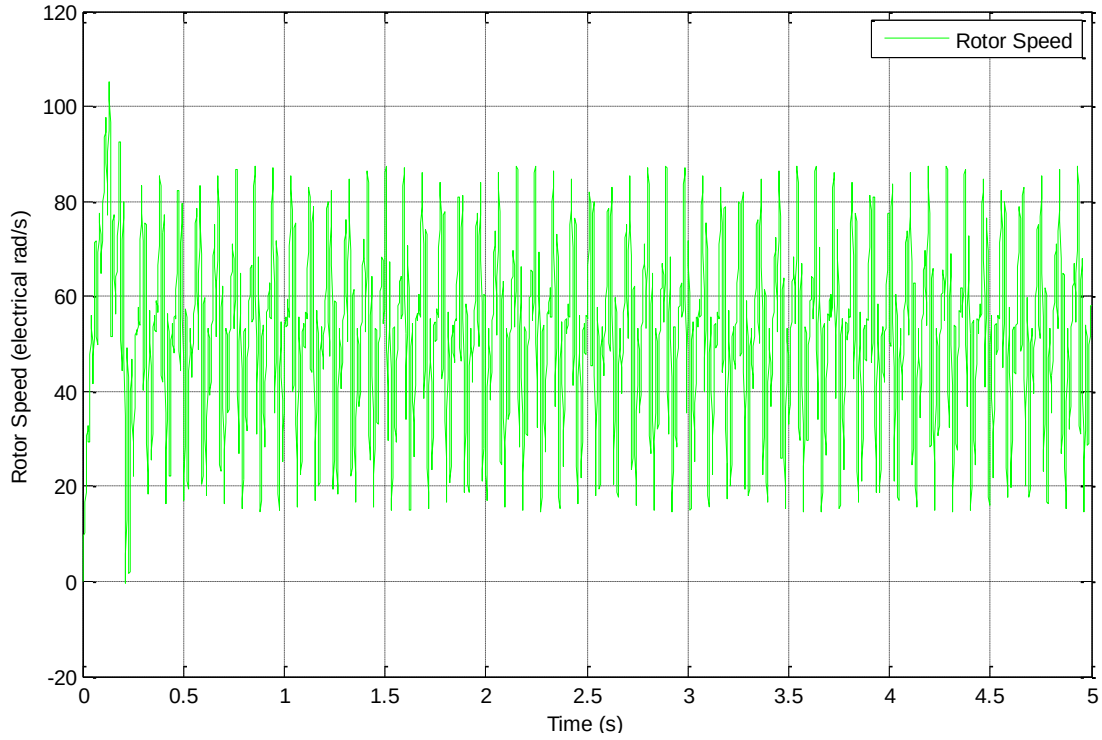

(a)

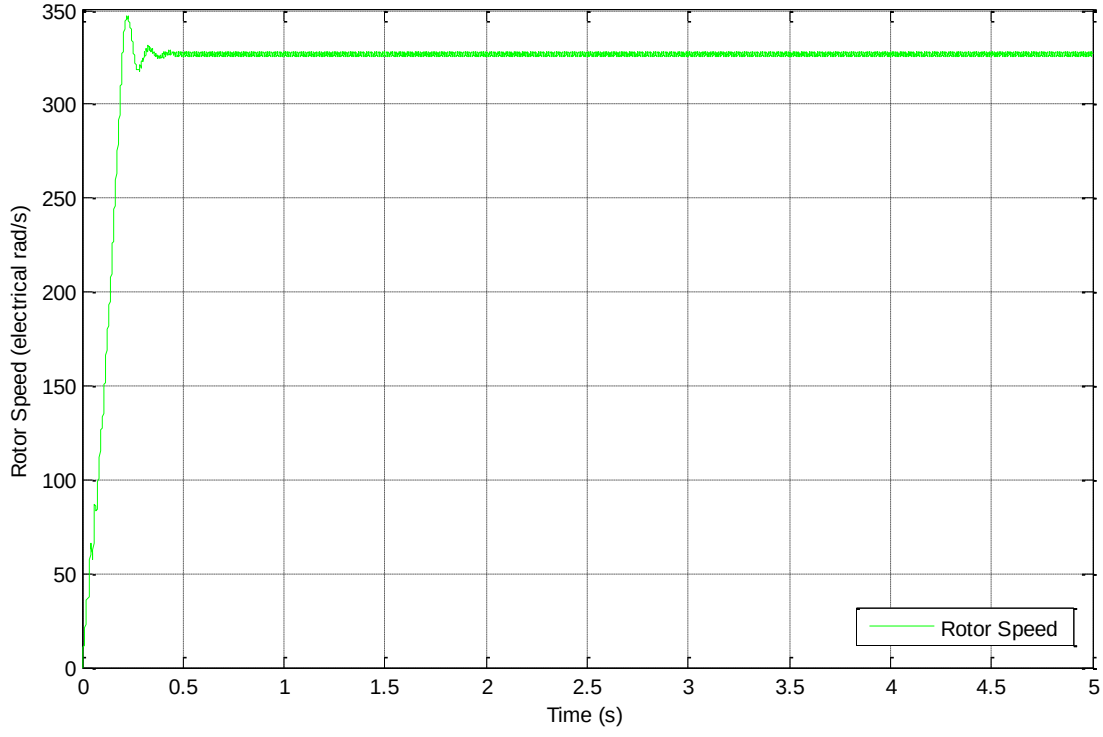

(b)

Fig. 5.2.5. Rotor speed (a) Existing model (b) Improved model

The results obtained from the improved model confirm that the system becomes steady after a transient time less than 0.5 s and current and voltage waveforms are purely sinusoidal with a frequency of 50 Hz. However, the results from the existing model are unstable throughout the period of testing. Therefore, the dynamic model given in the literature is not reliable and was not used for any future development in this thesis.

In order to verify the increased accuracy of the comprehensive model developed in Chapter 3, the already verified improved model is used as means of comparison.

5.3 Verification of the Increased Accuracy of the Comprehensive Model

Five different test cases are performed to verify the improved accuracy of the comprehensive model which takes into account the effects of core losses and magnetic saturation. The simulation results of comprehensive model and improved model are compared with the corresponding experimental results obtained in the laboratory. In order to obtain 230 V at the output winding on the laboratory experimental setup, the operational conditions required for each test case are given in Table 5.3.1. The same operational parameters are used to obtain the simulation results from both comprehensive and improved models.

Table 5.3.1
Operational parameters required in each test case

Test Case	Load Resistance (Ω)	Fixed Capacitance (μF)	Rotor Speed (rpm)	Excitation Control Voltage (V)
A	93.4	30	1580	130
B	93.4	**40**	1580	121.4
C	**52.9**	40	1580	149.6
D	52.9	40	**1525**	177.2
E	52.9	**30**	1525	181.3

The experimental and the predicted results of voltage and current in both excitation control winding and output winding of the improved and the comprehensive models are given in Table 5.3.2.

Also, a numerical comparison of the error between experimental and computer simulation results is given as a percentage of the corresponding experimental value. Similarly, a comparison of power factors and active power of the two windings are made in Tables 5.3.3 and 5.3.4 respectively.

Table 5.3.2
Comparison of Current and Voltage of Improved and Comprehensive Models

Test case	Experimental				Improved Model				Comprehensive Model				Error % of Improved Model				Error % Comprehensive Model			
	Vse (V)	Ise (A)	Vso (V)	Iso (A)	Vse (V)	Ise (A)	Vso (V)	Iso (A)	Vse (V)	Ise (A)	Vso (V)	Iso (A)	Vse	Ise	Vso	Iso	Vse	Ise	Vso	Iso
A	130.0	6.0	230.5	3.3	130.0	6.24	238.93	3.44	130.0	5.92	235.04	3.37	0.0	4.0	3.7	4.4	0.0	-1.3	2.0	2.2
B	121.4	5.1	229.6	3.8	121.4	5.31	238.44	3.95	121.4	4.98	231.72	3.85	0.0	4.1	3.8	4.0	0.0	-2.3	0.9	1.4
C	149.6	3.5	229.9	5.1	149.6	3.42	243.95	5.53	149.6	3.45	236.10	5.42	0.0	-2.3	6.1	8.5	0.0	-1.4	2.7	6.3
D	177.2	6.1	230.2	5.1	177.2	5.75	242.04	5.51	177.2	6.22	235.18	5.37	0.0	-5.7	5.1	8.0	0.0	1.9	2.2	5.3
E	181.3	6.3	230.8	4.8	181.3	5.81	238.37	5.09	181.3	6.41	234.05	4.97	0.0	-7.8	3.3	6.1	0.0	1.8	1.4	3.6

When the generator system is not regulated, the output voltage of the improved model is much higher than that of the experimental value. However, the maximum discrepancy of the output voltage between the experimental and the comprehensive models is 2.7% only. Similarly, the error percentages of excitation control and output windings currents of the improved model are almost twice those in the comprehensive model. The maximum error percentages of excitation control and output windings currents of the comprehensive model are 2.3% and 6.3% respectively while those in the improved model are -7.8% and 8.5% respectively. In particular, the comprehensive model provides significant improvement in the accuracy of the excitation control power factor. In the worst case, when the excitation control power factor of the improved model is 41.4%, that of the comprehensive model is reduced up to 17.6%. In Table 5.3.4, it is noticed that the deviation of active power in both windings of the comprehensive model is dramatically reduced compared to that of the improved model, as indicated by the experimental values. The error percentage of almost all the results obtained from the comprehensive model is less than 5% while several others are slightly higher than that.

Table 5.3.3

Comparison of Excitation Control and Output Power Factors of Improved and Comprehensive Models

Test case	Experimental		Improved Model		Comprehensive Model		Error % Improved Model		Error % Comprehensive Model	
	Excitation Power Factor	Output Power Factor	Excitation Power Factor	Output Power Factor	Excitation Power Factor	Output Power Factor	Excitation Power Factor	Output Power Factor	Excitation Power Factor	Output Power Factor
A	-0.78	-0.74	-0.88	-0.75	-0.83	-0.75	12.3	1.4	6.0	1.4
B	-0.89	-0.64	-0.96	-0.66	-0.93	-0.64	7.9	3.3	4.5	-0.4
C	-0.50	-0.83	-0.71	-0.83	-0.59	-0.84	41.4	-0.4	17.6	1.7
D	0.86	-0.83	0.89	-0.83	0.84	-0.83	3.6	-0.4	-1.8	-0.4
E	0.75	-0.89	0.79	-0.89	0.75	-0.89	5.4	0.1	0.0	0.1

Table 5.3.4

Comparison of Excitation Control and Output Power of Improved and Comprehensive Models

Test case	Experimental		Improved Model		Comprehensive Model		Error % Improved Model		Error % Comprehensive Model	
	Excitation Power (W)	Output Power (W)	Excitation Power (W)	Output Power (W)	Excitation Power (W)	Output Power (W)	Excitation Power	Output Power	Excitation Power	Output Power
A	-608.4	-562.9	-711.0	-617.3	-636.7	-594.7	16.9	9.7	4.7	5.6
B	-551.0	-558.4	-619.0	-623.4	-562.2	-569.0	12.3	11.6	2.0	1.9
C	-261.8	-973.2	-361.7	-1116.0	-303.4	-1080.3	38.2	14.7	15.9	11.0
D	929.6	-974.4	907.8	-1103.1	930.1	-1044.8	-2.3	13.2	0.1	7.2
E	856.6	-986.0	832.1	-1081.1	871.8	-1037.2	-2.9	9.7	1.8	5.2

The accuracy of the comprehensive model has been increased due to the losses being taken into account in developing the mathematical model. Therefore, the comprehensive model is used for studying the transient performance of the unregulated generator system discussed in the next section.

5.4 Voltage Build-up Process of the Generator

A constant voltage and a smooth sinusoidal waveform are important for safe operation of the electrical equipments. Therefore, the knowledge of voltage build-up process of the induction generator is important when it is employed to generate decentralized power for individual or co-operate consumption at the local generation point. In order to study the voltage build-up process of the novel single-phase induction generator used in this thesis, the results obtained from the already verified improved model in Section 5.2 are used. The transient behaviour of the output winding voltage and current are carefully analysed to understand the voltage build-up process of the generator when a constant voltage is supplied at the excitation control winding. This analysis is presented in this section as below.

Using Fig. 5.2.3 and 5.2.4, the voltage build-up process of the generator is observed during the transient period, i.e. 0 - 0.5 s of both output winding voltage and current waveforms as shown in Fig. 5.4.1 and 5.4.2 respectively.

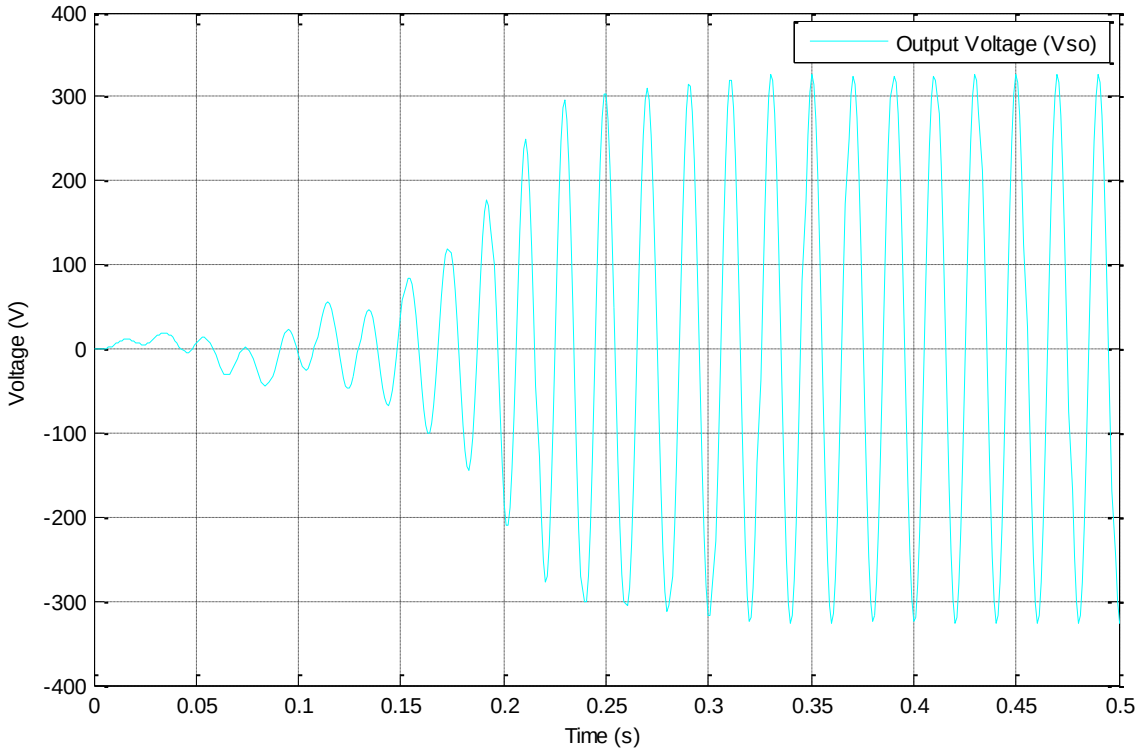

Fig. 5.4.1 Transients of Output Winding Voltage

At the starting point i.e. 0 s, when the rotor is standstill, the output voltage is zero. When the machine starts to rotate with a constant voltage of 146 V is supplied at the

excitation control winding, a small voltage is built-up at the output winding due to the fixed capacitance connected in parallel to the consumer load. When the rotor speed increases, the output voltage increases because of the increased filed strength. This process continues until voltage reaches to a steady condition at a constant rotor speed. This scenario is illustrated in Fig. 5.4.1.

Similarly, with the small field strength, a small output winding current is generated just after the machine began to operate. When the field strength increases with the increasing rotor speed, the output winding current also increases until reaches the steady condition at a constant rotor speed. This is shown in Fig. 5.4.2.

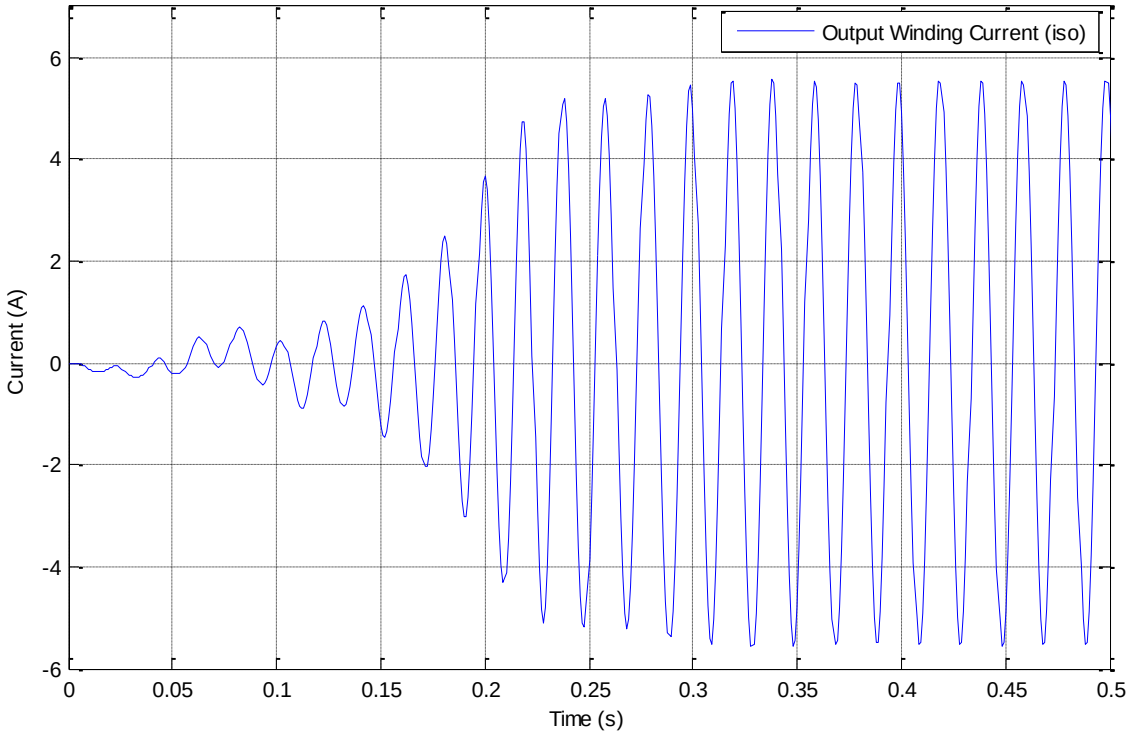

Fig. 5.4.2 Transients of Output Winding Current

Starting from 0, both output winding voltage and current gradually increase up to the desired output. None of the variables exceeds the rated condition. It is noticed that, just after a few seconds, both the waveforms acquire the expected sinusoidal curve with the accurate frequency. Therefore, employing this novel single-phase generator in off-grid operation will provide a high quality output to the local consumers connected to the electrical generation scheme.

5.5 Performance Analysis in Transient-State

In order to arrive at the results presented in this section, first, the normal operating condition of the generator was selected. This operating condition was specified so as to generate the voltage of 230 V at the output for a desired consumer load. The selected rotor speed did not exceed the rated value. A small capacitance was selected as the fixed capacitance connected in the output winding.

The excitation control voltage, the fixed capacitance, the consumer load and the rotor speed are considered as the operational parameters and all other parameters that depend on these operational parameters are considered as the variable parameters of the system. The effects of changing each of these parameters are studied separately by Matlab simulations in the following sections of this chapter. The verification of these theoretical studies based on the comprehensive dynamic model was made by comparing the corresponding experimental results obtained on the laboratory experimental set-up.

5.5.1 The Transient due to Sudden Change in Consumer Load

In this study, instead of a general load with resistance and inductance, a single resistive R load is considered as the consumer load of the system to make the analysis easier. The operational parameters required generating the voltage of 230 V/ 50 Hz at the output when the load of 93.4 Ω (i.e. 56.6% of full-load current at desired output voltage) is connected are measured using the experimental set-up. In order to study the transient performance due to sudden change in consumer load, at 0.25 s, the load is increased in a step to 52.9 Ω (i.e. 84.3% full-load current at desired output voltage) while other operational parameters are kept constant. The simulations are carried out under the same operational conditions as those given in Table 5.5.1.1.

Table 5.5.1.1
Operational parameters used for load change

Parameter	Load (Ω)	Fixed Capacitance (μF)	Excitation Control Voltage (V)	Rotor Speed (rpm)
Value	93.4	30	130	1580

Figure 5.5.1.1 shows the voltage waveform of the excitation control winding. This remains unchanged throughout the period of testing. Excitation control winding

current, output winding voltage and output winding current are shown in Figs. 5.5.1.2-5.5.1.4 respectively. When the load is increased at 0.25 s, both the excitation control winding current and the output winding voltage reduce while the output winding current increases similar to the behaviour of a self-excited induction generator [148]. The increase in consumer load draws more power to the output winding. Since the mechanical torque decreases due to the increase of consumer load at a constant rotor speed, the mechanical power from the prime mover is dropped. Therefore, the real power supplies to the excitation control winding decreases. This causes the drop in the excitation control current. Due to the increase in output power at the reduced load resistance, output winding current starts to increase. However, with the increasing load, the output voltage decreases. In all results, the transient period lasts for only 3 to 4 cycles. The close matching of simulated results with the experimental results verify the accuracy of the comprehensive dynamic model.

In order to discover the frequencies of the obtained results, the time domain signal is converted into the frequency domain using the Fast Fourier Transform (FFT). The FFT of experimental and simulated excitation control winding voltages is given in Fig. 5.5.1.5. Similarly Figs. 5.5.1.6 - 5.5.1.8 show the FFTs of experimental and simulated output voltage, excitation control winding current and output winding current respectively. The frequencies of the simulated results are exactly the same as those of the excitation control voltage generated by the simulation itself. However, in the experimental results, several other frequencies components exist due to the harmonics of the fundamental frequency. The simulated waveforms and the frequency domain signals of rotor currents in phase ‘α’ and phase ‘β’ are shown in Figs. 5.5.1.9 and 5.5.1.10 respectively. The frequencies of rotor currents are the same as those of the stator currents. This relationship of stator and rotor components has been used to develop the steady-state model of the single-phase induction generator described in the latter part of the Chapter 3.

The rotor speed and the mechanical torque obtained from the computer simulations are depicted in Figs. 5.5.1.11 and 5.5.1.12 respectively. These graphs demonstrate that, due to a sudden change in the consumer load, the rotor speed and the torque possess a transient period before becoming steady. A numerical comparison of experimental and theoretical results of voltage and current in both excitation control winding and output winding obtained before and after the transient period is given in

Test Case A of Table 5.7.1. Similar comparisons of power factor and active power of both windings are given in Test Case A of Tables 5.7.2 and 5.7.3 respectively.

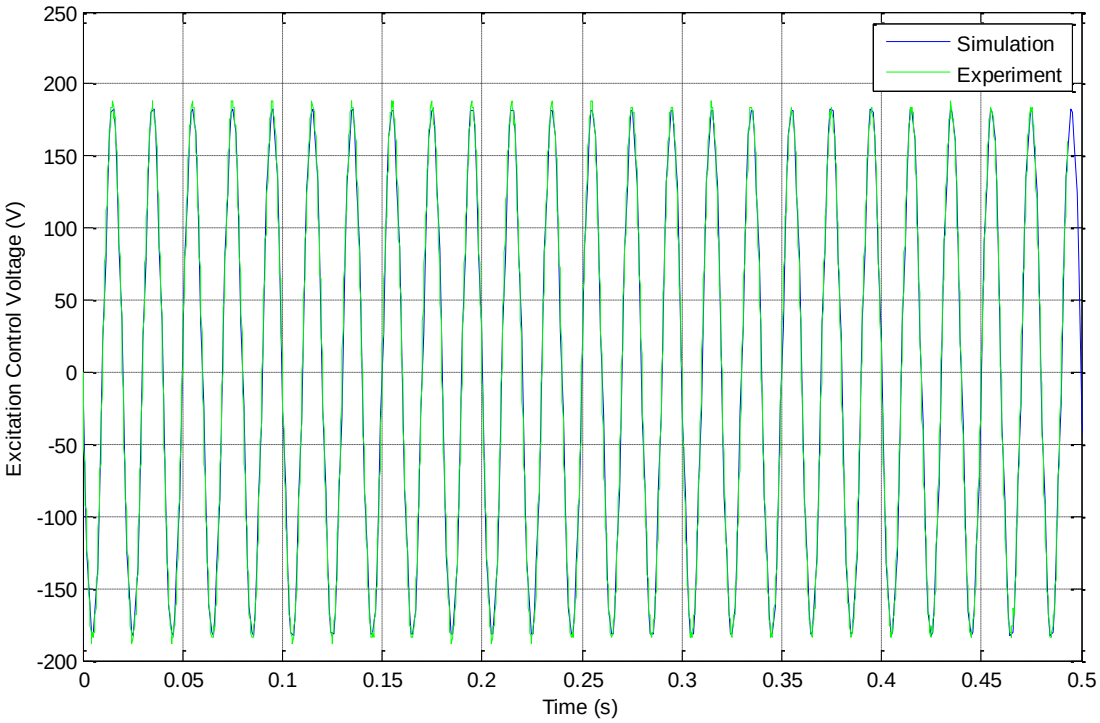

Fig. 5.5.1.1 Excitation control winding voltage

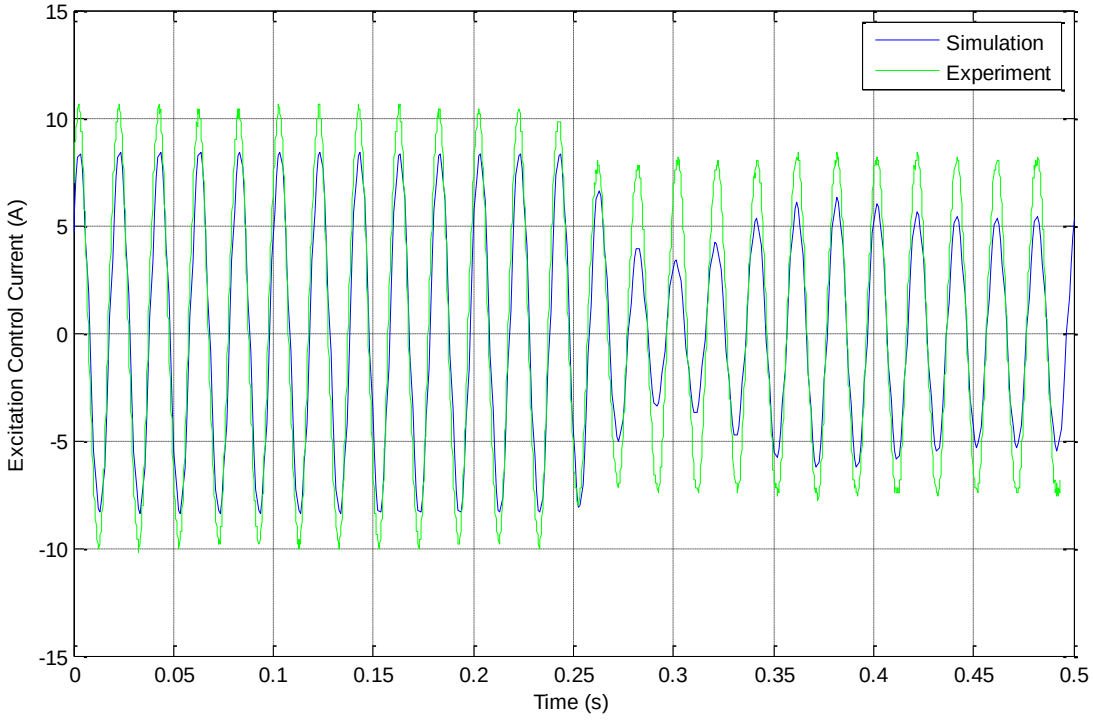

Fig. 5.5.1.2 Transients of excitation control winding current due to a step change in load resistance from 93.4 Ω to 52.9 Ω at t=0.25s

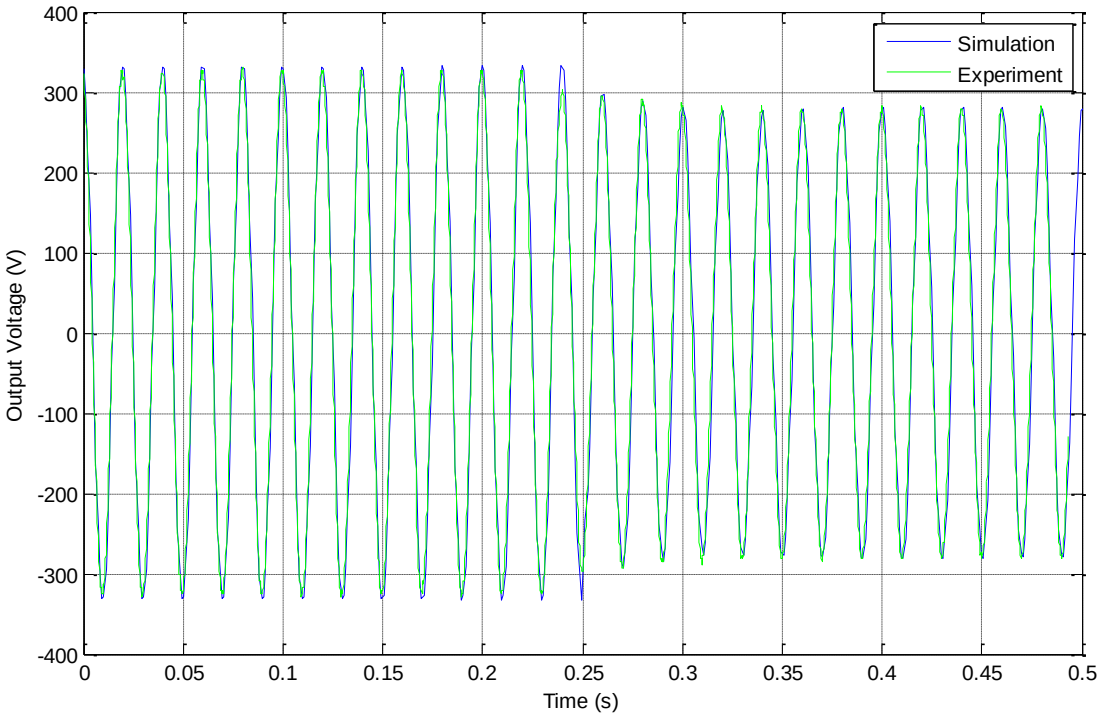

Fig. 5.5.1.3 Transients of output voltage due to a step change in load resistance from 93.4 Ω to 52.9 Ω at t=0.25s

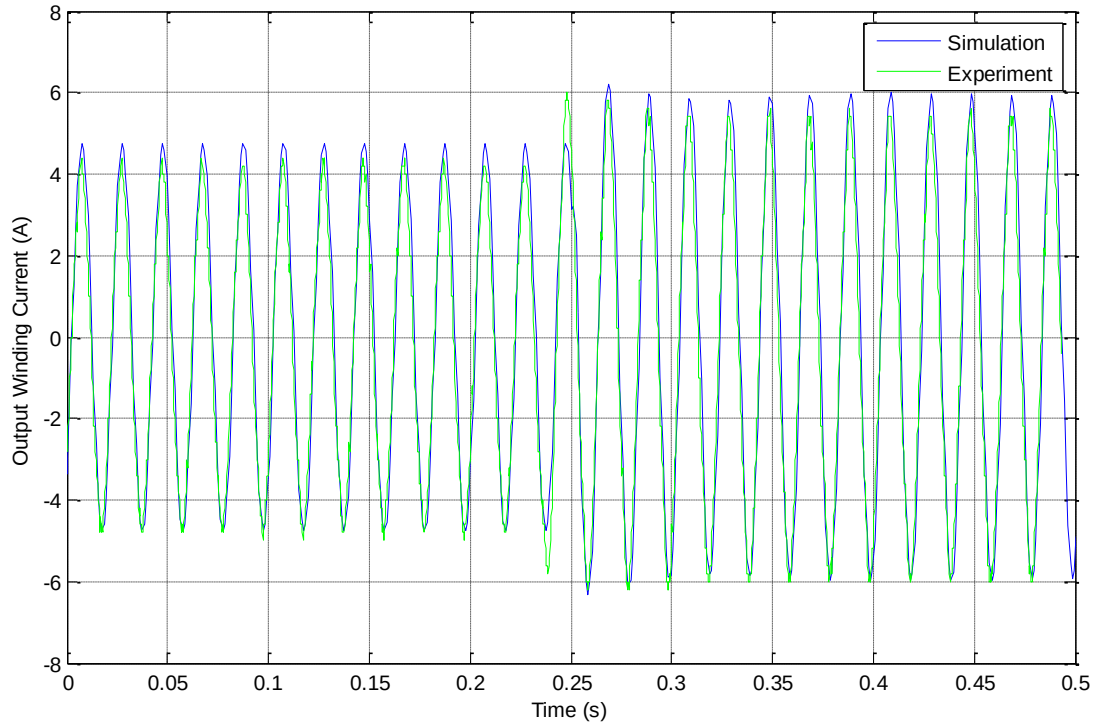

Fig. 5.5.1.4 Transients of output winding current due to a step change in load resistance from 93.4 Ω to 52.9 Ω at t=0.25s

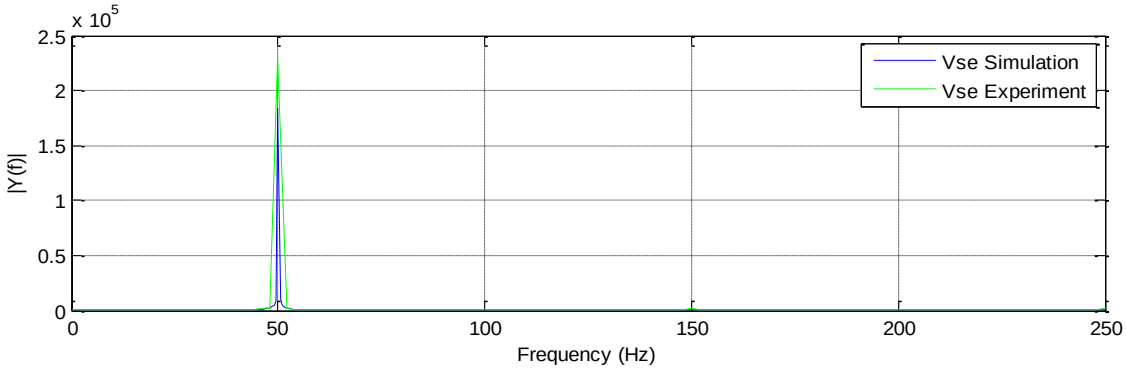

Fig. 5.5.1.5 FFT of the excitation control voltage

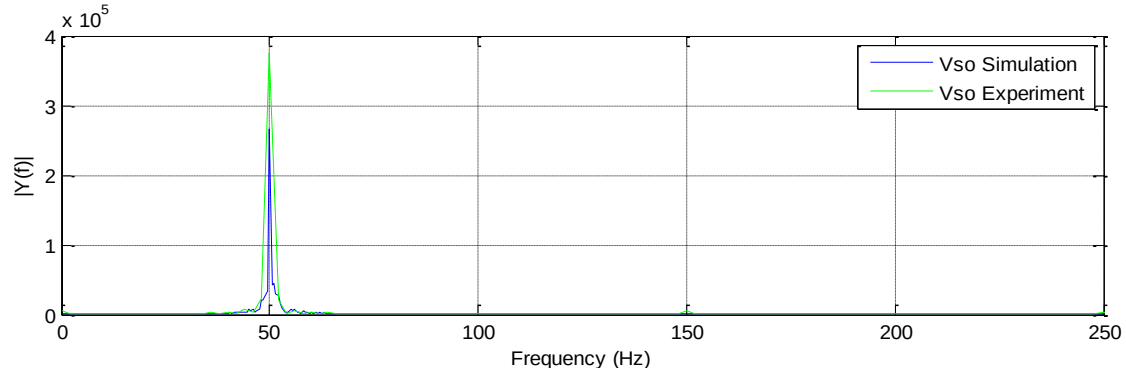

Fig. 5.5.1.6 FFT of the output voltage

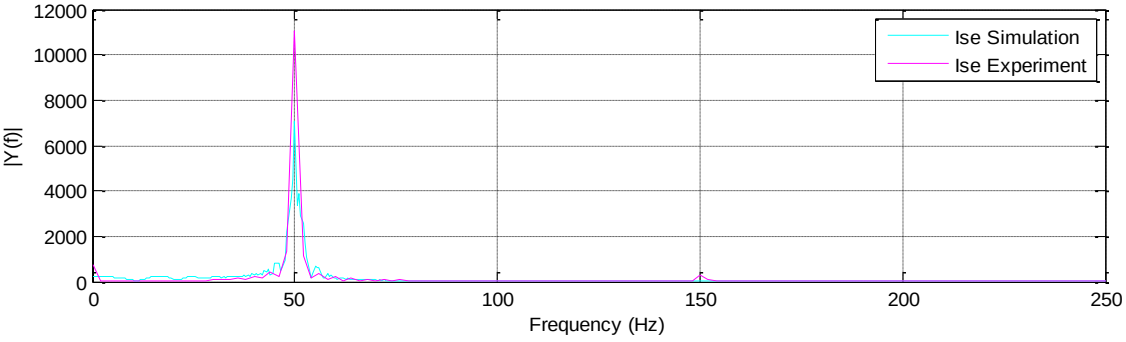

Fig. 5.5.1.7 FFT of the excitation control current

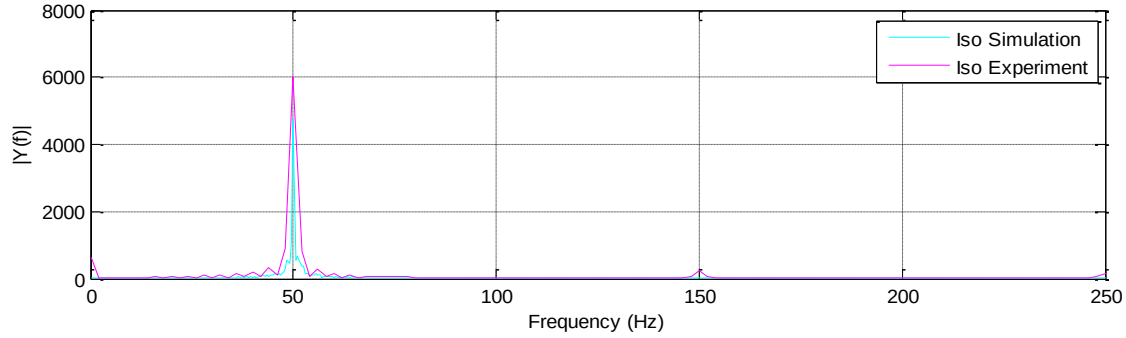

Fig. 5.5.1.8 FFT of the output current

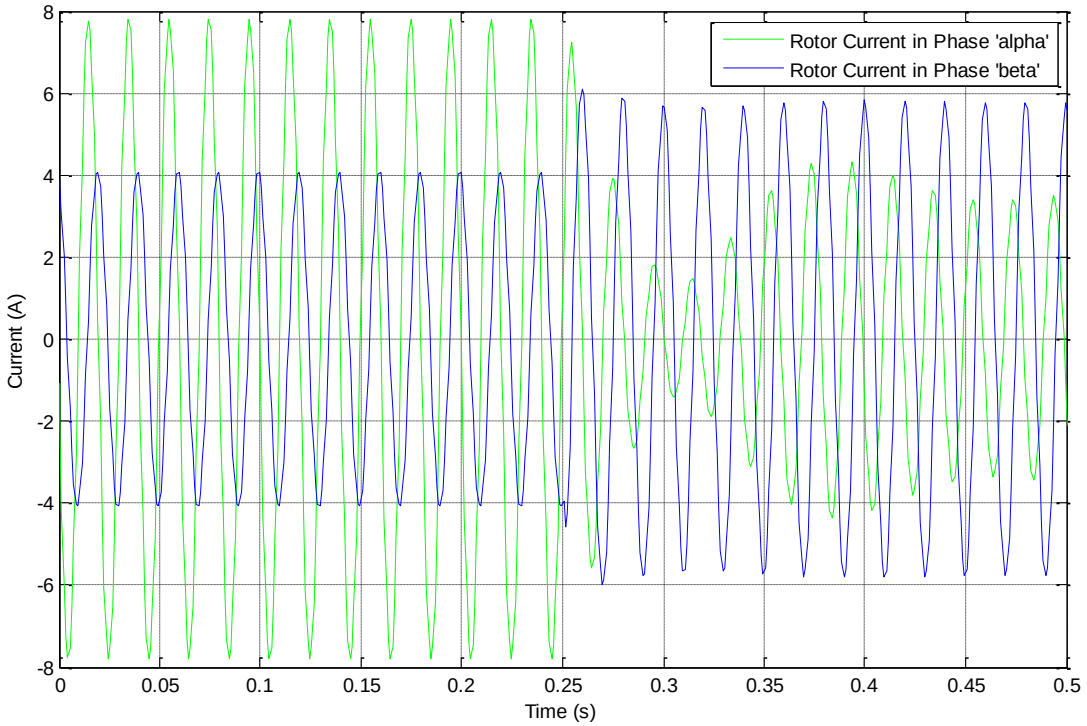

Fig. 5.5.1.9 Transients of rotor currents due to a step change in load resistance from 93.4 Ω to 52.9 Ω at t=0.25s

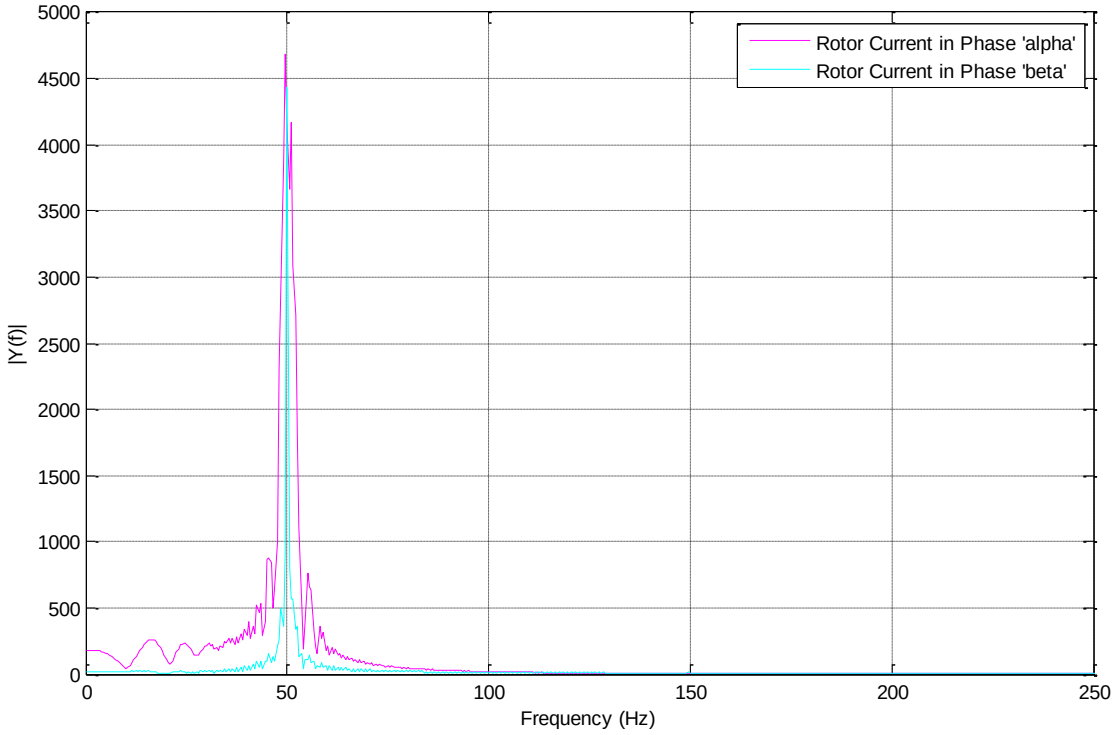

Fig. 5.5.1.10 FFT of the rotor currents

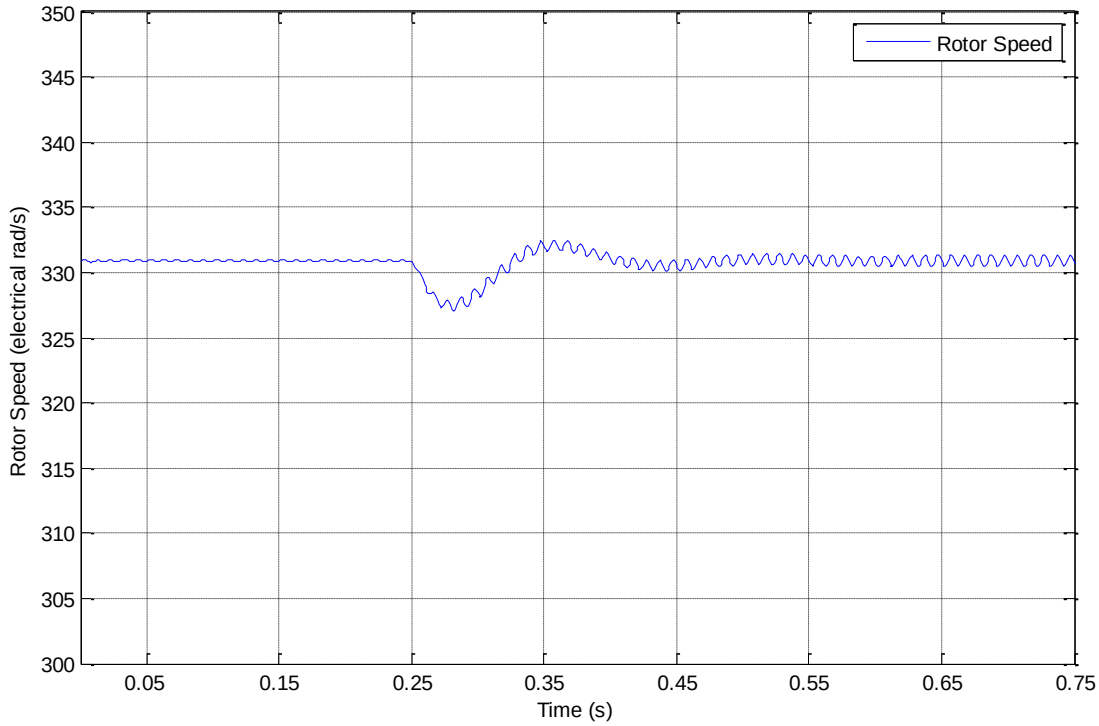

Fig. 5.5.1.11 Characteristics of rotor speed

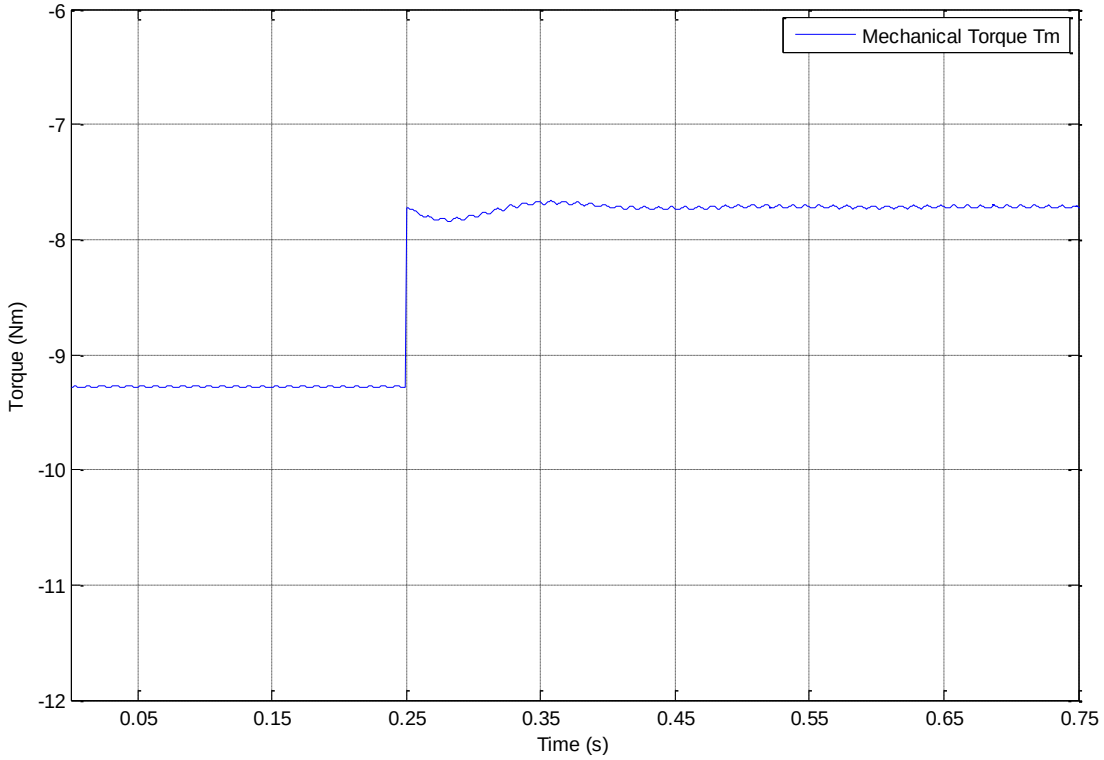

Fig. 5.5.1.12 Characteristics of mechanical torque

5.5.2 The transient due to sudden change in fixed capacitance

The effect of sudden change in the fixed capacitance on the performance of the generator system is studied in this section. The operational parameters required generating the voltage of 230 V/ 50 Hz at the output when the fixed capacitance of 40 µF is connected in parallel with the resistive load of 52.9 Ω (i.e. the full-load current at desired output voltage) are measured using the experimental set-up the same as in the previous section. In order to study the transient performance due to sudden change in the fixed capacitance, at 0.25 s, the capacitance is reduced in a step from 40 µF to 30 µF (i.e. 95.2 % of full-load current at desired output voltage) while other operational parameters are kept constant. The same operational conditions given in Table 5.5.2.1 are used for the simulations carried out for theoretical analysis of the transient behaviour due to sudden change in fixed capacitance.

Table 5.5.2.1
Operational parameters used for capacitance change

Parameter	Load (Ω)	Fixed Capacitance (µF)	Excitation Control Voltage (V)	Rotor Speed (rpm)
Value	52.9	40	145	1580

Figures 5.5.2.1 – 5.5.2.4 show the waveforms of excitation control winding voltage, current, output voltage and output winding current respectively. At 0.25 s when the capacitance is decreased down to 30 µF, the total impedance connected at the output winding increases. This will result to decrease both voltage and current in the output winding. Decrease in voltage and current in output winding decreases the power at the output terminal. However, as the rotor speed remains unchanged, the additional mechanical power generation causes an increase of the active power of excitation control winding in order to maintain the active power balance in the system. Therefore, the current in the excitation control winding increases when the voltage remains constant. In each figure, it is noticed that due to a sudden change to the fixed capacitance, the system requires 2 to 3 cycles to build up its steady condition once again. A very good agreement between simulation and experimental results confirms the accuracy of the comprehensive model. The frequency spectrum of excitation control voltage, output voltage, excitation control winding current and output winding current are illustrated in Figs. 5.5.2.5 – 5.5.2.8 respectively.

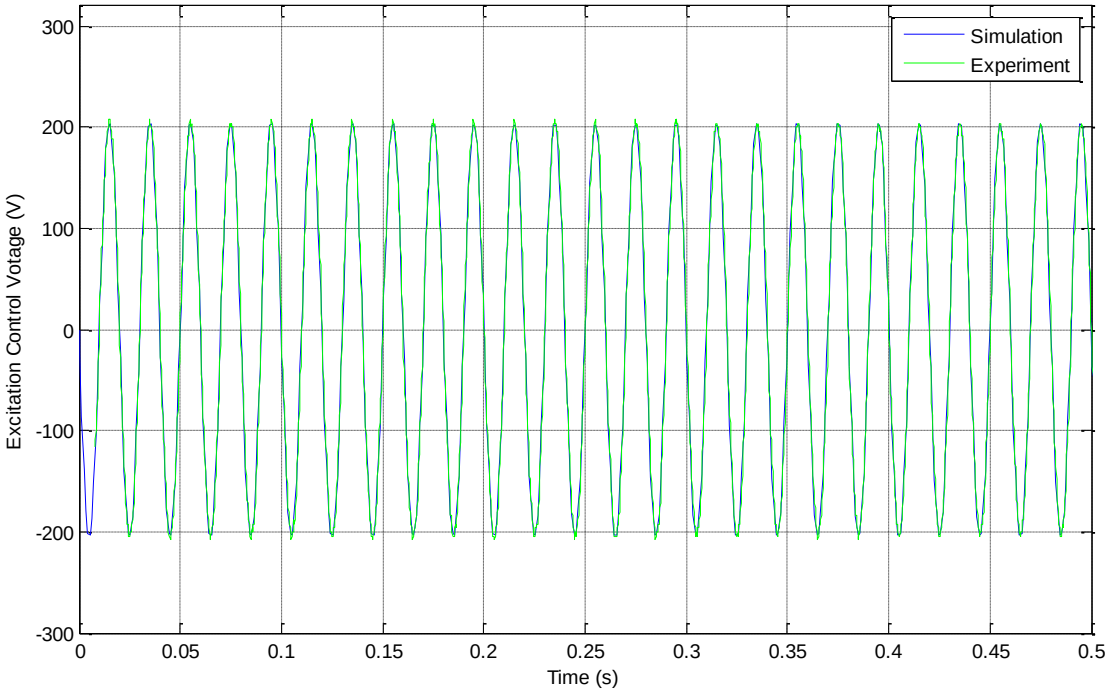

Fig. 5.5.2.1 Excitation control winding voltage

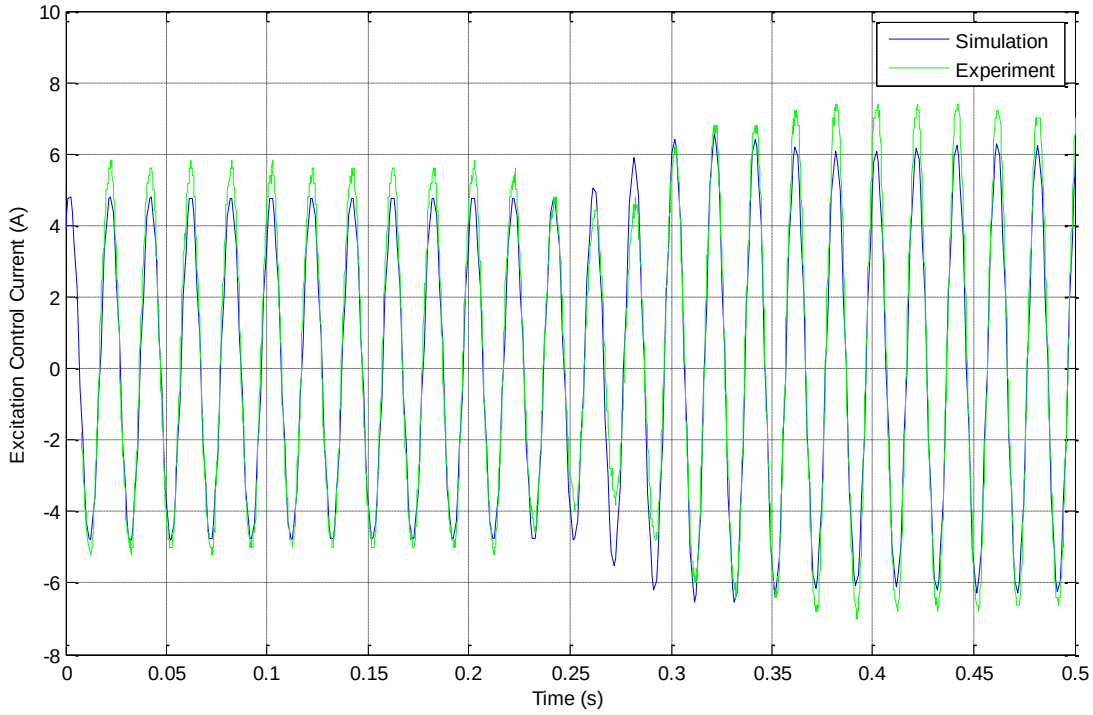

Fig. 5.5.2.2 Transients of excitation control winding current due to a step change in fixed capacitance from 40 μF to 30 μF at t=0.25s

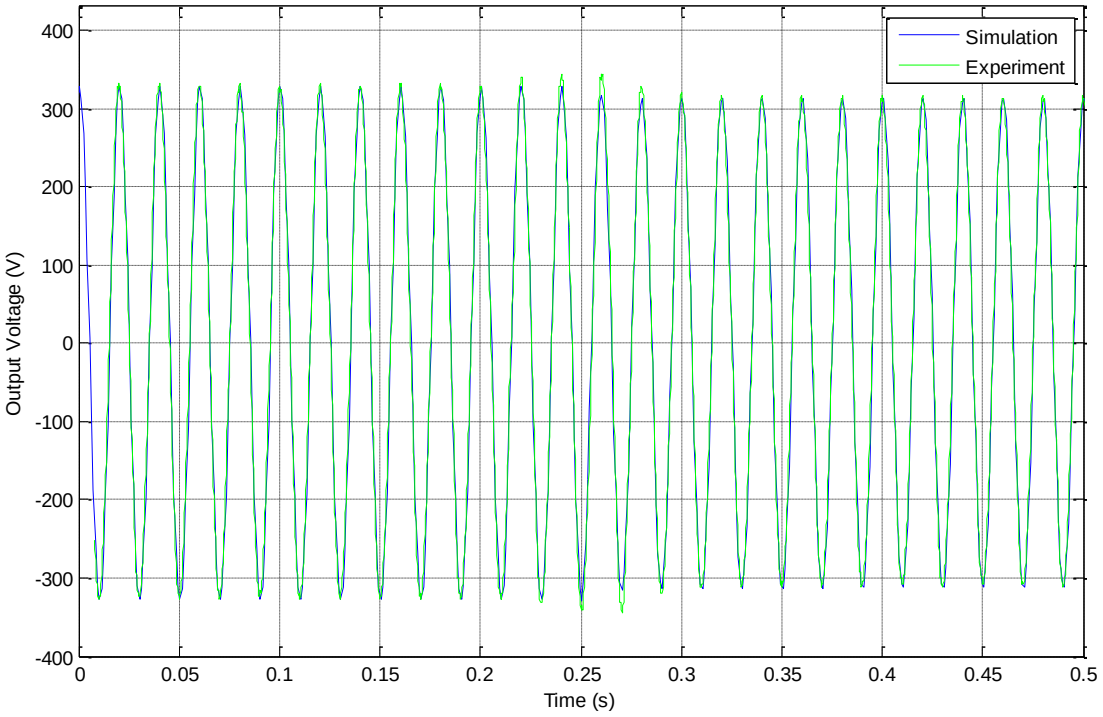

Fig. 5.5.2.3 Transients of output voltage due to a step change in fixed capacitance from 40 µF to 30 µF at t=0.25s

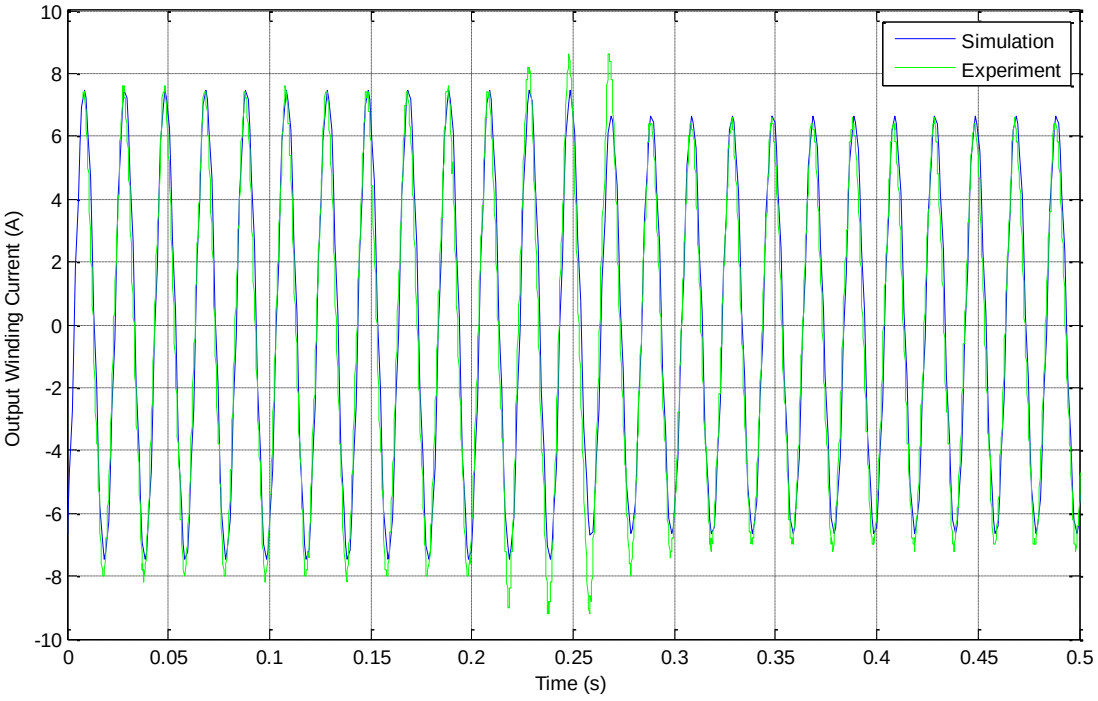

Fig. 5.5.2.4 Transients of output winding current due to a step change in fixed capacitance from 40 µF to 30 µF at t=0.25s

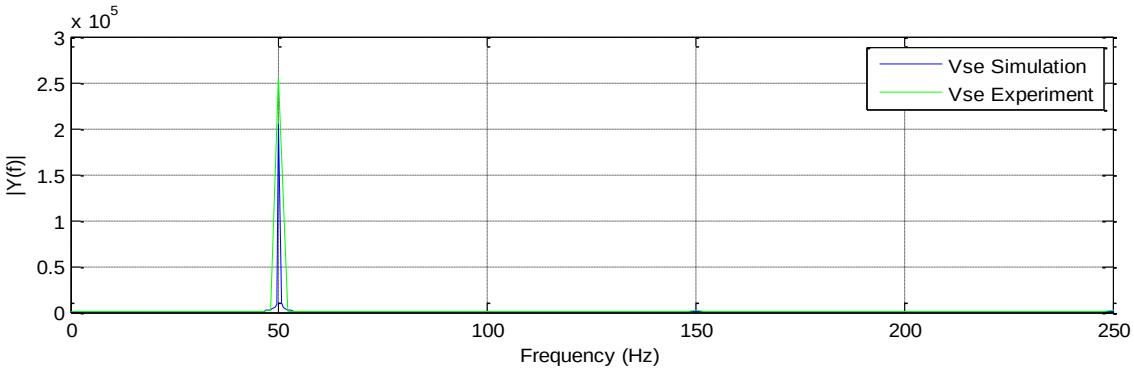

Fig. 5.5.2.5 FFT of the excitation control voltage

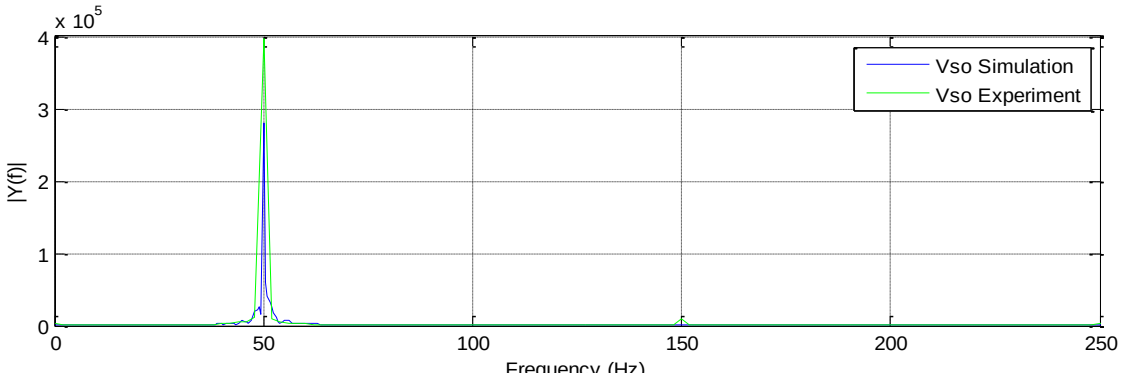

Fig. 5.5.2.6 FFT of the output voltage

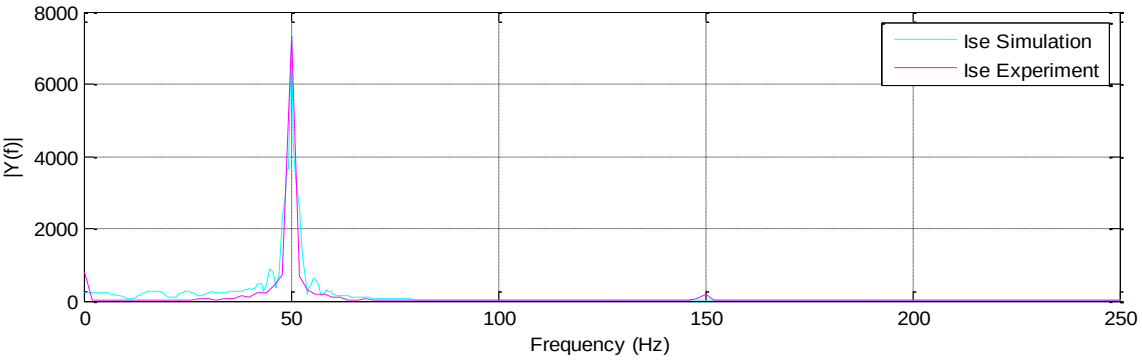

Fig. 5.5.2.7 FFT of the excitation control current

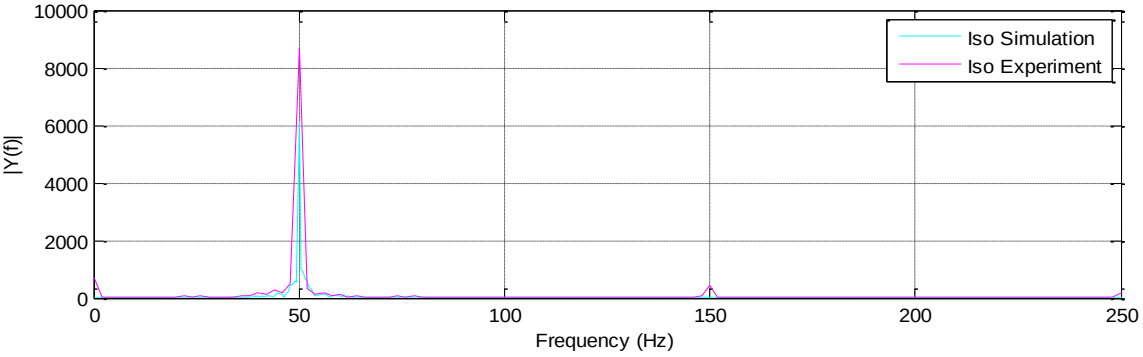

Fig. 5.5.2.8 FFT of the output current

The simulated results of the currents and the FFT analyses of rotor in the αβ frame are shown in Figs. 5.5.2.9 and 5.5.2.10 respectively. The fundamental frequencies of the rotor currents are the same as those of the stator as discussed in the previous section.

The rotor speed and the mechanical torque obtained from the computer simulations are illustrated in the Figs. 5.5.2.11 and 5.5.2.12 respectively. These graphs demonstrate that the sudden change to the fixed capacitance establishes a transient period for the rotor speed and the mechanical torque before they become steady. After the transient period, the rotor speed is back to its initial speed. However, the mechanical torque decreases with the decrease of the fixed capacitance. The reduction in output power causes the mechanical torque to decrease in order to maintain a constant rotor speed.

The voltage and current in both excitation control winding and output winding obtained from the experiments and simulations are tabulated in Test Case B of Table 5.7.1. A numerical comparison of the results before and after the transient period is presented. Similar comparisons carried out for the power factor and the active power of both windings are given in Test Case B of Tables 5.7.2 and 5.7.3 respectively.

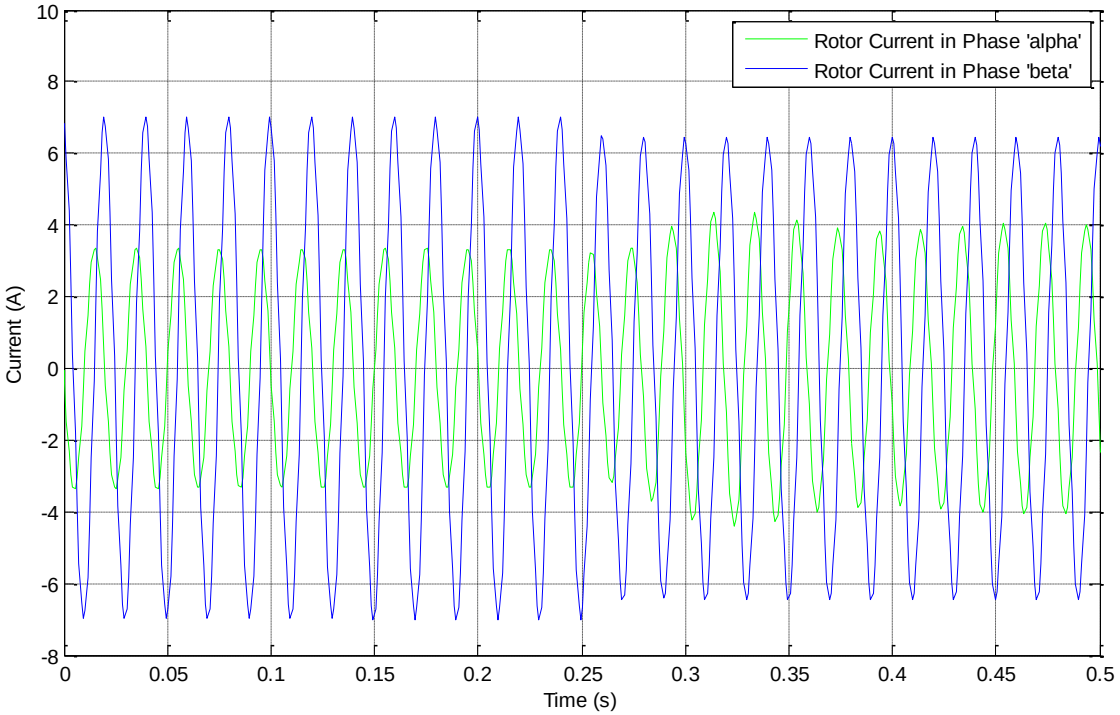

Fig. 5.5.2.9 Transients of rotor currents due to a step change in fixed capacitance from 40 μF to 30 μF at t=0.25s

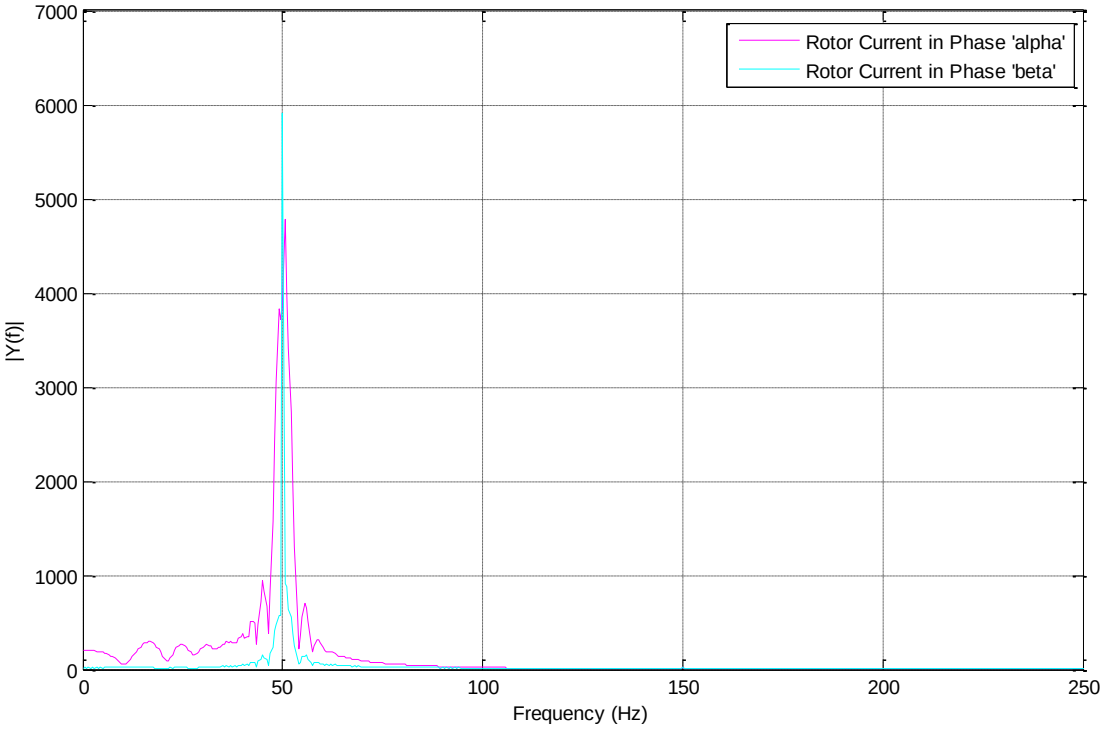

Fig. 5.5.2.10 FFT of the rotor currents

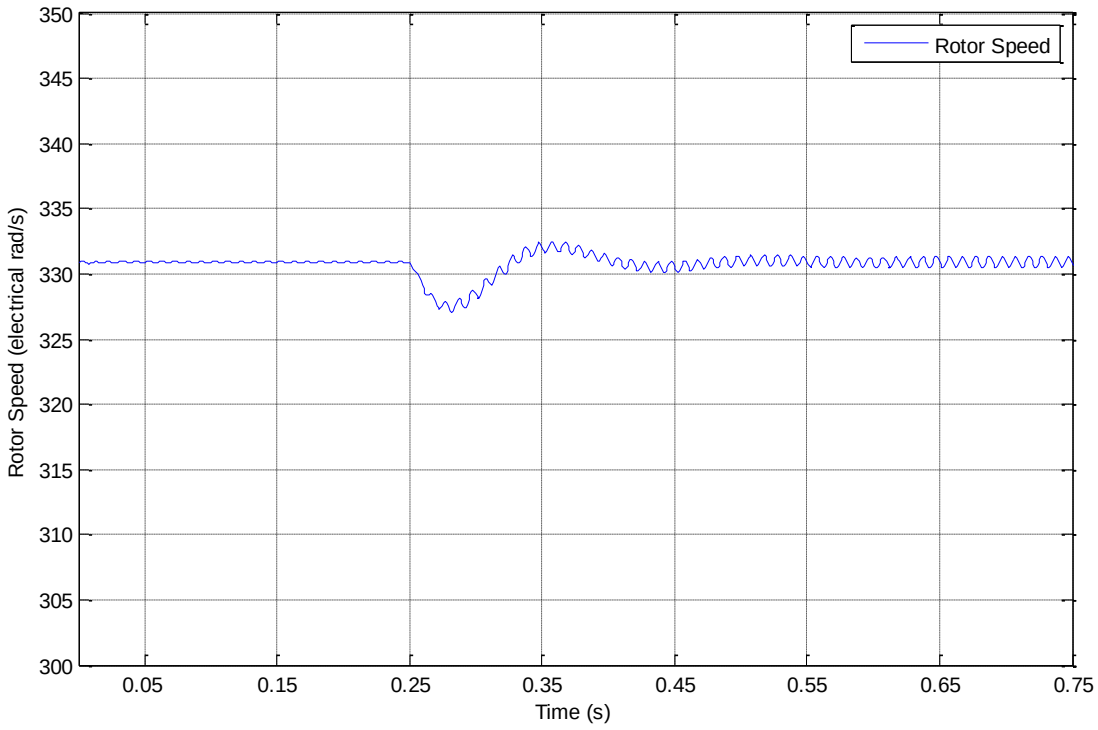

Fig. 5.5.2.11 Characteristics of rotor speed

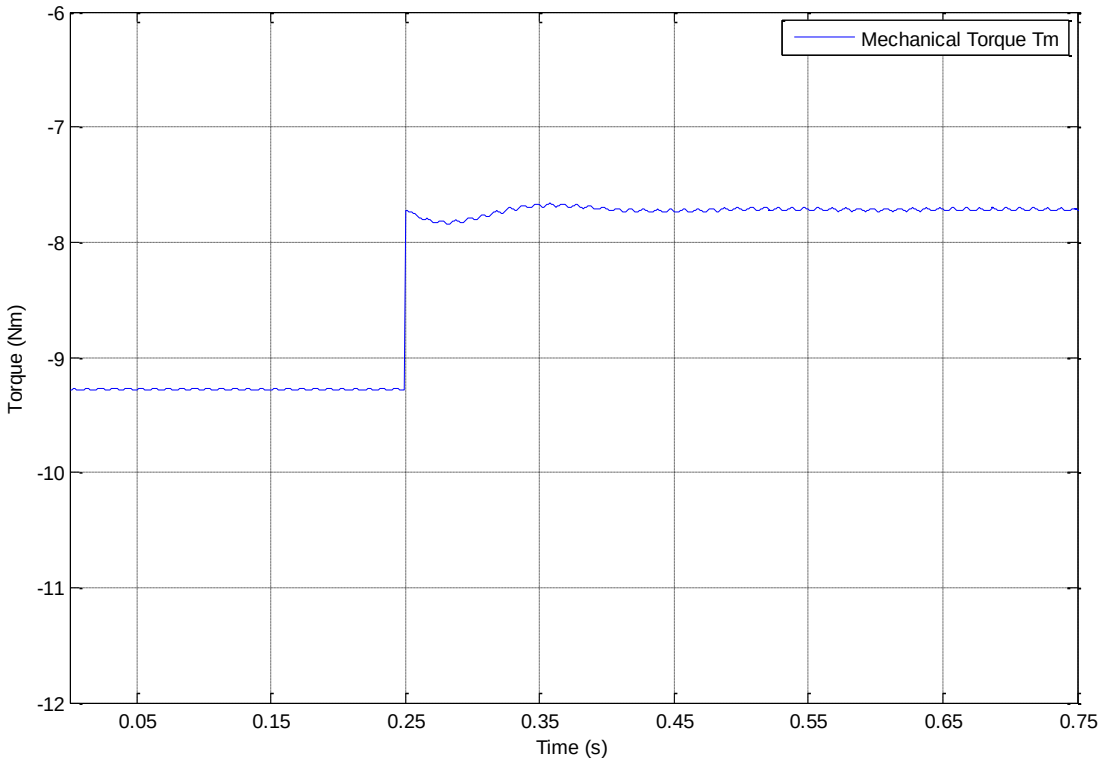

Fig. 5.5.2.12 Characteristics of Mechanical Torque

5.5.3 The transient due to sudden change in rotor speed

The dynamic behaviour of the single-phase induction generator due to the sudden change of rotor speed is discussed in this section. Similar to the previous analyses, initially the voltage of 230 V/ 50 Hz is generated at the output winding. The generator is operated at full-load condition with a rotor speed of 1580 rpm. The dynamic analysis of the generator due to the sudden change in rotor speed was performed by decreasing the rotor speed to 1556 rpm (i.e. 92.2% of full-load current at desired output voltage) at t=0.25 s while other operational parameters remain unchanged. The effects of sudden change of rotor speed on the variable parameters of the generator are observed using an oscilloscope connected to the laboratory experimental set-up. In the experiment, the operational parameters given in Table 5.5.3.1, except the rotor speed, are established before and after the change in rotor speed. In order to compare the experimental results with the simulation results obtained from the comprehensive dynamic model, the same operational parameters are used for the simulations performed in Matlab software. The analysis of dynamic behaviour due to the sudden change in rotor speed using the experimental and the theoretical results of the unregulated generator system is presented below.

Table 5.5.3.1
Operational parameters used for rotor speed change

Parameter	Load (Ω)	Fixed Capacitance (μF)	Excitation Control Voltage (V)	Rotor Speed (rpm)
Value	52.9	30	153	1580

The transients of voltages and currents in excitation control winding and output winding due to the sudden change of rotor speed are shown in Figs. 5.5.3.1 – 5.5.3.4 respectively. In both experimental and simulation results, all the variable parameters decrease with the decreasing rotor speed. The real power of the output winding decreases when the mechanical power decreases due to the low rotor speed. This causes either a reduction or absorption of the real power to or from the ESS. Thus, output winding voltage, current and excitation control current decrease with the reduction in real power in the system. In both experimental and simulation results, each variable parameter requires 3-4 cycles to become the steady condition. The results obtained from the experiments and simulations match each other with a good degree of accuracy. The simulated FFT analysis of excitation control voltage, output voltage, excitation control current and output winding current are depicted in Figs. 5.5.3.5 – 5.5.3.8 respectively. As predicted, the fundamental frequency at the output winding is maintained at the rated frequency 50 Hz. The simulation results of the rotor currents in phase 'α' and phase 'β' are shown in Fig 5.5.3.9. The frequency domain signals of the rotor currents are given in Fig. 5.5.3.10. The fundamental frequency of the rotor currents is the same as that of the stator which is equal to 50 Hz in this analysis.

The changes of rotor speed and the mechanical torque due to the sudden change in rotor speed are shown in Figs. 5.5.3.11 and 5.5.3.12 respectively. When the rotor speed is reduced from 1580 rpm to 1556 rpm, the mechanical torque decreases from -10 to -6 respectively.

A numerical comparison of experimental and simulated values of voltages and currents in both excitation control winding and output winding before and after the transient period are given in the Test Case C of the Table 5.7.1. Similarly, experimental and simulation results of the power factor and active power of both

excitation control and output winding are given in Test Case C of Tables 5.7.2 and 5.7.3 respectively.

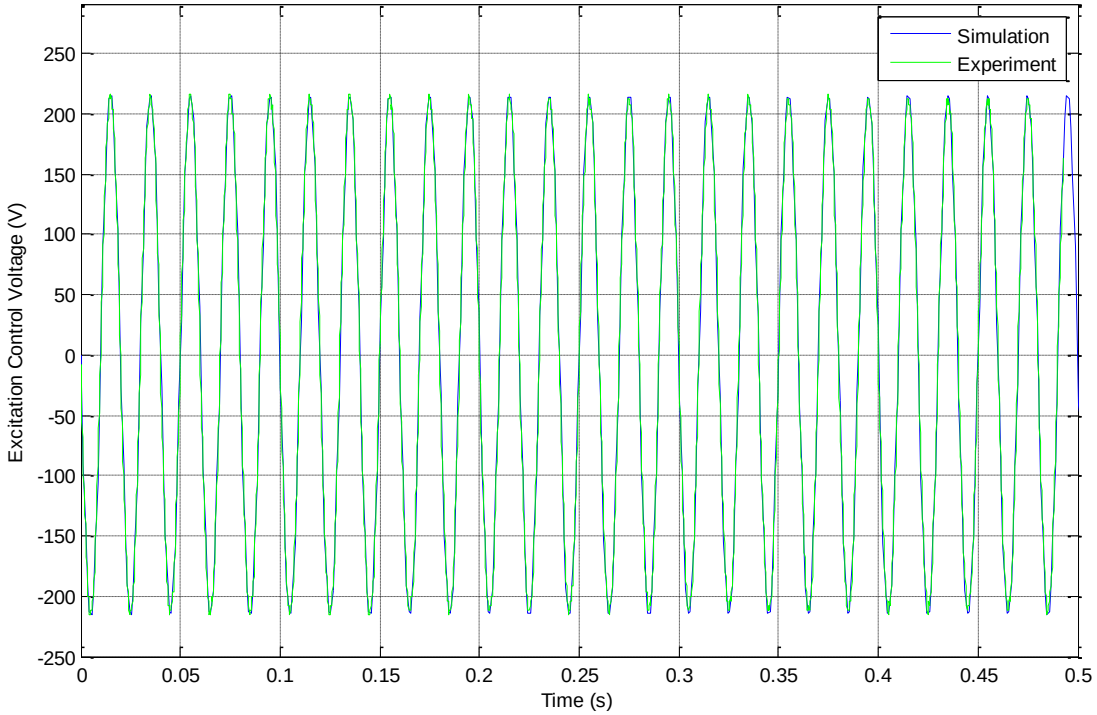

Fig. 5.5.3.1 Excitation control winding voltage

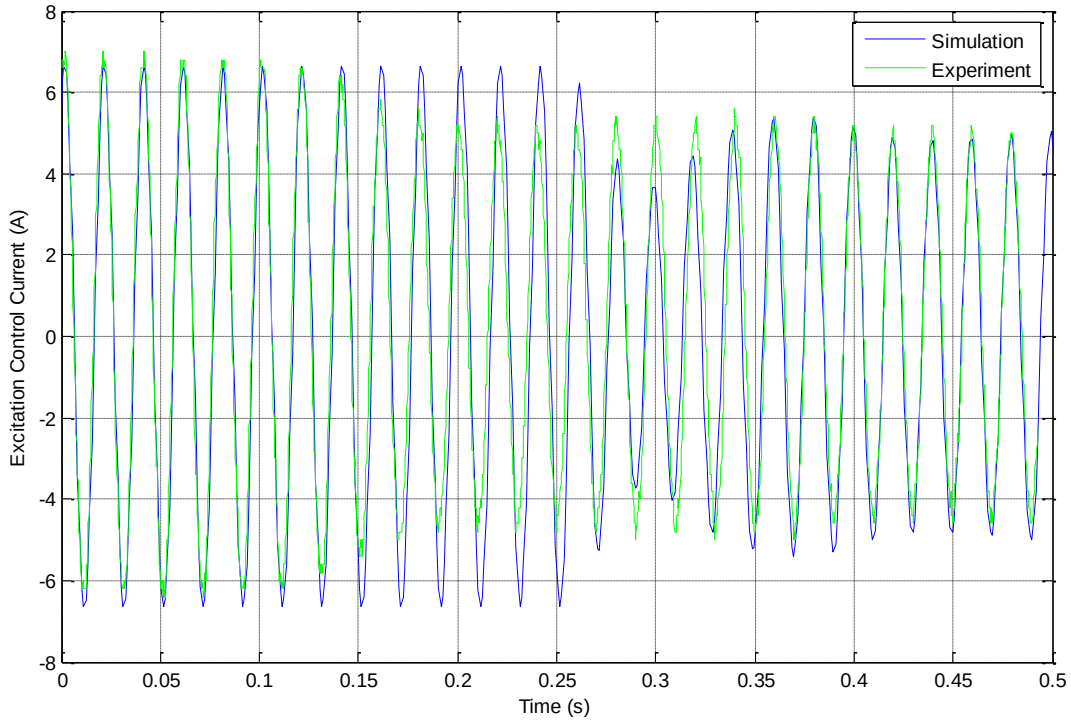

Fig. 5.5.3.2 Transients of excitation control winding current due to a step change in rotor speed from 1580 rpm to 1556 rpm at t=0.25s

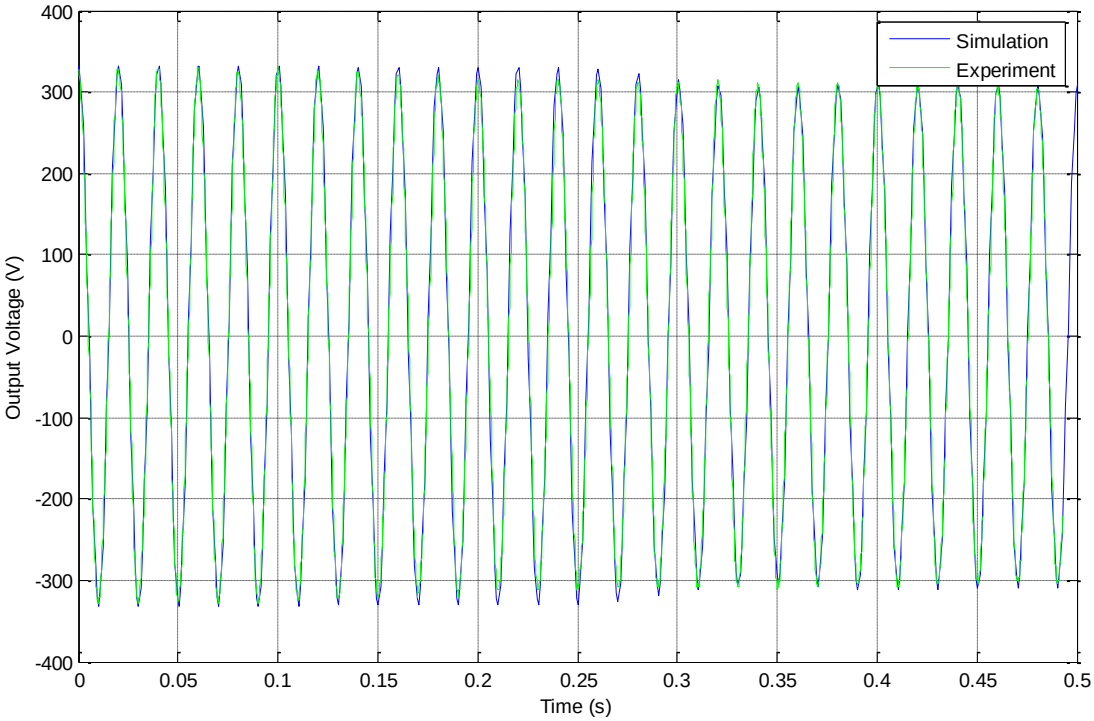

Fig. 5.5.3.3 Transients of output voltage due to a step change in rotor speed from 1580 rpm to 1556 rpm at t=0.25s

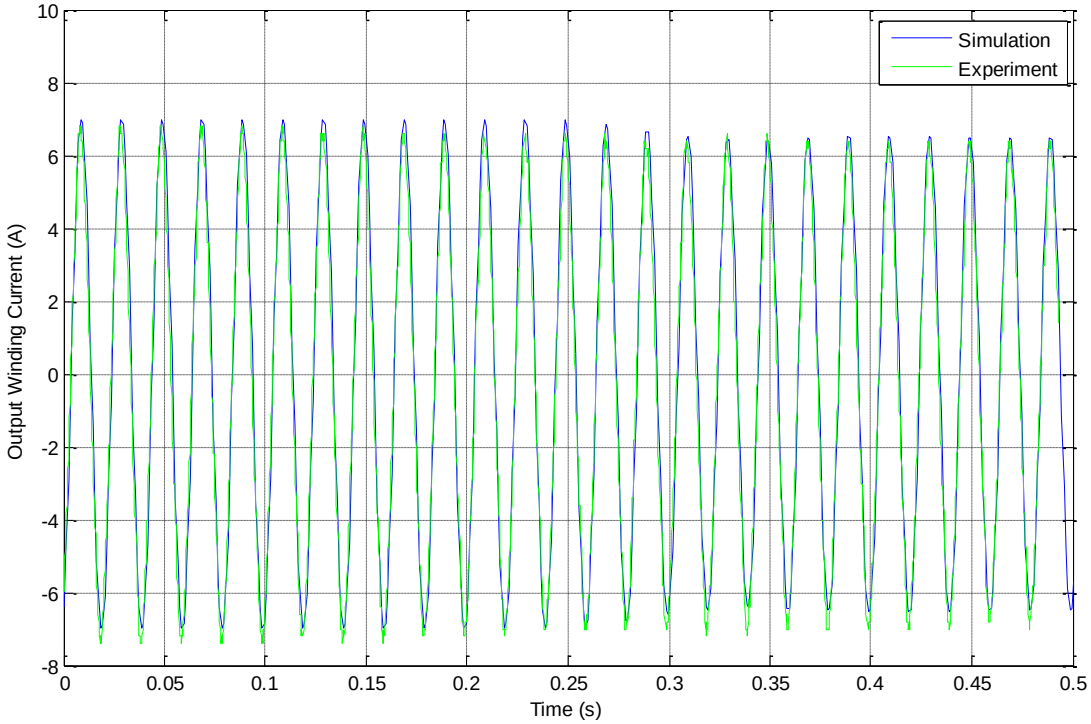

Fig. 5.5.3.4 Transients of output winding current due to a step change in rotor speed from 1580 rpm to 1556 rpm at t=0.25s

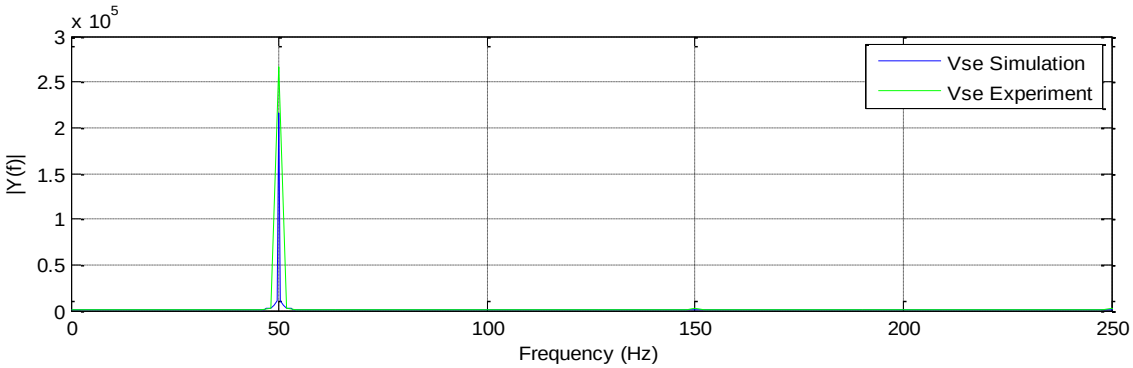

Fig. 5.5.3.5 FFT of the excitation control voltage

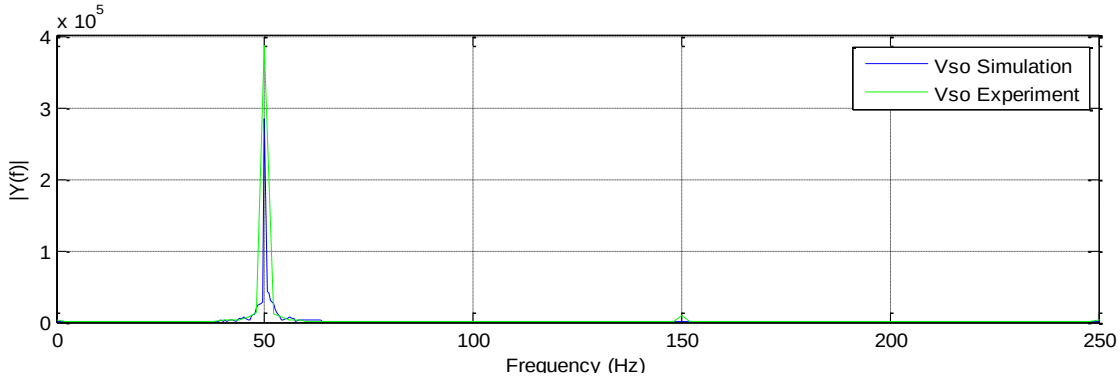

Fig. 5.5.3.6 FFT of the output voltage

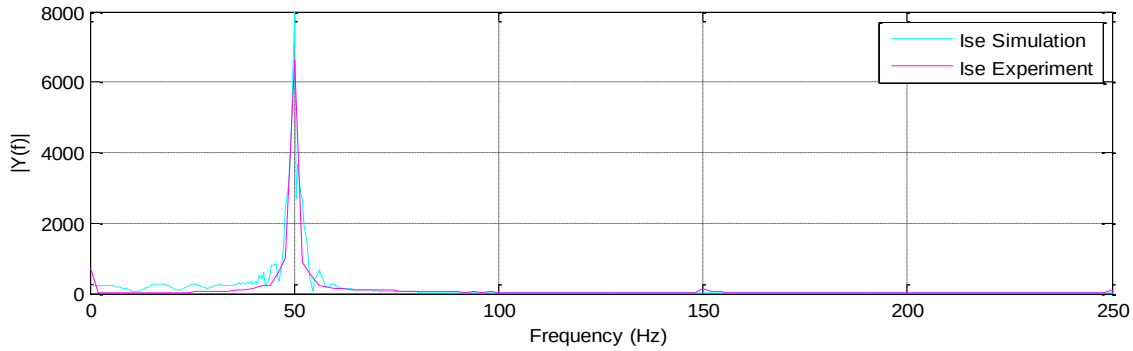

Fig. 5.5.3.7 FFT of the excitation control current

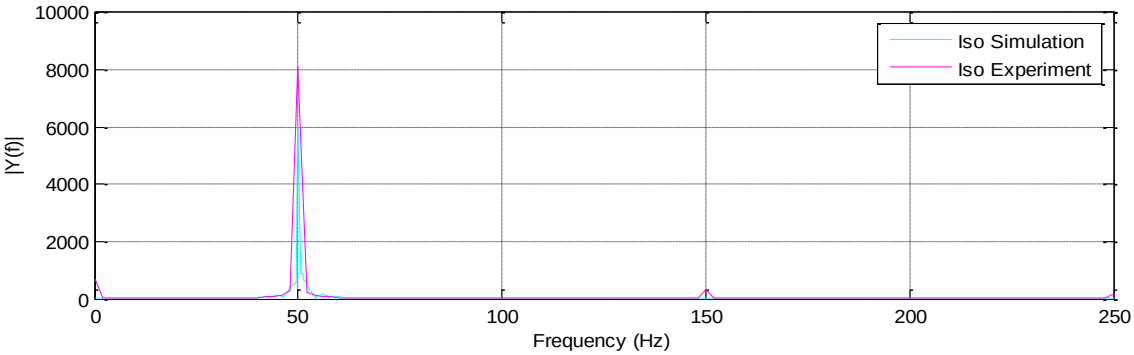

Fig. 5.5.3.8 FFT of the output current

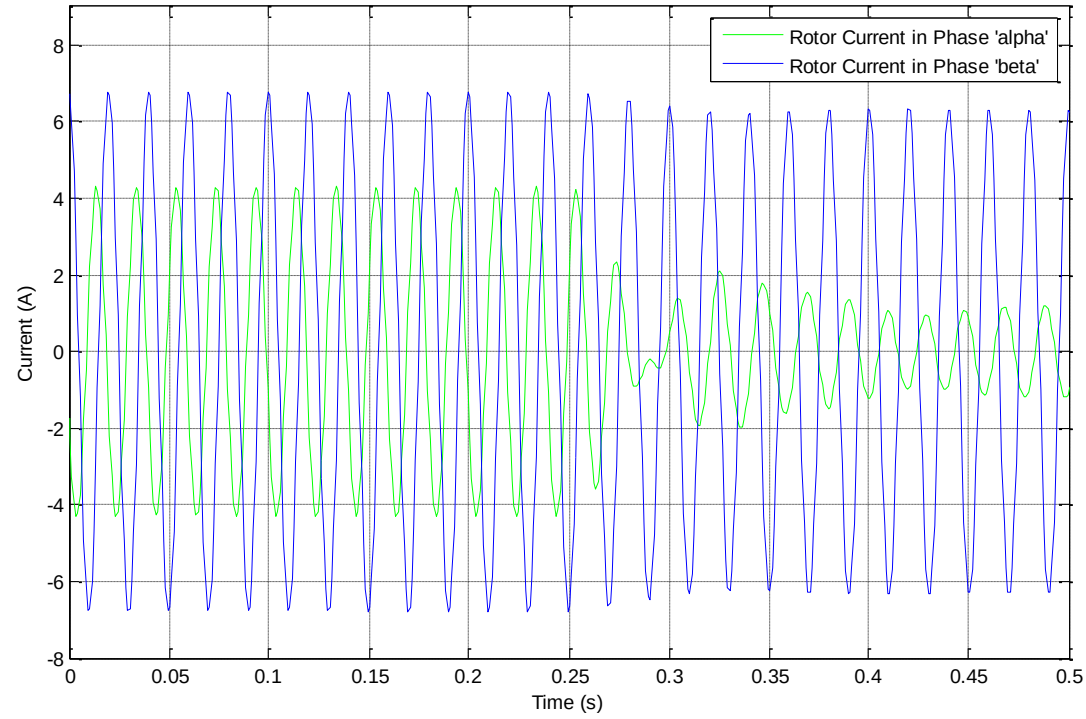

Fig. 5.5.3.9 Transients of rotor currents due to a step change in rotor speed from 1580 rpm to 1556 rpm at t=0.25s

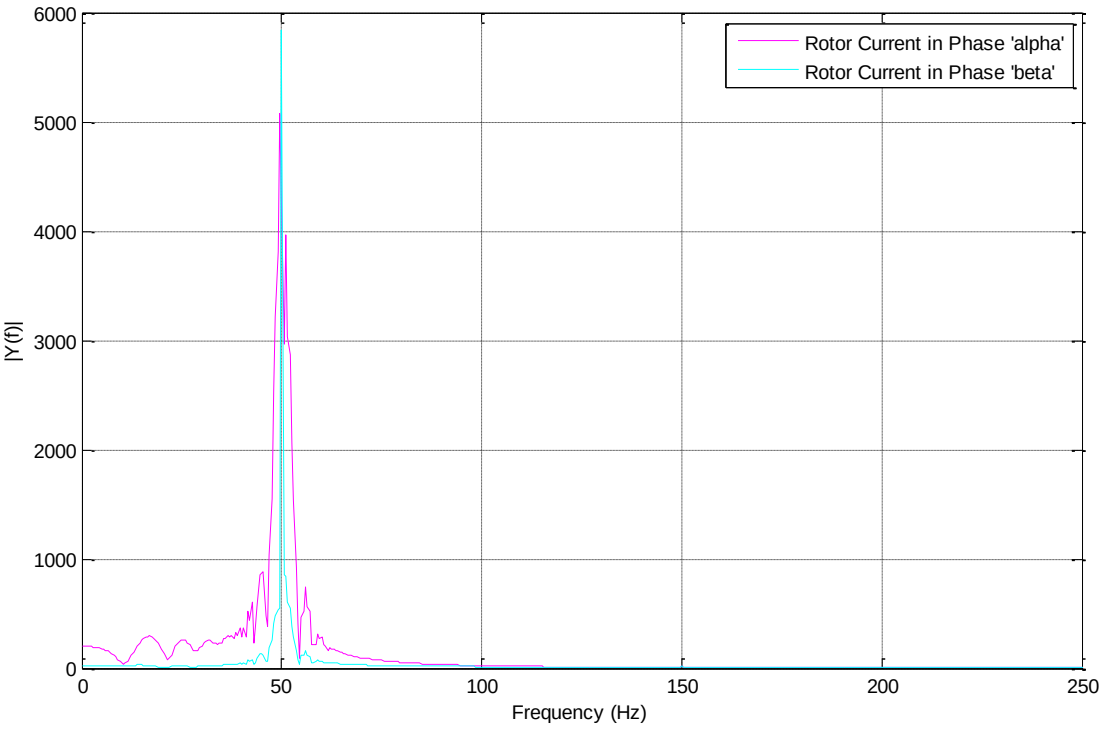

Fig. 5.5.3.10 FFT of the rotor currents

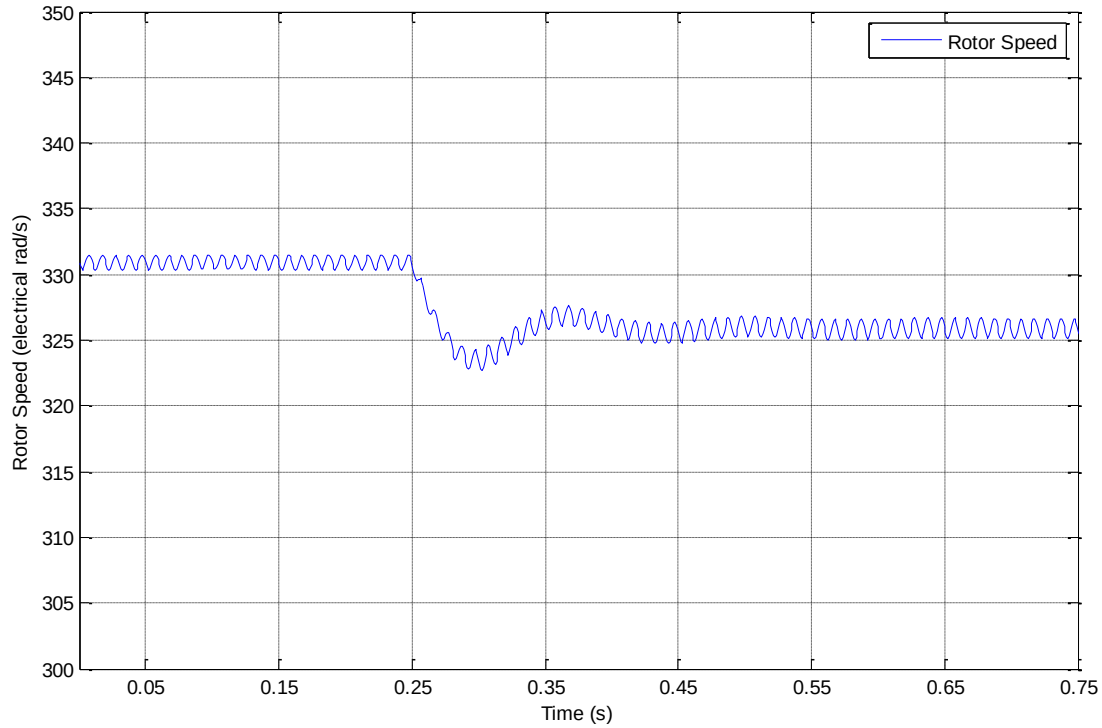

Fig. 5.5.3.11 Characteristics of rotor speed

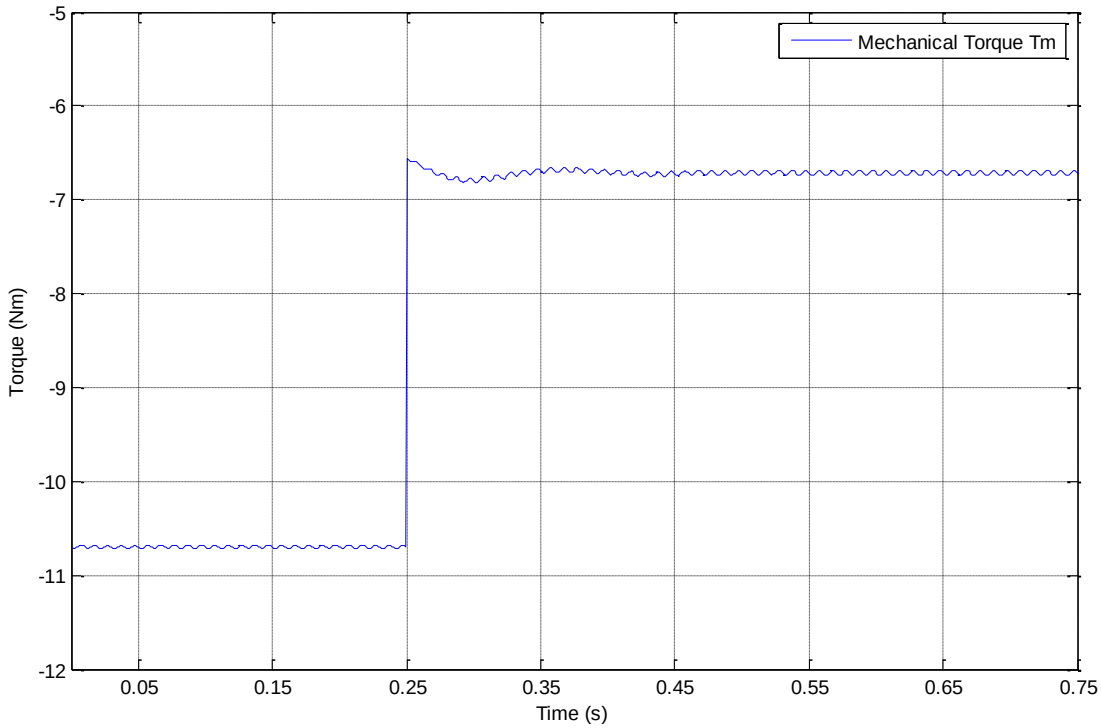

Fig. 5.5.3.12 Characteristics of mechanical torque

5.5.4 The transient due to sudden change in excitation control voltage

In this section, the dynamic behaviour of the unregulated generator system due to the sudden change in excitation control voltage is discussed. At the beginning, the generator is operating in a steady-state condition at rotor speed of 1580 rpm when a load of 52.9 Ω (i.e. full-load current at desired output voltage) is connected in parallel with a 30 μF capacitance. The voltage of 153 V/ 50 Hz is supplied from the excitation control winding to generate 230 V/ 50 Hz at the output winding. When the excitation control voltage is changed from 153 V to 110 V (i.e. 75.0 % of full-load current at desired output voltage) at t=0.2 s, the transient behaviour of the single-phase generator is studied using the results obtained from the experiments and simulations. The operational parameters given in Table 5.5.4.1 are used for both experiments and simulations.

Table 5.5.4.1
Operational parameters used for excitation control winding voltage change

Parameter	Load (Ω)	Fixed Capacitance (μF)	Excitation Control Voltage (V)	Rotor Speed (rpm)
Value	52.9	30	153	1580

The transients of excitation control winding voltage, current, output voltage and output winding current are depicted in Figs. 5.5.4.1 – 5.5.4.4 respectively. With the sudden decrease of the excitation control winding voltage at the 0.2 s, all the variable parameters decrease. The decrease in excitation control winding voltage causes both the excitation control winding current and the output voltage to decrease. Decrease in output voltage decreases the output winding current. Therefore, the active power in both output winding and excitation control winding drop. In order to maintain the active power balance in the system, the mechanical torque of the generator system decreases as the rotor speed remains constant. Similar to the above three analyses, the transient period lasts for only 3-4 cycles. A very good alignment of simulated and experimental results verifies the accuracy of the comprehensive dynamic model. The frequency domain signals of excitation control voltage, output voltage, excitation control wining current and output winding current are shown in Figs. 5.5.4.5 – 5.5.4.6respectively. Each signal has a fundamental frequency component of 50 Hz which is equal to the given frequency of the excitation control winding voltage. In

addition, some harmonics of the fundamental frequency are present in the experimental results.

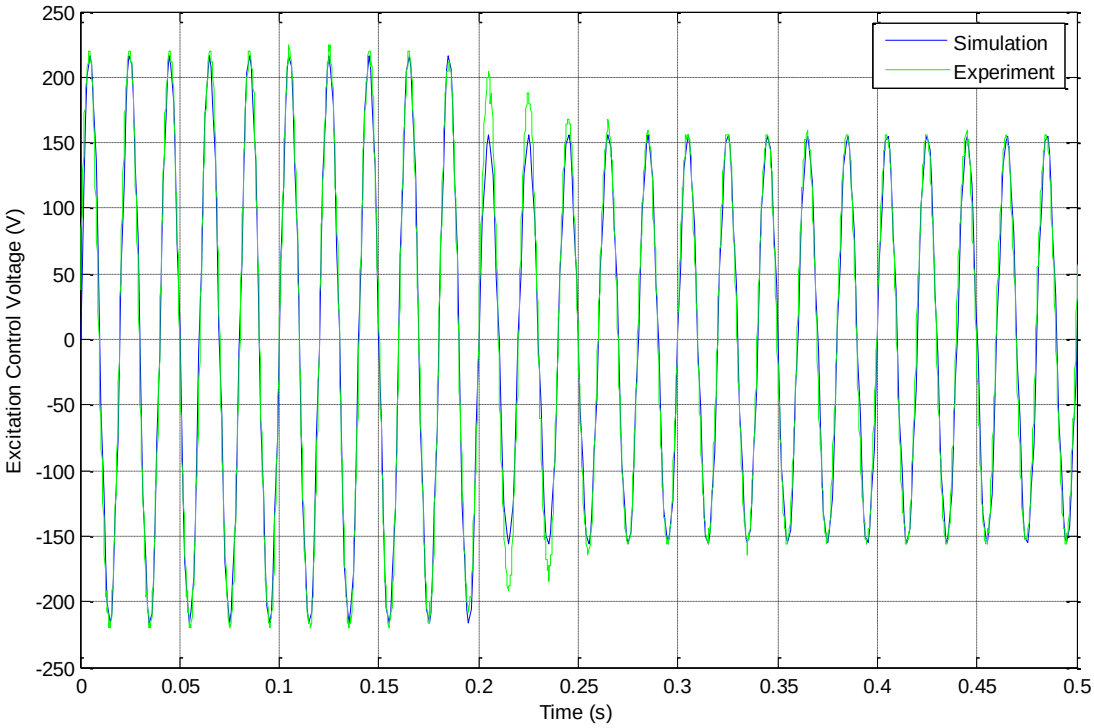

Fig. 5.5.4.1 Excitation control winding voltage

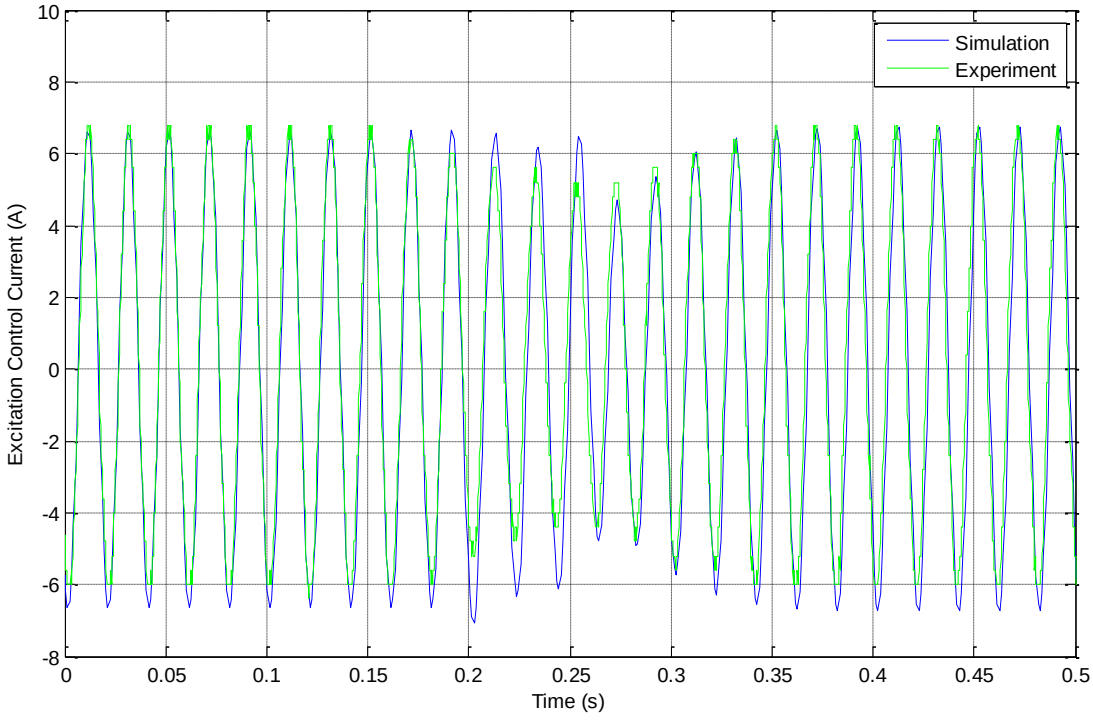

Fig. 5.5.4.2 Transients of excitation control winding current due to a step change in excitation control voltage from 153 V to 110 V at t=0.2s

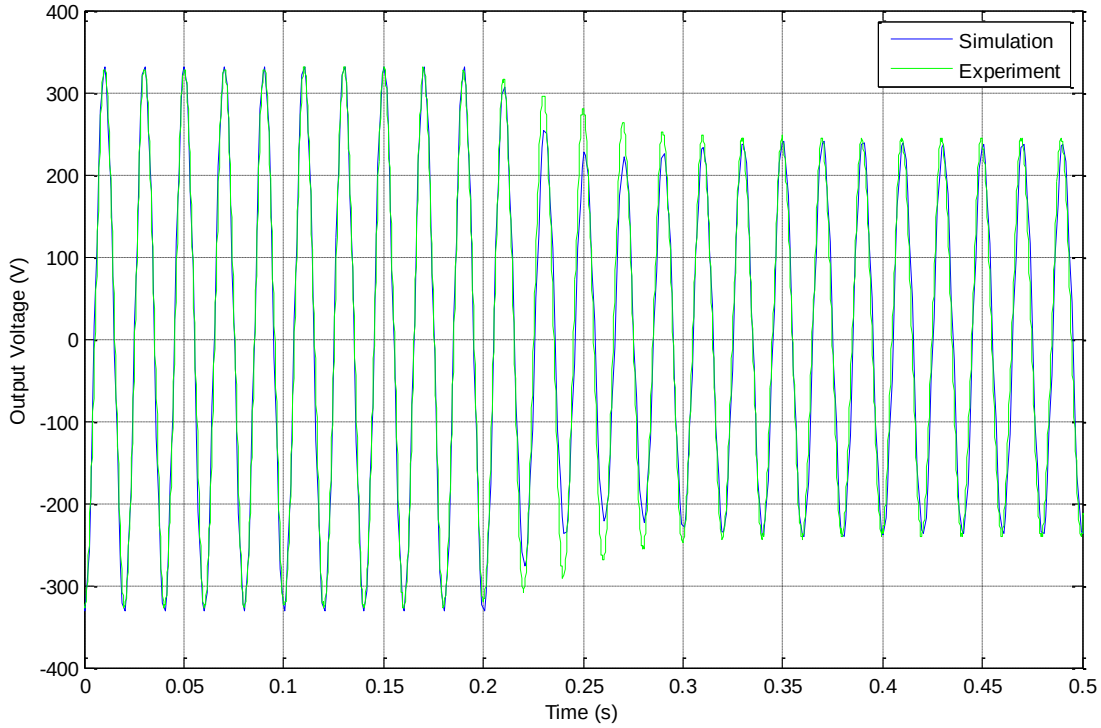

Fig. 5.5.4.3 Transients of output voltage due to a step change in excitation control voltage from 153 V to 110 V at t=0.2s

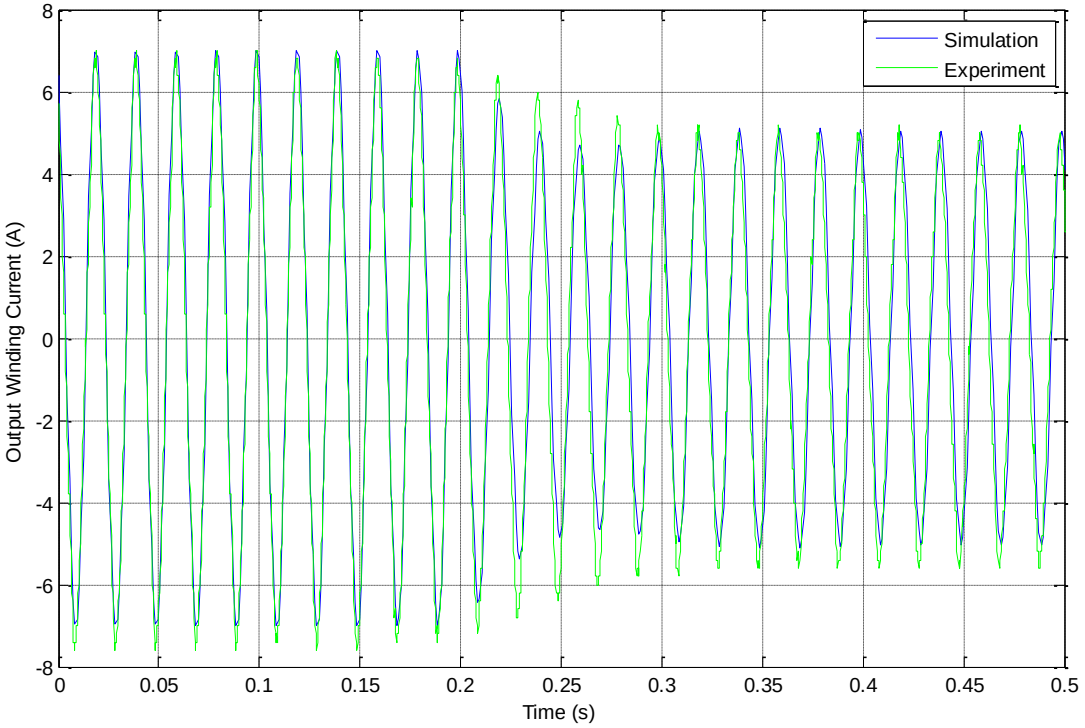

Fig. 5.5.4.4 Transients of output winding current due to a step change in excitation control voltage from 153 V to 110 V at t=0.2s

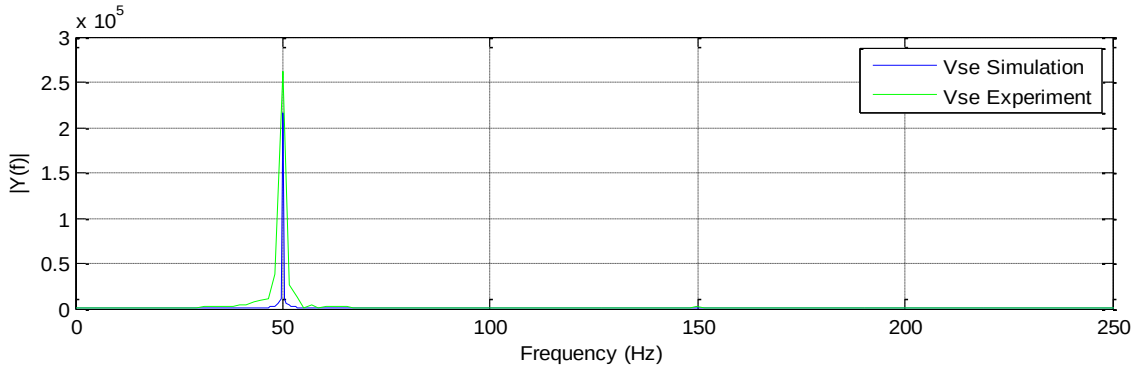

Fig. 5.5.4.5 FFT of the excitation control voltage

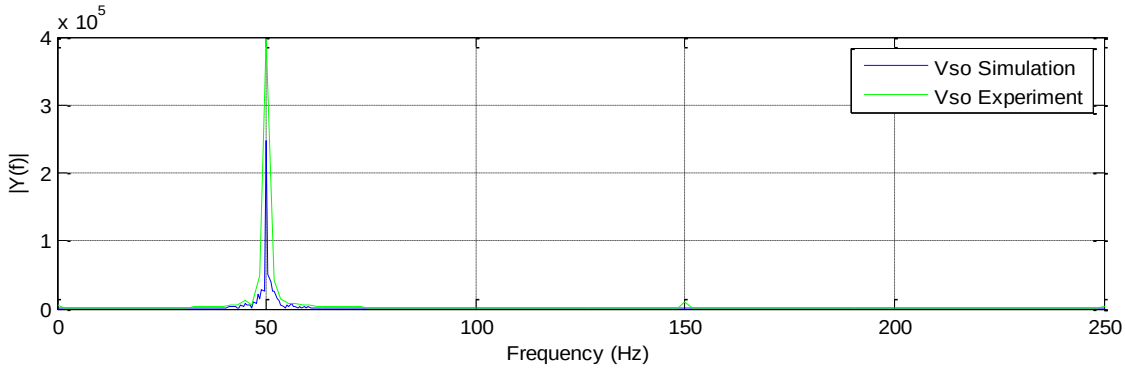

Fig. 5.5.4.6 FFT of the output voltage

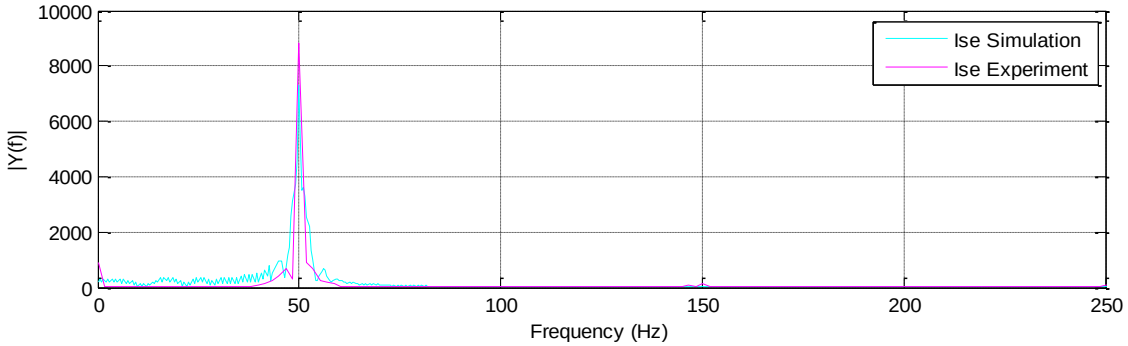

Fig. 5.5.4.7 FFT of the excitation control current

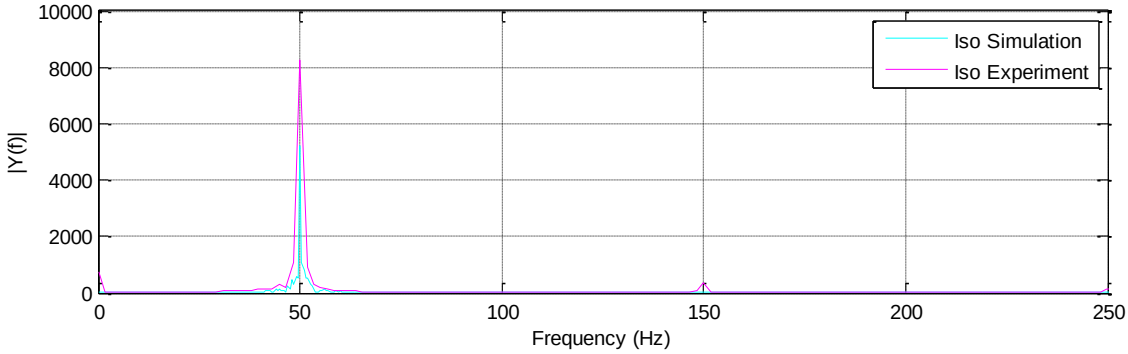

Fig. 5.5.4.8 FFT of the output winding current

The simulation results of the rotor currents in ‘αβ’ reference frame obtained from the comprehensive model are illustrated in Fig. 5.5.4.9. The frequency domain signals of the rotor currents are shown in Fig. 5.5.4.10. Similar to the above three analyses, the fundamental frequencies of the rotor currents are equal to those of the stator currents.

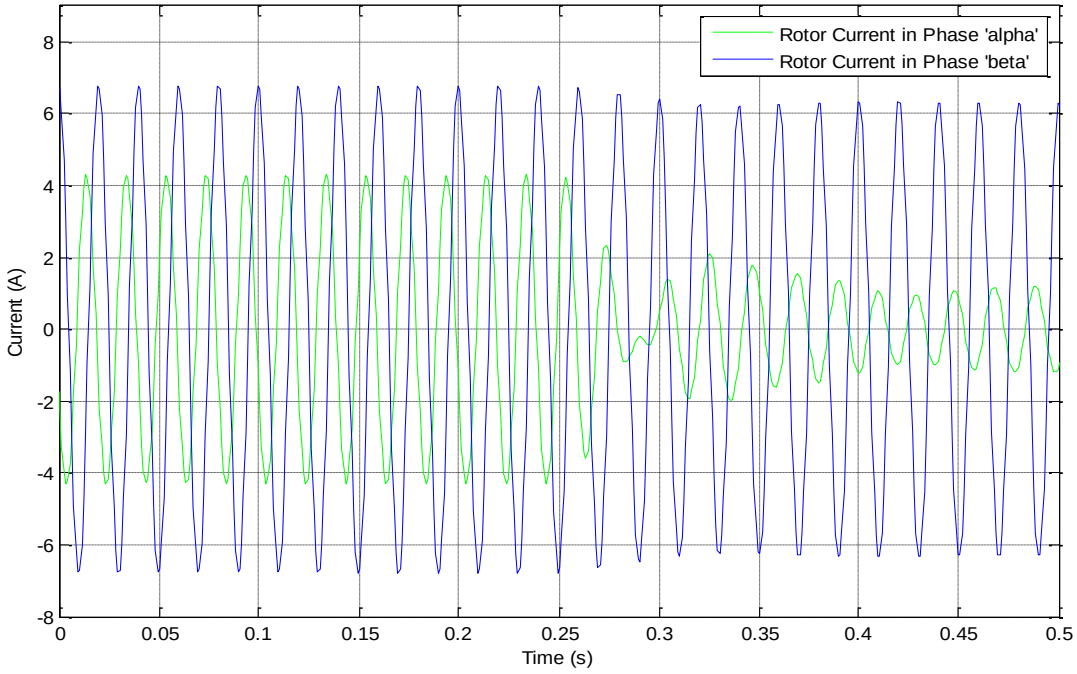

Fig. 5.5.4.9 Transients of rotor currents due to a step change in excitation control voltage from 153 V to 110 V at t=0.2s

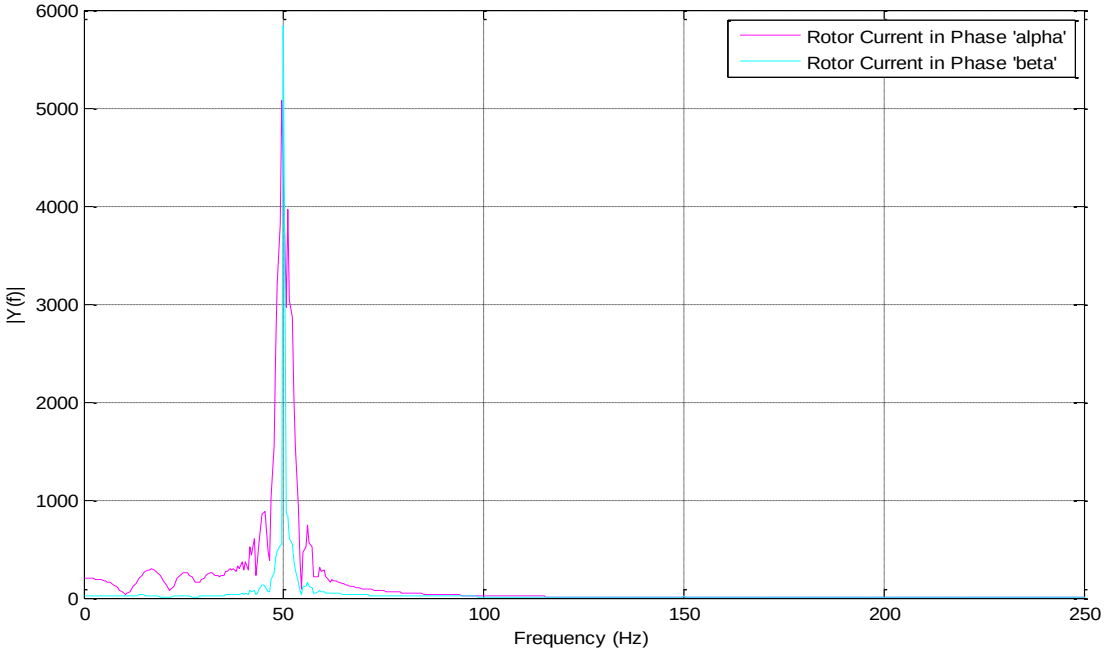

Fig. 5.5.4.10 FFT of the rotor currents

The changes in rotor speed and the mechanical torque due to the sudden change in excitation control winding voltage can be studied using the simulated results obtained from the comprehensive model. These results are illustrated in Figs. 5.5.4.11 and 5.5.4.12 respectively.

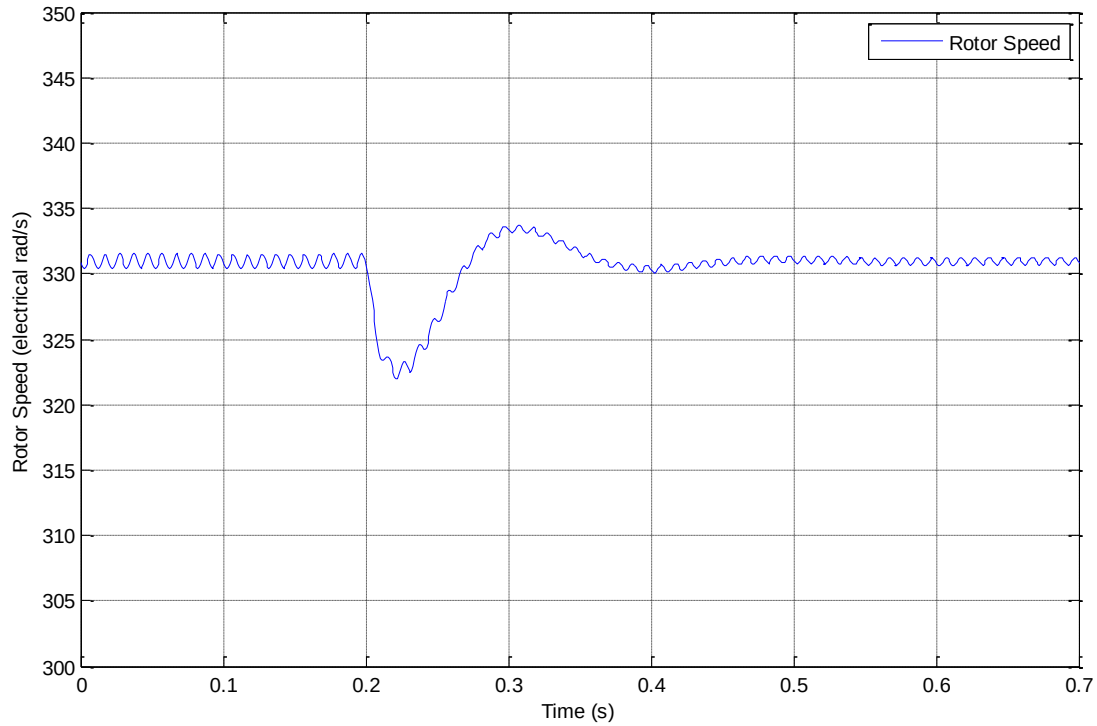

Fig. 5.5.4.11 Characteristics of rotor speed

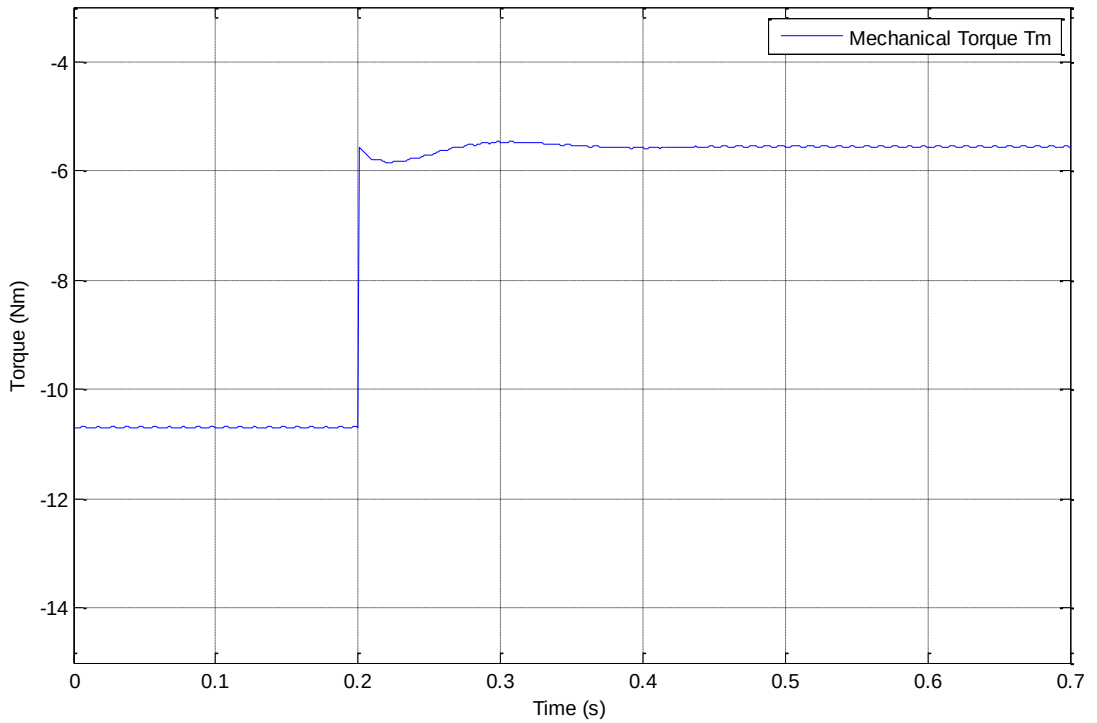

Fig. 5.5.4.12 Characteristics of mechanical torque

The mechanical torque has a significant decrease at 0.2 s. Thus, the input mechanical power has been dropped by a considerable amount. This is a result of the decrease in active power of both output winding and excitation control winding with the decrease of excitation control winding voltage. After a transient period, the rotor speed becomes steady at its initial value.

The numerical comparison of experimental and simulated results of voltages and currents in both excitation control and output windings before and after the transient period are given in Test Case D of Table 5.7.1. A similar comparison of power factors in both windings is given in Table 5.7.2. Experimental and simulated results of active power in both windings are compared in Test Case D of Table 5.7.3.

5.6 The transient due to the short circuit condition

The most severe transient condition is the short circuit of the system. In this section, the dynamic behaviour of the unregulated generator system due to the short circuit condition is discussed.

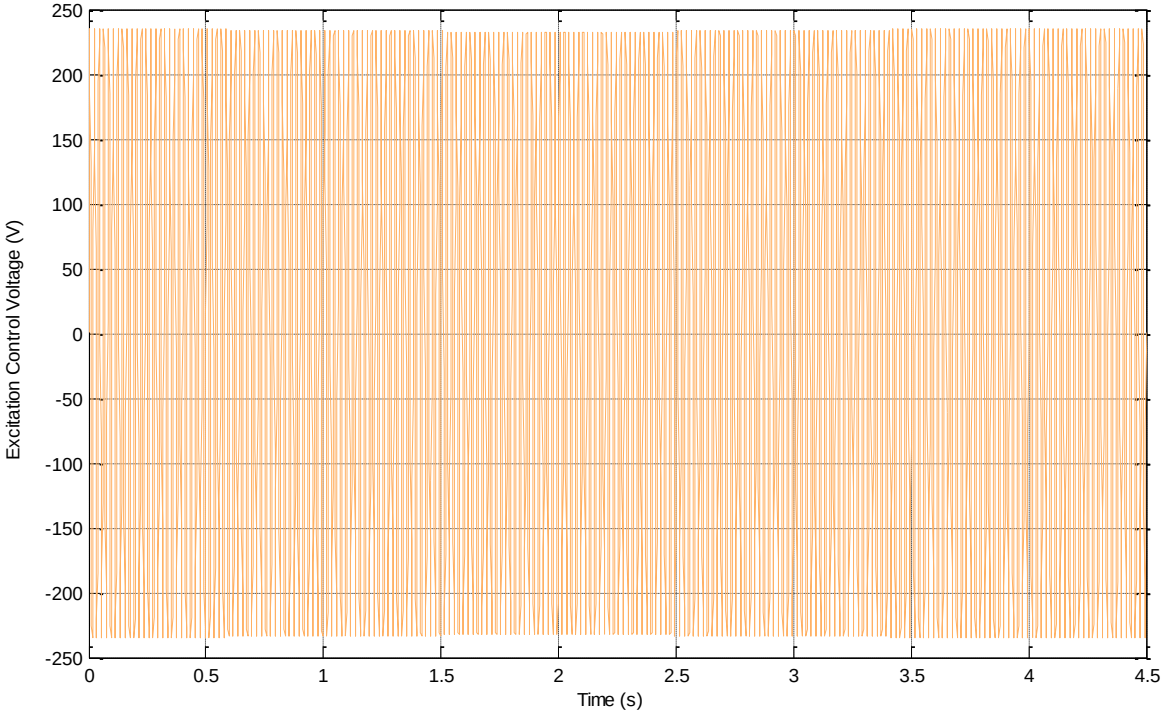

Fig. 5.6.1 Excitation Control Winding Voltage

At the beginning, the generator is operating in a steady-state condition at rotor speed of 1544 rpm when a load of 52.9 Ω (i.e. full-load current at desired output voltage) is connected in parallel with a 30 μF capacitance. In order to generate 230 V/ 50 Hz at the output winding, 166 V/ 50 Hz voltage is supplied from the excitation control

winding. The transient behaviour of the single-phase generator due to the short circuit condition at 0.5 s is illustrated in Fig. 5.6.1 – 5.6.5.

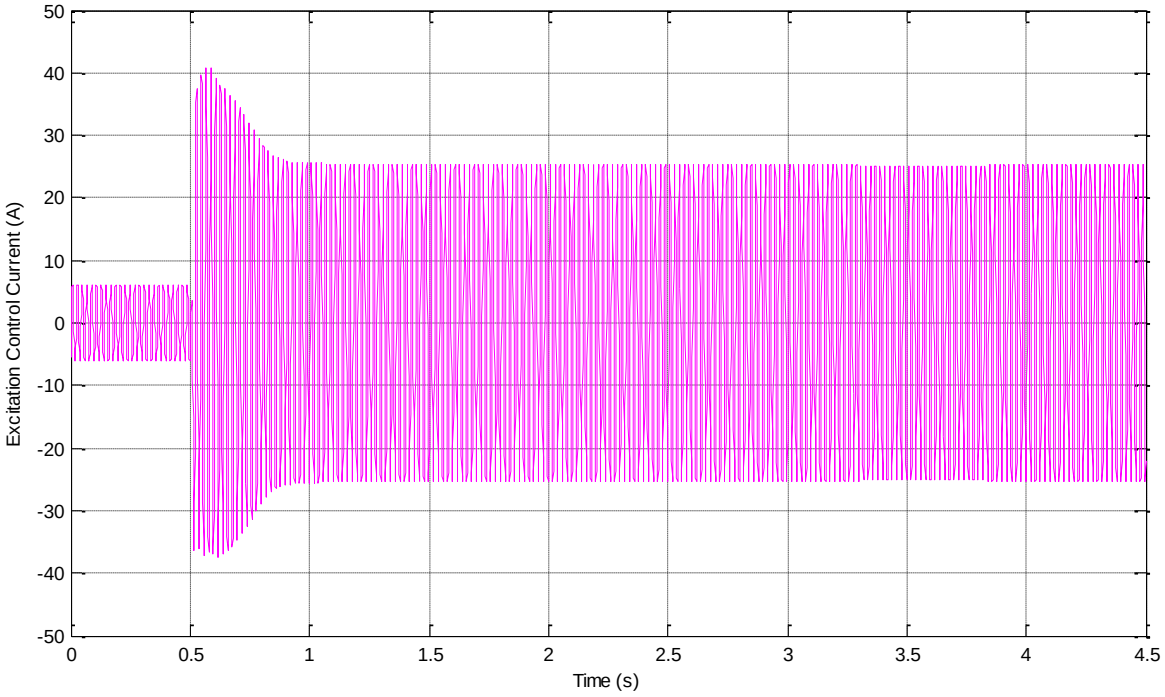

Fig. 5.6.2 Transient of excitation control winding current due to short circuit condition at 0.5 s

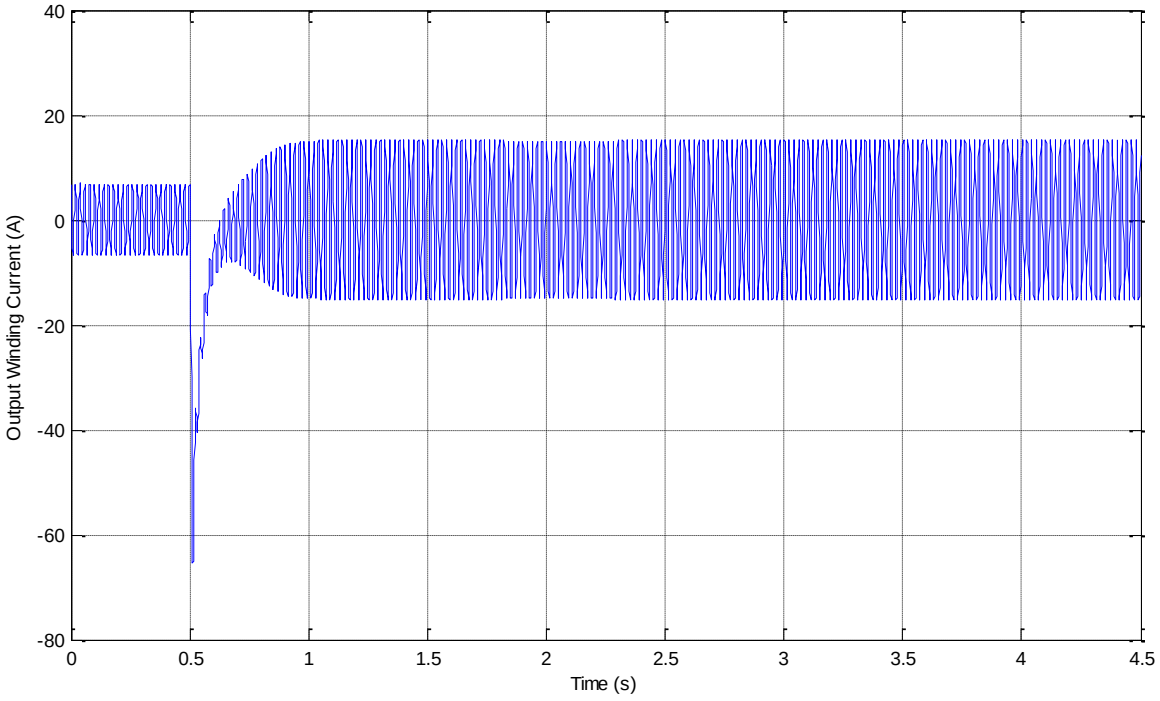

Fig. 5.6.3 Transient of output winding current due to short circuit condition at 0.5 s

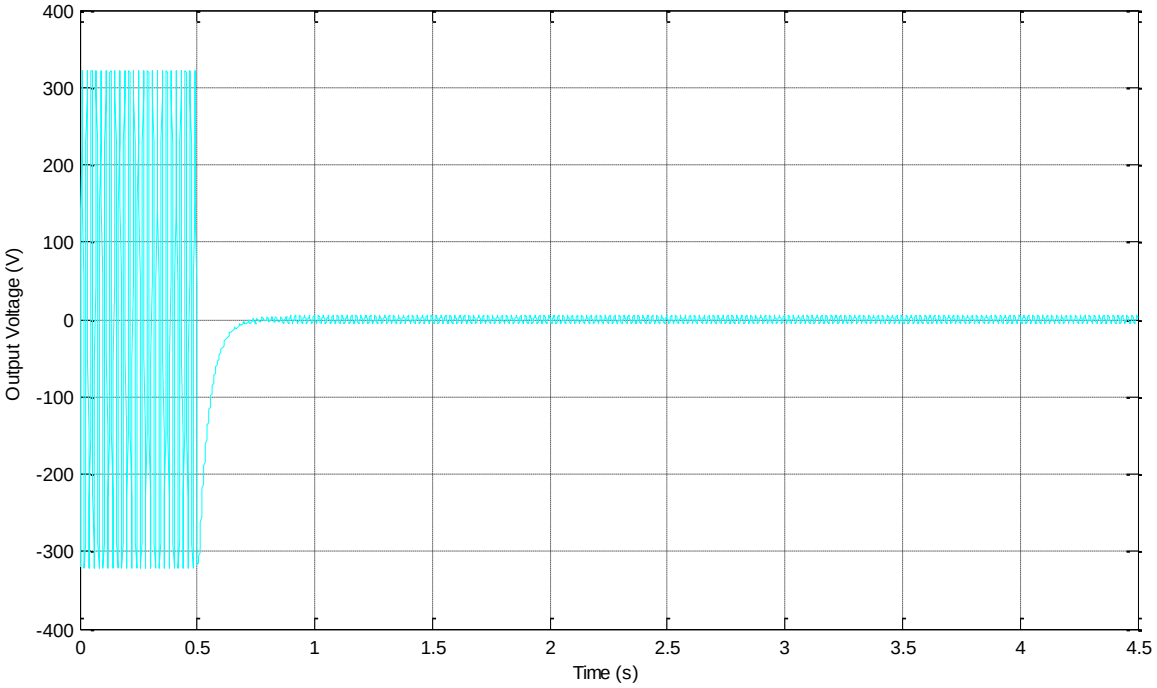

Fig. 5.6.4 Transient of output winding voltage due to short circuit condition at 0.5 s

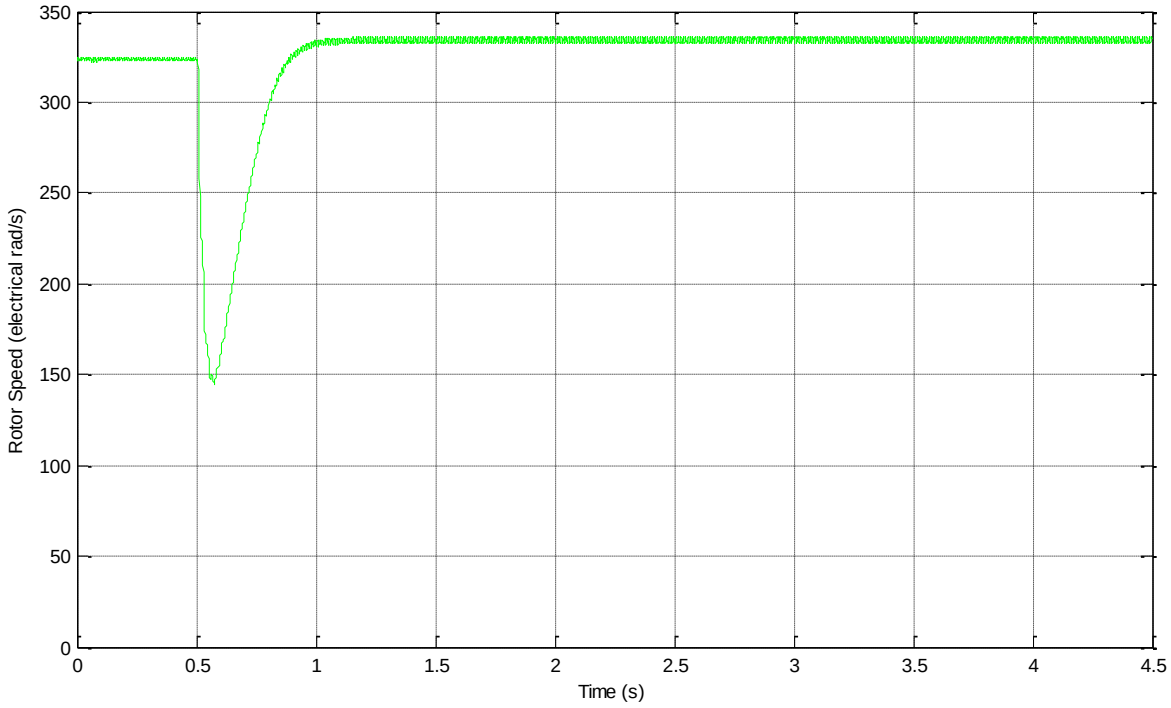

Fig. 5.6.5 Transient of rotor speed due to short circuit condition at 0.5 s

The excitation control voltage shown in Fig. 5.6.1 is constant during the period of testing. Prior to the sudden short circuit at 0.5 s, the excitation control winding

current is steady at 4.3 A. Just after the fault occurs, it increases above 28.7 A. After the transient period of 0.5 s, excitation control winding current becomes steady at 17.8 A as illustrated in Fig. 5.6.2. The behaviour of output winding current due to the short circuit condition is depicted in Fig. 5.6.3. Before the short circuit fault, the steady-state current in the output winding is 4.9 A. At 0.5 s, the current overshoot is noted as 46.3 A. Just after the instantaneous increment, the current gradually decreases and becomes steady at 10.7 A within the same transient period of excitation control winding current. The increase of current in both the windings may damage the circuit as well as the equipment connected at the load side. As shown in Fig. 5.6.4, prior to the short circuit fault, 230 V/ 50 Hz voltage is supplied to the consumer load connected at the output winding. At 0.5 s, the voltage gradually decreases and becomes almost zero after the transient period. Due to the short circuit fault, as the load at the output is reduced significantly, the speed of the prime mover increases. This is illustrated in Fig. 5.6.5. Since in the real world, the short circuit fault of a single-phase generator can be expected, in order to overcome the damage caused by the unpredicted variation of current and rotor speed, a control system should be properly designed for this generator system.

5.7 Chapter Conclusions

A comparison of experimental results and corresponding simulation results obtained from comprehensive dynamic model developed in Chapter 3 are presented in this section. Table 5.7.1 shows the numerical comparison of experimental and theoretical values of the voltage and the current in both excitation control winding and output winding of the generator. A, B, C and D denote the tests performed to study the system performance due to the sudden change in consumer load, fixed capacitance, rotor speed and excitation control winding voltage respectively. Comparison of experimental and theoretical values of power factors in excitation control winding and output winding are presented in Table 5.7.2. Similar comparison in real power in both the windings is given in Table 5.7.3.

From the voltage and current results presented in Table 5.7.1, it can be clearly seen that, with the exception of a few cases, experimental and theoretical results match each other with less than 3% discrepancy. In the worst case the discrepancy between experimental and theoretical values is 8.6% only.

Simulation and experimental results of power factor and active power of both windings presented in Tables 5.7.2 and 5.7.3 respectively match each other very well. Therefore, the comprehensive dynamic model described in Chapter 3 can be used as a tool to build a steady-state model of this generator configuration which is yet to be developed. With a full understanding of the dynamic behaviour of the single-phase generator, the generator system can be utilized in many renewable energy generation schemes with no uncertainties.

Table 5.7.1
Comparison of experimental and theoretical values of current and voltage

Test Case	Impact	Experimental				Simulation				Error Percentage (%)			
		Vse(V)	Ise(A)	Vso(V)	Iso (A)	Vse (V)	Ise (A)	Vso(V)	Iso (A)	Vse	Ise	Vso	Iso
A	Before Transient	132.9	6.5	231.93	3.2	130.0	5.94	233.63	3.37	-2.2	-8.6	0.7	5.2
	After Transient	130.1	4.20	197.99	4.24	130.0	3.98	197.35	4.22	-0.1	-5.2	-0.3	-0.6
B	Before Transient	147.1	3.5	231.93	5.1	145.0	3.35	232.00	5.26	-1.4	-4.4	0.0	3.2
	After Transient	144.2	4.50	220.62	4.67	145.0	4.39	219.84	4.70	0.5	-2.5	-0.4	0.7
C	Before Transient	153.0	4.8	230.1	4.8	153.0	4.67	234.55	4.91	0.0	-2.7	1.9	2.2
	After Transient	152.7	3.50	217.79	4.53	153.0	3.50	218.71	4.62	0.2	-0.1	0.4	2.0
D	Before Transient	153.0	4.8	230.1	4.8	153.0	4.67	234.55	4.92	0.0	-2.6	1.9	2.4
	After Transient	110.0	4.6	167.1	3.5	110.0	4.74	167.44	3.57	0.0	3.0	0.2	2.0

Table 5.7.2
Comparison of experimental and theoretical values of power factor

Test Case	Impact	Experimental		Simulation		Error Percentage	
		Excitation Control Terminal	Output Terminal	Excitation Control Terminal	Output Terminal	Excitation Control Terminal	Output Terminal
A	Before Transient	-0.79	-0.75	-0.83	-0.75	4.7	0.7
	After Transient	-0.48	-0.89	-0.51	-0.90	5.7	1.6
B	Before Transient	-0.57	-0.83	-0.59	-0.84	3.1	1.6
	After Transient	-0.45	-0.88	-0.48	-0.90	6.1	3.3
C	Before Transient	-0.49	-0.89	-0.51	-0.90	4.5	1.6
	After Transient	0.19	-0.88	0.19	-0.90	0.0	3.3
D	Before Transient	-0.49	-0.89	-0.48	-0.90	-1.1	1.6
	After Transient	-0.67	-0.89	-0.68	-0.90	2.2	1.3

Table 5.7.3
Comparison of experimental and theoretical values of active power

Test Case	Impact	Experimental		Simulation		Error Percentage	
		Excitation Control Terminal	Output Terminal	Excitation Control Terminal	Output Terminal	Excitation Control Terminal	Output Terminal
A	Before Transient	-682.6	-552.9	-638.7	-589.9	-6.4	6.7
	After Transient	-263.3	-748.4	-263.4	-753.2	0.0	0.6
B	Before Transient	-293.4	-982.9	-285.2	-1030.8	-2.8	4.9
	After Transient	-294.7	-902.2	-306.5	-934.7	4.0	3.6
C	Before Transient	-357.7	-984.1	-363.9	-1041.5	1.7	5.8
	After Transient	100.2	-863.7	100.2	-913.5	0.1	5.8
D	Before Transient	-357.7	-984.1	-344.5	-1043.6	-3.7	6.0
	After Transient	-339.0	-522.3	-356.8	-540.9	5.2	3.6

CHAPTER 6- MODEL VERIFICATION AND SYSTEM PERFORMANCE IN STEADY-STATE

6.1 Introduction

This chapter presents the verification of the steady-state model of the single-phase induction generator developed in Chapter 3 and the analysis of the system performance in the steady-state. Since the steady-state model of this novel configuration has not been reported in the literature, the steady-state behaviour of the generator system has yet to be analysed. However, in order to design a regulated ECS, it is necessary to know the unregulated system performance in the steady-state.

In the first section of this chapter, the theoretical values of the operating parameters required to achieve the current and voltage balance in the generator are obtained using the computational techniques described in Chapter 4. The desired values of output voltage and frequency are considered as the rated values of the machine. Since the rated values of the voltage, the current and the frequency are 230 V, 6.4 A and 50 Hz respectively, in order to achieve both voltage and current balance in single-phase induction machine, the voltage and the current in excitation control winding are expected to be $230/\sqrt{3}$ V and 6.4 A respectively. The theoretical values obtained for the operating parameters in order to fulfil these conditions are verified using the experiments carried out on the laboratory experimental set-up described in Chapter 5. Thus, the operational range of these parameters is defined to achieve a minimum unbalance of the system.

In the next section of this chapter, the system variables for a given set of operating parameters are calculated. Considering the output voltage and the frequency are as the desired rated values, the system variables are calculated for a given rotor speed using the computational methods developed in section 4.2. For a load dependant rotor speed, the computational procedure described in section 4.3 is used to calculate

the system variables. In order to study the effects of changing one of the operating parameters on system variables, the calculations are repeated for the different values of the same operating parameter while other operating parameters remain unchanged. The simulation results obtained using Matlab Software are compared with the corresponding experimental results as shown in the figures in the latter sections of this chapter.

The load impedance, the fixed capacitance and the rotor speed are considered as the main operating parameters of the system. The effects of changing one of these parameters are studied separately and presented in this chapter. In order to simplify the experimental set-up, a unity power factor load is employed in this analysis, although in a practical system, the consumer load may be a series connected RL load.

6.2 Calculation of the Operating Parameters

The operating parameters required to achieve the voltage and current balance in the generator are calculated using the computational procedure described in section 4.4. Considering a unity power factor load at the output, the minimum capacitance required to keep the excitation control winding current below the rated values is calculated as 45.0 μF. The rotor speed, the power factor at the excitation control winding and the load impedance needed to obtain the minimum capacitance required for the phase balancing are given in Table 6.2.1. In order to verify the accuracy of values of the obtained parameters, the theoretical results are compared with the experimental values needed to achieve the same outcomes. This comparison is shown in Table 6.2.1.

Table 6.2.1
The comparison of the theoretical and experimental values of operating parameters required to achieve the phase balancing of the generator

Parameter	Theoretical values	Experimental values
Fixed capacitance (μF)	45.0	47.0
Load impedance (Ω)	50.4	57.1
Rotor Speed (rpm)	1611.82	1610
Excitation Control Power factor	-0.8305	-0.814

Thus, the operational range of the fixed capacitance is selected as ±60% of the calculated value. The load impedance is selected in between the full-load impedance and the no-load impedance. The operational range of the rotor speed is set between the synchronous speed and the full-load speed. The values of the operational range of each operating parameter are given in Table 6.2.2.

Table 6.2.2
The operational range of operating parameters

Parameter	Minimum Values	Maximum Values
Fixed capacitance (μF)	18	72
Load impedance (Ω)	28.7	No-load impedance
Rotor Speed (rpm)	1500	1622.4
Excitation Control Voltage (V)	0.8*230/√3=106.2	230

6.3 Changing the Consumer Load

The effect of changing the consumer load on the system variables was studied for following two different cases.

1. Changing the unity power factor load
2. Changing the lagging power factor load

The simulation results obtained to study the effect of changing the unity power factor load on the system variables were verified using the experimental results. However, due to the limited resources, the effect of changing lagging power factor load on the system variables were studied using the simulation results obtained using Matlab.

6.3.1 Changing the Unity Power Factor Load

In order to obtain the results presented in this section, the normal operating point is selected such that the output voltage and the frequency are equal to 230 V and 50 Hz respectively. At this point, the output winding current is considered as 56.6 % of full-load current at desired output voltage. The operating parameters required to produce this condition are measured experimentally and presented in Table 6.3.1.1.

Using the same operating parameters, the theoretical values of the system variables due to the effects of changing the unity power factor load while all other operating parameters remain constant, are calculated by solving the equations described in

section 4.2. In order to maintain the output voltage and the frequency remain at the normal operating conditions, the effects of changing the load on other system variables are demonstrated using Fig. 6.3.1.1-6.3.1.6. When the fixed capacitance is unchanged, the same test is repeated for another three different values of the rotor speeds. The horizontal axis shows the load conductance. Thus, the loading of the generator increases from left to right along the horizontal axis.

Table 6.3.1.1
Operating parameters required to obtain the normal operating point

Parameter	Values
Fixed capacitance (μF)	30
Load impedance (Ω)	93.4
Rotor speed (rpm)	1510

Figure 6.3.1.1 shows the variations of the voltage in excitation control winding when the load is changed within the defined operational range. In the legend of this figure, 'S' and 'E' denote the simulated and experimental results respectively. 'Sp' denotes the mechanical speed of rotor which is same as ω_m.With the increasing load conductance, the voltage in excitation control winding increases linearly to maintain desired voltage at the output.

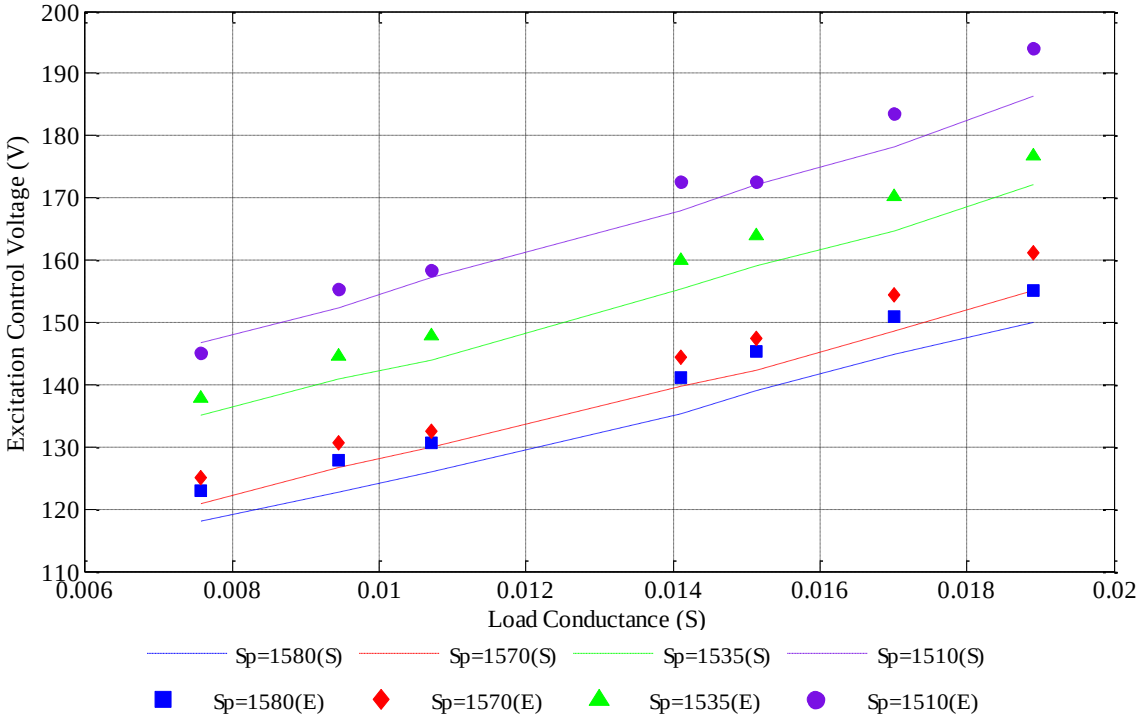

Fig. 6.3.1.1. Variation of excitation control voltage with changing load conductance

For a change of load conductance by 60 % from the given value, the voltage in excitation control winding changes by 13.6 %. This variation is independent of the value of the rotor speed. The simulation results and experimental results match each other, thereby confirming the accuracy of the developed steady-state model of the generator.

The variation of the current in excitation control winding for the same change of load conductance for the four different values of rotor speed is illustrated in Fig. 6.3.1.2. For the higher values of the rotor speed, the excitation control winding current decreases with the increasing load conductance. However, for lower values of rotor speed, this current increases with the increasing load conductance. For the highest value of the rotor speed considered, the excitation control current decreases by 18.3 % when the load conductance is increased by 60 %. For the same change in the load conductance, the excitation control winding current increases by 65.6 % at the lowest value of rotor speed. This is because at the lower speed of the prime mover, the excitation control winding supplies the real power to the load and at the higher speed of the prime mover, excitation control winding absorbs the additional generating power of the generator.

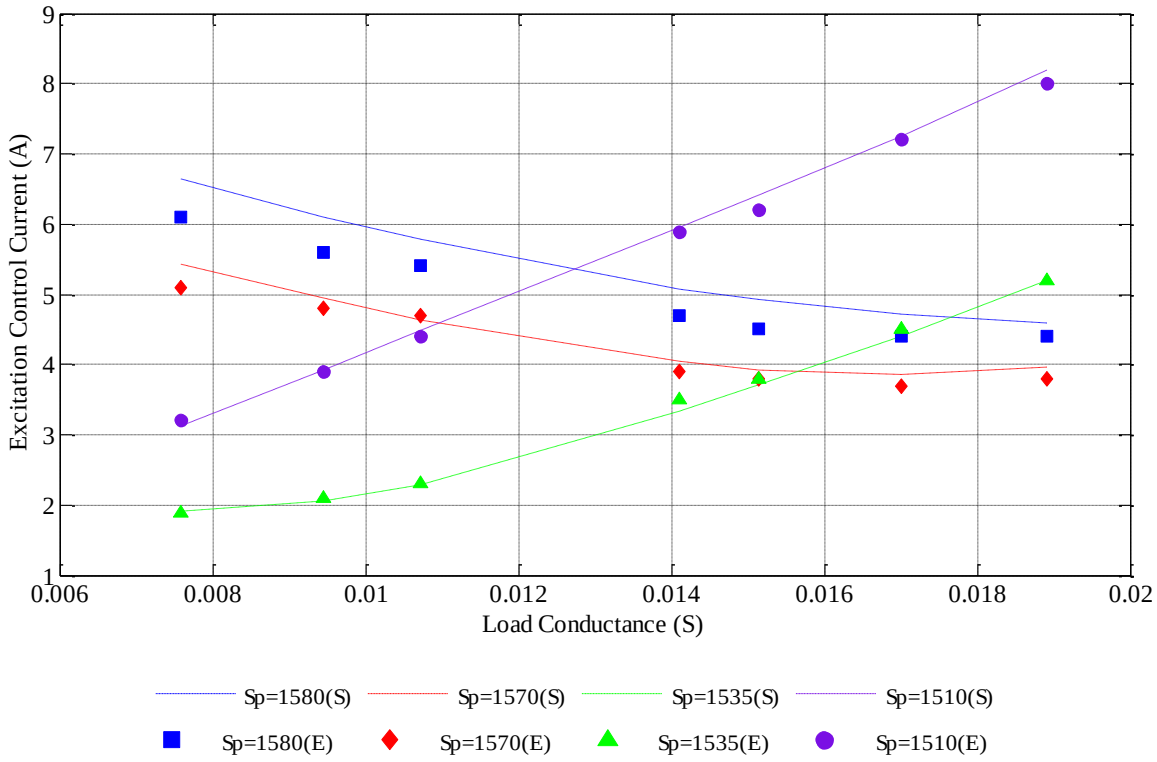

Fig. 6.3.1.2. Variation of excitation control current with changing load conductance

The simulation results denoted by 'S' follow the same pattern as those of the experimental results denoted by 'E'. The values of simulated and experimental results match with a very good degree of accuracy. These results verify the steady-state modelling and the computational procedure.

The variation of real power in excitation control winding is illustrated in Fig. 6.3.1.3.

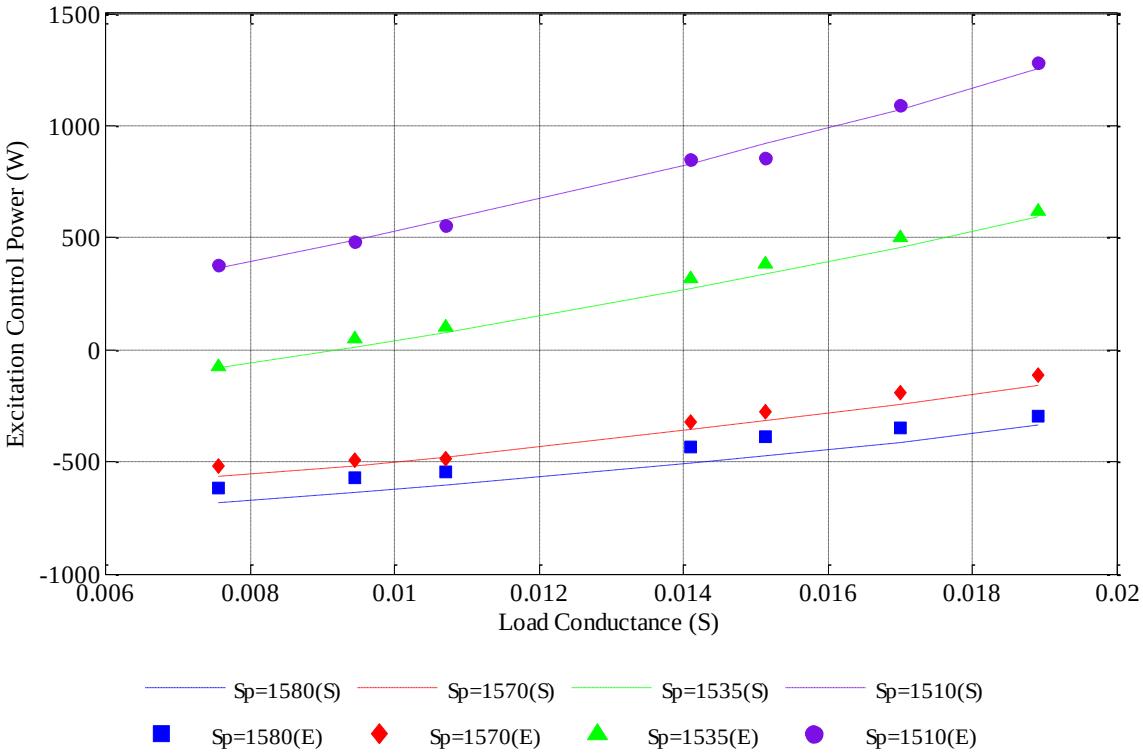

Fig. 6.3.1.3. Variation of real power in excitation control winding with changing load conductance

For the lower values of rotor speed, the real power in excitation control winding increases with the increasing load conductance. For the lower rotor speed, the real power in excitation control winding increases by 100 % when the load conductance is increased by 60 %. However, for the higher values of the rotor speeds, the real power in excitation control winding goes in the opposite direction and decreases with the increasing load conductance as shown in Fig. 6.3.1.3. As discussed in Fig. 6.3.1.2, at the lower rotor speeds, the excitation control winding supplies the deficit real power requirement at the output. Thus, when the load is increased, the real power required from the excitation control winding increases. This may cause an increase in both the current and the voltage in the excitation control winding.

However, at the higher rotor speeds, the excitation control winding absorbs the additional power generated by the generator. Therefore, the real power in excitation control winding is obtained as a negative value. When the load is increased, the output winding requires more real power in order to maintain a constant output voltage and frequency. Thus, the real power supplied to the excitation control winding decreases, resulting in a decrease in the current in the same winding. At the highest rotor speed, the real power in excitation control winding decreases by 32 % when the load conductance is increased by 60 %. Simulation and experimental results denoted by 'S' and 'E' respectively strongly match each other, thereby verifying the accuracy of the developed model.

In order to ensure that the voltage remains unchanged at the output, the variation of current in the same winding with the changing of load is illustrated in Fig. 6.3.1.4. It is noticed that for all the rotor speeds, the current in the output winding increases almost linearly with the increasing load conductance.

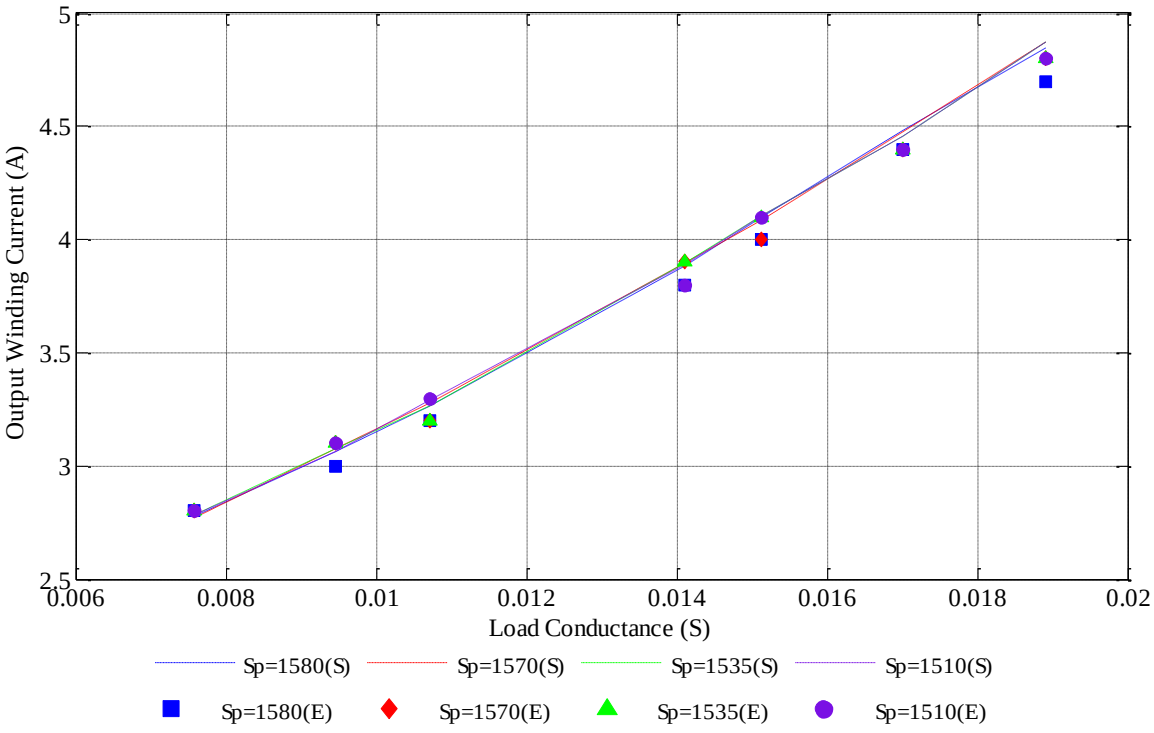

Fig. 6.3.1.4. Variation of output winding current with changing load conductance

Regardless of the value of the rotor speed, the output winding current increases by 32.8 % when the load conductance is increased by 60 %. The real power

consumption of a unity power factor load can be given as $\frac{V^2}{R}$. Since $\frac{1}{R}$ is increasing from left to right along the horizontal axis, the real power consumption increases with the increasing load conductance as the voltage at the output remains unchanged. Therefore, the winding current increases to achieve this power level. However, this current is independent of the speed of the prime mover. The obtained simulated results are shown by the broken lines denoted by 'S' and corresponding experimental results are shown by the markers denoted by 'E'. The greater degree of agreement between these two results confirms the accuracy of the steady-state model.

Due to the limited resources in the laboratory, the mechanical torque could not be measured experimentally. However, the input mechanical power and the mechanical torque were obtained using the Matlab simulations. The variation of input mechanical power with the changing load conductance is illustrated in Fig. 6.3.1.5.

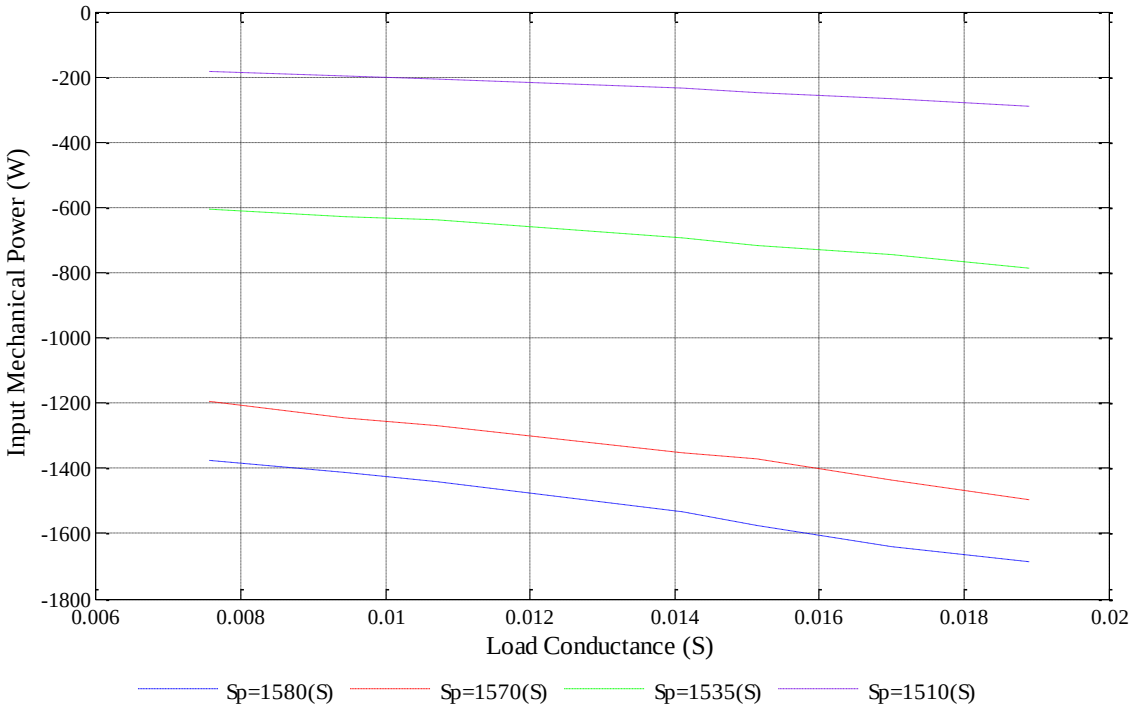

Fig. 6.3.1.5. Variation of input mechanical power with changing load conductance

Input mechanical power increases almost linearly with the increasing load conductance. The input mechanical power increases by 11.1 % and 30 % for the highest and the lowest rotor speeds respectively when the load conductance is increased by 60 %. Since the power consumption at the output winding increases

when the load is increased, the mechanical power increases to supply the real power requirement at the output. However, this is not possible for all the rotor speeds. Thus, the deficit of real power is supplied from the ESS connected at the terminals of the excitation control winding. On the other hand, when the input mechanical power is higher than what is required at the output, the additional power is stored in the ESS. At the lowest rotor speed considered in this analysis, the renewable energy source supplies the lowest power, and at the highest rotor speed, it supplies the highest real power to the generator. Thus, at the lower speeds of the prime mover, the real power is supplied from the excitation control winding and at the higher speeds of the prime mover, the real power is absorbed by the excitation control winding as shown in Fig. 6.3.1.3.

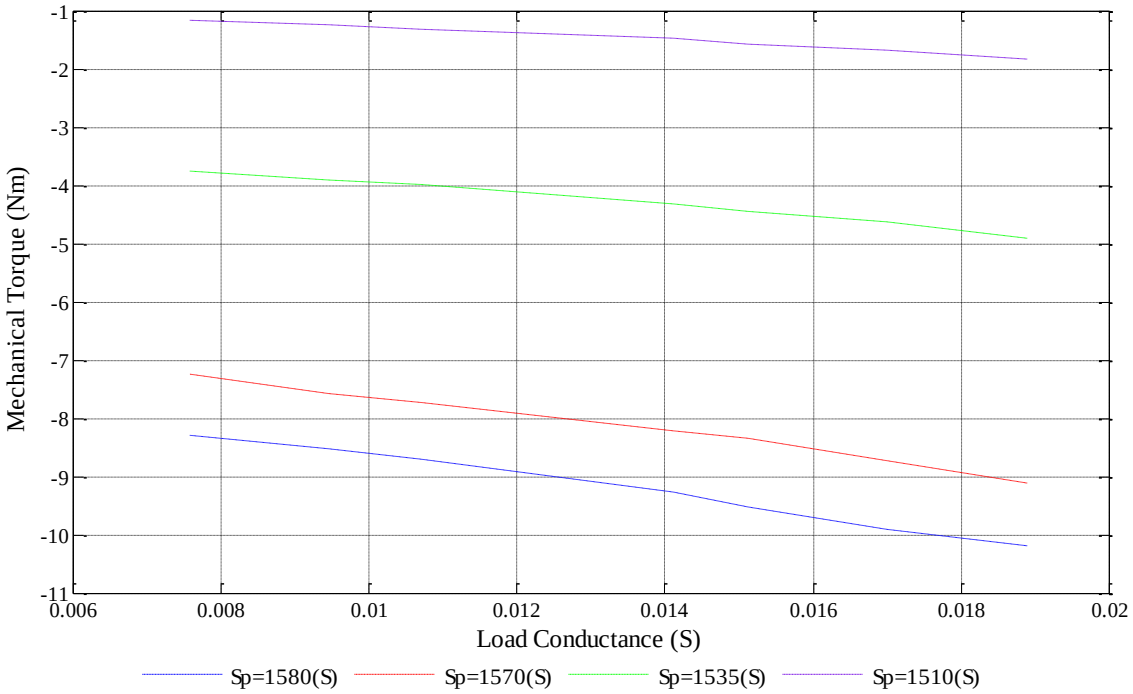

Fig. 6.3.1.6. Variation of mechanical torque with changing load conductance

The change in mechanical torque with the changing load conductance is illustrated in Fig. 6.3.1.6. Similar to the variation of input mechanical power, the mechanical torque also increases with the increasing load conductance.

6.3.2 Changing the Lagging Power Factor Load

In this section, the system behaviour due to changing the general resistive and inductive load is studied using the simulation results obtained using Matlab. The

normal operating point is selected to generate 230 V/ 50 Hz at the output winding of the single-phase generator. Similar to Section 6.3.1, at the normal operating point, the output winding current is considered as 56.6 % of full-load current at desired output voltage. Considering the reactance to the resistance ratio changes proportionately and maintains at 0.75 for all the test cases, the operating parameters required to produce this condition are calculated using (4.4.80)-(4.4.82) and presented in Table 6.3.2.1.

Table 6.3.2.1
Operating parameters required to obtain the normal operating point

Parameter	Values
Fixed capacitance (μF)	55.6
Load resistance (Ω)	59.8
Load inductance (H)	0.1427
Rotor speed (rpm)	1510

In order to obtain the output voltage and the frequency as at the normal operating conditions, the same test is repeated for different lagging power factor load at the same rotor speed. For better understanding of effect of changing load on system variables, the test is continued for another three different values of the rotor speeds with the fixed capacitance remains at the original value. Obtained simulation results are depicted using Fig. 6.3.2.1-6.3.2.6. The horizontal axis shows the load admittance. Thus, similar to the previous section, the loading of the generator increases from left to right along the horizontal axis. It is noted that, all the variables behave almost in the same manner as with the changing unity power factor load.

However, the change of each system variable as a percentage of its original value varies than that with the resistive load. The excitation control winding voltage and current increase by 20% and 80% respectively for increase of the load admittance by 20%. At the higher rotor speeds, the excitation control winding current begins to increase at lower load admittance than with the unity power factor load. The excitation control winding power and input mechanical power increase by 100% and 50% for the change of load admittance by 66.6% and 83.3% respectively. Same as

previous analysis, the output winding current is independent from the speed of the prime mover.

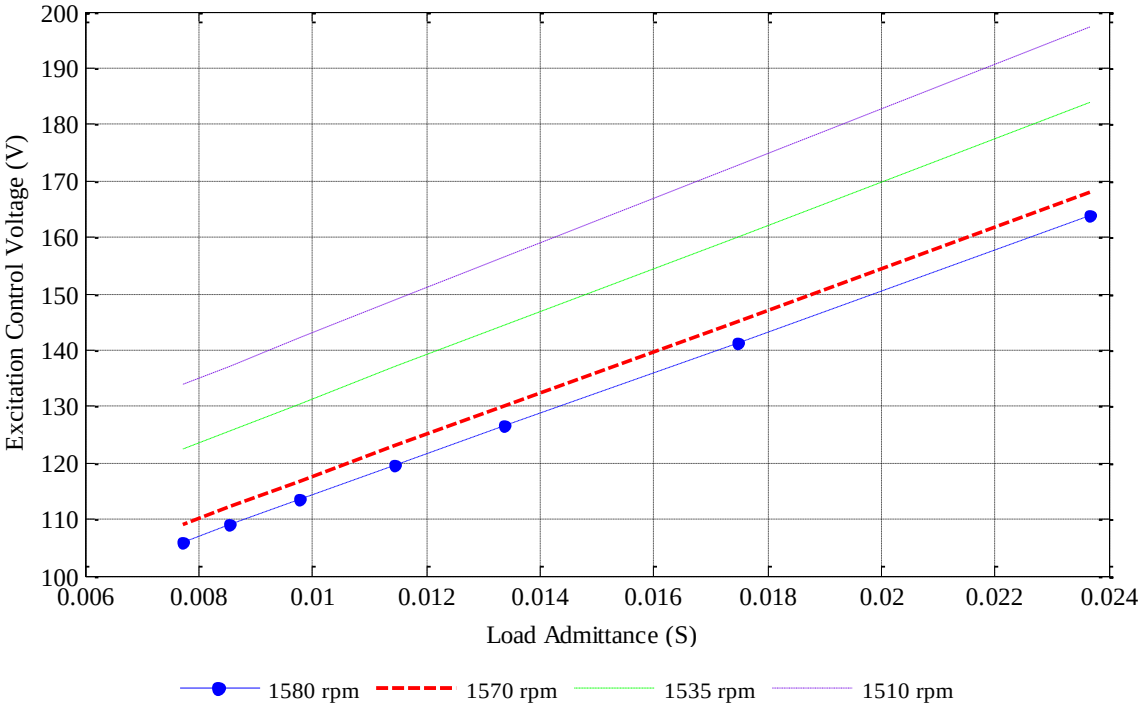

Fig. 6.3.2.1. Variation of excitation control voltage with changing load admittance

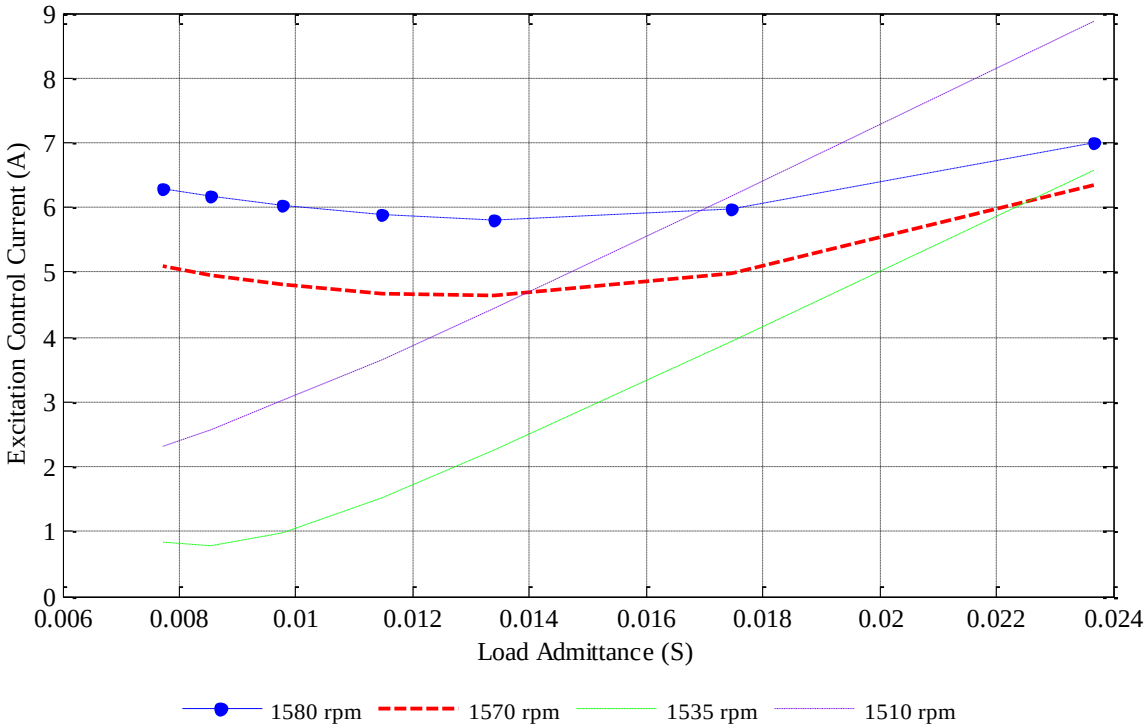

Fig. 6.3.2.2. Variation of excitation control current with changing load admittance

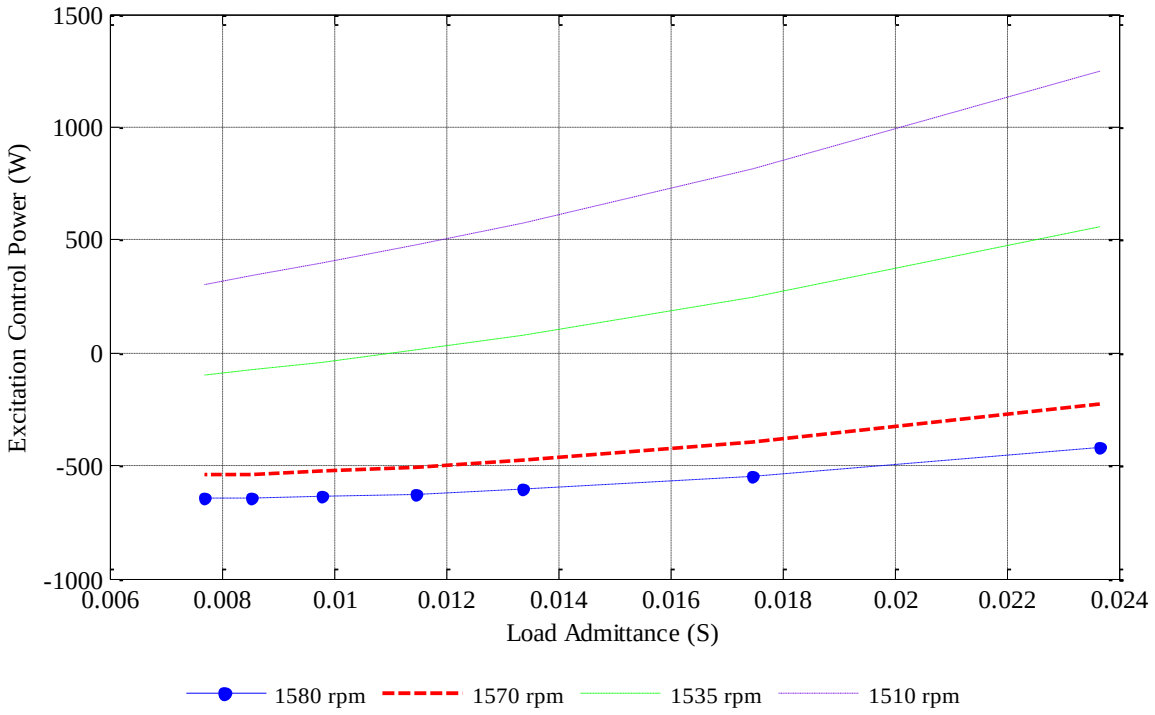

Fig. 6.3.2.3. Variation of excitation control power with changing load admittance

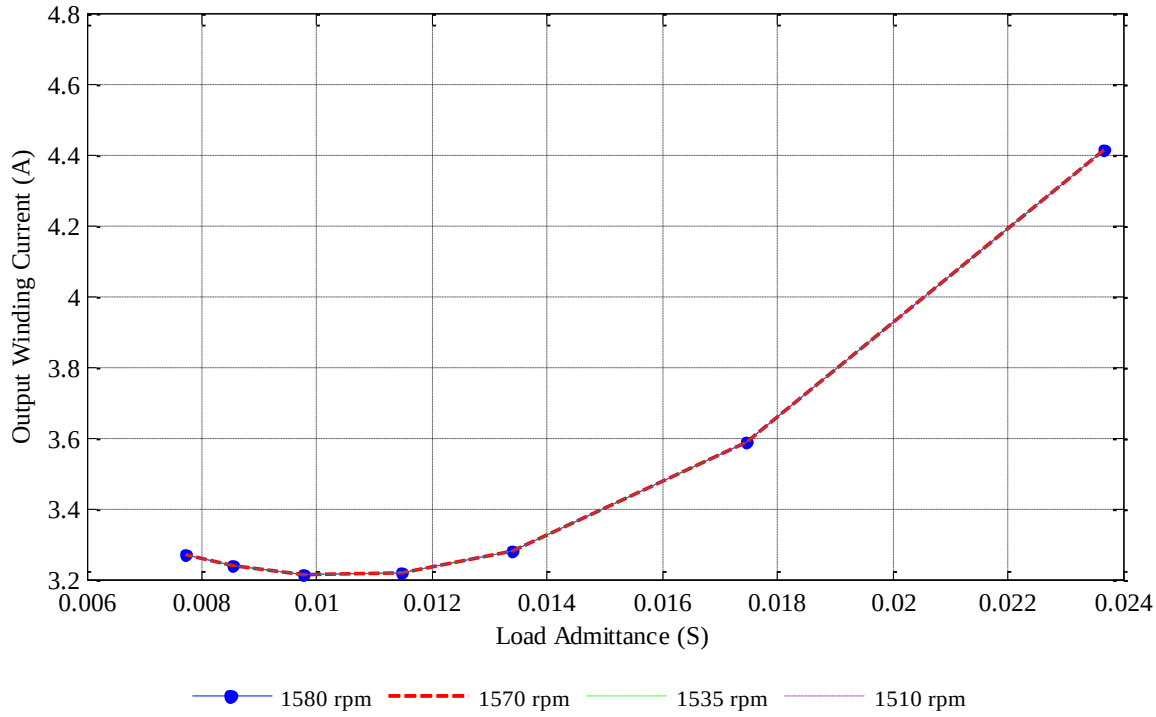

Fig. 6.3.2.4. Variation of output winding current with changing load admittance

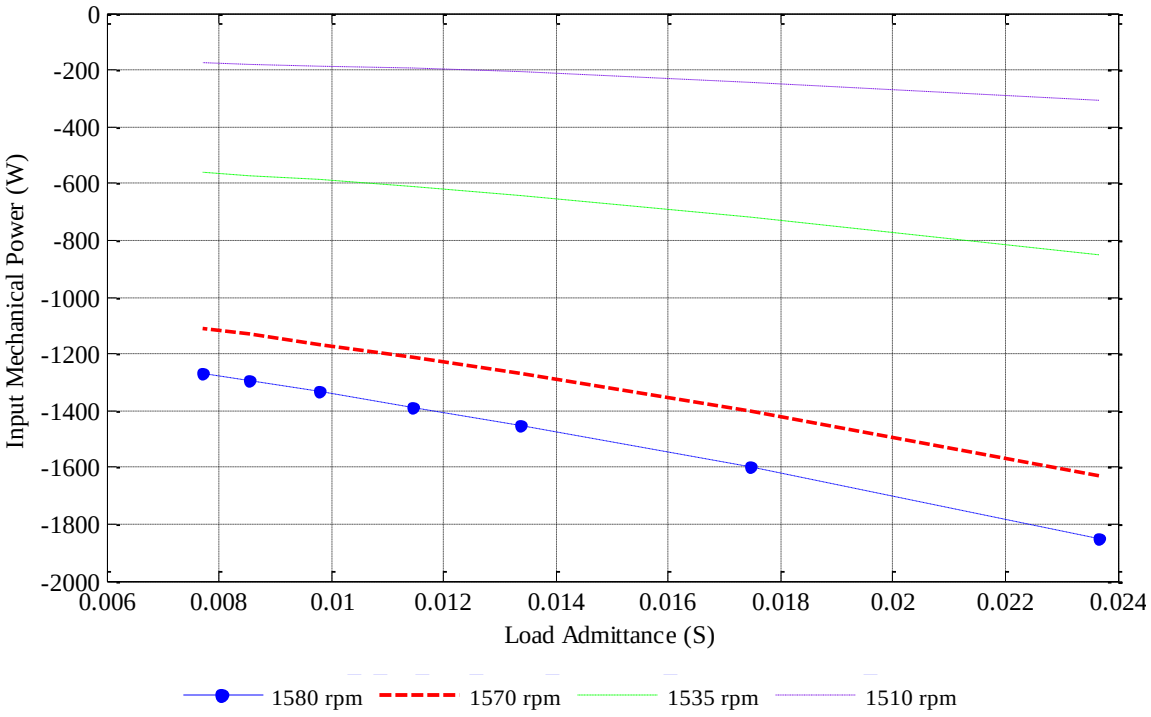

Fig. 6.3.2.5. Variation of input mechanical power with changing load admittance

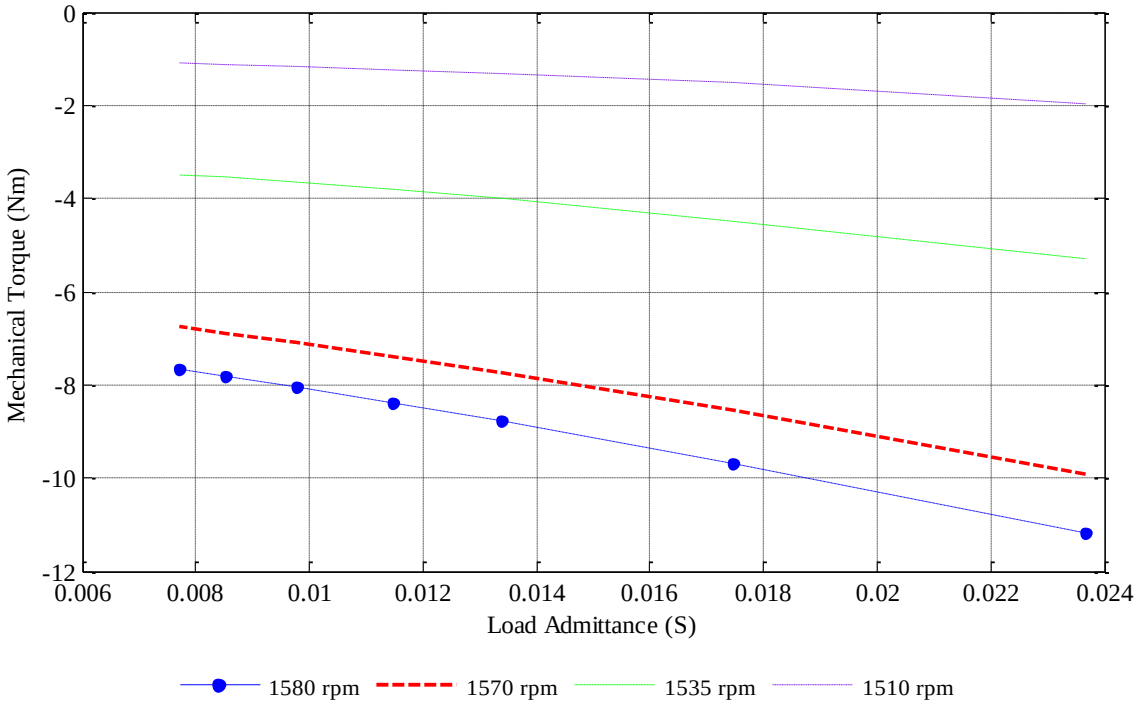

Fig. 6.3.2.6. Variation of mechanical torque with changing load admittance

6.4 Changing the Fixed Capacitance

In order to study the effect of changing the fixed capacitance on the system variables, the system variables are calculated for seven different values of the fixed capacitance while rotor speed and load impedance remain unchanged. In the first part of this section, the variations of system variables due to the changing fixed capacitance are studied for four different values of load impedances when the rotor speed remains unchanged at 1510 rpm. In the second part of this section, the same study is carried out for a rotor speed of 1580 rpm. Similar to the previous analysis, the figures illustrate the variation of system variables due to the changing fixed capacitance, 'S' and 'E' denote the simulation and experimental results respectively.

6.4.1 Changing the Fixed Capacitance at the rotor speed of 1510 rpm

The normal operating point is selected to generate 230 V/ 50 Hz at the output winding as described in section 6.3. The operating parameters are the same as those shown in Table 6.3.1.

The variations of system variables are calculated using the computational techniques described in section 4.2 for the given set of operating parameters, while the fixed capacitance is changed from 20 to 50 μF. Figs. 6.4.1.1 to 6.4.1.3 illustrate the variations of excitation control winding related variables when the fixed capacitance is increased. The voltage in excitation control winding decreases with the increasing fixed capacitance as shown in Fig. 6.4.1.1.

The increase of fixed capacitance by 50 % causes a 7 % decrease in the voltage in excitation control winding. The fixed capacitance is employed to keep the magnitude of excitation control winding related variables below the rated values of the machine. The increasing fixed capacitance increases the reactive power supply to the generator. Therefore, the voltage and the current in the excitation control winding decreases in order to maintain the reactive power balance in the system. However, the current in the excitation control winding decreases until it reaches the minimum value and then increases gradually with the increasing capacitance as it can be reduced no further due to the real power balance in the system. This is illustrated in Fig. 6.4.1.2. The current in the excitation control winding decreases by 12 % for the increase of the fixed capacitance by 75 % for the given operating condition. The

same current increases by 4.5 % when the fixed capacitance is increased by 25 %. The same behaviour can be observed for both the experimental and simulation results.

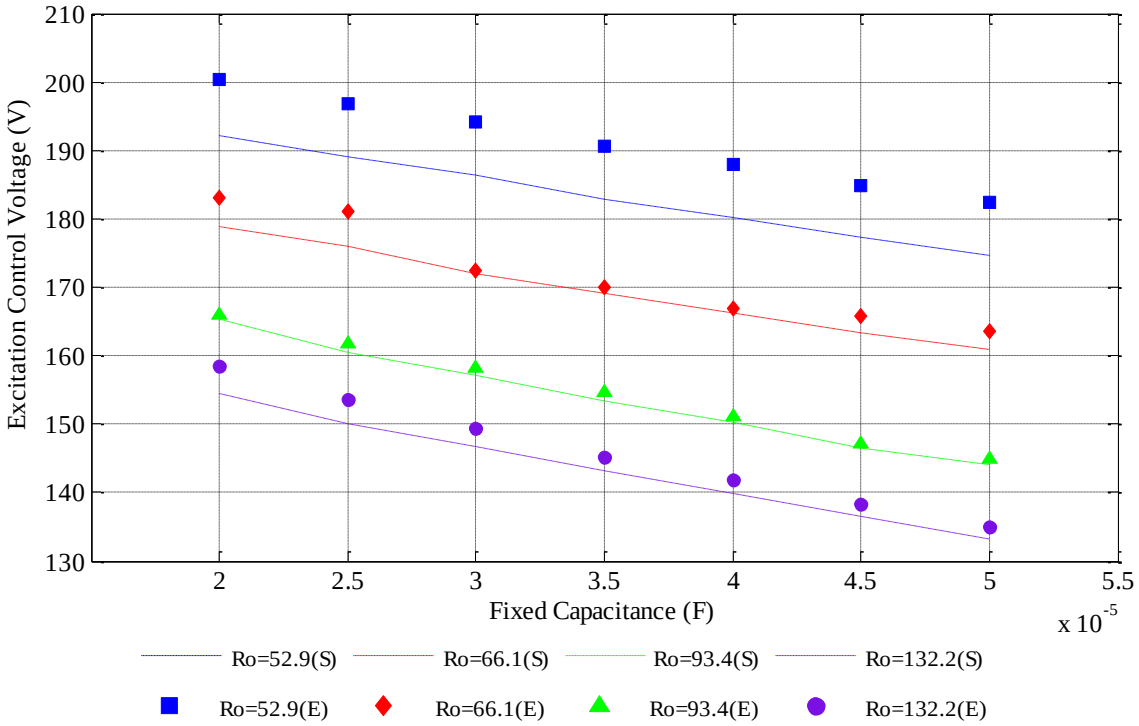

Fig. 6.4.1.1. Variation of voltage in excitation control winding with changing fixed capacitance

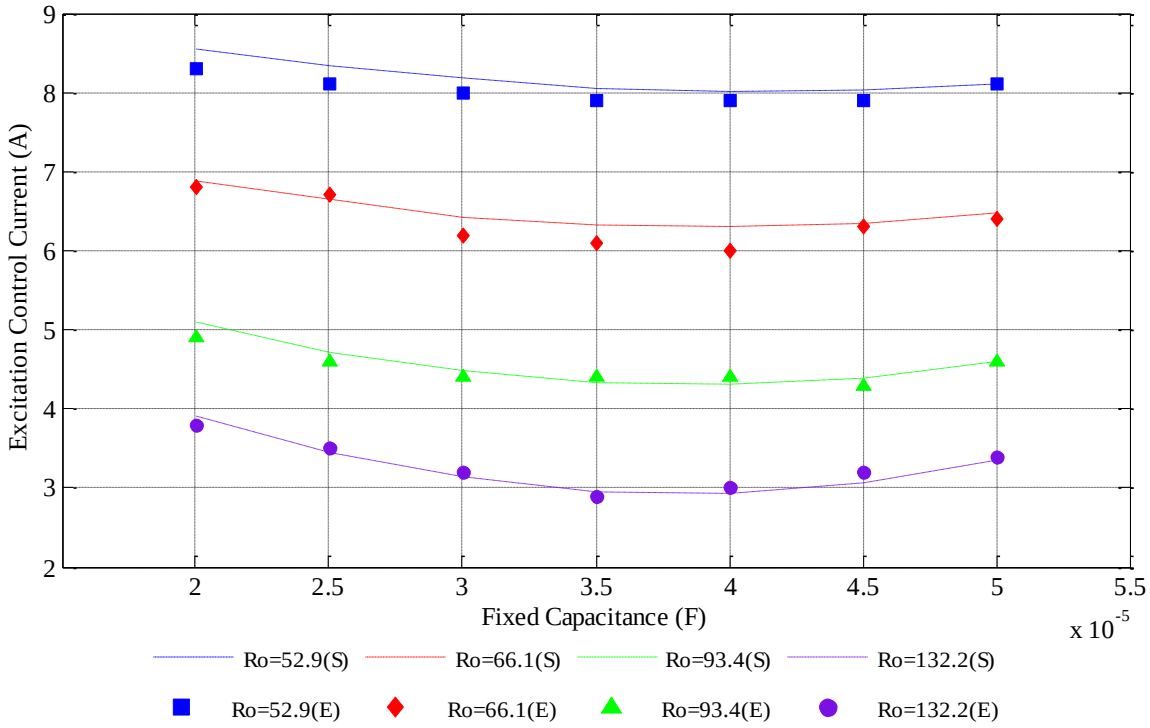

Fig. 6.4.1.2. Variation of current in excitation control winding with changing fixed capacitance

The variation of real power in excitation control winding with the changing fixed capacitance is illustrated in Fig. 6.4.1.3. It is clear that the real power in excitation control winding increases with the increasing fixed capacitance. Increasing the current through the fixed capacitance increases the output current in the generator, resulting in high resistive losses in the system. In order to compensate for these losses, the active power in the excitation control winding increases. This can be further understood with the variation of input mechanical power with the changing fixed capacitance presented later in this section.

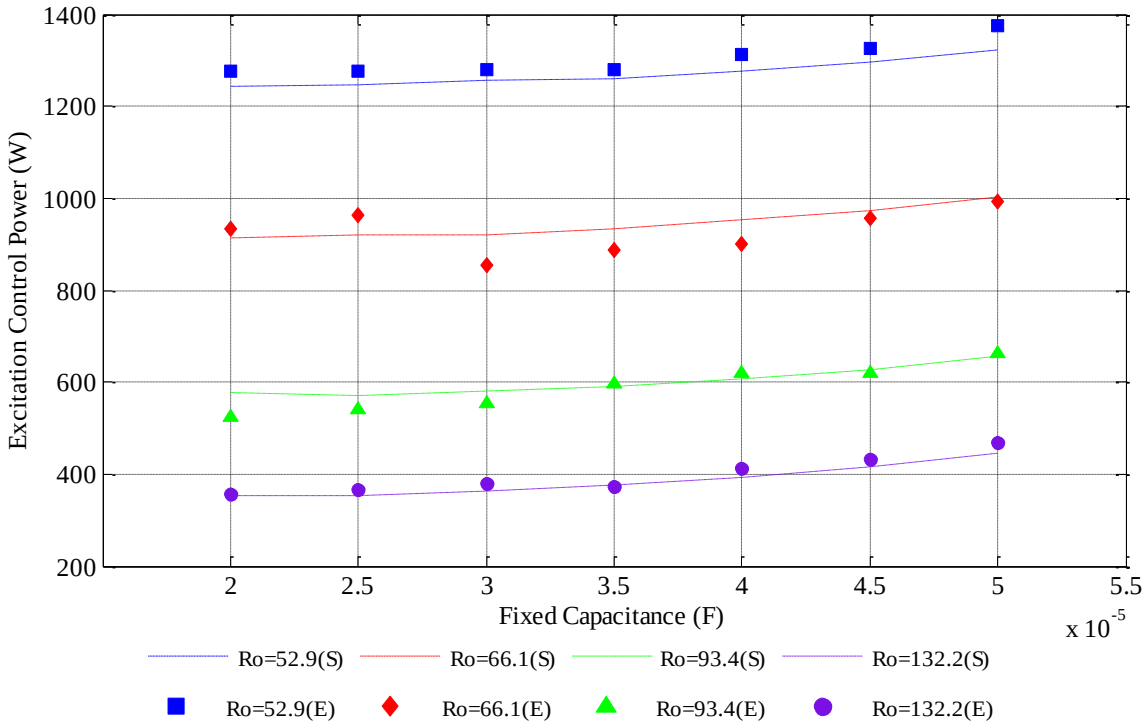

Fig. 6.4.1.3. Variation of real power in excitation control winding with changing fixed capacitance

The variation in the current in output winding is depicted in Fig. 6.4.1.4. The total current in the output winding increases with the increasing fixed capacitance. For the increase of fixed capacitance by 50 %, the current in the output winding increases by 21.2 %. Both experimental and simulated results show the same variation in the output winding current with the increasing fixed capacitance.

With the increasing fixed capacitance, the real power supplied from the renewable energy source decreases slightly for the lower values of the fixed capacitance. After reaching the maximum, it increases slightly with the increasing fixed capacitance.

However, it is difficult to identify changes in the input mechanical power as the variations are small. This is illustrated in Fig. 6.4.1.5.

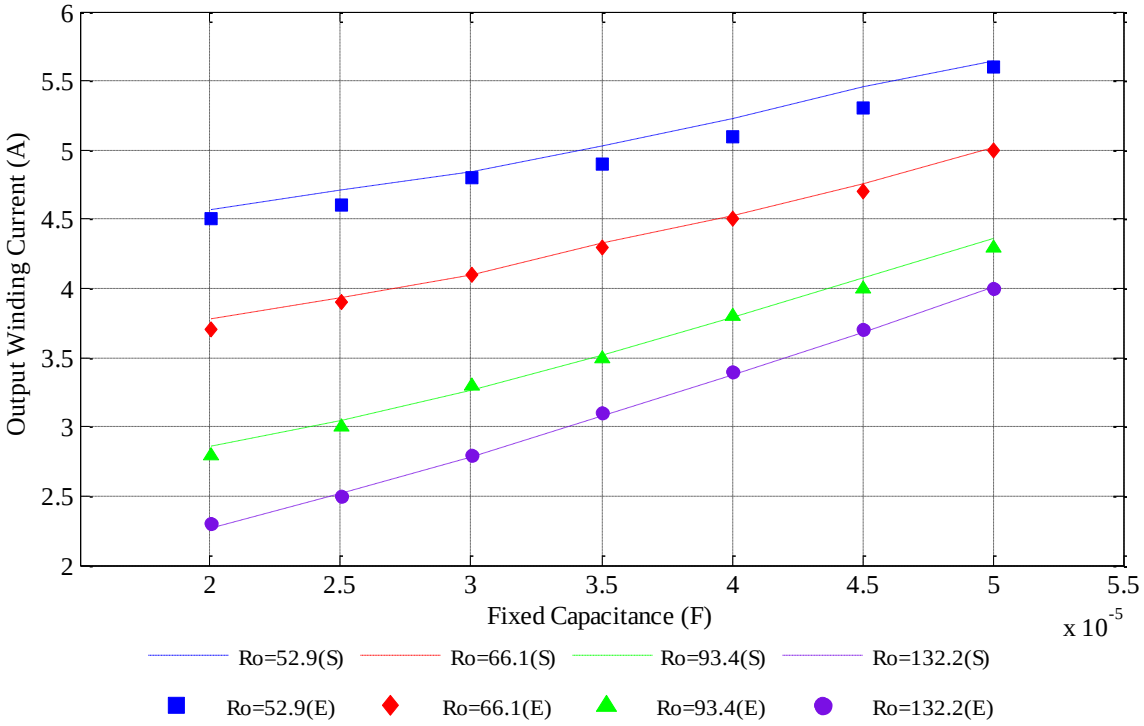

Fig. 6.4.1.4. Variation of current in output winding with changing fixed capacitance

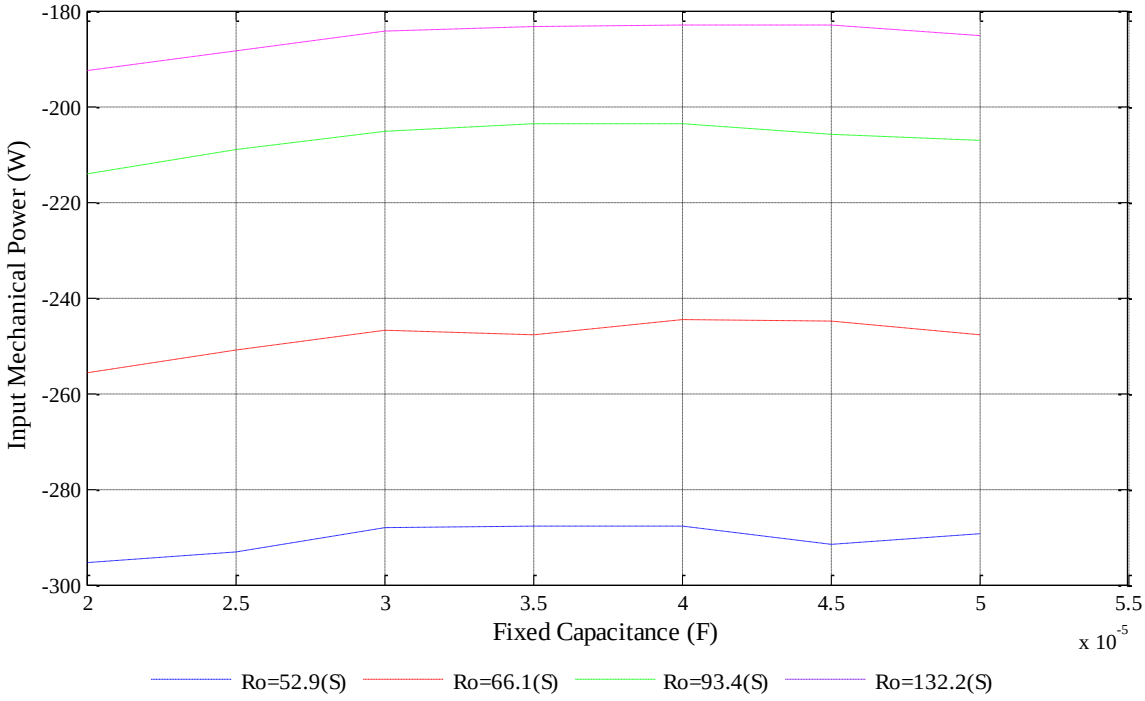

Fig. 6.4.1.5. Variation of input mechanical power with changing fixed capacitance

As demonstrated in Fig. 6.4.1.3, the generator requires additional real power to compensate for the resistive losses resulting from the higher current in the output winding. At lower rotor speeds such as 1510 rpm, the deficit real power requirement of the generator is supplied by the ESS.

Thus, with the increasing resistive losses, the real power supplied from the excitation control winding increases while that from the renewable energy source remains almost unchanged.

The variation of the mechanical torque with the changing fixed capacitance is illustrated in Fig. 6.4.1.6. A variation similar to that of the input mechanical power can be observed for the mechanical torque obtained using Matlab simulations.

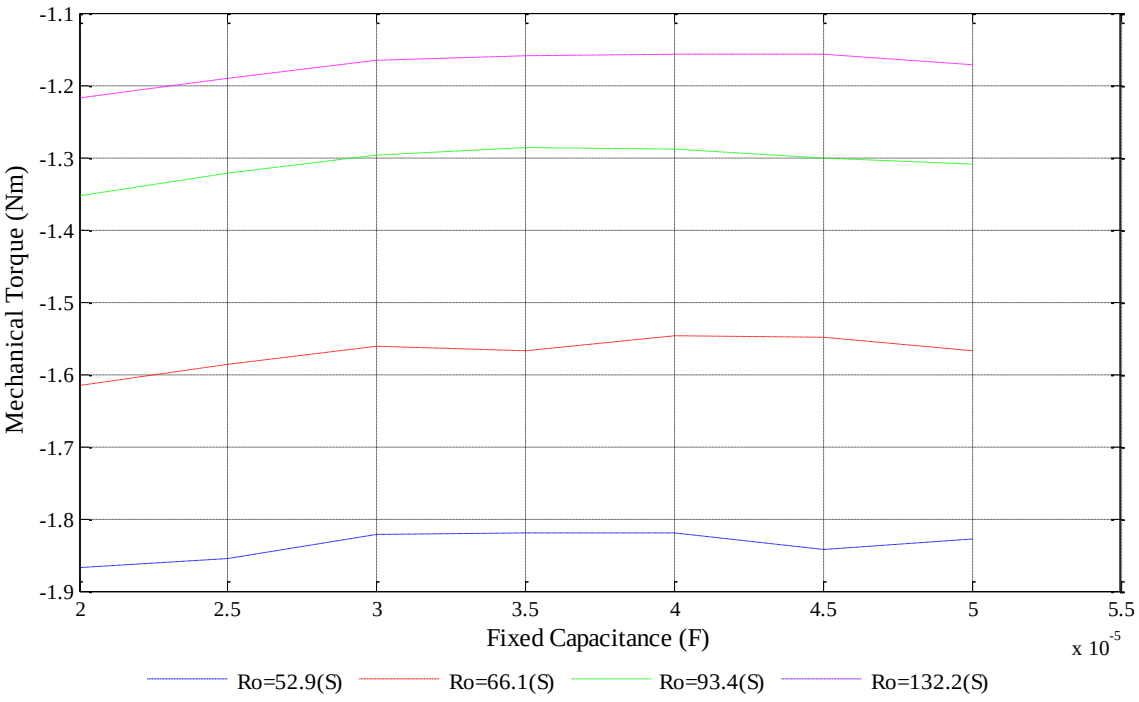

Fig. 6.4.1.6. Variation of mechanical torque with changing fixed capacitance

6.4.2 Changing the Fixed Capacitance at the rotor speed of 1580 rpm

In this analysis, the normal operating point is selected to generate the voltage of 230 V at a frequency of 50 Hz at the output winding of the generator. At this point, the output winding current is considered as 56.6 % of the full-load current at desired output voltage. The measured operating parameters required to produce this condition are given in the Table 6.4.2.1.

Using the same operating parameters, the theoretical values of the system variables due to the effects of changing the fixed capacitance while all other operating parameters remain constants are calculated using the computational techniques given in section 4.2. Similar to the previous analyses, the output voltage and the frequency are maintained constant at the normal operating conditions. When the rotor speed is unchanged, the same test is repeated for another three different values of the load impedances. The effects of changing the fixed capacitance on other system variables are demonstrated in Figs. 6.4.2.1-6.4.2.7.

Table 6. 4.2.1
Operating parameters required to obtain the normal operating point

Parameter	Values
Fixed capacitance (μF)	30
Load impedance (Ω)	93.4
Rotor speed (rpm)	1580

The variation of the voltage in excitation control winding with the changing fixed capacitance at a rotor speed of 1580 rpm is illustrated in Fig. 6.4.2.1.

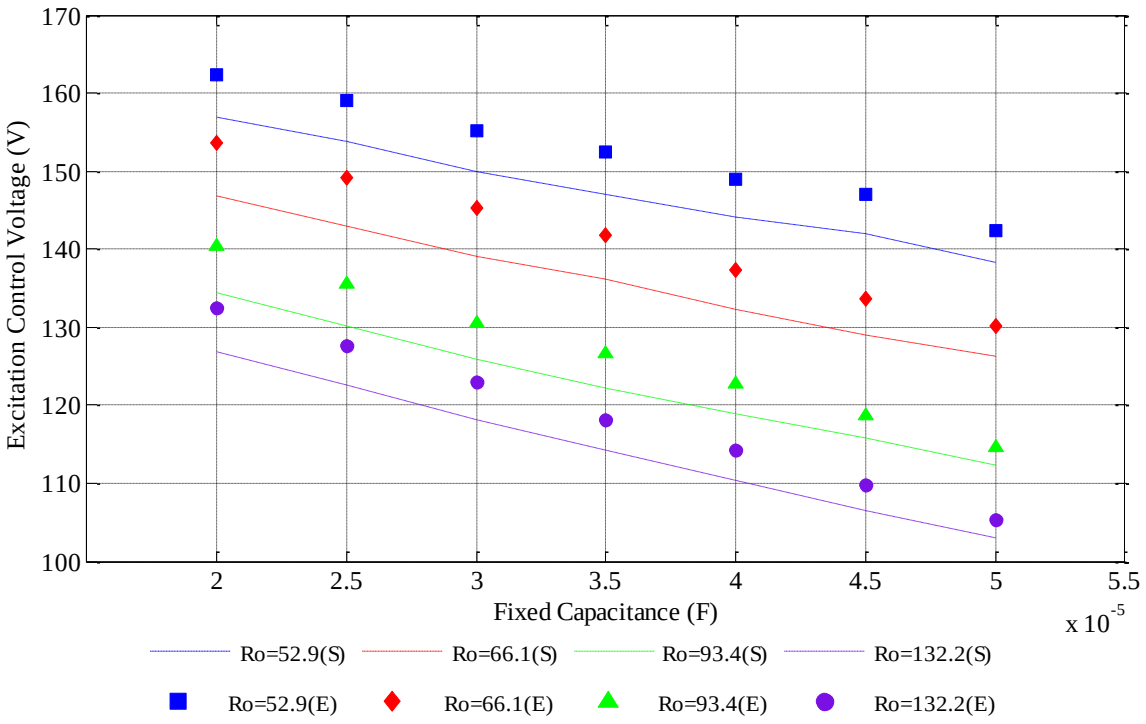

Fig. 6.4.2.1. Variation of voltage in excitation control winding with changing fixed capacitance

Similar to the previous analysis, the voltage in the excitation control winding decreases with the increasing fixed capacitance. For a change in fixed capacitance of 50 %, the voltage in excitation control winding decreases by 8.5 %. Figure 6.4.2.2 depicts the variation in current in the excitation control winding when fixed capacitance is increased. This behaviour differs from that of the previous analysis. The increase in the speed of the prime mover increases the mechanical power supplied by the renewable energy source. Thus, the input mechanical power will balance a portion of the resulting resistive losses due to the increase in fixed capacitance. In order to balance the reactive power of the system, the current in the excitation control winding decreases with the increasing fixed capacitance.

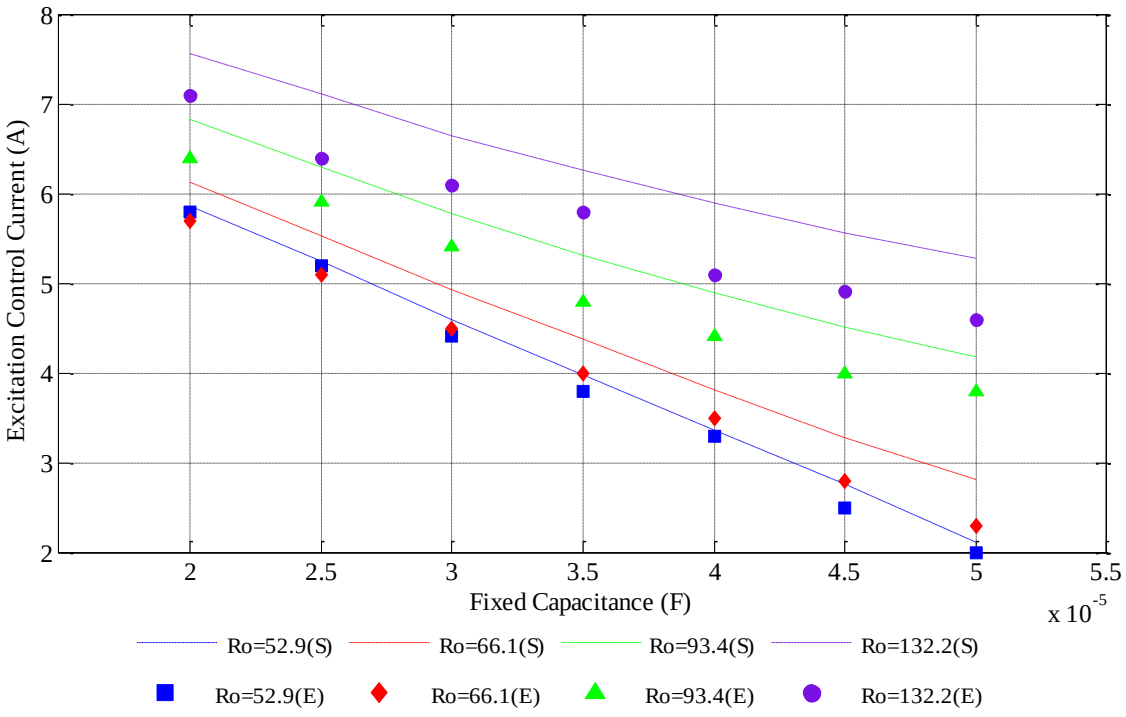

Fig. 6.4.2.2. Variation of current in excitation control winding with changing fixed capacitance

This behaviour can be better understood using Fig. 6.4.2.3 which illustrates the variation in real power in the excitation control winding with the changing fixed capacitance. At the higher speed of the prime mover, the excitation control winding absorbs the real power generated by the generator system. Therefore, in Fig. 6.4.2.3, this power is presented as a negative value. However, the amount of the real power absorbed by the excitation control winding decreases with the increasing fixed

capacitance. The real power in excitation control winding decreases by 16.4 %, when the fixed capacitance increases by 50 %. This is proportional to the increase in the resistive losses resulting from the increase in fixed capacitance.

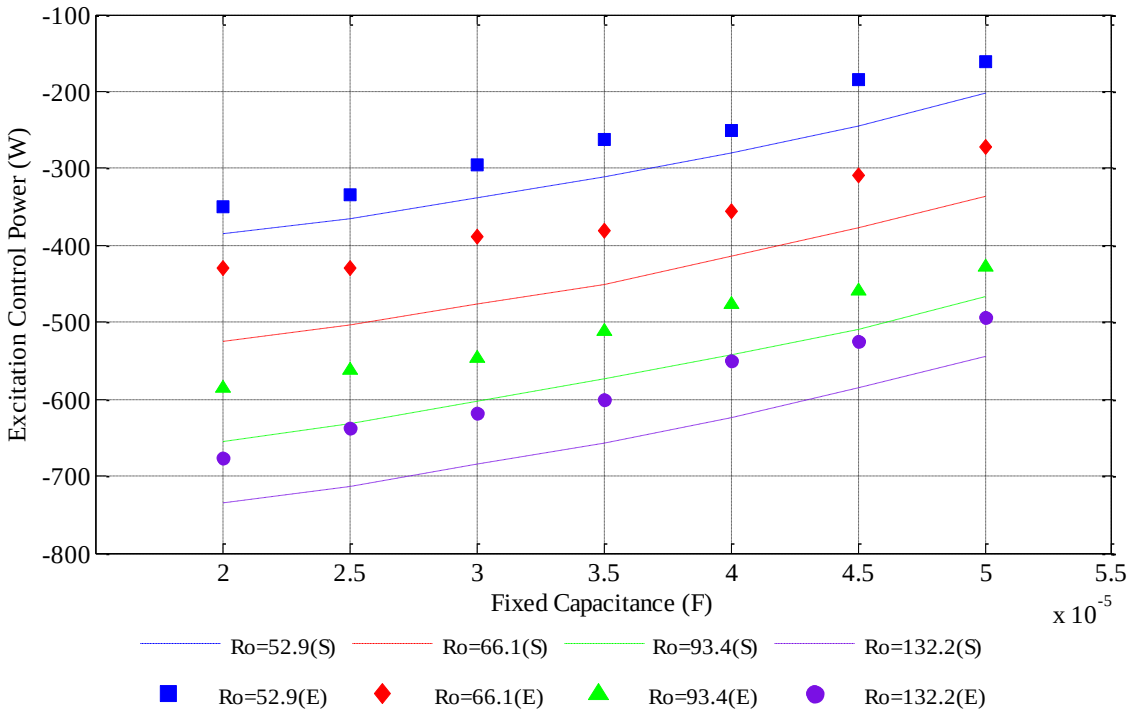

Fig. 6.4.2.3. Variation of real power in excitation control winding with changing fixed capacitance

Similar to the Fig. 6.4.1.4, the variation in current in output winding increases with the increasing fixed capacitance. This is depicted in Fig. 6.4.2.4.

Unlike the previous analysis, the input mechanical power decreases with the increasing fixed capacitance. This is illustrated in Fig. 6.4.2.5. Since both the voltage and current in the excitation control winding decrease in order to maintain the reactive power balance in the system, the input mechanical power cannot be further increased at a fixed consumer demand at the output. The input mechanical power decreases by 6 % when the fixed capacitance is increased by 50 %.

The variation in the mechanical torque due to the changing fixed capacitance is illustrated using the simulation results in Fig. 6.4.2.6. The mechanical torque follows the same behaviour in the input mechanical power to keep the rotor speed constant as given at the beginning.

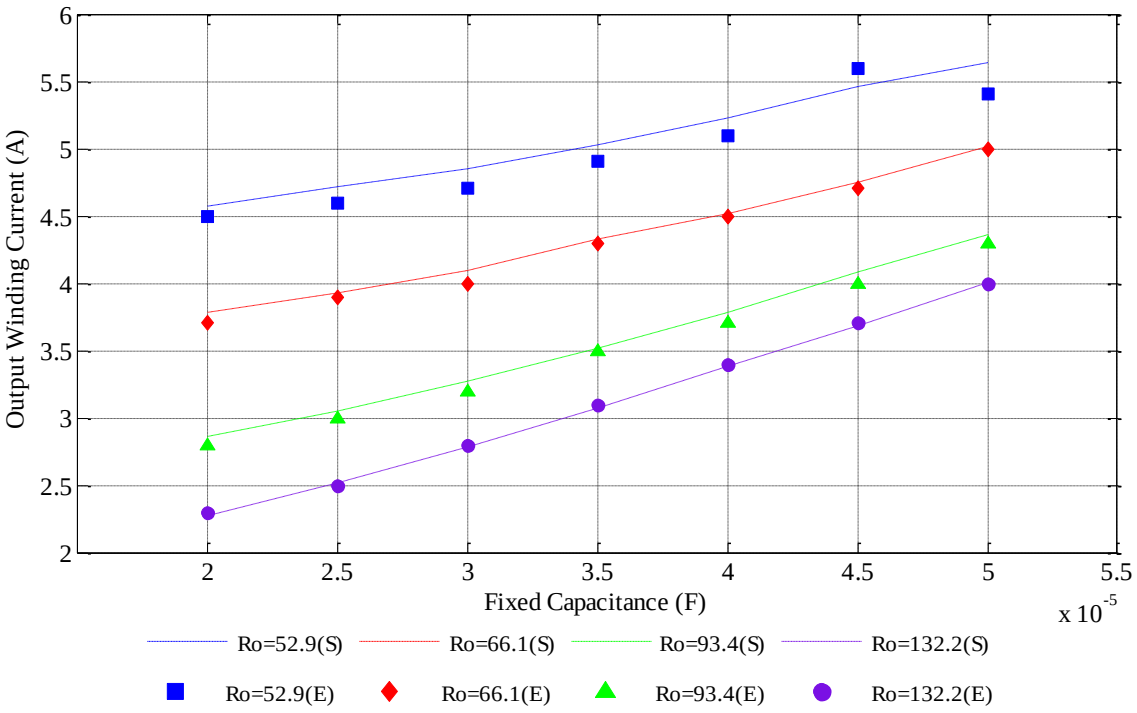

Fig. 6.4.2.4. Variation of current in output winding with changing fixed capacitance

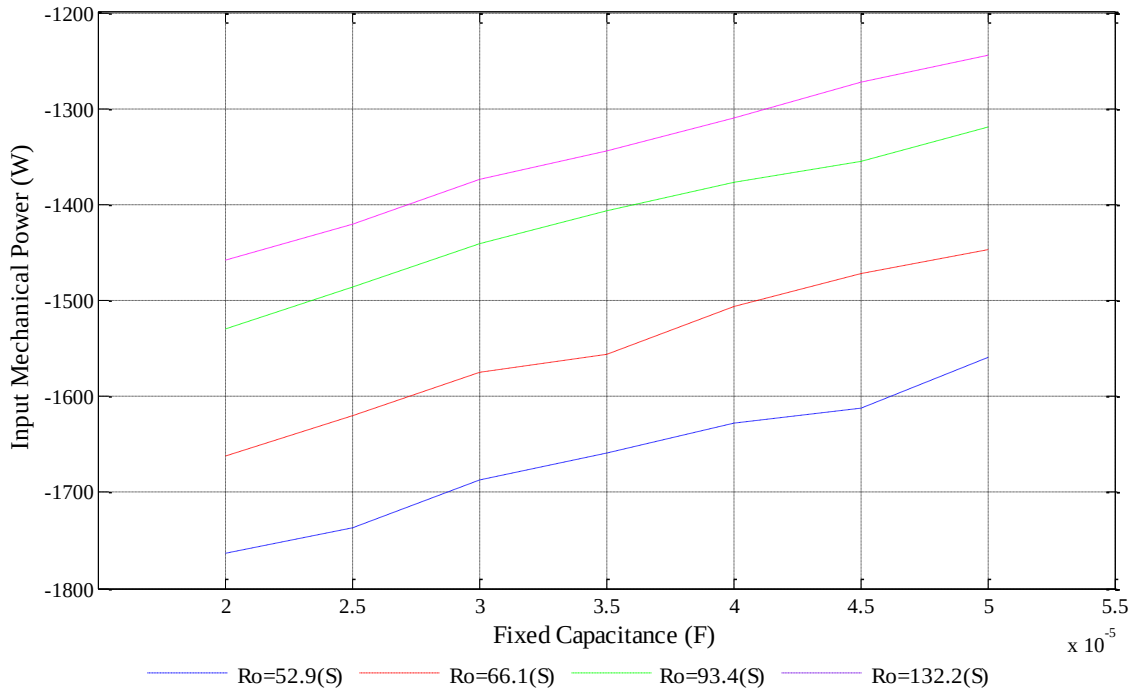

Fig. 6.4.2.5. Variation of input mechanical power with changing fixed capacitance

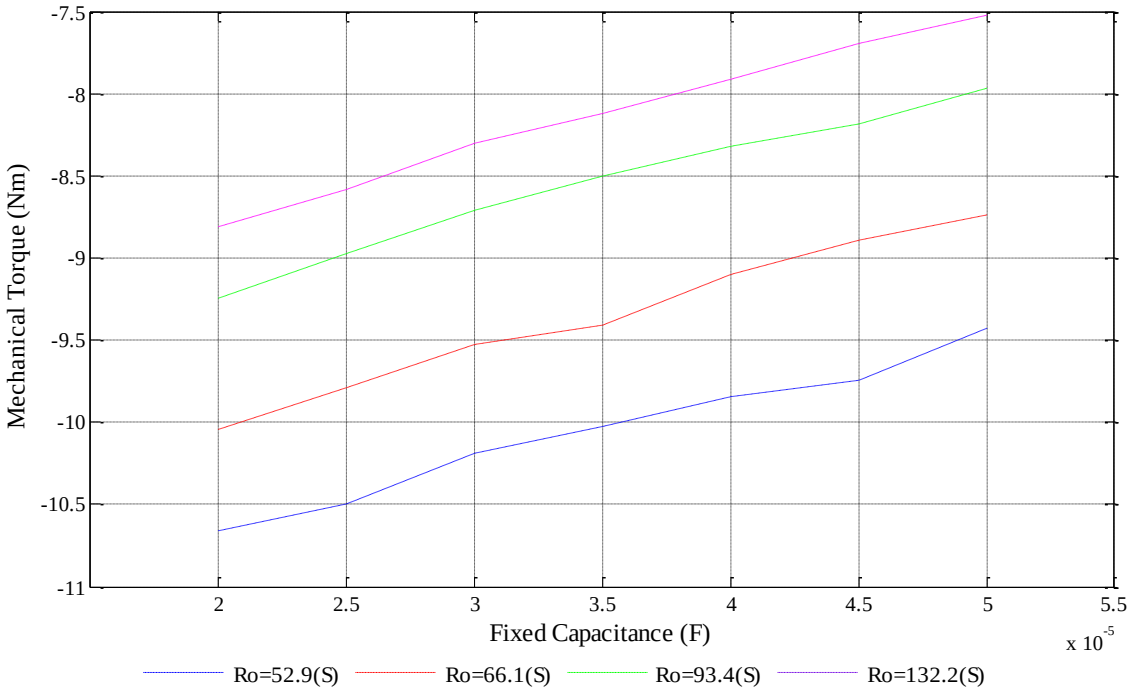

Fig. 6.4.2.6. Variation of mechanical torque with changing fixed capacitance

6.5 Changing the Rotor Speed

In order to extract the maximum power available from the renewable energy source, the proposed energy conversion system employs an unregulated prime mover. Depending on the speed of the prime mover, the system variables will be changed. Therefore, prior to designing the controlled system, it is necessary to study the effects on the system variables when the speed of the prime mover is changed. These analyses are carried out for two different load conditions as described in sections 6.5.1 and 6.5.2.

6.5.1 Changing Rotor Speed at the Load Impedance of 93.4 Ω

Similar to the previous analyses, the normal operating condition of the machine is selected to generate the voltage and the frequency of 230V and 50 HZ respectively at the output. The output winding current is considered as 56.6 % of the full-load current at desired output voltage. The operating parameters required to produce this condition are given in Table 6.5.1.1. All the operating parameters with the exception of the rotor speed are kept constant under the normal operating condition and the values of the system variables in steady-state are calculated using the computational

techniques described in section 4.2. The same test is repeated for another six fixed capacitances. These results are compared with the corresponding experimental values and shown by the figures later in this section. Similar to the previous analyses, 'S' and 'E' denote the simulated and the experimental results respectively.

Table 6. 5.1.1
Operating parameters required to obtain the normal operating point

Parameter	Values
Fixed capacitance (μF)	40
Load impedance (Ω)	93.4
Rotor speed (rpm)	1560

The variations in voltage, current and real power in the excitation control winding due to the changing rotor speed are illustrated in Figs. 6.5.1.1 to 6.5.1.3 respectively.

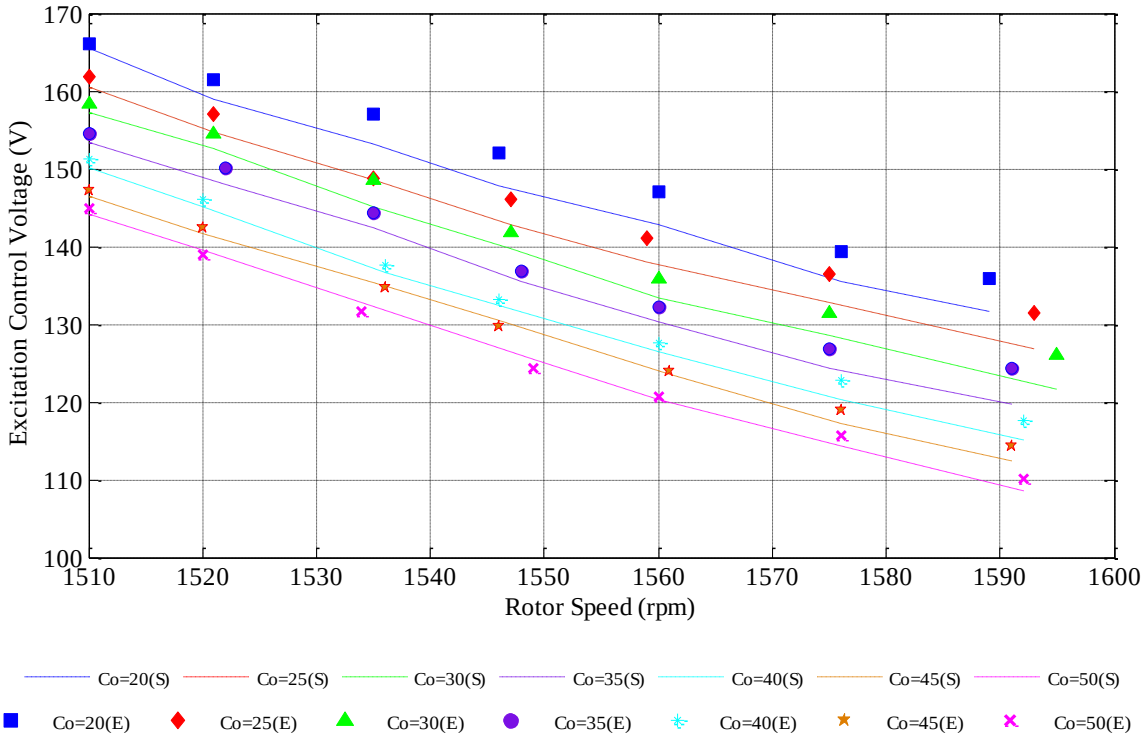

Fig. 6.5.1.1. Variation of voltage in excitation control winding with changing rotor speed

Since the input mechanical power increases with the increasing rotor speed, the real power supplied by the ESS decreases. Thus, both the voltage and the current in

excitation control winding decreases with the increasing rotor speed until the current reaches the minimum value. Up to this point, the real power in the excitation control winding is positive and decreases with the increasing rotor speed. This is due to the real power supplied from the ESS at the low rotor speeds. After the excitation control winding starts to absorb the additional real power generated by the system, both the real power and the current in the same winding gradually increases with the increasing rotor speed to maintain the real power balance in the system. The same behaviour is demonstrated by both the experimental and simulation results.

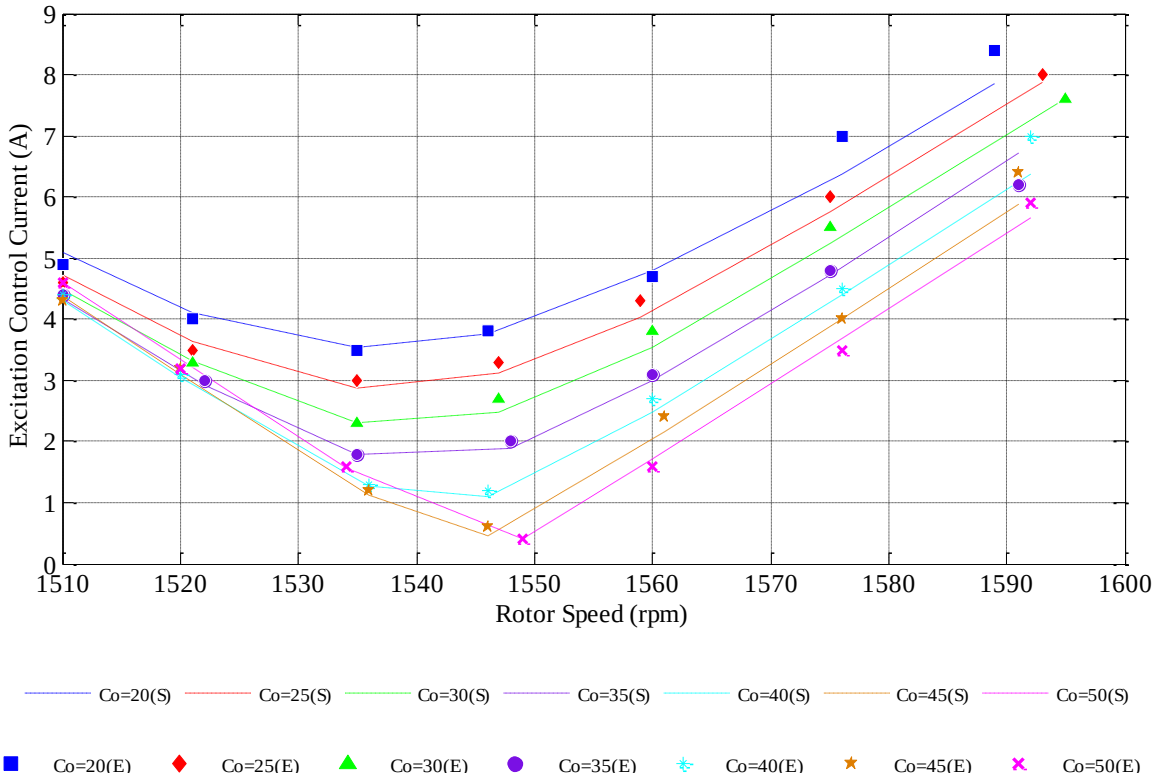

Fig. 6.5.1.2. Variation of voltage in excitation control winding with changing rotor speed

The dependency of the current in output winding with the changing rotor speed is depicted in Fig. 6.5.1.4. It is noted that the current in output winding remains unchanged with the increasing rotor speed. Thus, the current in output winding is independent of the rotor speed. Figures 6.5.1.5 and 6.5.1.6 illustrate the simulated results of the variations of input mechanical power and mechanical torque with the changing rotor speed respectively.

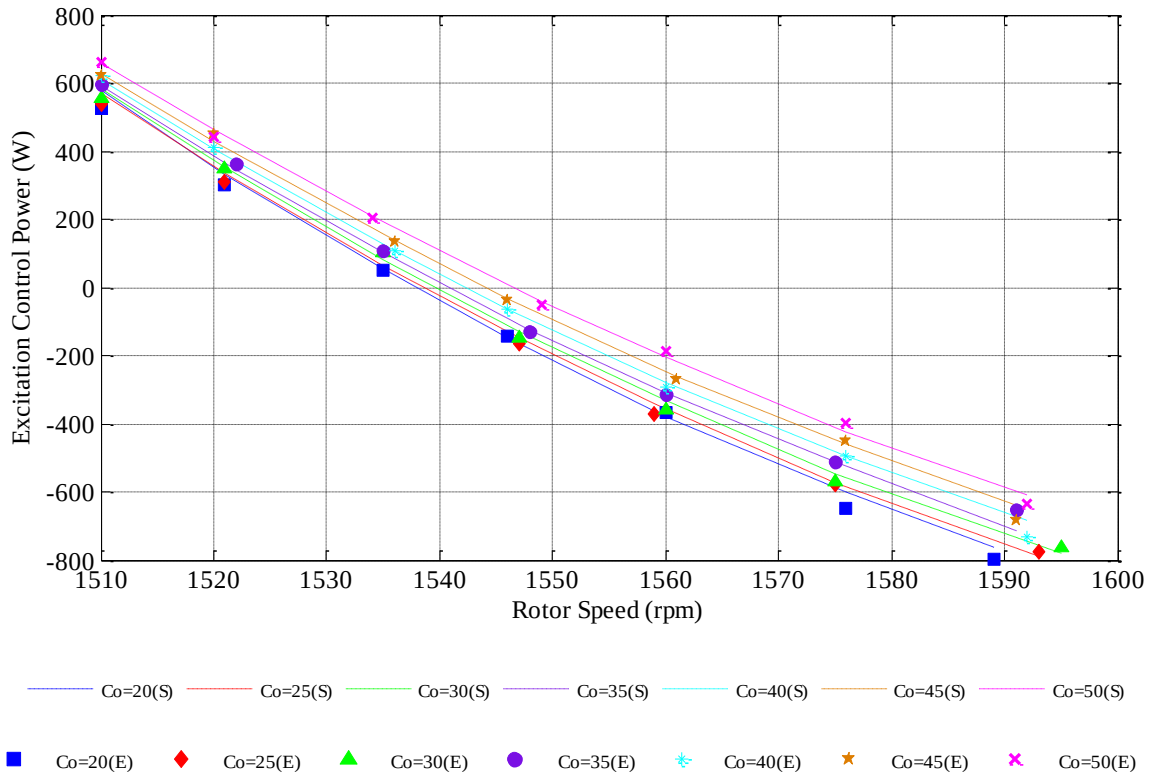

Fig. 6.5.1.3. Variation of real power in excitation control winding with changing rotor speed

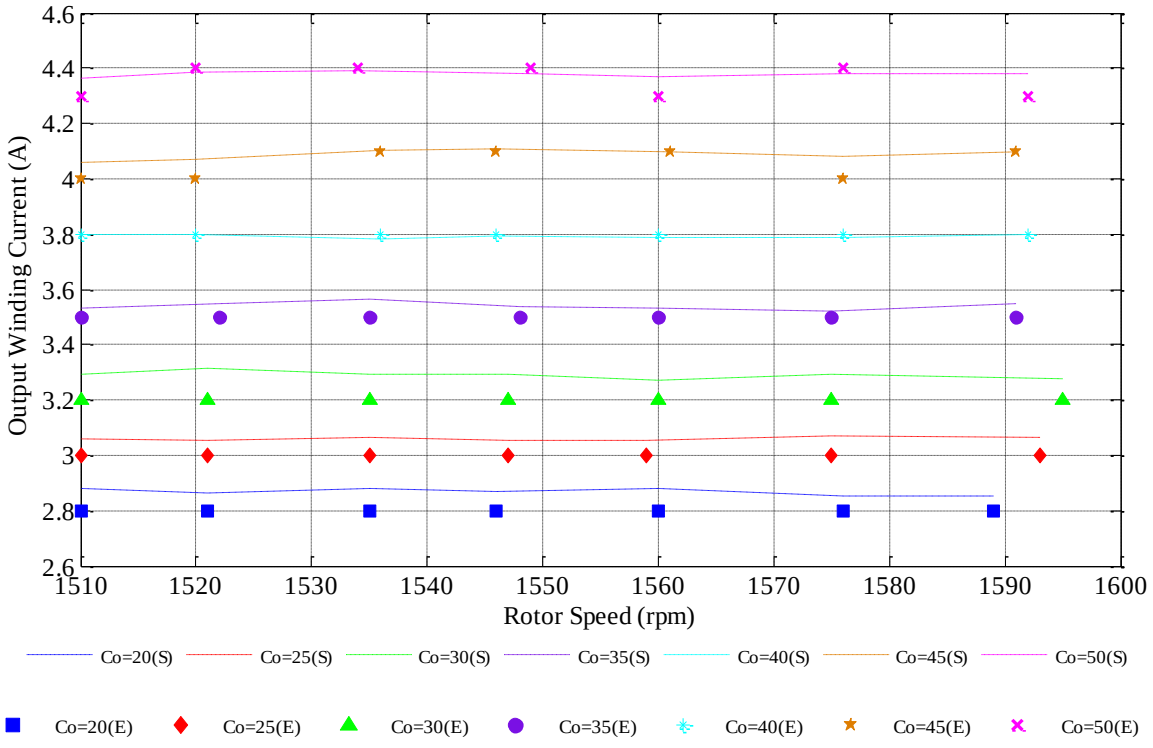

Fig. 6.5.1.4. Variation of current in output winding with changing rotor speed

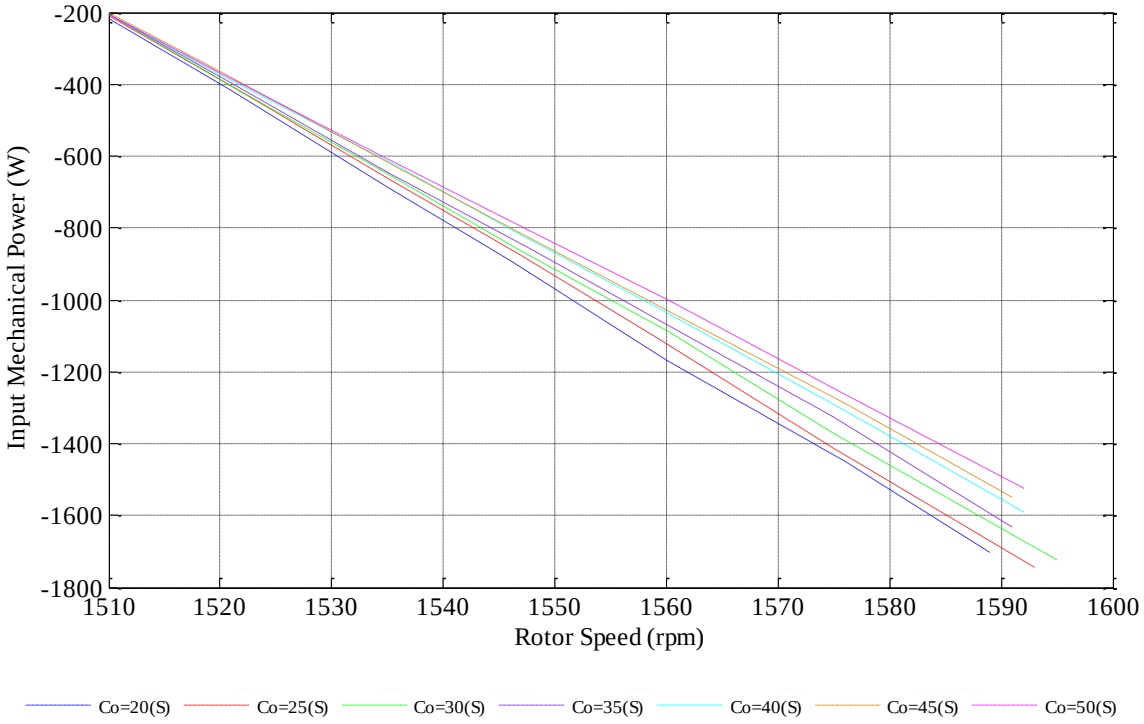

Fig. 6.5.1.5. Variation of input mechanical power with changing rotor speed

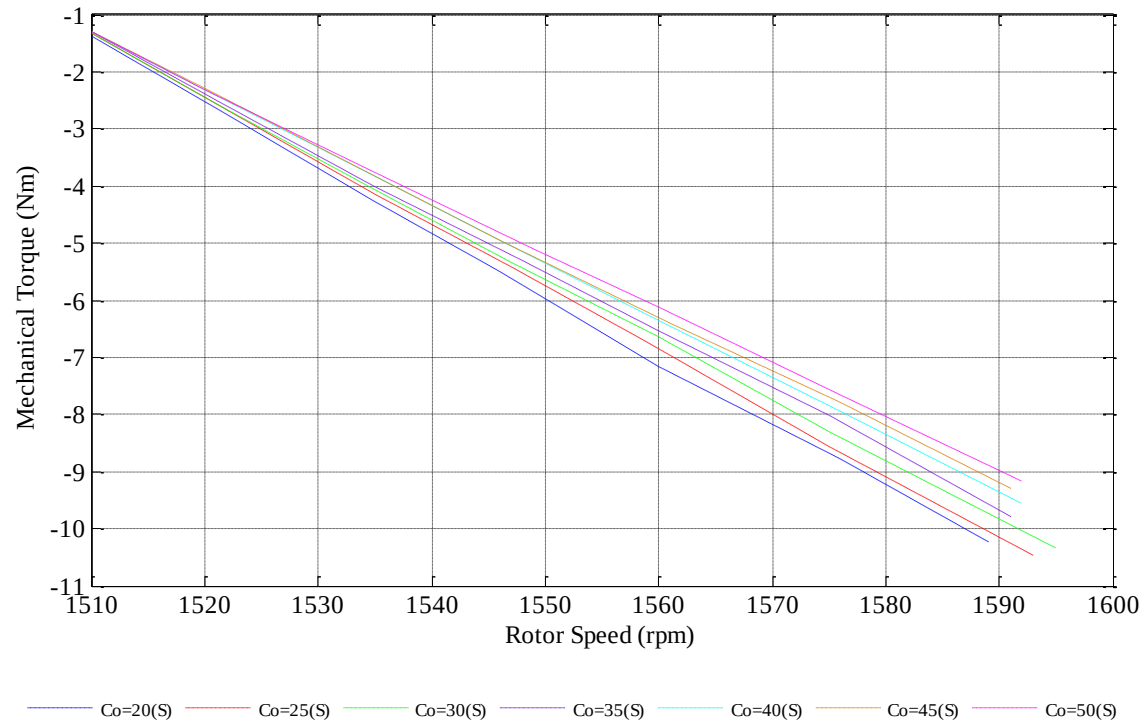

Fig. 6.5.1.6. Variation of mechanical torque with changing rotor speed

The input mechanical power increases with the increasing rotor speed. The mechanical torque follows the same behaviour as that of the input mechanical power at a constant fixed capacitance and a consumer load.

6.5.2 Changing Rotor Speed at the Load Impedance of 52.9 Ω

Similar to the previous analyses, the voltage and the frequency at the output are selected as 230V and 50 HZ respectively as the normal operating condition of the machine. The output winding current is considered as the full-load current at desired output voltage. The operating parameters required to produce this condition are given in Table 6.5.2.1.

The variations of system variables in steady-state due to the changing rotor speed are analysed for the given set of operating parameters. The same test is repeated for another six fixed capacitances at the constant load impedance of 52.9 Ω. The simulation and the experimental results are demonstrated using the figures shown later in this section. Similar to the previous analyses, 'S' and 'E' denote the simulation and the experimental results respectively.

Table 6. 5.2.1
Operating parameters required to obtain the normal operating point

Parameter	Values
Fixed capacitance (μF)	40
Load impedance (Ω)	52.9
Rotor speed (rpm)	1560

The variations in voltage, current and real power in the excitation control winding due to the changing rotor speed are illustrated in Figs. 6.5.2.1 to 6.5.2.3 respectively. All these variables follow the same behaviour demonstrated by Figs. 6.5.1.1 to 6.5.1.3 respectively. However, the current in the excitation control winding reaches the minimum at a higher rotor speed than that described in section 6.5.1. Since the real power consumption at the output winding increases with the increasing load, the ESS needs to supply the deficit power for a broad range of rotor speeds. Thus, the real power in excitation control winding changes the direction at a higher rotor speed.

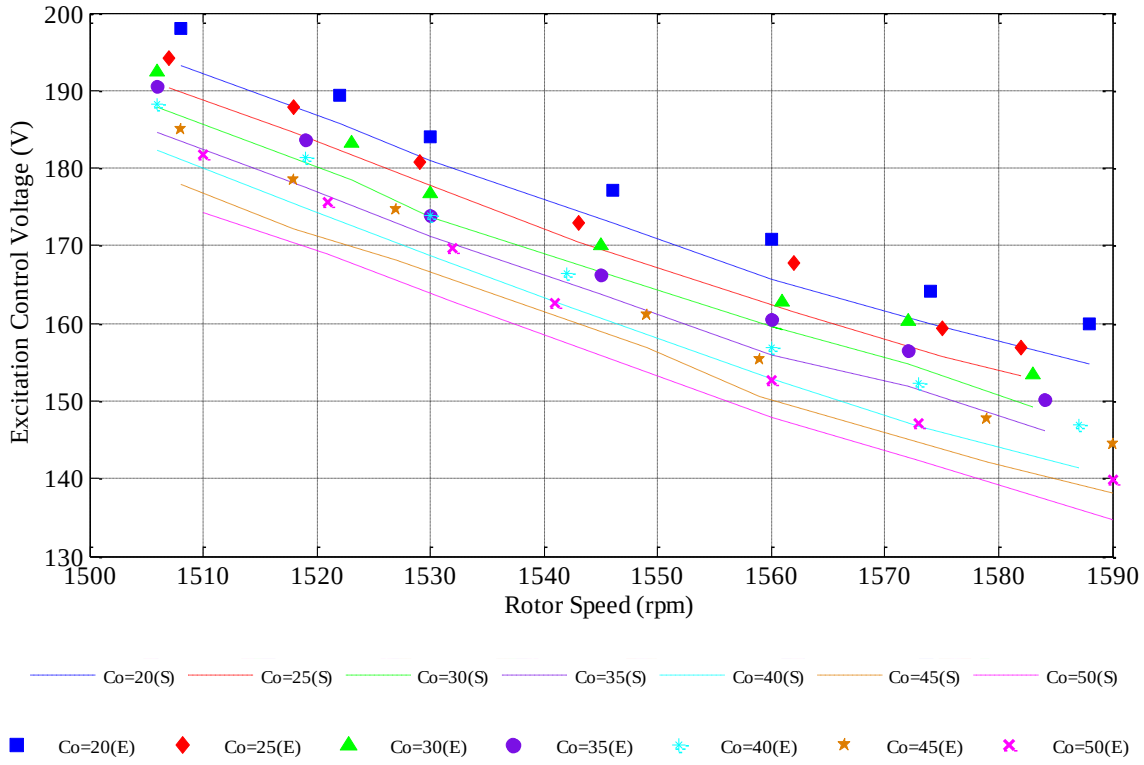

Fig. 6.5.2.1. Variation of voltage in excitation control winding with changing rotor speed

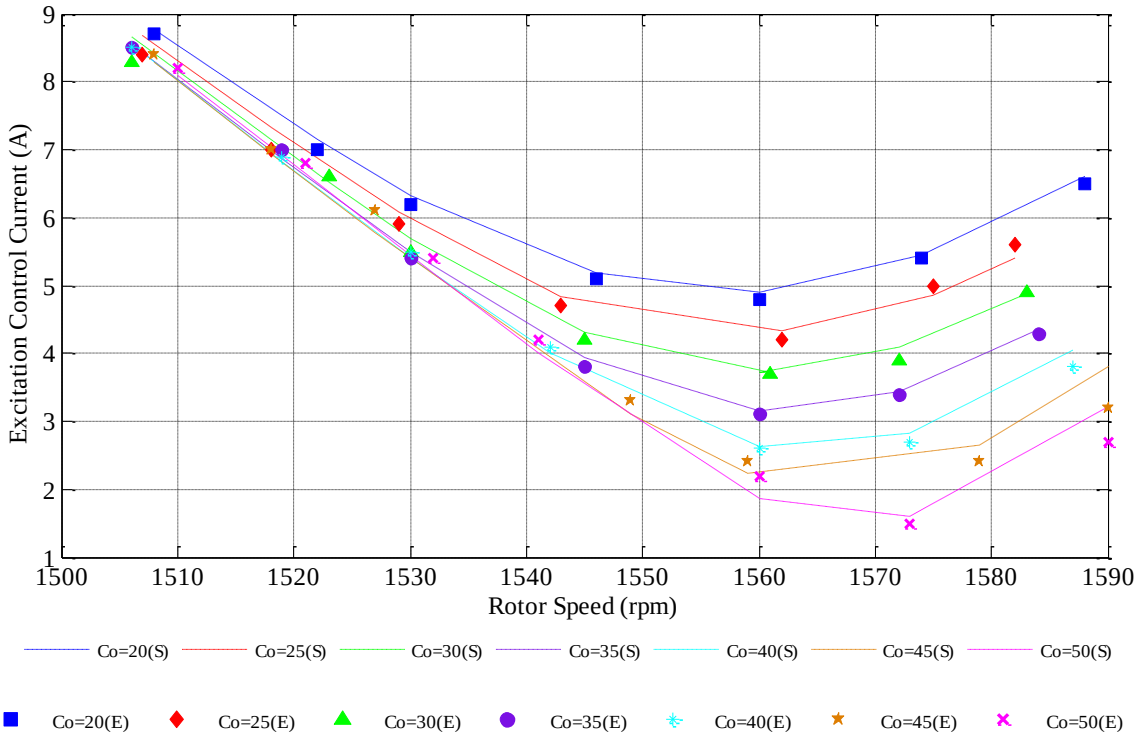

Fig. 6.5.2.2. Variation of current in excitation control winding with changing rotor speed

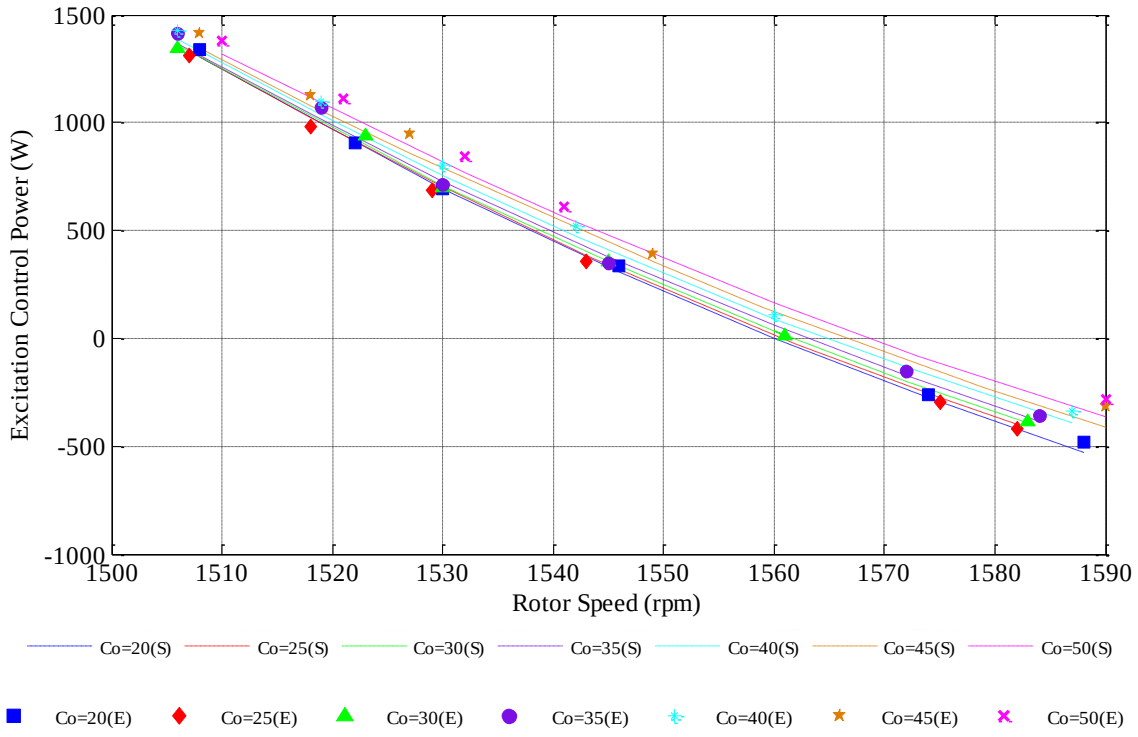

Fig. 6.5.2.3. Variation of real power in excitation control winding with changing rotor speed

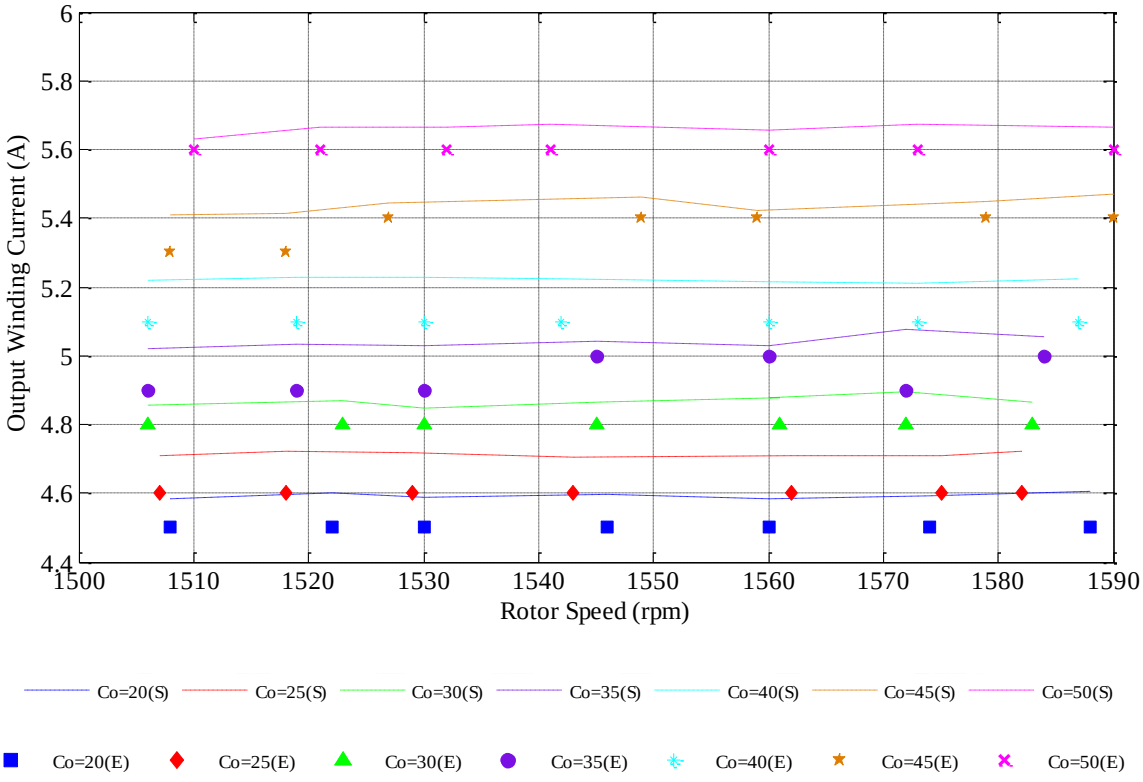

Fig. 6.5.2.4. Variation of current in output winding with changing rotor speed

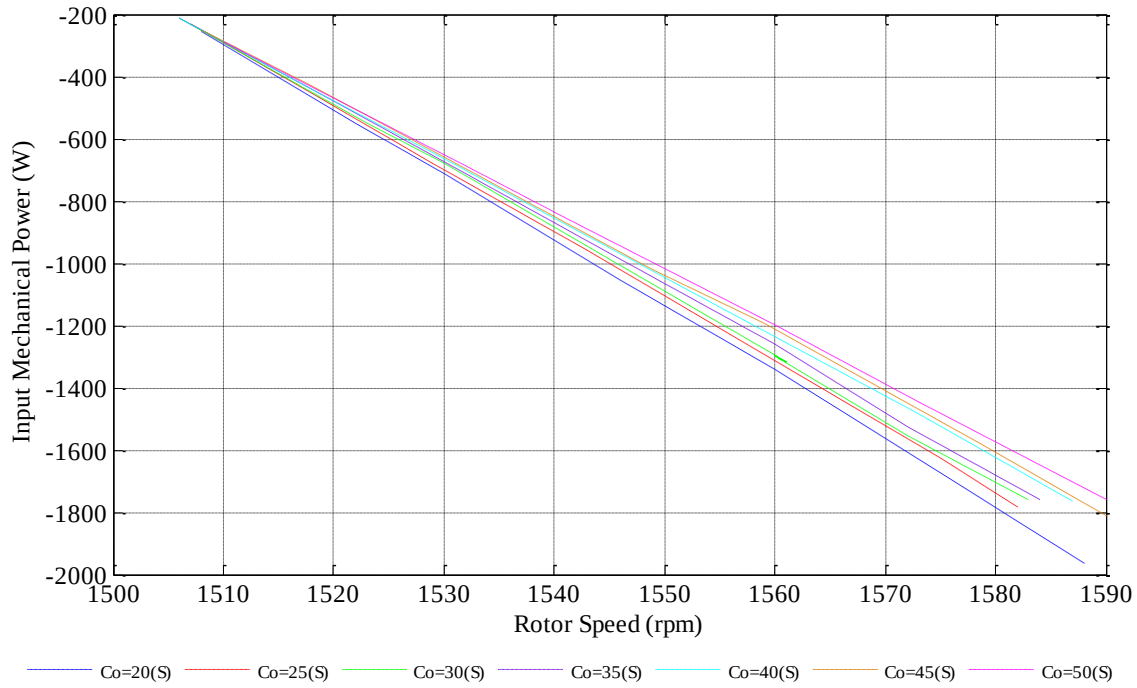

Fig. 6.5.2.5. Variation of input mechanical power with changing rotor speed

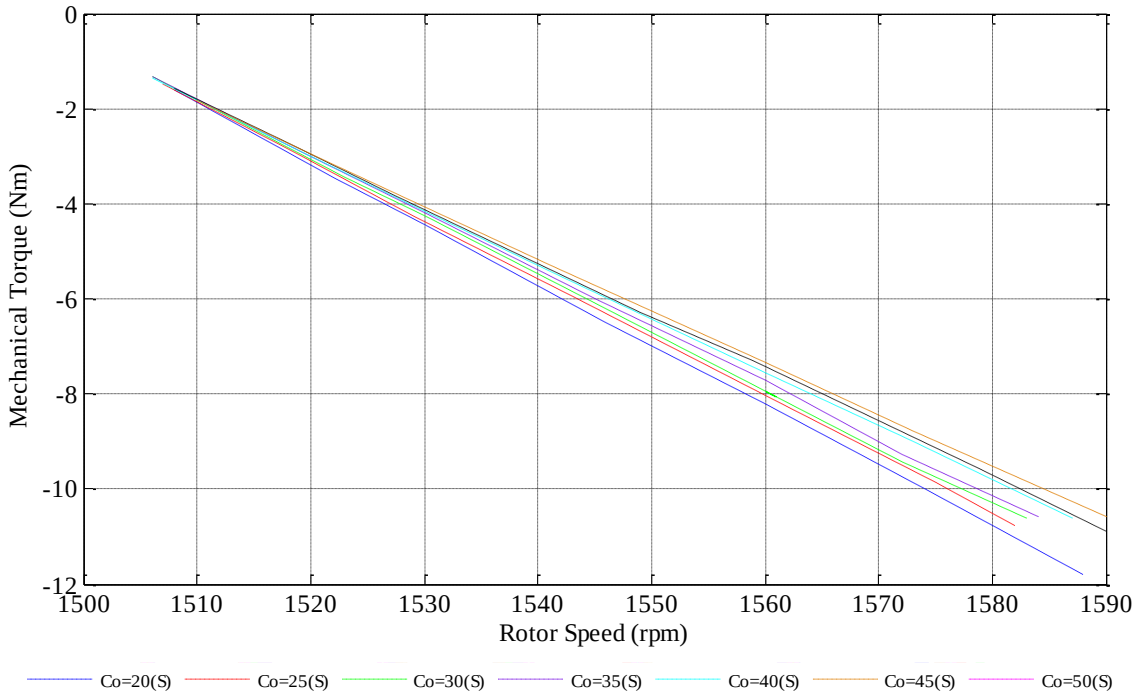

Fig. 6.5.2.6. Variation of mechanical torque with changing rotor speed

Figure 6.5.2.4 illustrates the variation of current in the output winding with the changing rotor at the consumer load of 52.9 Ω. As discussed in the section 6.5.1, the current in the output winding is independent from the rotor speed.

The variations in input mechanical power and mechanical torque are depicted in Fig. 6.5.2.5 and 6.5.2.6 respectively. These two variables are slightly higher than in the magnitude when compared with the same results presented in section 6.5.1. However, both the analysis presents the same behaviour of the input mechanical power and mechanical torque with changing rotor speeds.

6.6 Chapter Conclusions

By observing all the results presented in the preceding sections, it is concluded that the developed steady-state model, computational techniques and experimental measurements are accurate. Since the effect of changing each operating parameter on the system variables are known, the characteristics of the novel single-phase induction generator can be understood. Especially, the knowledge of generator characteristics with changing load and rotor speed is important to use it as an off-grid generation plant. Since the mechanical power absorbed by the generator varies with the fluctuations of renewable energy source, the sizing of ESS can be estimated using the obtained results. In general, at the rotor speed higher than 1540 rpm, the generator is capable of supplying load demand without using the battery energy supply. However, when the load demand is low, with the increasing rotor speed, the excitation control winding current will exceed the rated value at the lower capacitance. For the safe operation of the generator, these analyses can be used when designing a small-scale energy conversion system that can be utilized in a renewable energy generation scheme. The designing of the ESS, bi-directional DC-AC inverter, regulating the output voltage and the frequency and analysis of the influence of wind turbine characteristics are presented in the Chapter 7.

CHAPTER 7- ENERGY MANAGEMENT SYSTEM

7.1 Introduction

This chapter presents the design and control of a renewable energy generation system employing the novel single-phase induction generator. The selection of the most suitable characteristics of each component of the energy conversion system is important to improve the quality and the efficiency of the generator scheme in an effective and economically friendly manner. In order to achieve these objectives, the following attempts are made in this chapter.

Due to the intermittent nature of renewable energy sources such as wind and hydro, the generation of electricity using these sources introduces more uncertainties at the output of the generator. Also, due to the varying load demand in the isolated power generation schemes, it becomes a huge challenge to maintain a constant voltage and a constant frequency at the output. Thus, it is necessary to have an energy storage system. The ESS used with the proposed single-phase generator plays a vital role in maintaining the voltage and the frequency constant at the output winding. When the availability of the renewable energy source is high, the additional power generated in the system is stored in the ESS, whereas in other situations where the availability of renewable energy source is low, it supplies the deficit power requirement at the output in order to supply the constant voltage at constant frequency to the consumer load. This ESS should be capable of storing a reasonable amount of energy for the desired operation. Thus, the size of the ESS is highly important if it is to produce the desired output at all the times. However, due to the capital investment required for the installations, ESS should be carefully and specifically designed for a particular generation scheme.

The energy stored in the DC ESS needs to be converted into AC before being supplied to the generator output. On the other hand, the generated AC power needs to be converted into DC before being stored in the BESS. Thus, a bi-directional inverter

which is capable of converting DC to AC and AC to DC should be connected at the terminals of the excitation control winding. Also, this converter should be capable of supplying most of the reactive power requirements of the generator system. Due to the economic factors, the inverters with high power ratings are not appropriate for small scale renewable energy generation schemes. Thus, in this thesis, a bi-directional inverter with low power ratings is designed to to be used with a step-up voltage transformer connected at the AC side.

In selecting the prime mover of the ECS, the power ratings and the speed should match the load demand at the output of the generator. Also, it is necessary to know the gradients of the torque-speed characteristics curves of different types of prime movers in order to decide which types of gradients are suitable for this generator configuration. Thus, in this thesis, the influence of the gradient of torque-speed characteristics curves on the system variables is taken into account when selecting a suitable prime mover for this energy conversion scheme.

In order to generate the constant voltage at constant frequency at the output, a control system needs to be designed for this ECS. As the first step of the design process, the developed dynamic model of the single-phase induction machine in the stationary 'αβ' reference frame (presented in Chapter 3) is used to obtain the equivalent circuit of the generator in synchronous reference frame. In the next step, the transfer function of the ECS is obtained using the developed dynamic equations. In order to develop the feedback control system of the generator scheme, the coefficient of Proportional (P) and Integral (I) terms are calculated using the derived closed-loop transfer function. A comprehensive analysis of the performance of the controlled system is presented later in this chapter.

7.2 Sizing of Battery Energy Storage System

A pack of one or more electrochemical cells is known as a battery. Depending on the weather conditions, the battery will charge or discharge to balance the real power in the renewable energy generation scheme. Prior to sizing the BESS, it is essential to understand the behaviour of a battery during both charge and discharge conditions. The voltage of a battery depends on three factors: current, temperature and the state of charge [149]. In the process of sizing the BESS, it is assumed that they are

operating at the ambient temperature of 25^0C. The voltage and the current are calculated for both the charging and discharging conditions as discussed below.

The energy storage in a battery is typically given in Ampere-hour (Ah) at the nominal voltage and a specified discharge rate. However, a typical battery of the nominal voltage of 48 V will reach the maximum and the minimum values of the voltage of 52 V and 44 V when charging and discharging respectively. The required storage capacity of the battery is calculated for the continuous operation of the ECS during the days or the periods when the availability of the renewable energy supply is extremely low. However, satisfying these conditions increases the size of the ESS than the average requirement throughout the rest of the year [69]. In this study, the storage system is designed to supply the real power at the output of the generator for a continuous three days. The maximum real power absorbs or releases by the ESS depending on the ratings of voltage and current in the excitation control winding. In order to maintain the voltage and current in the same winding below the rated values of the machine, the maximum power supply from the ESS is considered as 1/3 of the rated power of the three phase-induction generator. Since a 3 kW three-phase induction machine is employed for experimental purposes, the maximum power supplied by the ESS is considered as 1 kW.

The maximum energy supplied by the inverter to the generator system during a day can be calculated as [150]

$$Energy\ supplied\ by\ inverter = 1\ kW * 24\ h \tag{7.2.1}$$

If the total efficiency of the inverter and the step-up voltage transformer is 80 %, the DC power required from the battery can be given as [150]

$$DC\ power\ required\ from\ battery = \frac{Energy\ supplied\ by\ inverter}{Efficiency\ of\ the\ inverter\ system} = \frac{24\ kWh}{80\ \%} \tag{7.2.2}$$

Considering the nominal voltage of the battery is 48 V, the DC power required from the battery can be given in the unit of ampere-hour as in (7.2.3) [150].

$$DC\ power\ required\ from\ battery\ (Ah) = \frac{24\ kWh}{80\ \%} * \frac{1}{48\ V} \tag{7.2.3}$$

The battery is required to supply the load demand for a continuous three days. Thus, the usable storage of the BESS can be calculated as (7.2.4) [150].

$$Usable\ Storage = DC\ power\ required\ from\ battery\ (Ah) * number\ of\ days = \frac{24\ kWh}{80\ \%} * \frac{1}{48\ V} * 3\ days \quad (7.2.4)$$

Discharging a battery below the minimum allowable value of the capacity will reduce its life time or destroy the battery. Therefore, the maximum allowable depth of discharge (DOD) is a crucial factor to be considered when sizing the BESS. Assuming the maximum allowable DOD is 80% and allowing 10% of additional daily energy consumption due to expose to a different temperature and the battery losses, the capacity of the BESS can be calculated using (7.2.5) as [150]

$$Battery\ Capacity = \frac{24\ kWh * 3\ days * 1.1}{80\ \% * 48\ V * 80\ \%} = 2578.1\ Ah \quad (7.2.5)$$

The rate of discharge can be obtained by the ratio of the Ampere-hour capacity and the period of discharging time. Thus, the current delivered during the discharging period can be calculated by (7.2.6).

$$Discharging\ Current = \frac{Battery\ Capacity\ in\ Ampere{-}hour}{Period\ of\ discharge} \quad (7.2.6)$$

The current delivered over a period of one hour using a 48 V, 2578.1 Ah of proposed ESS is calculated as

$$I_d = \frac{2578.1\ Ah}{3{*}24\ h} = 35.8\ A \quad (7.2.7)$$

Since, in a practical system, the charging losses will be 40% of the capacity of the battery, the total storage capacity is equal to

$$Storage\ Capacity = Battery\ Capacity * 1.4 = 2578.1\ Ah * 1.4 = 3609.3\ Ah \quad (7.2.8)$$

Thus, the rate of charge can be defined as the ratio of storage capacity and discharging current. Thus, the rate of charge of the ESS can be calculated by

$$Rate\ of\ Charge = \frac{Storage\ Capacity\ in\ Ampere{-}hour}{Discharging\ Current} \quad (7.2.9)$$

Substituting from (7.2.7) and (7.2.8), the rate of charge (h) is calculated as

$$h = \frac{3609.3\ Ah}{35.8\ A} = 100.8\ h \tag{7.2.10}$$

The discharge behaviour of the BESS for the rate of C/72 is illustrated in Fig. 7.2.1. The voltage characteristics during the battery discharge can be interpolated using 4th order polynomials as (7.2.11).

$$V = -0.000000000002955 * C^4 + 0.000000010763329 * C^3 - 0.000011550589997 * C^2 + 0.001664197768521 * C + 49.926193118722011 \tag{7.2.11}$$

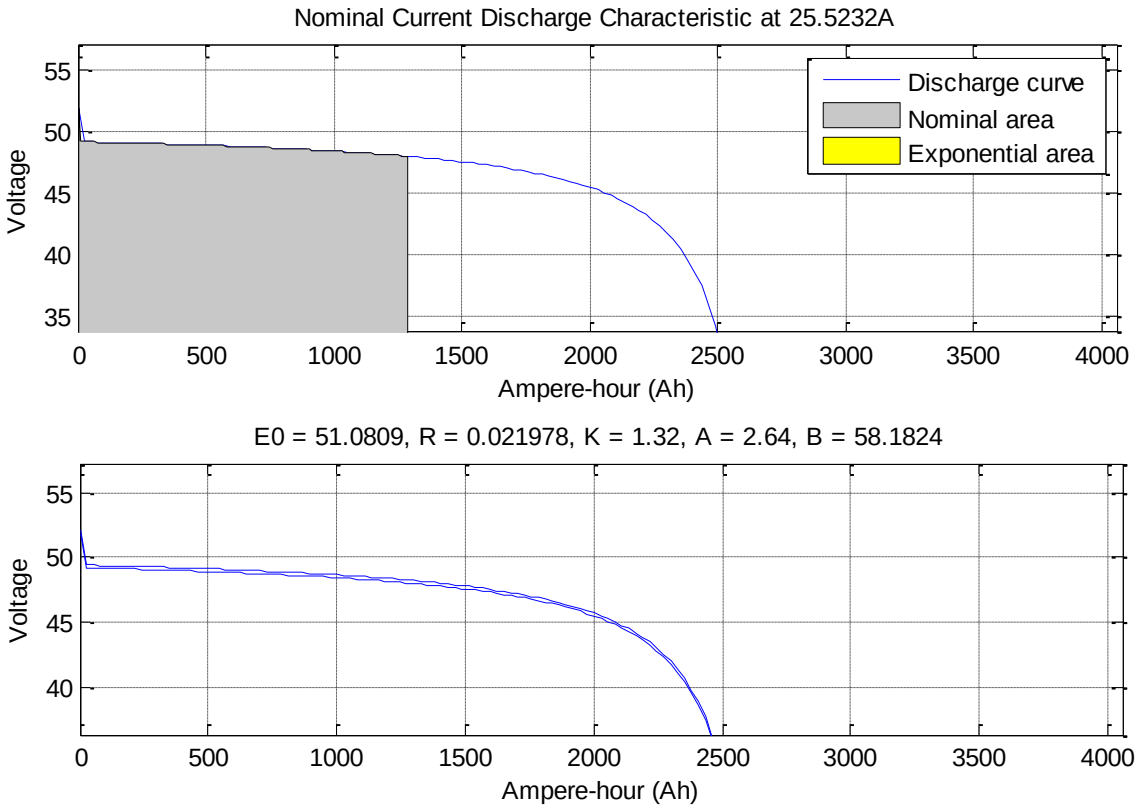

Fig. 7.2.1 Discharging characteristics of the ESS

7.3 Design of Bi-directional DC-AC inverter

During the discharging mode of the BESS, the DC current should be converted to sinusoidal AC current in order to comply with the generator regulations. Similarly, during the charging mode of the BESS, the sinusoidal AC current supplied by the

generator system needs to be converted into DC in order to store it in the batteries. Thus, a converter which is capable of functioning in both directions should be employed in the excitation control winding of the single-phase induction generator. The general topology of a bi-directional inverter is depicted in Fig. 7.3.1.

In addition to the function of the bi-directional inversion, there are several important factors to be considered when designing a converter circuit. Since the ideal circuits do not exist in the real world, the output power is less than the input of the converter circuit. Thus, the efficiency of the proposed bi-directional inverter is a crucial factor to be taken into account when designing the converter circuit.

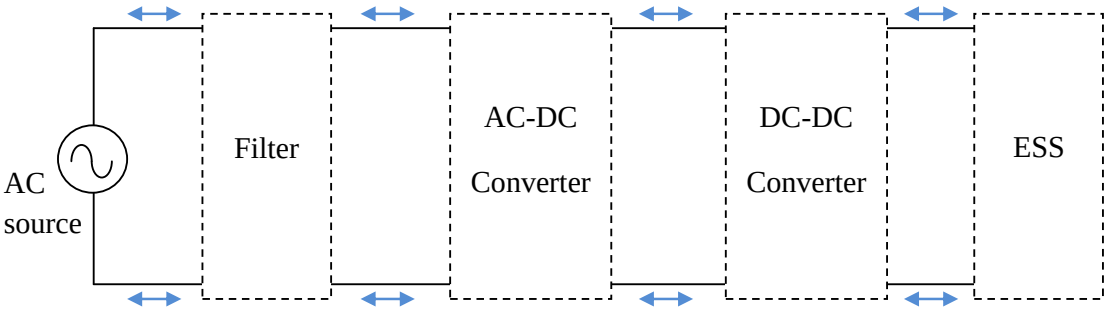

Fig. 7.3.1. General topology of the bi-directional conversion process

During the AC-DC conversion, it is not realistic to obtain an ideal DC output. Output will contain the ripple of the AC source. Thus, the ripple of the DC output is one of the most important factors to be considered. Similarly, during DC-AC conversion, if an inappropriate filter is selected at the AC side of the converter, the total harmonic distortion (THD) of the output AC signal will be increased. The sizing of the filter capacitors is essential when designing the converter circuit. During both the charging and the discharging process of the BESS, the DC voltage across the batteries will vary with the time. As discussed in section 7.2, it is essential to maintain the maximum and the minimum voltage at all the time to ensure the years of safe operation of the batteries. Therefore, the regulation of the ESS is another important factor to be taken into account. In addition to these operational factors, several external factors must be considered when designing the bi-directional inverter of the ECS. Size, weight and cost are the major physical characteristics of the converter that should be included in the designing process. In addition, the reliability of the

converter system is more important for the continuous operation of a renewable energy generation scheme.

In order to step up and down the converter voltage during DC-AC and AC-DC conversion, the boost and buck converters can be employed as the DC-DC converters of the conversion process respectively. However, these converters cannot provide the bi-directional power flow required by this ECS [151]. A comprehensive review of different types of converters is given in [93]. In order to design a converter circuit based on the operational and the physical characteristics discussed above, the DC-DC converter circuit is replaced by a filter capacitor connected at the DC side and step-up voltage transformer connected at the AC side of the converter. Among the AC-DC converter topologies i.e. half-bridge PWM AC-DC converter, full-bridge PWM AC-DC converter and three-level PWM AC-DC converter, the second type of the converter system is selected for the proposed ECS. The schematic diagram of the bi-directional AC-DC converter is illustrated in Fig. 7.3.2.

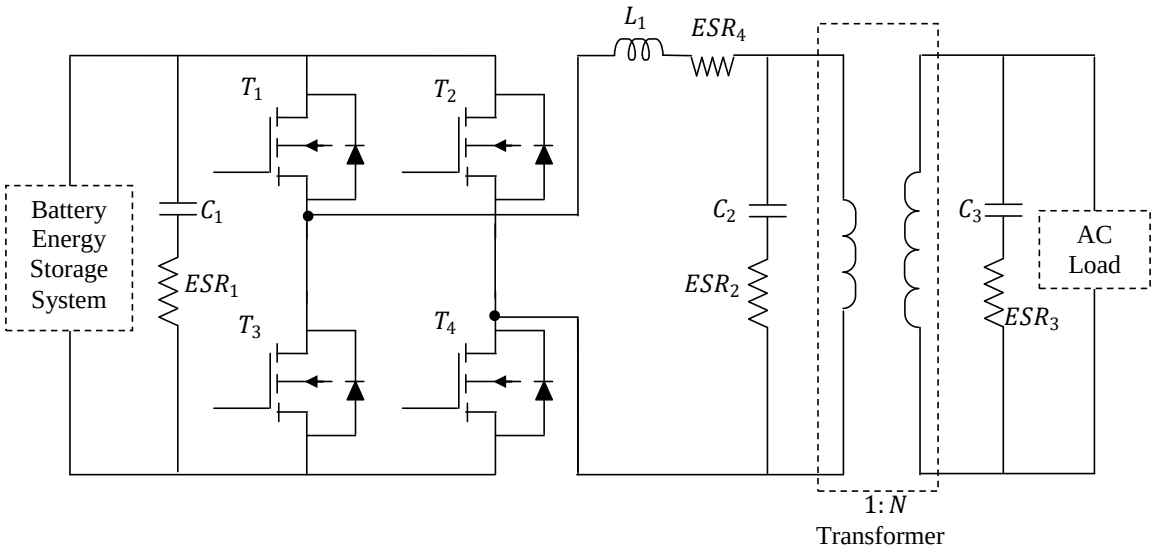

Fig. 7.3.2. Application of full-bridge PWM bi-directional single-phase AC-DC converter in the renewable ECS

When the bi-directional converter operates as an inverter, the combination of the transistors T1 and T4 or T2 and T3 is turned on to apply the DC voltages as a sinusoidal voltage across the AC side of the converter. If the DC voltage is considered as V_{dc}, when T1 and T4 are turned on, the voltage at the AC side will be $+V_{dc}$. On the other hand, when T2 and T3 are turned on, the voltage at the AC side

will be $-V_{dc}$. This output waveform is boosted by the turns ratio of the transformer. Using the inductive and resistive components connected at the ac side, the output waveform is smoothed out to form the desired sin wave.

During the rectifier mode of operation of the bi-directional converter, internal diodes are forward biased to circulate the current through the rectifier circuit. If the amplitude of the sinusoidal AC voltage is considered as V_{ac}, this voltage is stepped down by the turns ratio of the transformer connected at the AC side of the converter. At the positive half cycle of the sinusoidal voltage, internal diodes of transistors T1 and T4 forward bias and generate the voltage of $+V_{ac}$' across the capacitor parallel to the ESS. Similarly, at the negative half cycle of the AC voltage, internal diodes of transistors T2 and T3 become forward biased and generate the same voltage across the capacitor.

Using the PWM control of each transistor, the desired output can be obtained. The inverter and the rectifier mode of operations of the bi-directional converter are illustrated in Fig. 7.3.3 and 7.3.4 respectively.

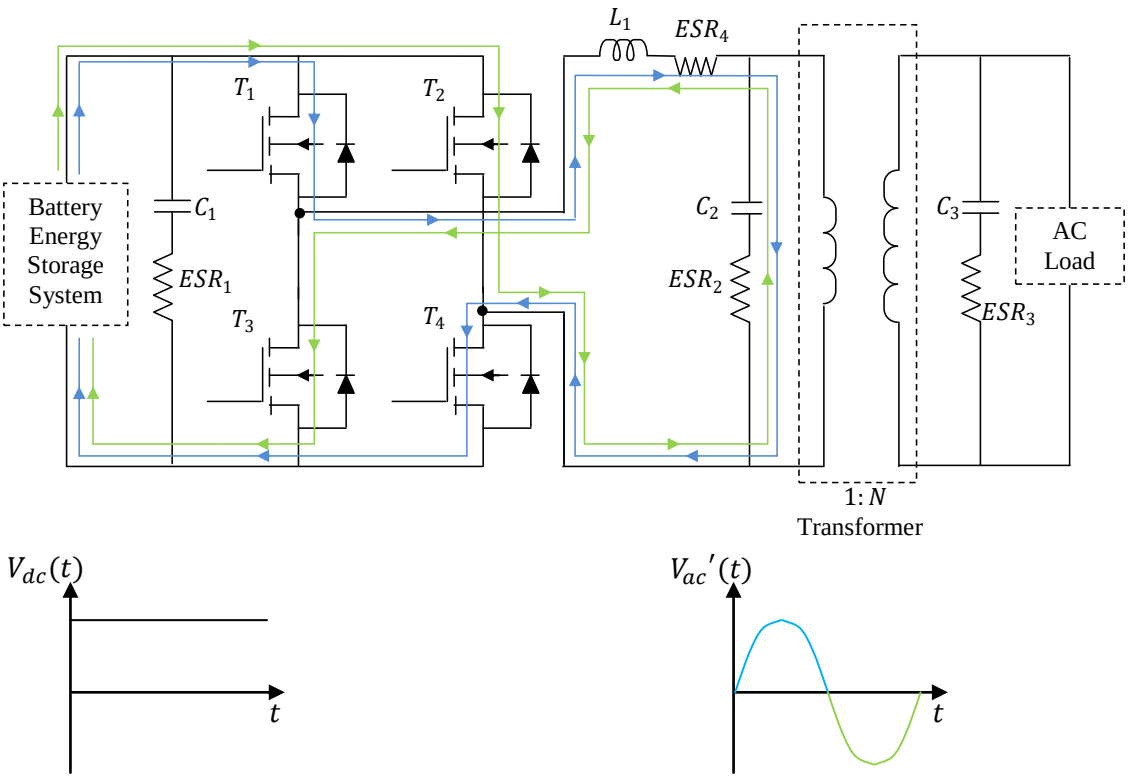

Fig. 7.3.3. Inverter mode of operation

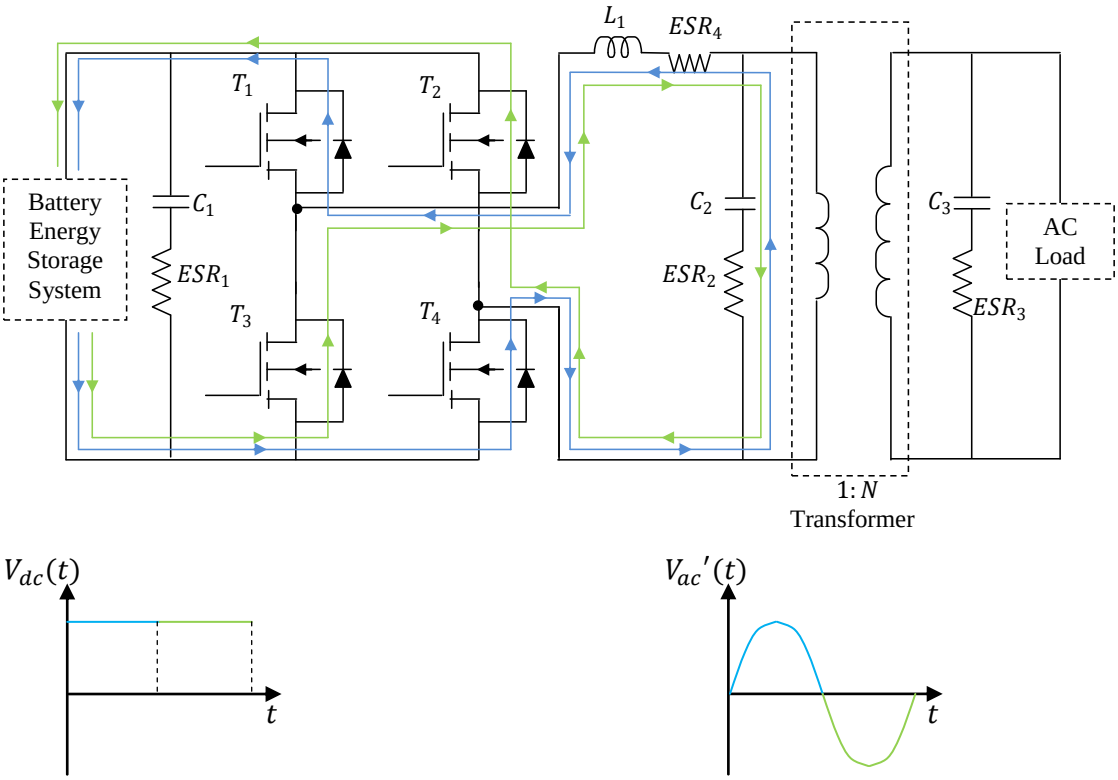

Fig. 7.3.4. Rectifier mode of operation

The power delivered or absorbed by the ESS at point A in Fig. 7.3.5 can be written as,

$$VA_{ESS} = DC\ Voltage * DC\ Current = V_{DC} I_{DC} \tag{7.3.1}$$

Using (7.2.3) and the rated voltage of the battery, power at point A can be calculated as,

$$VA_{ESS} = 48\ V * \frac{24\ kWh}{80\%} * \frac{1}{48\ V} * \frac{1}{24\ h} = 1250.0\ VA \tag{7.3.2}$$

If the modulation index m_a and the efficiency of the bi-directional inverter are given, the peak amplitude of the voltage at the AC side of the inverter can be written as (7.3.3).

$$V_{\_C} = m_a * DC\ Voltage \tag{7.3.3}$$

Assuming the efficiency of the bi-directional inverter is as 95 %, the power at point C can be calculated using (7.3.2) as

$$VA_{\_C} = \eta_{inv} * VA_{ESS} = 0.95 * 1250.0\ VA \tag{7.3.4}$$

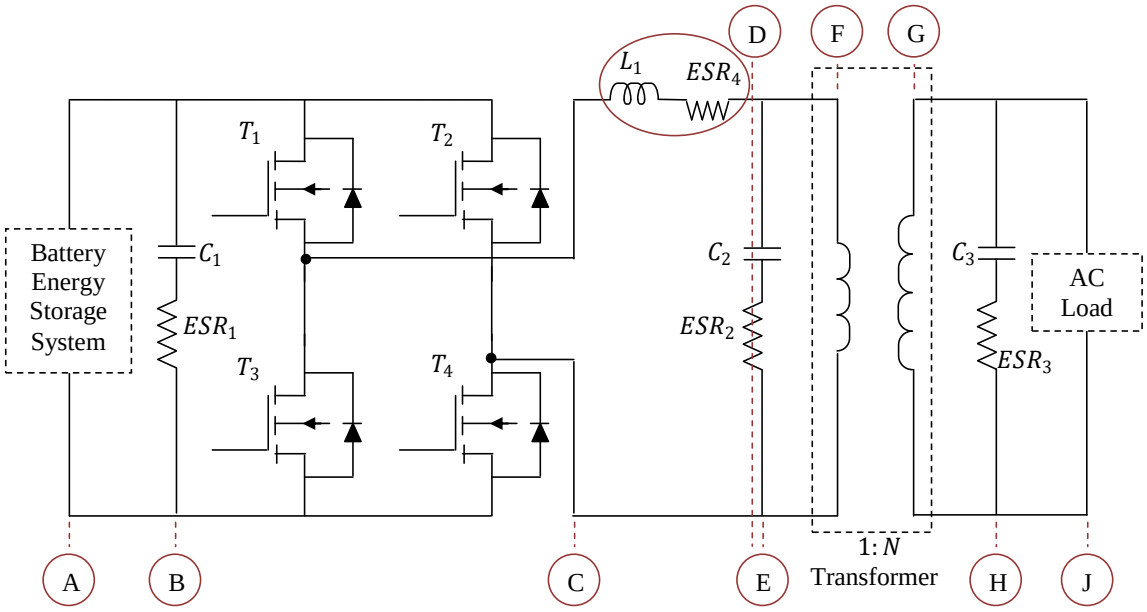

Fig. 7.3.5 Bi-directional AC/DC converter

In general, the size of the inductor L_1 is selected to consume 5% of the power delivered by the inverter. Thus, the power in the inductor can be given as

$$VA_{\_L1} = \eta_{inv} * VA_{ESS} * 0.05 = 0.95 * 1250.0 * 0.05\ VA \tag{7.3.5}$$

In this design, the inductor L_1 is selected to achieve the unity power factor at the secondary winding of the transformer. Considering the turns ratio of the transformer as 1:N, the voltage and current at point F can be defined as (7.3.6) and (7.3.7) respectively.

$$V_{\_F} = V_{se}\ \cos \omega_1 t\ /\ N \tag{7.3.6}$$

$$i_{\_F} = N * I_{se}\ \cos \omega_1 t \tag{7.3.7}$$

where ω_1 is the angular frequency of the voltage and current at the generator output.

The power at point F can be given as

$$VA_{\_F} = \frac{V_{se}I_{se}}{2} + \frac{V_{se}I_{se}}{2} \cos 2\omega_1 t \tag{7.3.8}$$

Assuming 15 % losses in the transformer windings and the filter, the power at point C can be written using (7.3.8) as,

$$VA_{\_C} = \frac{V_{se}I_{se}}{2*0.85} + \frac{V_{se}I_{se}}{2*0.85}\cos 2\omega_1 t \tag{7.3.9}$$

Substituting from (7.3.1) and (7.3.5), the current in the BESS can be defined as a sum of DC and AC components as given in (7.3.10).

$$I_{DC} = I_{DC} + I_{DC}\cos 2\omega_1 t = (I_{DC})_{DC} + (I_{DC})_{ac} \tag{7.3.10}$$

The capacitor C_1 can be selected to smooth out the ripple of the DC current produced during the rectifying process of the converter. ESR_1 is the equivalent series resistance of the selected capacitors.

Considering the switching frequency and the cut-off frequency are 12 kHz and ω_c respectively, the filter capacitor C_2 can be defined to achieve the relationship in (7.3.11).

$$\omega_c = \frac{1}{\sqrt{L_1 C_2}} \tag{7.3.11}$$

Using the calculated currents and voltages, the turns ratio of the transformer to deliver the desired voltage can be determined. Thus, the size of the required transformer can be selected.

The capacitor C_3 connected in parallel with the secondary side of the step-up transformer delivers most of the reactive power requirement of the single-phase induction generator. The maximum power absorbed or supplied by the excitation control winding is equal to the per-phase rated power of the three-phase induction machine at the rated current. Thus, the maximum reactive power to be supplied by the capacitor C_3 can be calculated as

$$Q_{C3} = \left((V_{se}I_{se})^2 - {P_{ph\_rated}}^2\right)^{1/2} \tag{7.3.13}$$

The minimum capacitance required to deliver the reactive power at the rated conditions can be determined by

$$C_3 = \frac{Q_{C3}}{\omega_1 {V_{se}}^2} \tag{7.3.14}$$

The system specifications of the proposed bi-directional AC/DC converter are given in Table 7.3.1.

Table 7.3.1
System specification of the bi-directional AC/DC converter

Property		Value
AC Side	$v_{ac}(rms)$	230/√3 V (rated) $v_{ac} \leq$ 230 V
	$i_{ac}(rms)$	$i_{ac} \leq$ 6.4 A
	P_{ac_phase}	1000 W
	frequency	50 Hz
DC Side	V_{dc}	48 V (rated) 44 V $\leq V_{dc} \leq$ 52 V

Assuming the converter power factor is 0.98, power, voltage and current at each point of the bi-directional AC/DC converter are calculated using the aforementioned methods and shown in Table 7.3.2. In order to select the same ratio between the currents and voltages in primary and secondary windings of the transformer, the power factor of the excitation control winding is considered as 0.8034.

Table 7.3.2
Calculated power, voltage and current at each point of the bi-directional AC/DC converter

Point	Parameter				
	Power (VA)	Active Power (W)	Reactive Power (VAr)	Voltage (V)	Current (A)
A	1250.0	-	-	48.0	26.0
B	1250.0	-	-	48.0	26.0
C	1187.5	1161.3	235.8	32.2∠0	36.8∠-0.2003
L_1	59.4	13.5	57.3	1.6∠1.140	36.8∠-0.2003
D	1161.5	1149.1	178.7	31.6∠-0.046	36.8∠-0.2003
E	9.5	-0.00003	-9.5	31.6∠-0.046	0.30∠1.5248
After E	1162.9	1147.6	187.9	31.6∠-0.046	36.8∠-0.2083
F	1012.8	1012.8	0.0	27.9∠-0.046	36.3 ∠-0.046
G	1012.8	1012.8	0.0	195.1∠-0.046	5.19 ∠-0.046
H	741.4	12.5	-741.2	195.1∠-0.046	3.8 ∠1.5079
J	1244.7	1000.0	741.2	195.1∠-0.046	6.38∠-0.6838

The simulation parameters of the bi-directional AC/DC converter are listed in Table 7.3.3. At the frequencies of 10 kHz to 20 kHz, the ripple current factor of a capacitor of 3900 μF is 1.2 at 100V. The ripple current rating of the capacitor is given as 5400 mA. Thus, at 12 kHz, each capacitor can handle the current of 1.2 x 5400mA = 6.48 A. In order to smooth the ripple current of 26 A, four capacitors with above ratings are needed to connect in parallel with the BESS.

Table 7.3.3
Simulation parameters of the bi-directional AC/DC converter

Parameter	Value
Ripple current factor at 10-50 kHz	1.15
C_1	3900 μF *4
ESR_1	0.045 * 4
Modulation Index m_a	0.95
L_1	135.9 μH
ESR_4	0.01 Ω
C_2	30 μF
ESR_2	0.06 Ω
Cut-off frequency ω_c	15661 rad/s
Turns Ratio 1:N	1:7
C_3	62.0 μF
ESR_3	0.7 Ω

The required values of the transformer parameters to achieve the predicted results are given in Table 7.3.4.

Table 7.3.4
Transformer parameters

Parameter	Primary Winding	Secondary Winding
Winding resistance (Ω)	0.05	2.45
Winding Inductance (H)	2.55×10^{-5}	1.25×10^{-3}
Core resistance (Ω)	1348.5	
Magnetizing Inductance (H)	0.0146	

7.4 Wind Turbine Characteristics

Small-scale wind turbines are generally rated at 10 kW or less. When a consistent wind flow is available throughout the day, a 10 kW wind turbine generates 25000 kWh while a 3 kW wind turbine generates 9000 kWh per year. Thus, it is important to select an appropriate size of prime mover for the continuous operation of the wind energy generation system. Figure 7.4.1 shows the estimated annual power generation of different wind turbines with different wind speeds [152]. The generator employed in the wind energy generator scheme described in this thesis consumes the maximum real power of 2 kW. Therefore, the required energy generation can be calculated as

$$Required\ energy\ generation\ =\ 2\ kW * 24h * 365days\ =$$
$$17520\ kWh\ per\ year \tag{7.4.1}$$

However, the load demand may vary from time to time. The additional amount of power supplied by the prime mover is stored as DC power in the batteries connected at the excitation control winding. Therefore, a portion of the annual energy requirement can be supplied by the BESS. In order to achieve the estimated energy requirement of a year, a wind turbine with the power ratings of 5 kW or more is required at the generation site.

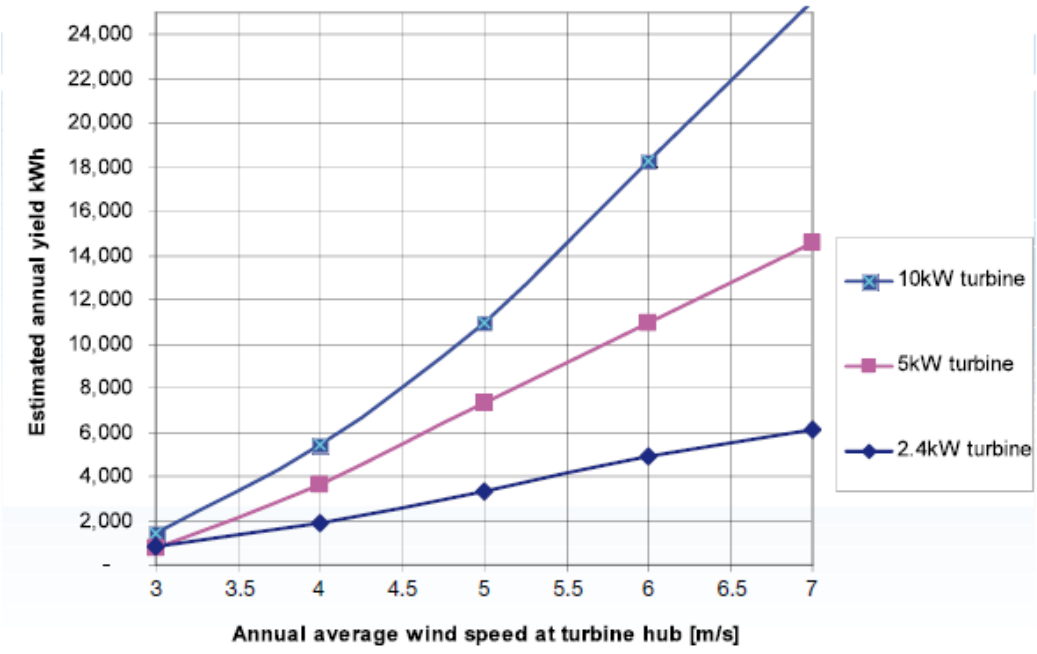

Fig. 7.4.1 Estimated energy generation with annual average wind speed

The annual average wind speed in the country varies according to the location. Rural areas, hilltops, coastal line and tall buildings in the city can capture strong wind resources. Before building the wind generation scheme, the wind patterns in the selected locations have to be monitored to determine the confidence in the turbine's performance. When the turbine speed is high enough to overcome the friction, it will start to produce the power. This start-up wind speed is usually below 3 m/s. Therefore, the annual average wind speed at the selected location should be at least 4 m/s. The annual average wind speed at 9 am and 3 pm at a selected location is depicted in Fig. 7.4.2 and 7.4.3 respectively [153]. At 9 am, the annual average wind speed varies between 4.7 m/s and 6.1 m/s, whereas at 3 pm this variation is between 5.3 m/s and 8.3 m/s.

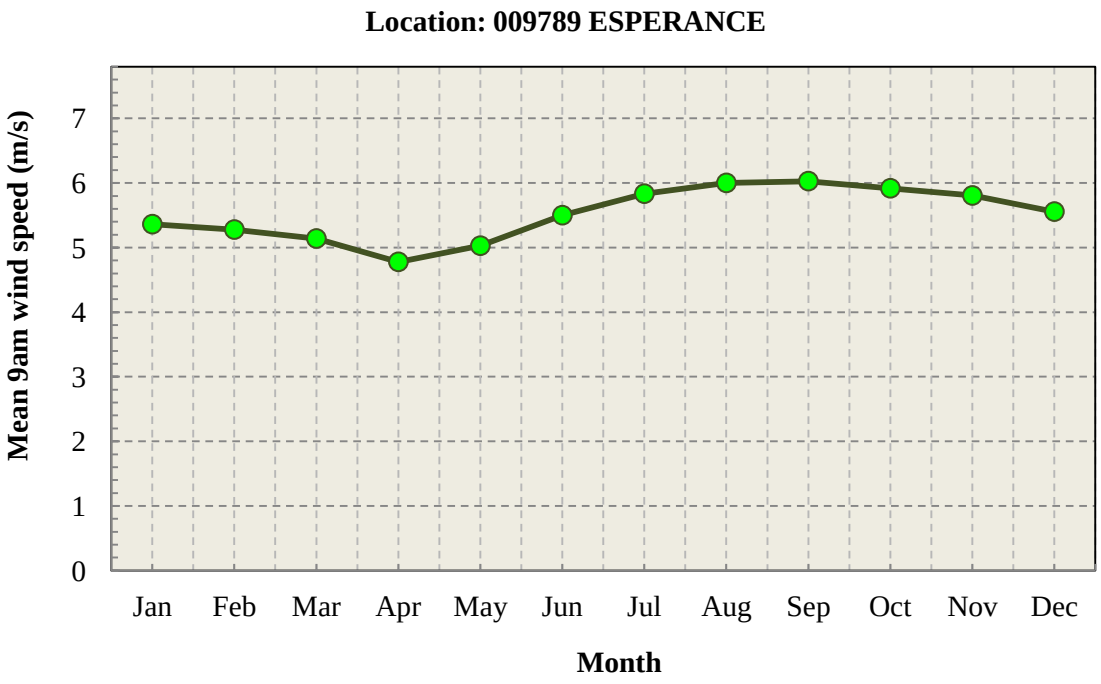

Fig. 7.4.2 Annual average wind speed at 9 am

In this thesis, a 5 kW vertical axis wind turbine with the specifications given in Table 7.4.1 is selected as the suitable prime mover of the renewable energy generation scheme. The turbine starts to generate the power at the start-up wind speed of 1.5 m/s. The maximum rotating speed of the turbine is limited to 260 rpm even at the wind speeds of 30 m/s or 40 m/s. The power curve of the wind turbine with different wind speeds is illustrated in Fig. 7.4.4. This turbine generates power of 2 kW at the

wind speed of 7.5 m/s. At the wind speeds below 7.5 m/s, the wind turbine is not able to produce the required power at the generator output. However, if installed at the given location, this turbine will generate more power than required at the output.

In addition to the size, the maintenance requirement and its safety ratings have to be considered when selecting a wind turbine. Also, the noise of the turbine is crucial if it is going to be located in a metropolitan area. An acceptable clearance has to be maintained from the residential areas.

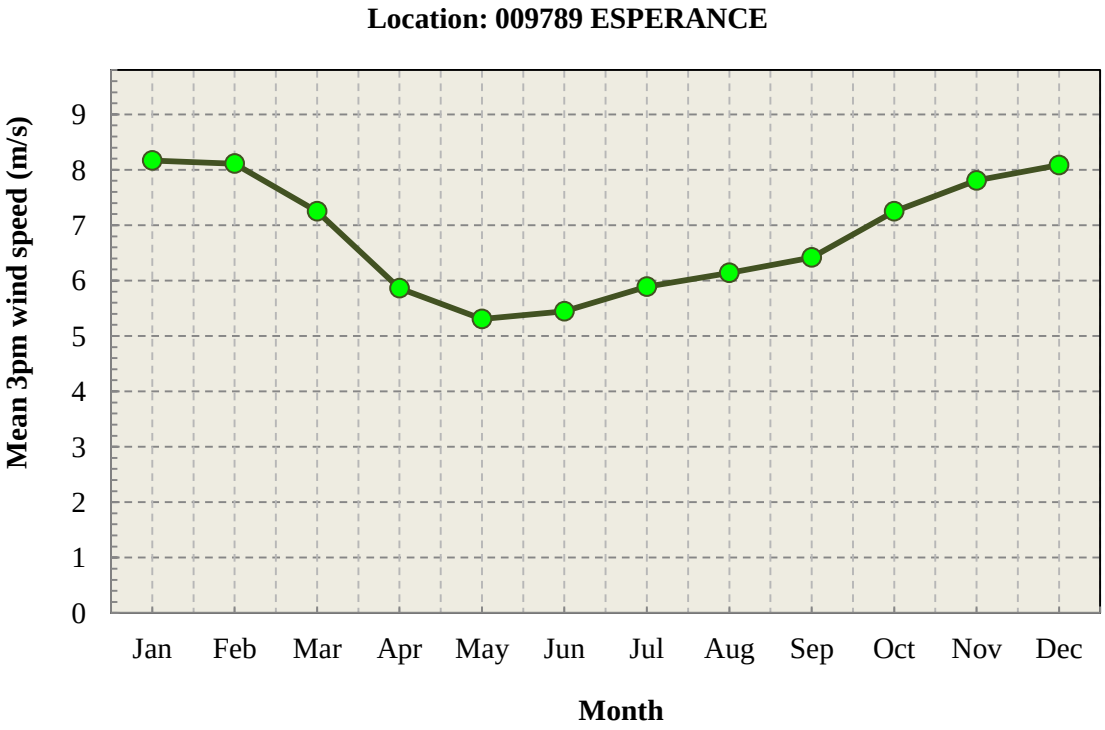

Fig. 7.4.3 Annual average wind speed at 3 pm

Table 7.4.1
Technical specification of 5 kW H-type vertical axis wind turbine

Rated Power	5 kW
Maximum Output Power	6 kW
Rotor Height	3.6 m
Rotor Diameter	3.0 m
Number of blades	3
Start-up Wind Speed	1.5 m/s
Rated Wind Speed	10 m/s
Survival Wind Speed	50 m/s

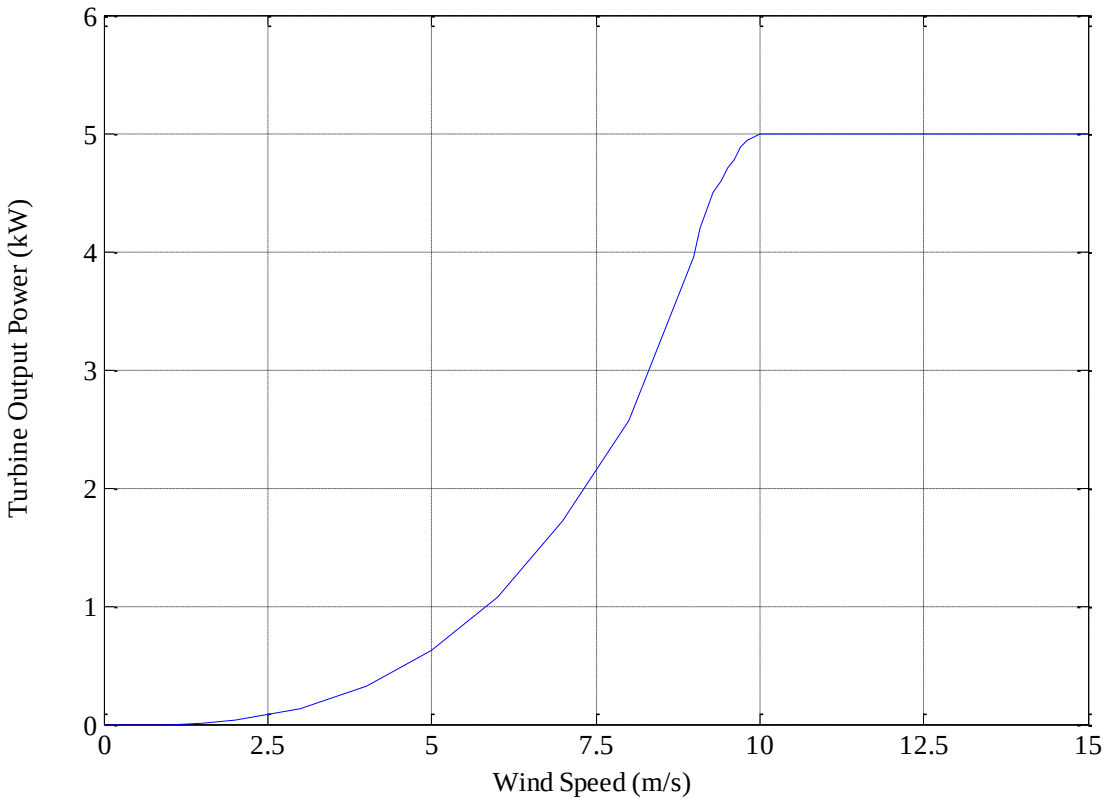

Fig. 7.4.4 Power curve of wind turbine with the different wind speeds

The power extracted from the wind by the prime mover depends on the power coefficient of the turbine. Thus, a wind turbine can be characterized by curve of power coefficient to tip-speed ratio. The tip-speed ratio can be defined as

$$Tip\ Speed\ Ratio\ (\lambda) = \frac{\omega_t * R_t}{V_w} \tag{7.4.2}$$

The power coefficient is expressed by various approximations. In this thesis, the power coefficient $C_p(\lambda)$ to tip-speed ratio of the selected wind turbine is approximated by a 5^{th} order polynomial given in (7.4.3).

$$C_p(\lambda) = 0.02632\,\lambda^5 - 0.12066\,\lambda^4 + 0.05119\,\lambda^3 + 0.18314\,\lambda^2 + 0.05241\,\lambda - 0.00022 \tag{7.4.3}$$

The resulting curve fit polynomial is shown in Fig. 7.4.5.

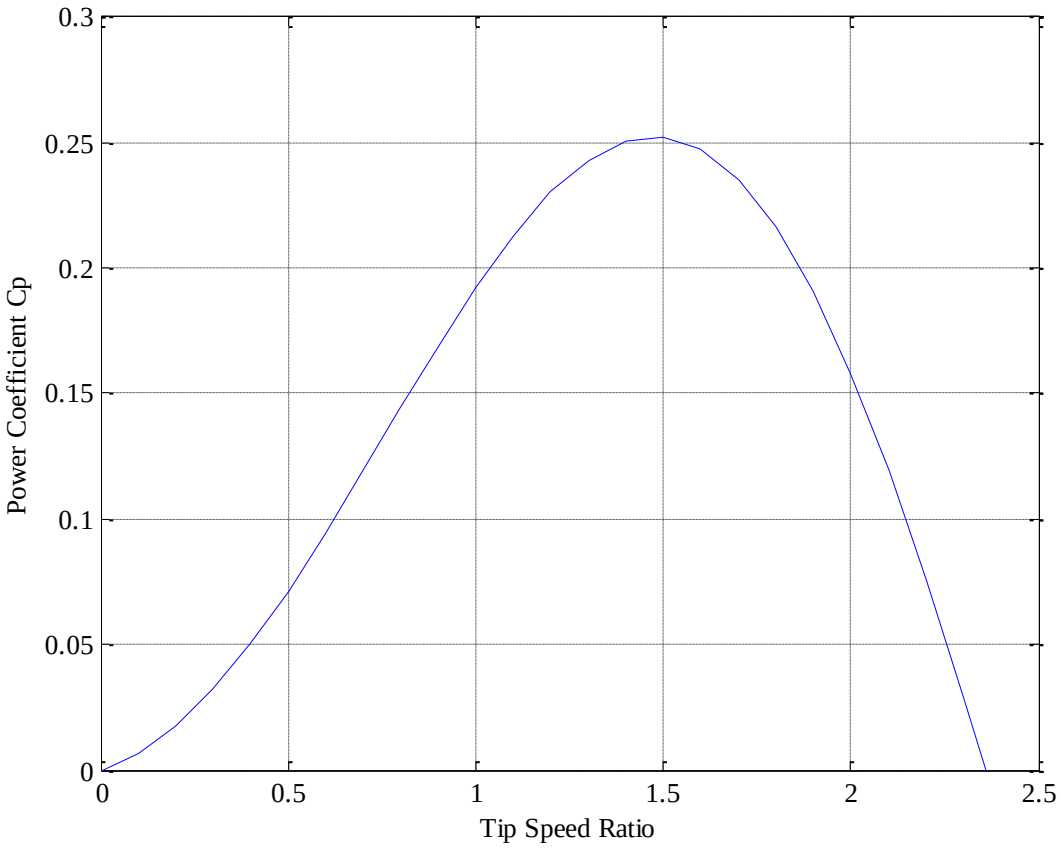

Fig. 7.4.5 Power coefficient verses tip-speed ratio

The mechanical power of a wind turbine as a function of power coefficient can be given by

$$P_T = \frac{1}{2}\,\rho . A_t . {V_w}^3 . C_p(\lambda) \tag{7.4.4}$$

When the turbine rotates at the speed of ω_t, the mechanical torque of the turbine is defined as

$$T_T = \frac{1}{2}\,\rho . R_t . A_t . {V_w}^2 . C_t(\lambda) \tag{7.4.5}$$

The torque coefficient $C_t(\lambda)$ is given as

$$C_t(\lambda) = \frac{C_p(\lambda)}{\lambda} \tag{7.4.6}$$

After applying the gear ratio of 1:23 in between the wind turbine and the generator, the variations of the mechanical torque with the rotational speed at different wind speeds are depicted in Fig. 7.4.6.

Considering the wind turbine is operated on after peak region of the torque-speed characteristics curve, both the electromagnetic torque and the mechanical torque can

be plotted in the same graph as in Fig. 7.4.7. The operating speed of the generator can be obtained at the intersecting point of these two curves.

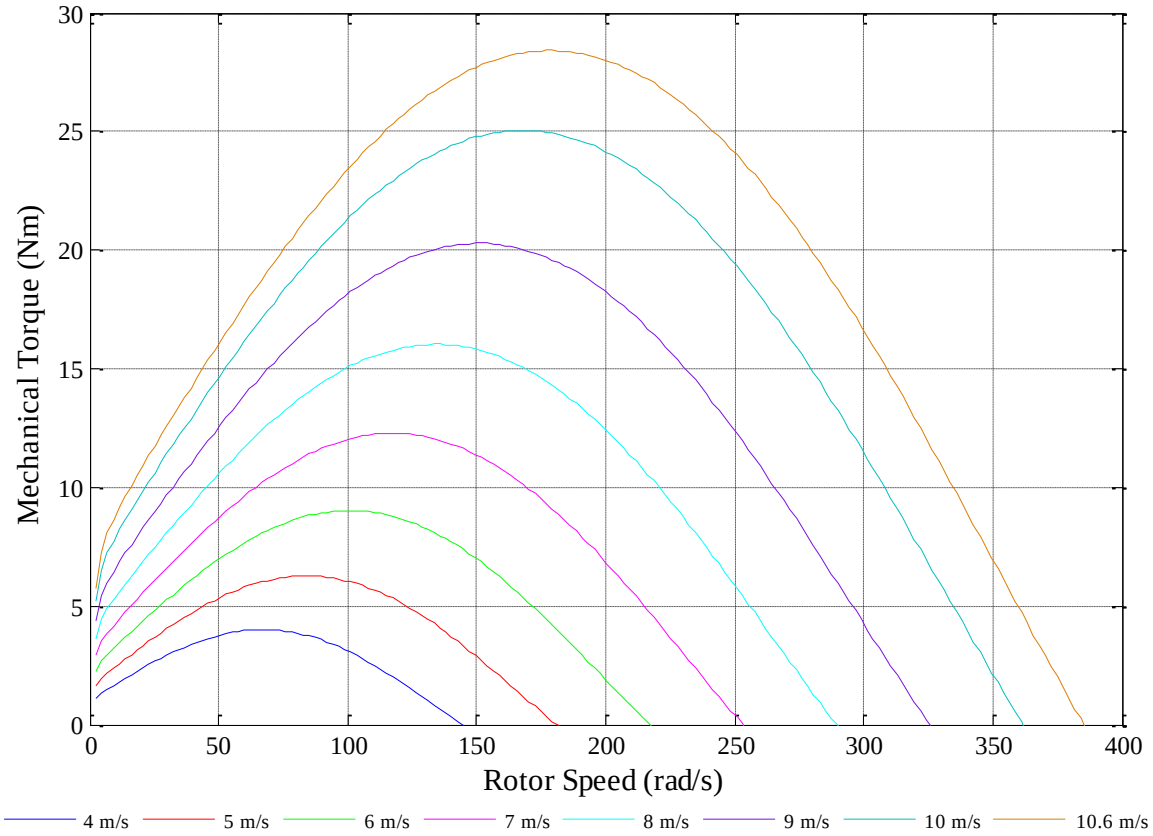

Fig. 7.4.6 Mechanical torque-speed characteristics curves at different wind speeds

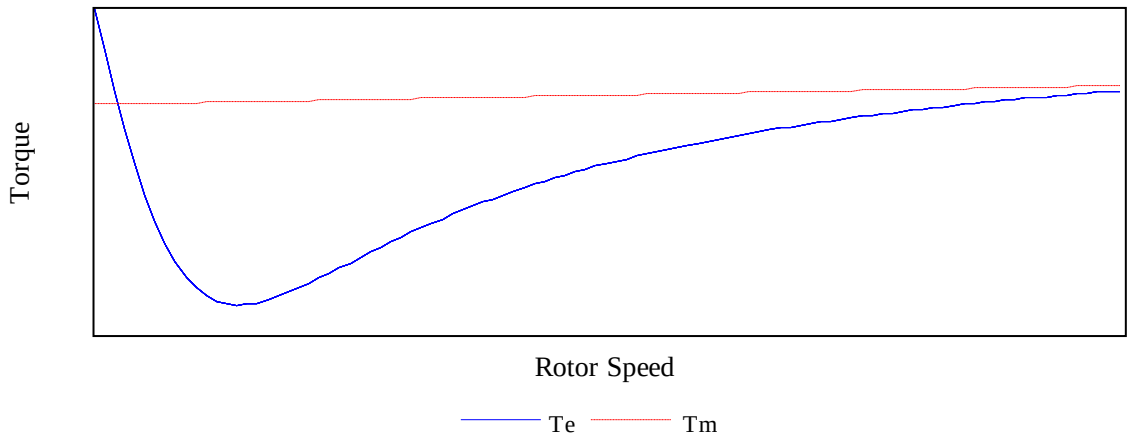

Fig. 7.4.7 Electromagnetic and mechanical torque speed characteristics curves

The variations of output power of the wind turbine with changing rotor speeds are shown in Fig. 7.4.8 for the different sets of wind speeds.

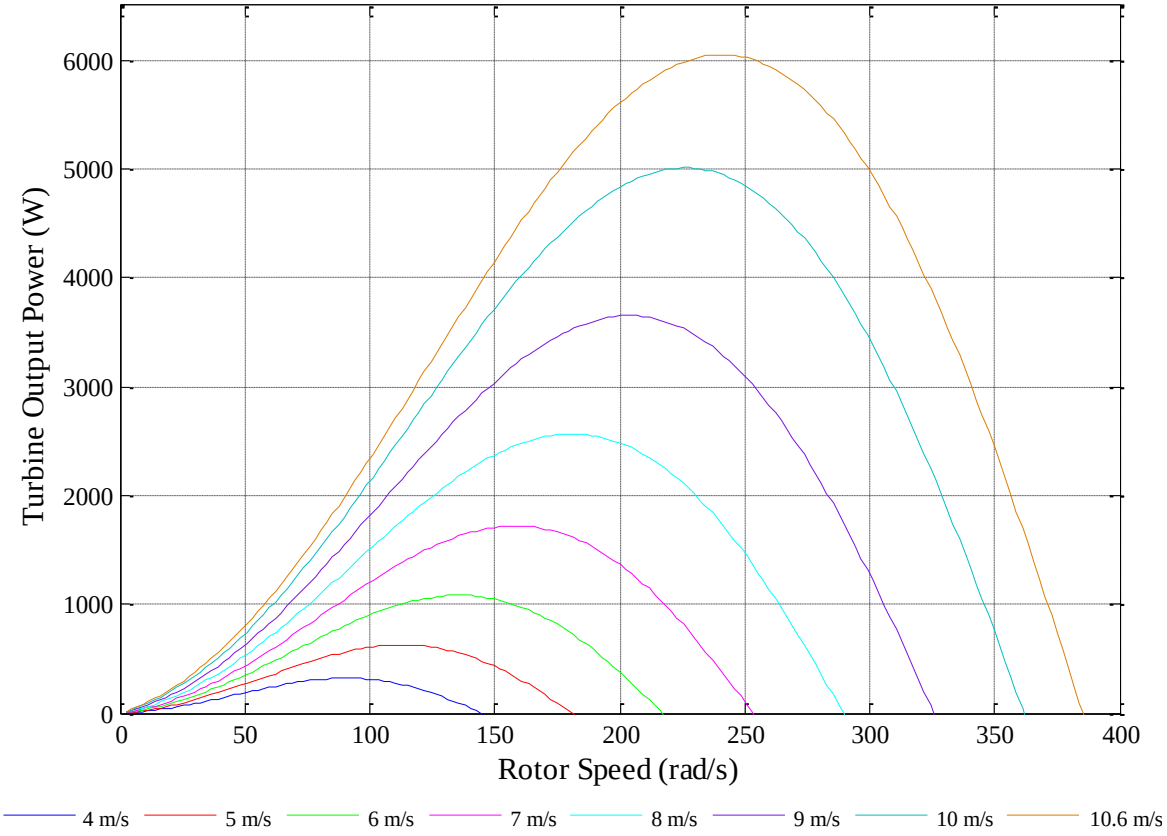

Fig. 7.4.8 Mechanical power verses rotor speed

7.5 Equivalent Circuit of Single-Phase Generator in Synchronous Reference Frame

Using (3.3.4) and (3.3.5), the voltage equations of stator and rotor in the stationary 'αβ' reference frame can be re-written as (7.5.1) and (7.5.2) respectively.

$$\begin{bmatrix} V_{se} \\ V_{so} \end{bmatrix} = R_s \begin{bmatrix} 1 & 0 \\ 0 & 2 \end{bmatrix} \begin{bmatrix} i_{se} \\ i_{so} \end{bmatrix} + L_{ls} \begin{bmatrix} 1 & 0 \\ 0 & 2 \end{bmatrix} \frac{d}{dt} \begin{bmatrix} i_{se} \\ i_{so} \end{bmatrix} + L_{ms} \begin{bmatrix} 1 & 0 \\ 0 & 3 \end{bmatrix} \frac{d}{dt} \begin{bmatrix} i_{mse} \\ i_{mso} \end{bmatrix} + L_{ms} \begin{bmatrix} \frac{3}{2} & 0 \\ 0 & \frac{3\sqrt{3}}{2} \end{bmatrix} \frac{d}{dt} \begin{bmatrix} i_{mr\alpha} \\ i_{mr\beta} \end{bmatrix} \tag{7.5.1}$$

$$\begin{bmatrix} 0 \\ 0 \end{bmatrix} =$$

$$R_r \begin{bmatrix} i_{r\alpha} \\ i_{r\beta} \end{bmatrix} + L_{lr} \frac{d}{dt} \begin{bmatrix} i_{r\alpha} \\ i_{r\beta} \end{bmatrix} + \omega_r L_{lr} \begin{bmatrix} 0 & 1 \\ -1 & 0 \end{bmatrix} \begin{bmatrix} i_{r\alpha} \\ i_{r\beta} \end{bmatrix} + \frac{3}{2} L_{ms} \frac{d}{dt} \begin{bmatrix} i_{mr\alpha} \\ i_{mr\beta} \end{bmatrix} + \frac{3}{2} \omega_r L_{ms} \begin{bmatrix} 0 & 1 \\ -1 & 0 \end{bmatrix} \begin{bmatrix} i_{mr\alpha} \\ i_{mr\beta} \end{bmatrix} +$$

$$L_{ms} \begin{bmatrix} 1 & 0 \\ 0 & \sqrt{3} \end{bmatrix} \frac{d}{dt} \begin{bmatrix} i_{mse} \\ i_{mso} \end{bmatrix} + \omega_r L_{ms} \begin{bmatrix} 0 & \sqrt{3} \\ -1 & 0 \end{bmatrix} \begin{bmatrix} i_{mse} \\ i_{mso} \end{bmatrix} \tag{7.5.2}$$

In order to develop these dynamic equations in the synchronous reference frame, first, an arbitrary reference frame is introduced such that the d-axis is leading the α-axis by angle 'δ' and q-axis is leading the d-axis by 90 degree. It is assumed that the arbitrary reference frame is rotating at a speed of ω_x. This transformation is illustrated in Fig. 7.5.1.

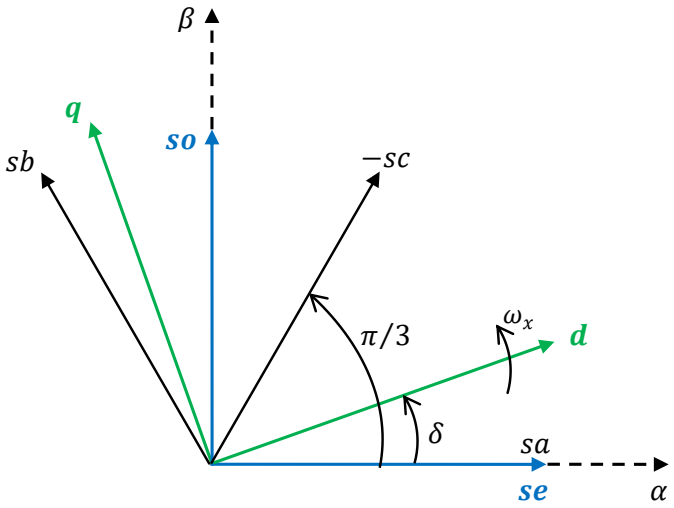

Fig. 7.5.1. dq transformation of αβ quantities

In the stationary 'αβ' reference frame, the vectors represent the sinusoidal currents and voltages of the induction generator can be represented by two separate components perpendicular to each other. One of the two vector components is assumed to be aligned with the α–axis, whereas the second vector component is perpendicular to the first one, i.e. aligned with the β-axis.

First, considering the excitation control winding related variables, the vector components of both voltage and current in the β-axis are equal to zero under all conditions since the axis of this winding is aligned with the α-axis. Thus, the vector component of the current in the α-axis can be given in (7.5.3).

$$i_{se\alpha} = i_{se} \tag{7.5.3}$$

Similarly, the vector component of the voltage in α-axis can be written as

$$V_{se\alpha} = V_{se} \tag{7.5.4}$$

The vectors of voltage and current in the output winding can be obtained using the vector sum of the b-axis and c-axis in the 'abc' reference frame. Using (4.4.7) and

(4.4.16), voltage and current vector components in the β-axis can be written as (7.5.5) and (7.5.6) respectively.

$$V_{so\beta} = V_{so} \tag{7.5.5}$$

$$i_{so\beta} = i_{so} \tag{7.5.6}$$

However, the vector components of both voltage and current in output winding along the α-axis become zero since vector sum of b-axis and c-axis are equal in magnitude and opposite in direction.

The vector components of stator currents and voltages in the α–axis and β–axis can be presented in matrix format in (7.5.7) - (7.5.10) respectively.

$$\begin{bmatrix} i_{se\alpha} \\ i_{se\beta} \end{bmatrix} = \begin{bmatrix} 1 \\ 0 \end{bmatrix} [i_{se}] \tag{7.5.7}$$

$$\begin{bmatrix} i_{so\alpha} \\ i_{so\beta} \end{bmatrix} = \begin{bmatrix} 0 \\ 1 \end{bmatrix} [i_{so}] \tag{7.5.8}$$

$$\begin{bmatrix} V_{se\alpha} \\ V_{se\beta} \end{bmatrix} = \begin{bmatrix} 1 \\ 0 \end{bmatrix} [V_{se}] \tag{7.5.9}$$

$$\begin{bmatrix} V_{so\alpha} \\ V_{so\beta} \end{bmatrix} = \begin{bmatrix} 0 \\ 1 \end{bmatrix} [V_{so}] \tag{7.5.10}$$

The αβ quantities of currents and voltages of both stator and rotor can be transformed into an arbitrary reference frame by the following transformation.

$$\begin{bmatrix} u_\alpha \\ u_\beta \end{bmatrix} = \begin{bmatrix} \cos\delta & -\sin\delta \\ \sin\delta & \cos\delta \end{bmatrix} \begin{bmatrix} u_d \\ u_q \end{bmatrix} \tag{7.5.11}$$

The inverse of this transformation can be given by

$$\begin{bmatrix} u_d \\ u_q \end{bmatrix} = \begin{bmatrix} \cos\delta & \sin\delta \\ -\sin\delta & \cos\delta \end{bmatrix} \begin{bmatrix} u_\alpha \\ u_\beta \end{bmatrix} \tag{7.5.12}$$

Using (7.5.7) – (7.5.12), the voltage equations of stator and rotor in (7.5.1) and (7.5.2) can be transformed into an arbitrary reference frame as given in (7.5.13) and (7.5.16) respectively.

$$\begin{bmatrix} V_{dse} \\ V_{qse} \end{bmatrix} = R_s \begin{bmatrix} i_{dse} \\ i_{qse} \end{bmatrix} + L_{ls} \frac{d}{dt} \begin{bmatrix} i_{dse} \\ i_{qse} \end{bmatrix} + L_{ms} \frac{d}{dt} \begin{bmatrix} i_{dme} \\ i_{qme} \end{bmatrix} + \omega_x L_{ls} \begin{bmatrix} 0 & -1 \\ 1 & 0 \end{bmatrix} \begin{bmatrix} i_{dse} \\ i_{qse} \end{bmatrix} + \omega_x L_{ms} \begin{bmatrix} 0 & -1 \\ 1 & 0 \end{bmatrix} \begin{bmatrix} i_{dme} \\ i_{qme} \end{bmatrix} \quad (7.5.13)$$

$$\begin{bmatrix} V_{dso} \\ V_{qso} \end{bmatrix} = 2R_s \begin{bmatrix} i_{dso} \\ i_{qso} \end{bmatrix} + 2L_{ls} \frac{d}{dt} \begin{bmatrix} i_{dso} \\ i_{qso} \end{bmatrix} + 3L_{ms} \frac{d}{dt} \begin{bmatrix} i_{dmo} \\ i_{qmo} \end{bmatrix} + \omega_x 2L_{ls} \begin{bmatrix} 0 & -1 \\ 1 & 0 \end{bmatrix} \begin{bmatrix} i_{dso} \\ i_{qso} \end{bmatrix} + \omega_x 3L_{ms} \begin{bmatrix} 0 & -1 \\ 1 & 0 \end{bmatrix} \begin{bmatrix} i_{dmo} \\ i_{qmo} \end{bmatrix} \quad (7.5.14)$$

$$\begin{bmatrix} 0 \\ 0 \end{bmatrix} = \frac{2}{3} R_r \begin{bmatrix} i_{dr\alpha}{}' \\ i_{qr\alpha}{}' \end{bmatrix} + \frac{2}{3} L_{lr} \frac{d}{dt} \begin{bmatrix} i_{dr\alpha}{}' \\ i_{qr\alpha}{}' \end{bmatrix} + L_{ms} \frac{d}{dt} \begin{bmatrix} i_{dme} \\ i_{qme} \end{bmatrix} + \omega_x \frac{2}{3} L_{lr} \begin{bmatrix} 0 & -1 \\ 1 & 0 \end{bmatrix} \begin{bmatrix} i_{dr\alpha}{}' \\ i_{qr\alpha}{}' \end{bmatrix} + \omega_x L_{ms} \begin{bmatrix} 0 & -1 \\ 1 & 0 \end{bmatrix} \begin{bmatrix} i_{dme} \\ i_{qme} \end{bmatrix} + \omega_r \frac{2}{\sqrt{3}} L_{lr} \begin{bmatrix} i_{dr\beta}{}' \\ i_{qr\beta}{}' \end{bmatrix} + \omega_r \sqrt{3} L_{ms} \begin{bmatrix} i_{dmo} \\ i_{qmo} \end{bmatrix} \quad (7.5.15)$$

$$\begin{bmatrix} 0 \\ 0 \end{bmatrix} = 2R_r \begin{bmatrix} i_{dr\beta}{}' \\ i_{qr\beta}{}' \end{bmatrix} + 2L_{lr} \frac{d}{dt} \begin{bmatrix} i_{dr\beta}{}' \\ i_{qr\beta}{}' \end{bmatrix} + 3L_{ms} \frac{d}{dt} \begin{bmatrix} i_{dmo} \\ i_{qmo} \end{bmatrix} + \omega_x 2L_{lr} \begin{bmatrix} 0 & -1 \\ 1 & 0 \end{bmatrix} \begin{bmatrix} i_{dr\beta}{}' \\ i_{qr\beta}{}' \end{bmatrix} + \omega_x 3L_{ms} \begin{bmatrix} 0 & -1 \\ 1 & 0 \end{bmatrix} \begin{bmatrix} i_{dmo} \\ i_{qmo} \end{bmatrix} - \omega_r \frac{2}{\sqrt{3}} L_{lr} \begin{bmatrix} i_{dr\alpha}{}' \\ i_{qr\alpha}{}' \end{bmatrix} - \omega_r \sqrt{3} L_{ms} \begin{bmatrix} i_{dme} \\ i_{qme} \end{bmatrix} \quad (7.5.16)$$

where;

$$\begin{bmatrix} i_{dme} \\ i_{qme} \end{bmatrix} = \begin{bmatrix} i_{dmse} \\ i_{qmse} \end{bmatrix} + \frac{3}{2} \begin{bmatrix} i_{dmr\alpha} \\ i_{qmr\alpha} \end{bmatrix} \quad (7.5.17)$$

$$\begin{bmatrix} i_{dmo} \\ i_{qmo} \end{bmatrix} = \begin{bmatrix} i_{dmso} \\ i_{qmso} \end{bmatrix} + \frac{\sqrt{3}}{2} \begin{bmatrix} i_{dmr\beta} \\ i_{qmr\beta} \end{bmatrix} \quad (7.5.18)$$

$$\begin{bmatrix} i_{dr\alpha}{}' \\ i_{qr\alpha}{}' \end{bmatrix} = \frac{3}{2} \begin{bmatrix} i_{dr\alpha} \\ i_{qr\alpha} \end{bmatrix} \quad (7.5.19)$$

$$\begin{bmatrix} i_{dr\beta}{}' \\ i_{qr\beta}{}' \end{bmatrix} = \frac{\sqrt{3}}{2} \begin{bmatrix} i_{dr\beta} \\ i_{qr\beta} \end{bmatrix} \quad (7.5.20)$$

Depending on the value of the speed of the arbitrary reference frame, the voltage equations of stator and rotor can be obtained in different reference frames. When the speed of the arbitrary reference frame is equal to the angular velocity of the supply voltage, the voltage equations can be obtained in synchronous reference frame. Thus, the stator and rotor voltages in the synchronous reference frame can be given by (7.5.21) - (7.5.24) respectively.

$$\begin{bmatrix} V_{dse} \\ V_{qse} \end{bmatrix} = R_s \begin{bmatrix} i_{dse} \\ i_{qse} \end{bmatrix} + L_{ls} \frac{d}{dt} \begin{bmatrix} i_{dse} \\ i_{qse} \end{bmatrix} + L_{ms} \frac{d}{dt} \begin{bmatrix} i_{dme} \\ i_{qme} \end{bmatrix} + \omega_1 L_{ls} \begin{bmatrix} 0 & -1 \\ 1 & 0 \end{bmatrix} \begin{bmatrix} i_{dse} \\ i_{qse} \end{bmatrix} + \omega_1 L_{ms} \begin{bmatrix} 0 & -1 \\ 1 & 0 \end{bmatrix} \begin{bmatrix} i_{dme} \\ i_{qme} \end{bmatrix} \quad (7.5.21)$$

$$\begin{bmatrix} V_{dso} \\ V_{qso} \end{bmatrix} = 2R_s \begin{bmatrix} i_{dso} \\ i_{qso} \end{bmatrix} + 2L_{ls} \frac{d}{dt} \begin{bmatrix} i_{dso} \\ i_{qso} \end{bmatrix} + 3L_{ms} \frac{d}{dt} \begin{bmatrix} i_{dmo} \\ i_{qmo} \end{bmatrix} + \omega_1 2L_{ls} \begin{bmatrix} 0 & -1 \\ 1 & 0 \end{bmatrix} \begin{bmatrix} i_{dso} \\ i_{qso} \end{bmatrix} + \omega_1 3L_{ms} \begin{bmatrix} 0 & -1 \\ 1 & 0 \end{bmatrix} \begin{bmatrix} i_{dmo} \\ i_{qmo} \end{bmatrix} \quad (7.5.22)$$

$$\begin{bmatrix} 0 \\ 0 \end{bmatrix} = \frac{2}{3} R_r \begin{bmatrix} i_{dr\alpha}{}' \\ i_{qr\alpha}{}' \end{bmatrix} + \frac{2}{3} L_{lr} \frac{d}{dt} \begin{bmatrix} i_{dr\alpha}{}' \\ i_{qr\alpha}{}' \end{bmatrix} + L_{ms} \frac{d}{dt} \begin{bmatrix} i_{dme} \\ i_{qme} \end{bmatrix} + \omega_1 \frac{2}{3} L_{lr} \begin{bmatrix} 0 & -1 \\ 1 & 0 \end{bmatrix} \begin{bmatrix} i_{dr\alpha}{}' \\ i_{qr\alpha}{}' \end{bmatrix} + \omega_1 L_{ms} \begin{bmatrix} 0 & -1 \\ 1 & 0 \end{bmatrix} \begin{bmatrix} i_{dme} \\ i_{qme} \end{bmatrix} + \omega_r \frac{2}{\sqrt{3}} L_{lr} \begin{bmatrix} i_{dr\beta}{}' \\ i_{qr\beta}{}' \end{bmatrix} + \omega_r \sqrt{3} L_{ms} \begin{bmatrix} i_{dmo} \\ i_{qmo} \end{bmatrix} \quad (7.5.23)$$

$$\begin{bmatrix} 0 \\ 0 \end{bmatrix} = 2R_r \begin{bmatrix} i_{dr\beta}{}' \\ i_{qr\beta}{}' \end{bmatrix} + 2L_{lr} \frac{d}{dt} \begin{bmatrix} i_{dr\beta}{}' \\ i_{qr\beta}{}' \end{bmatrix} + 3L_{ms} \frac{d}{dt} \begin{bmatrix} i_{dmo} \\ i_{qmo} \end{bmatrix} + \omega_1 2L_{lr} \begin{bmatrix} 0 & -1 \\ 1 & 0 \end{bmatrix} \begin{bmatrix} i_{dr\beta}{}' \\ i_{qr\beta}{}' \end{bmatrix} + \omega_1 3L_{ms} \begin{bmatrix} 0 & -1 \\ 1 & 0 \end{bmatrix} \begin{bmatrix} i_{dmo} \\ i_{qmo} \end{bmatrix} - \omega_r \frac{2}{\sqrt{3}} L_{lr} \begin{bmatrix} i_{dr\alpha}{}' \\ i_{qr\alpha}{}' \end{bmatrix} - \omega_r \sqrt{3} L_{ms} \begin{bmatrix} i_{dme} \\ i_{qme} \end{bmatrix} \quad (7.5.24)$$

Using (3.3.12) and (3.3.13), transforming the voltage across the core loss resistance in the α–axis and β-axis of the two-phase induction machine into an arbitrary reference frame, the air-gap voltages in each axis can be defined in terms of current through the core loss resistance as (7.5.25) and (7.5.26) respectively. Equation (7.5.21) together with (7.5.23) and (7.5.25) forms the excitation control winding in synchronous reference frame. Similarly, (7.5.22), (7.5.24) and (7.5.26) form the output winding in d-axis and q-axis in the synchronous reference frame. The equivalent circuit of the single-phase induction generator resulting from (7.5.21) to (7.5.26) is illustrated in Fig. 7.5.2.

$$\begin{bmatrix} V_{dm1} \\ V_{qm1} \end{bmatrix} = R_c \begin{bmatrix} i_{dc1} \\ i_{qc1} \end{bmatrix} \quad (7.5.25)$$

$$\begin{bmatrix} V_{dm2} \\ V_{qm2} \end{bmatrix} = 2R_c \begin{bmatrix} i_{dc2} \\ i_{qc2} \end{bmatrix} \quad (7.5.26)$$

where;

$$\psi_{dse} = L_{ls} i_{dse} + L_{ms} i_{dme} \quad (7.5.27)$$

$$\psi_{qse} = L_{ls} i_{qse} + L_{ms} i_{qme} \tag{7.5.28}$$

$$\psi_{dso} = 2L_{ls} i_{dso} + 3L_{ms} i_{dmo} \tag{7.5.29}$$

$$\psi_{qso} = 2L_{ls} i_{qso} + 3L_{ms} i_{qmo} \tag{7.5.30}$$

$$\psi_{dr\alpha}{}' = \tfrac{2}{3} L_{lr} i_{dr\alpha}{}' + L_{ms} i_{dme} \tag{7.5.31}$$

$$\psi_{qr\alpha}{}' = \tfrac{2}{3} L_{lr} i_{qr}{}' + L_{ms} i_{qme} \tag{7.5.32}$$

$$\psi_{dr\beta}{}' = 2L_{lr} i_{dr\beta}{}' + 3L_{ms} i_{dmo} \tag{7.5.33}$$

$$\psi_{qr\beta}{}' = 2L_{lr} i_{qr\beta}{}' + 3L_{ms} i_{qmo} \tag{7.5.34}$$

When the arbitrary reference frame is rotating at the synchronous speed, the angle between the d-axis and the α-axis at a time t can be expressed as

$$\delta = \omega_1 t + \delta_0 \tag{7.5.35}$$

where the δ_0 is the angle between the d-axis and α-axis at the time is equal to zero. If it is assumed that the d-axis of arbitrary reference frame is aligned with the α-axis of stationary reference frame at t is equal to zero, this angle also becomes zero. Thus, the angle δ can be simplified as

$$\delta = \omega_1 t \tag{7.5.36}$$

In order to design the control system, the stator voltages in the synchronous reference frame need to be expressed by the measurable quantities. Using (7.5.10) - (7.5.12), and substituting for δ from (7.5.36), the stator output voltage can be given in vector form as

$$V_{so} = V_{dso} + j\, V_{qso} \tag{7.5.37}$$

Using this equation, the magnitude of output winding voltage can be expressed in terms of the voltages in d and q axes as

$$V_{so} = \left({V_{dso}}^2 + {V_{qso}}^2 \right)^{1/2} \tag{7.5.38}$$

Since all the variables are known, the instantaneous voltage of the output winding can be calculated using the above equation.

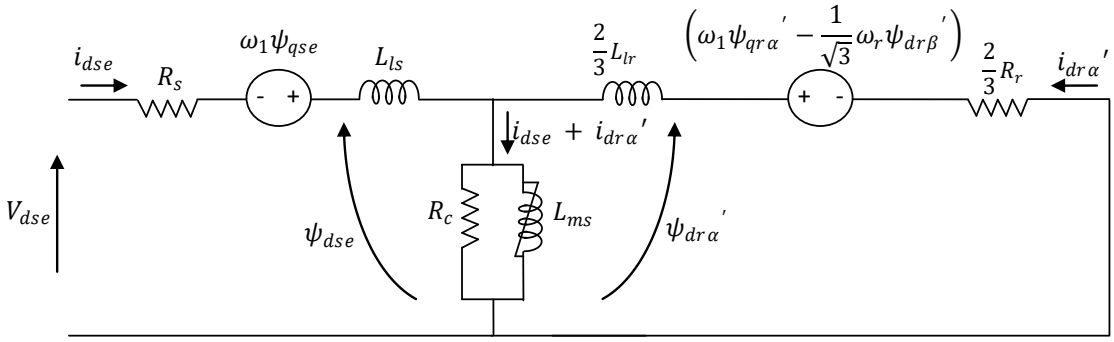

(a)

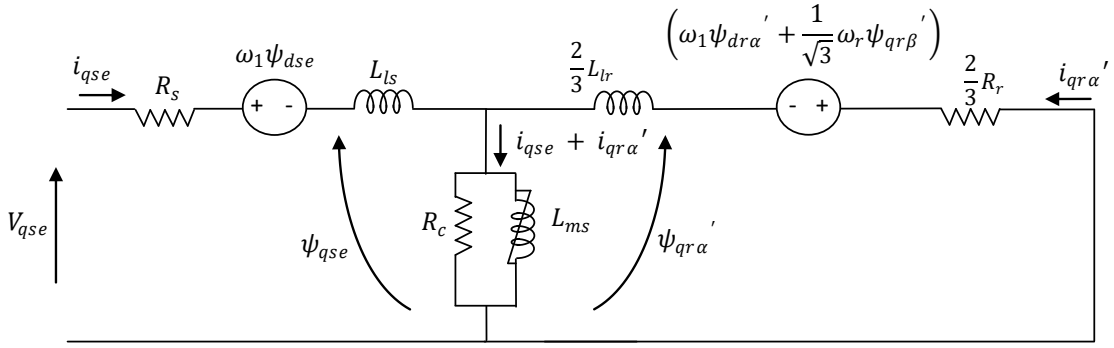

(b)

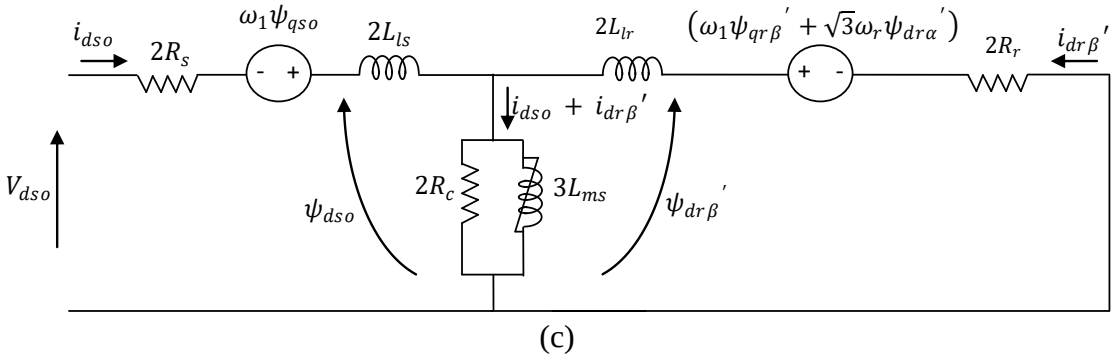

(c)

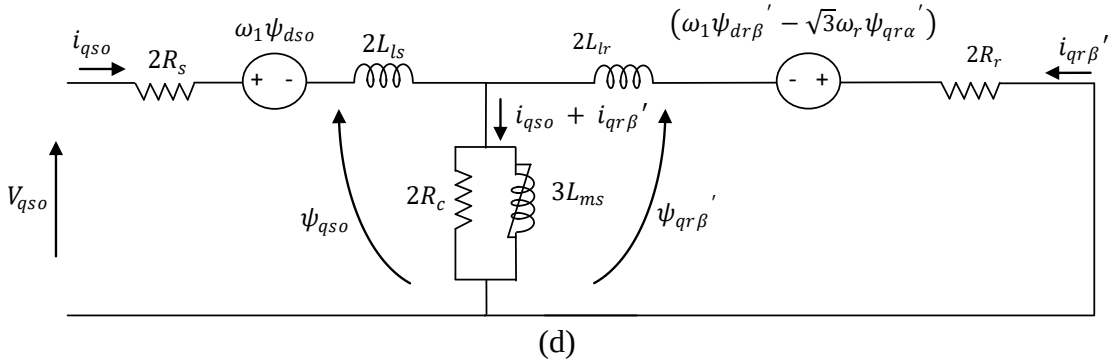

(d)

Fig. 7.5.2. Equivalent circuit of excitation control winding (a) d-axis (b) q-axis and output winding (c) d-axis (q) q-axis of the single-phase induction generator in synchronous reference frame

7.6 Control System

The quality of the renewable energy generation scheme depends on the voltage and the frequency of the load connected at the output. In order to maintain a good quality, these two parameters must be at their rated values despite the variations in available renewable energy source and in load demand. In this thesis, a standard PI controller is used for the control of both voltage and frequency at the output by regulating both magnitude and frequency of the voltage at excitation control winding. In addition, for the safety and the lifespan of the ESS, the charging and discharging characteristics of the battery need to be controlled. The schematic diagram of the proposed control system is illustrated in Fig. 7.6.1.

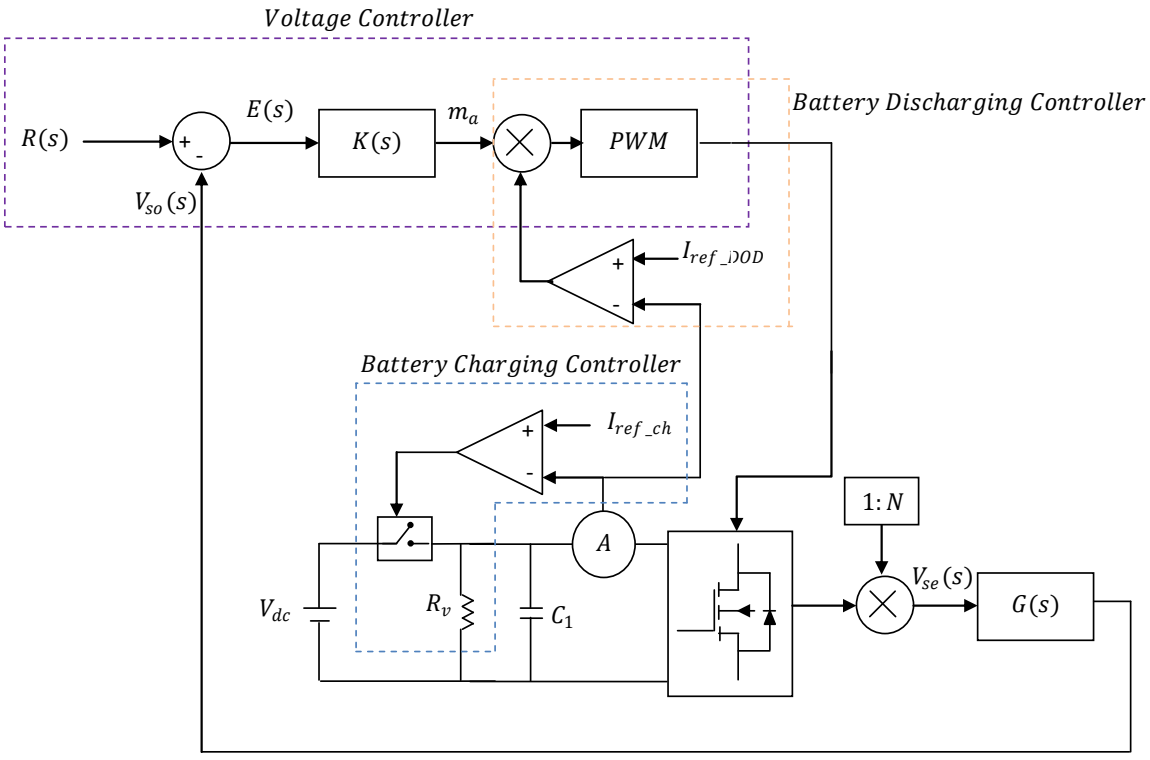

Fig. 7.6.1 Control system

7.6.1. Battery Charging Controller

During periods of high availability of the renewable energy source or low consumer demand, the battery will start to charge. If the same condition is continued for several hours or days, the battery will charge in fully. However, it cannot be over-charged due to the safety and the continuous operation of the whole system. Thus, in order to avoid the overcharging, the battery charging is needed to be controlled. A schematic

diagram of the battery charging controller depicted in Fig. 7.6.1.1 allows comparing the measured current of the BESS with a reference current. Using (7.2.7), this reference current can be calculated as 35.8 A. This reference current can be increased if fast charging is required. The output of the comparator determines ON or OFF of the switches connected before the BESS. If the measured current is higher than the reference current, the switch 1 is OFF whereas the switch 2 is ON and the generated power is dissipated through the variable resistor connected in parallel with the BESS. On the other hand, when the measured current is lower than the reference current, the switch 1 is ON whereas switch 2 is OFF and the battery is charging continuously.

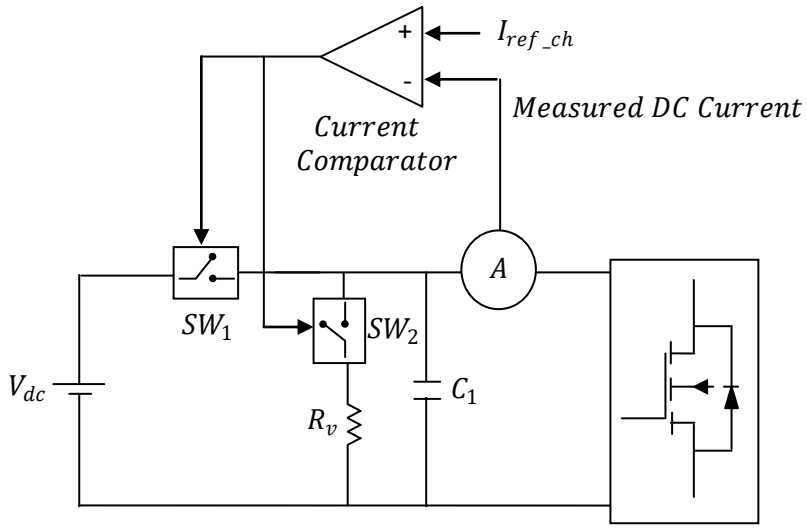

Fig. 7.6.1.1 Battery charging controller

7.6.2. Battery Discharging Controller

In the design, the batteries are not allowed to discharge below the maximum DOD. Thus, similar to the battery charging, battery discharging also needs to be controlled. The measured discharging current is compared with the reference current which is the battery current at maximum DOD. Depending on the output of the comparator, the gate pulses of the inverter are controlled. If the measured current is above or equal to the reference current, generated gate pulses are applied to the inverter. On the other hand, if the measured current is below the reference current, the gate pulses are set to zero, isolating the BESS from the generator circuit. This controlling is illustrated in Fig. 7.6.2.1.

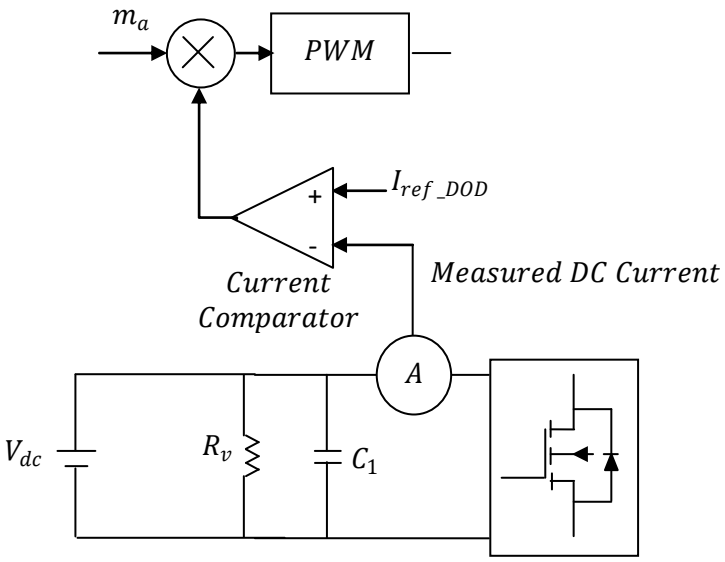

Fig. 7.6.2.1 Battery discharging controller

7.6.3. Closed-loop PI Controller

Output voltage and frequency of the single-phase induction generator are controlled using a feedback control system depicted in Fig. 7.6.3.1. Measured voltage at the output winding is compared with the reference voltage of 230 V which is the desired voltage at the output. The error signal is applied as the input of the proposed PI controller. The output of the PI controller is the modulation index (m_a) of PWM bi-directional power converter as given in (7.6.3.1).

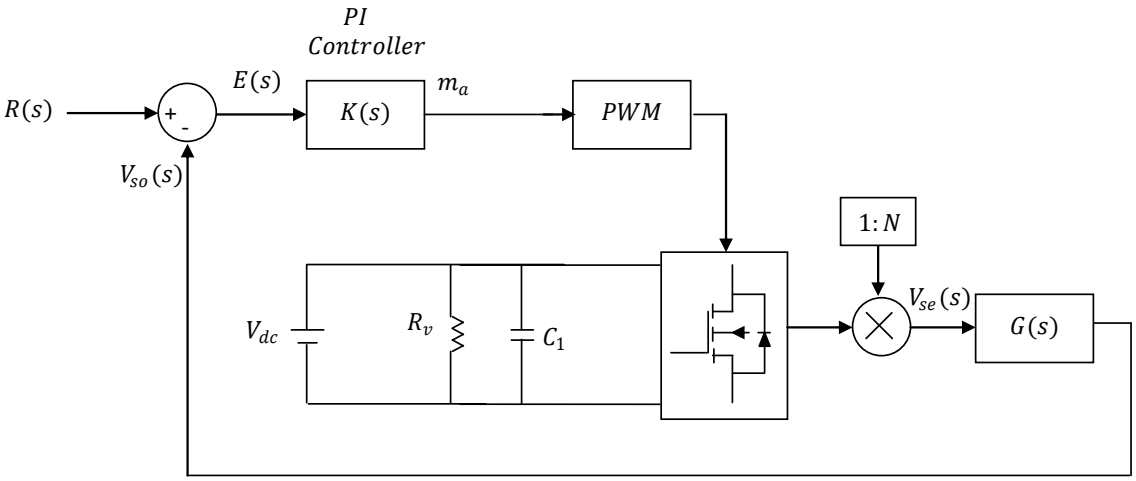

Fig. 7.6.3.1 Closed loop PI controller

$$m_a = E(s)K(s) \quad (7.6.3.1)$$

where $E(s)$ and $K(s)$ are the Laplace equations of the error signal and PI control signal respectively.

$E(s)$ can be written as the difference between the reference voltage and measured output voltage in S plane as

$$E(s) = R(s) - V_{so}(s) \tag{7.6.3.2}$$

Since the modulation index varies between 0 and 1, (7.6.3.1) and (7.6.3.2) can be re-written as

$$0 \leq [R(s) - V_{so}(s)]K(s) \leq 1 \tag{7.6.3.3}$$

Using (7.6.3.3), $V_{so}(s)$ and $K(s)$ can be written in terms of error $R(s)$ as (7.6.3.4) and (7.6.3.5) respectively.

$$V_{so}(s) \leq R(s) \tag{7.6.3.4}$$

$$K(s) \leq \frac{1}{[R(s) - V_{so}(s)]} \tag{7.6.3.5}$$

Since $V_{so}(S)$ can be changed in between ± 230 V, the maximum error can be obtained at $V_{so} = -230$ V. Thus, the ultimate gain of $K(s)$, K_u can be determined by (7.6.3.6).

$$K_u = \frac{1}{[230 - (-230)]} = 0.0022 \tag{7.6.3.6}$$

In order to find out the values of proportional and integral gains using the Ziegler–Nichols method, the oscillation period of the PI controller,T_u needs to be calculated. Using the dynamic equations, the transfer function of the generator, $G(s)$ can be written as

$$G(s) = \frac{V_{so}(s)}{V_{se}(s)} = \frac{K_a s}{s^7 + K_b s^6 + K_c s^5 + K_d s^4 + K_e s^3 + K_f s^2 + K_g s + K_h} \tag{7.6.3.7}$$

where constants K_a to K_h are defined as (7.6.3.8) to (7.6.3.15).

$$\mathrm{K_a} = \frac{1}{\mathrm{L_{ls} * K_{25}}} \tag{7.6.3.8}$$

$$\mathrm{K_b} = \frac{(\mathrm{R_s * K_{25}}) + (\mathrm{L_{ls} * K_{26}}) + (\mathrm{L_{m1} * K_{19}})}{\mathrm{L_{ls} * K_{25}}} \tag{7.6.3.9}$$

$$\mathrm{K_c} = \frac{(\mathrm{R_s * K_{26}}) + (\mathrm{L_{ls} * K_{27}}) + (\mathrm{L_{m1} * K_{20}})}{\mathrm{L_{ls} * K_{25}}} \tag{7.6.3.10}$$

$$K_d = \frac{(R_s * K_{27}) + (L_{ls} * K_{28}) + (L_{m1} * K_{21})}{L_{ls} * K_{25}} \quad (7.6.3.11)$$

$$K_e = \frac{(R_s * K_{28}) + (L_{ls} * K_{29}) + (L_{m1} * K_{22})}{L_{ls} * K_{25}} \quad (7.6.3.12)$$

$$K_f = \frac{(R_s * K_{29}) + (L_{ls} * K_{30}) + (L_{m1} * K_{23})}{L_{ls} * K_{25}} \quad (7.6.3.13)$$

$$K_g = \frac{(R_s * K_{30}) + (L_{ls} * K_{31}) + (L_{m1} * K_{24})}{L_{ls} * K_{25}} \quad (7.6.3.14)$$

$$K_h = \frac{R_s * K_{31}}{L_{ls} * K_{25}} \quad (7.6.3.15)$$

Constants K_{25} to K_{31} are defined in the Appendix E.

The excitation control voltage V_{se} is controlled by the feedback response of the controlled system. Depending on the modulation index m_a, the excitation control voltage varies in order to maintain a constant voltage at the output. Thus, the excitation control voltage can be written as a function of m_a as

$$V_{se}(s) = [R(s) - V_{so}(s)]K(s)\frac{NV_{dc}}{\sqrt{2}} \quad (7.6.3.16)$$

where, N and $V_{dc}$are the turns ratio of the step-up transformer and DC voltage of the battery respectively.

Using (3.6.3.7) and (3.6.3.16), closed loop transfer function of the controlled system $H(s)$ is defined as

$$H(s) = \frac{V_{so}(s)}{R(s)} = \frac{\frac{NV_{dc}}{\sqrt{2}}G(s)K(s)}{1+\frac{NV_{dc}}{\sqrt{2}}G(s)K(s)} \quad (7.6.3.17)$$

Considering the gain of the PI controller $K(s)$ is as K_u and substituting from (7.6.3.7), the first two rows of the Routh array [154] of the denominator of $H(S)$ can be presented by (7.6.3.18).

s^7	1	K_c	K_e	$K_g + K_a K_u \frac{NV_{dc}}{\sqrt{2}}$	(7.6.3.18)
s^6	K_b	K_d	K_f	K_h	

The first row of the Routh array can be re-written as

$$s^7 + K_c s^5 + K_e s^3 + \left(K_g + K_a K_u \frac{NV_{dc}}{\sqrt{2}}\right) s = 0 \quad (7.6.3.19)$$

Substituting for K_u from (7.6.3.6) and $s = j\omega_u$, $\omega_u$can be calculated by solving the polynomial equation in (7.6.3.20).

$$-\omega^6 + K_c \omega^4 - K_e \omega^2 + \left(K_g + K_a K_u \frac{NV_{dc}}{\sqrt{2}}\right) = 0 \quad (7.6.3.20)$$

The oscillation period of the PI controller,T_u can be calculated by

$$T_u = \frac{2\pi}{\omega_u} \quad (7.6.3.21)$$

The minimum value of the integral gain is obtained at the oscillation period of 0.018 s. Values of proportional and integral gains of the proposed PI controller, calculated using the Ziegler–Nichols method are presented in Table 7.6.3.1.

Table 7.6.3.1
Proportional (K_p) and Integral (K_i) gains of proposed PI controller

Control Type	K_p	K_i
PI	0.45 K_u	0.54 K_u/T_u
PI	0.00099	0.0652

7.7 Results and Discussion

The performance of the proposed control system is determined by the simulation results obtained using Matlab Simulink. The simulation block diagram is given in Appendix F. Initially, the generator was operated under a normal operating condition where output voltage and frequency are at the rated values. Then, at each time, one variable was changed to create a disturbance to the normal operating condition. The resulting transients of each system variable were recorded for each test case. Secondly, the same disturbance was applied to the closed-loop control system. The changes to each system variable due to the performance of the proposed control system were recorded. Using the obtained results, the performance of the proposed control system is analysed in sub-sections 7.7.1 – 7.7.4 below. For the convenience of comparison, all the results presented in this section are given in per-unit values as defined in Appendix G.

7.7.1. Changes in Consumer Load

In the first part of this section, the performance of a controlled system is studied for a change in consumer load with a unity power factor whereas in second section same analysis was performed for a change in consumer load with a lagging power factor.

First, the generator is operating under normal operating conditions with a consumer load of 0.92 pu (i.e. full-load current at rated voltage) at the wind speed of 6 m/s. In order to study the system performance due to a change in consumer load, the load resistance is increased up to 1.63 pu (i.e. 67.2% of full-load current at rated voltage) at time t=0.2 s while wind speed remains unchanged. Fixed capacitance of 0.54 pu is connected in parallel with the consumer load at all the times.

When this change is applied to the uncontrolled system, the output voltage increases up to 1.12 pu as shown by the broken line in Fig. 7.7.1.1. When the same change is applied to the controlled system, the output voltage is maintained at the rated value after a transient period of 0.1 s. This is illustrated by the solid line in Fig. 7.7.1.1.

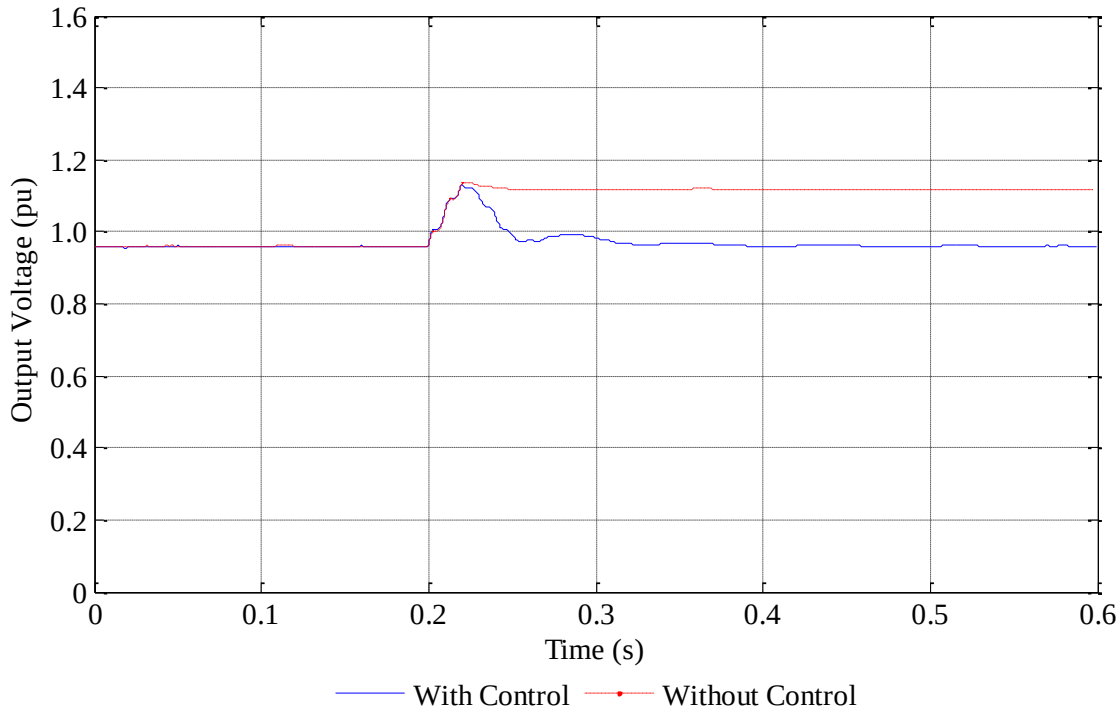

Fig. 7.7.1.1. Variation of output voltage with and without the feedback controller

In an unregulated generator system, when the load decreases, the output voltage increases in order to balance the real power in the system. Similar to the uncontrolled

system, output voltage in the regulated system increases with the decreasing consumer load just after the disturbance. However, after a transient period, it becomes stable at the rated voltage as shown in Fig. 7.7.1.1.

The variations of output current, excitation control voltage and excitation control current with and without control system is illustrated in Fig. 7.7.1.2 – 7.7.1.4 respectively. The variations of regulated system variables are shown by solid lines, whereas variations of unregulated system variables are shown by broken lines as given in the legend in each figure. With the decrease of consumer load, output current decreases in both the situations. However, due to the increased output voltage in an uncontrolled system, output current is also higher than that of a controlled system. In an unregulated system, excitation control voltage remains unchanged since the modulation index of the PWM inverter is fixed at a constant. In a regulated system, excitation control voltage is decreased by adjusting the modulation index of the inverter in order to maintain the constant voltage at the output. In both the scenarios, excitation control current decreases with the increasing consumer load. In this test, almost the same behaviour can be observed in both controlled and uncontrolled systems as depicted in Fig. 7.7.1.4.

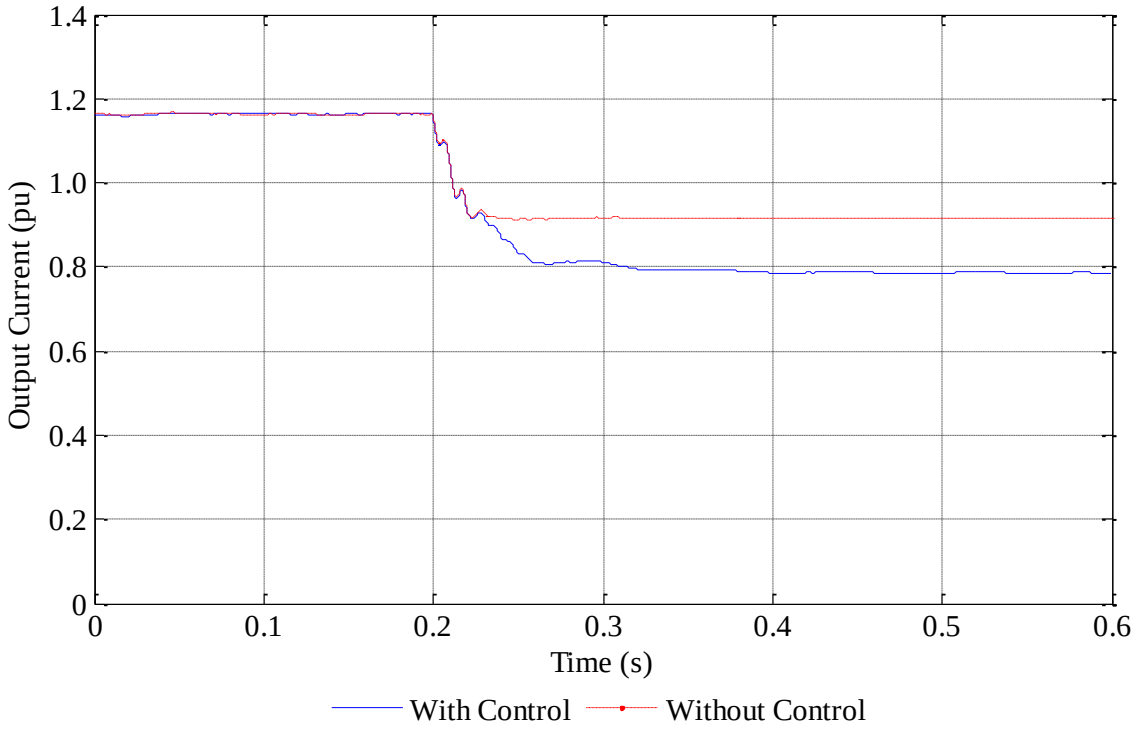

Fig. 7.7.1.2. Variation of output current with and without the feedback controller

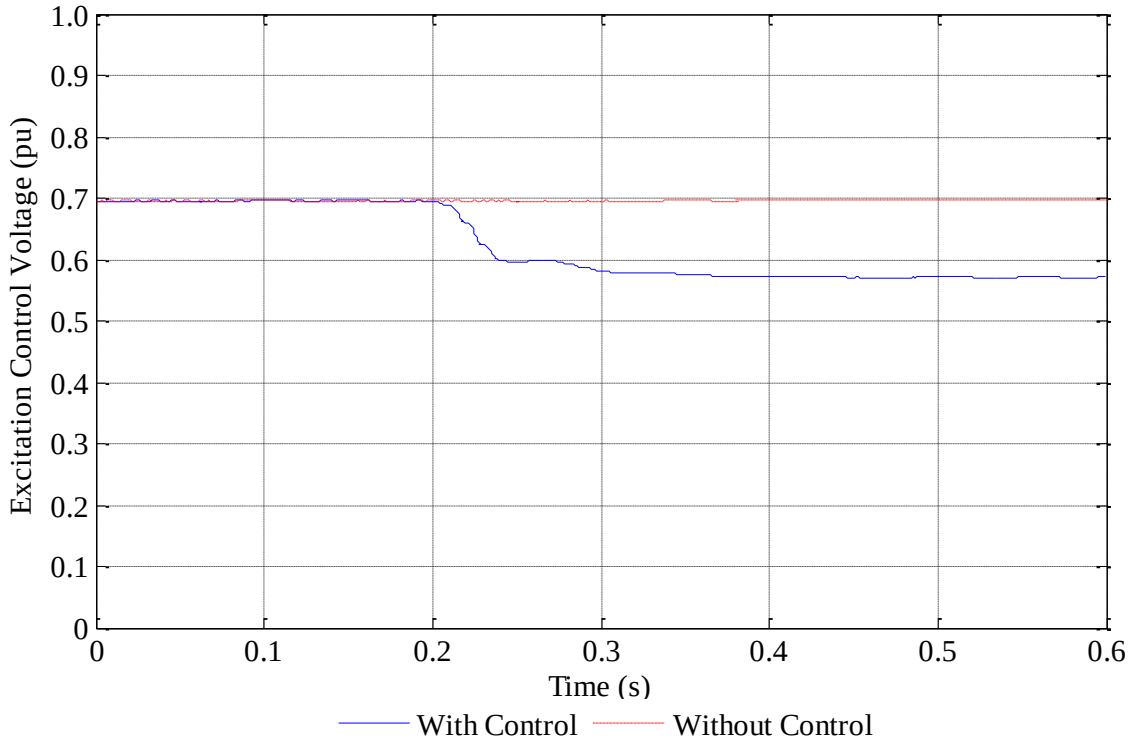

Fig. 7.7.1.3. Variation of excitation control voltage with and without the feedback controller

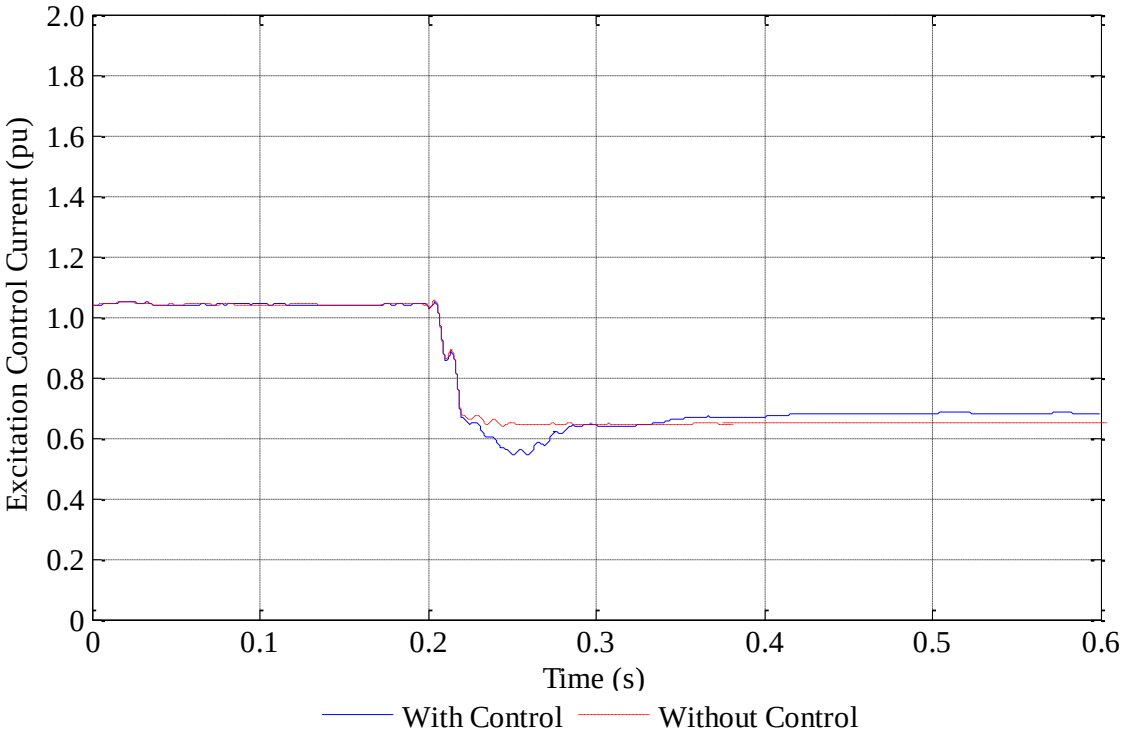

Fig. 7.7.1.4. Variation of excitation control current with and without the feedback controller

The variations in system variables due to the load change can be further studied by analysing the active power of the generator system. Figs. 7.7.1.5 – 7.7.1.7 illustrate the active power in output winding, excitation control winding and mechanical system respectively. In general, when the consumer load is decreased, active power required at the output decreases. Since in an unregulated generator, output voltage increases with the increasing load impedance, the active power requirement at the output is higher than that of the regulated system. Before the disturbance, the excitation control winding supplies some of the active power requirement of the generator as shown in Fig. 7.7.1.6. After the disturbance, this power significantly reduces with the decreasing consumer load demand. Therefore, in order to maintain the power balance in the unregulated system, input mechanical power slightly increases as shown in Fig. 7.7.1.7. On the other hand, in a regulated system, the excitation control winding absorbs the additional active power generated by mechanical system. However, due to the lower demand at the output, input mechanical power decreases after the disturbance.

The variation of mechanical torque due to the applied disturbance is depicted on the torque-speed characteristics curve of wind turbine in Fig. 7.7.1.8.

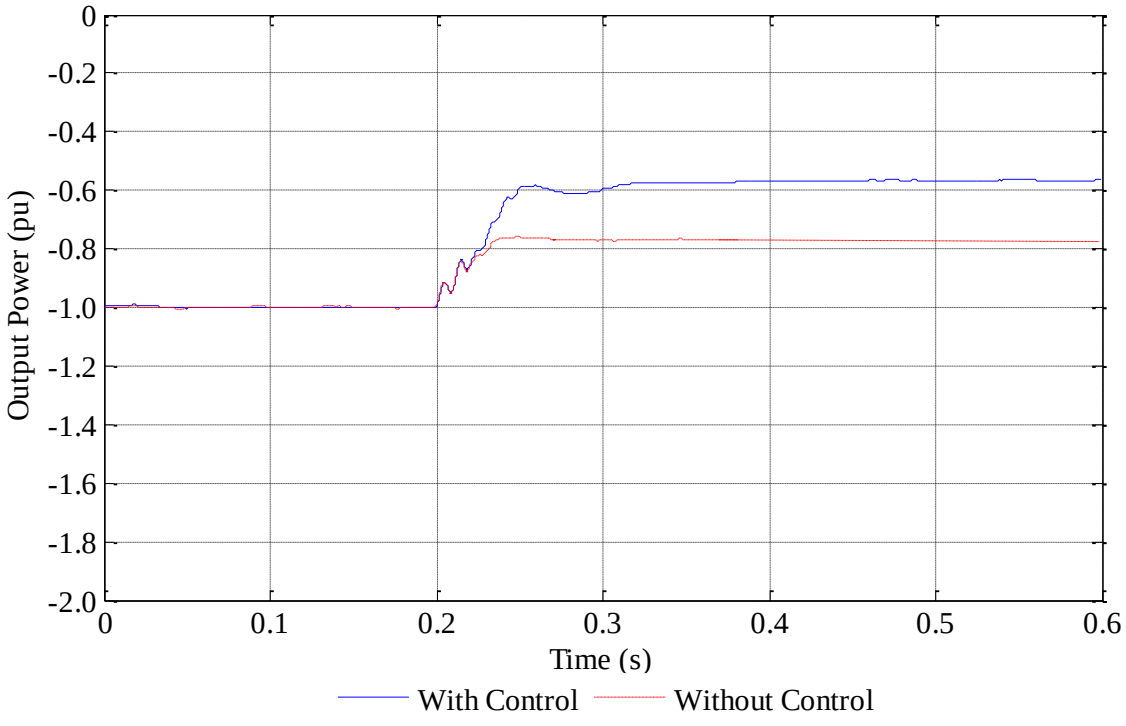

Fig. 7.7.1.5. Variation of output power with and without the feedback controller

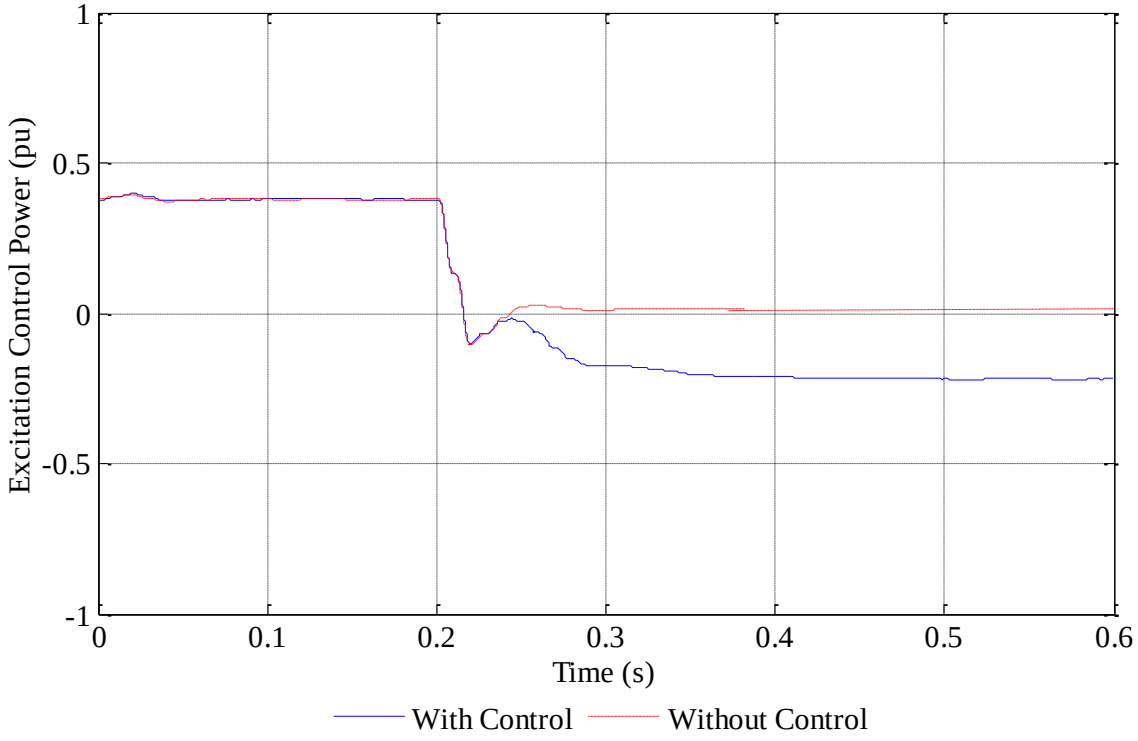

Fig. 7.7.1.6. Variation of excitation control power with and without the feedback controller

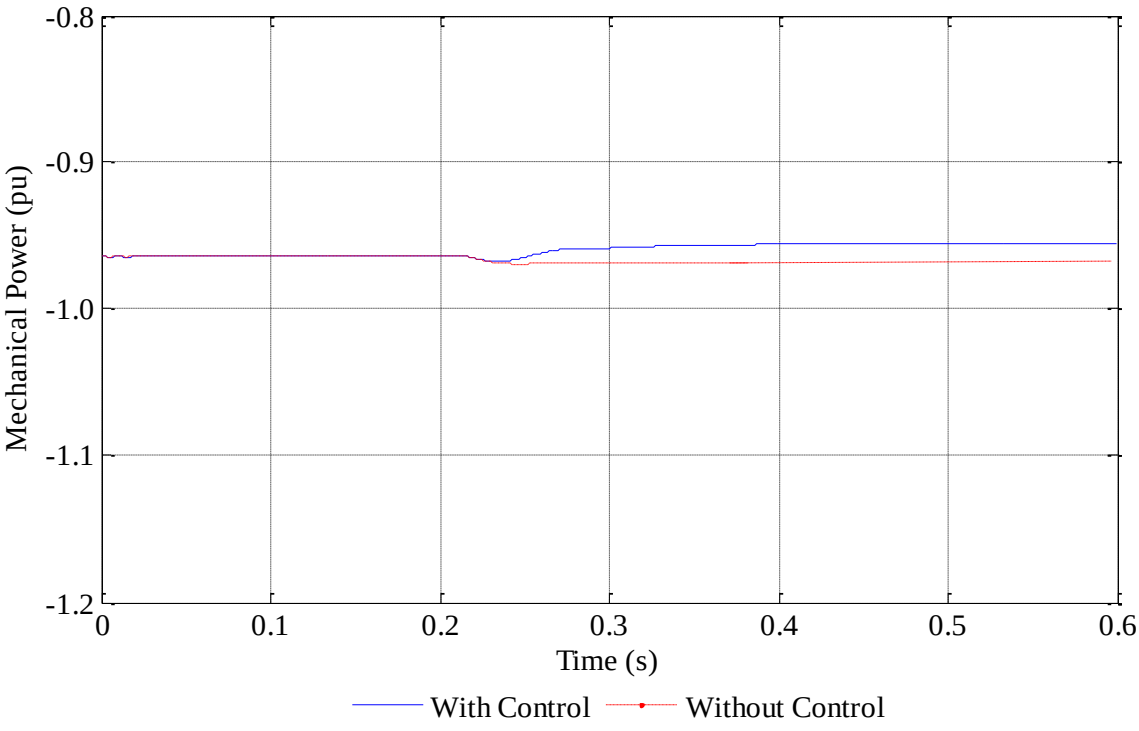

Fig. 7.7.1.7. Variation of mechanical power with and without the feedback controller

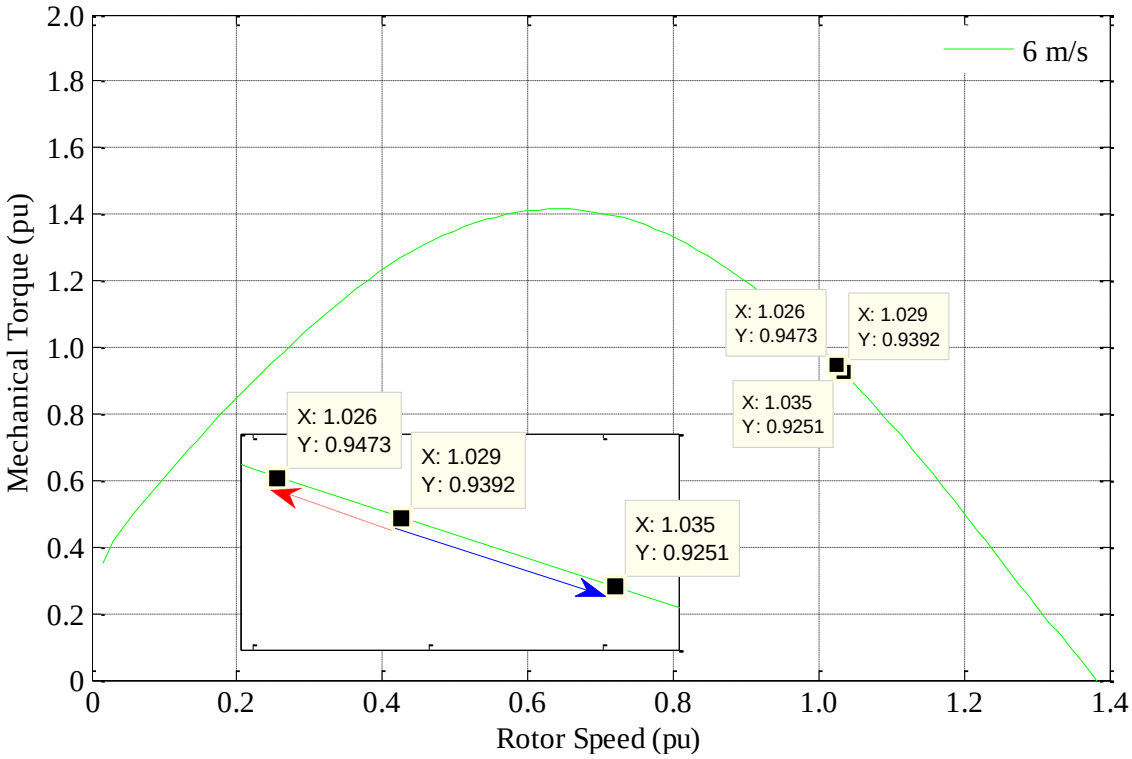

Fig. 7.7.1.8. Torque-speed characteristics of wind turbine at wind speed of 6 m/s

Since the power required at output winding decreases, mechanical torque in regulated system decreases by increasing the speed of the prime mover. This is illustrated using the solid arrow in Fig. 7.7.1.8. In the unregulated generator system, mechanical torque slightly increases by decreasing the speed of prime mover as shown by broken arrow.

For the means of comparison, the numerical values of system variables with and without the control system are given in Table 7.7.1.1.

Table 7.7.1.1
Values of System Variables

Parameter		V_{so} (pu)	V_{se} (pu)	I_{so} (pu)	I_{se} (pu)	Rotor Speed (pu)
Before disturbance		0.96	0.70	1.16	1.04	1.029
After Disturbance	Regulated System	0.96	0.57	0.79	0.68	1.035
	Unregulated System	1.12	0.7	0.91	0.65	1.026

Regulated and unregulated behaviour of the generator system due to change of lagging power factor load is illustrated using Figs. 7.7.1.9 – 7.7.1.16 below. Similar to previous test, initially, the generator is operating under normal operating conditions with a consumer load of 0.92 pu (i.e. full-load current at rated voltage) at the wind speed of 6 m/s. In order to study the system performance due to a change in consumer load with lagging power factor, the load impedances is increased up to 1.63 pu (i.e. 67.2% of full-load current at rated voltage) at time t=0.2 s while wind speed remains unchanged. The same fixed capacitance of 0.54 pu is connected in parallel with the consumer load at all the times. The variations of output voltage, output winding current, excitation control voltage and excitation control winding current are depicted in Figs. 7.7.1.9 – 7.7.1.12 respectively.

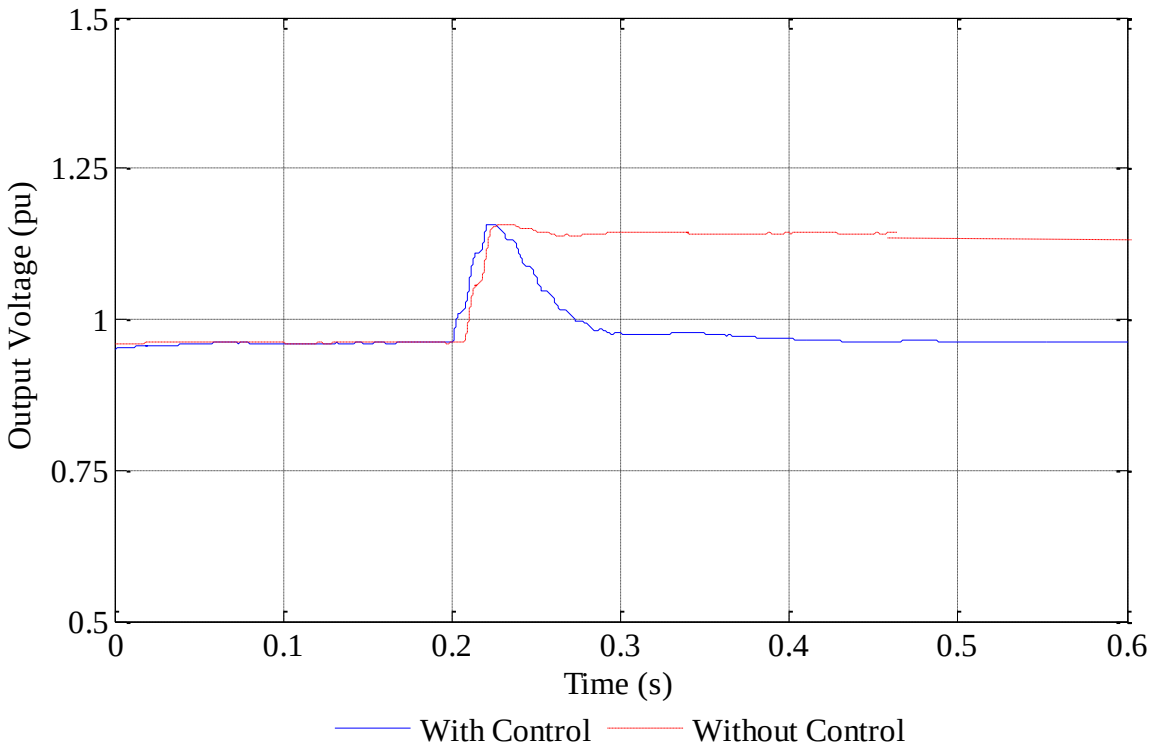

Fig. 7.7.1.9. Variation of output voltage with and without the feedback controller

The changes in output power, excitation control power and mechanical power due to the introduced disturbance are shown in Fig. 7.7.1.13 – 7.7.1.15 respectively. Variations of mechanical torque are illustrated on the torque-speed characteristic curve of wind turbine as in Fig. 7.7.1.16.

Due to the change in load with lagging power factor, each system variable follows the same behaviour discussed in the previous analysis. However, both the system

variables and the changes are different in magnitude compared to those due to the change in load with unity power factor.

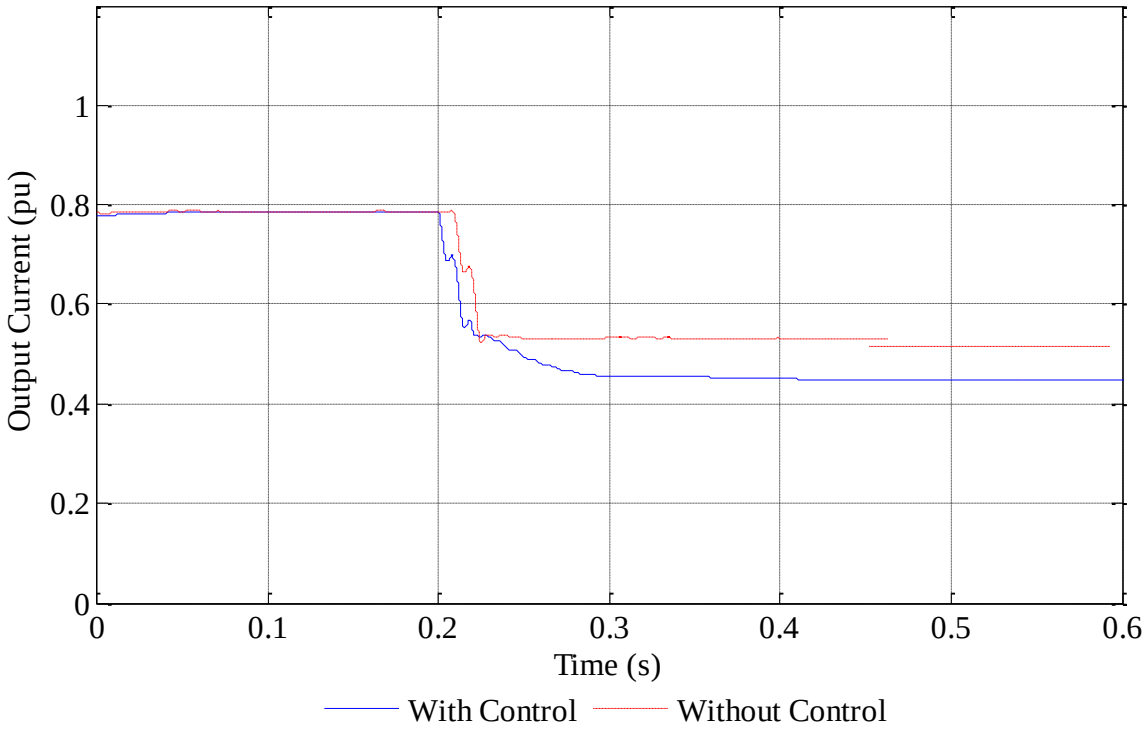

Fig. 7.7.1.10. Variation of output current with and without the feedback controller

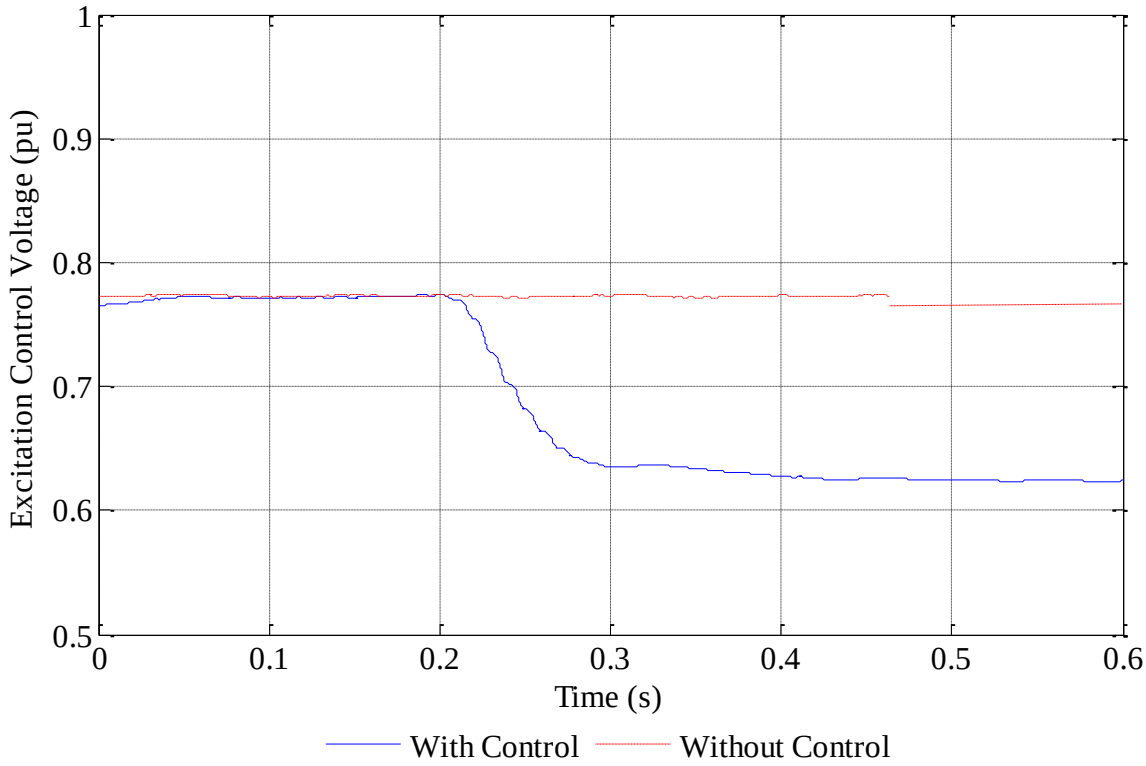

Fig. 7.7.1.11. Variation of excitation control voltage with and without the feedback controller

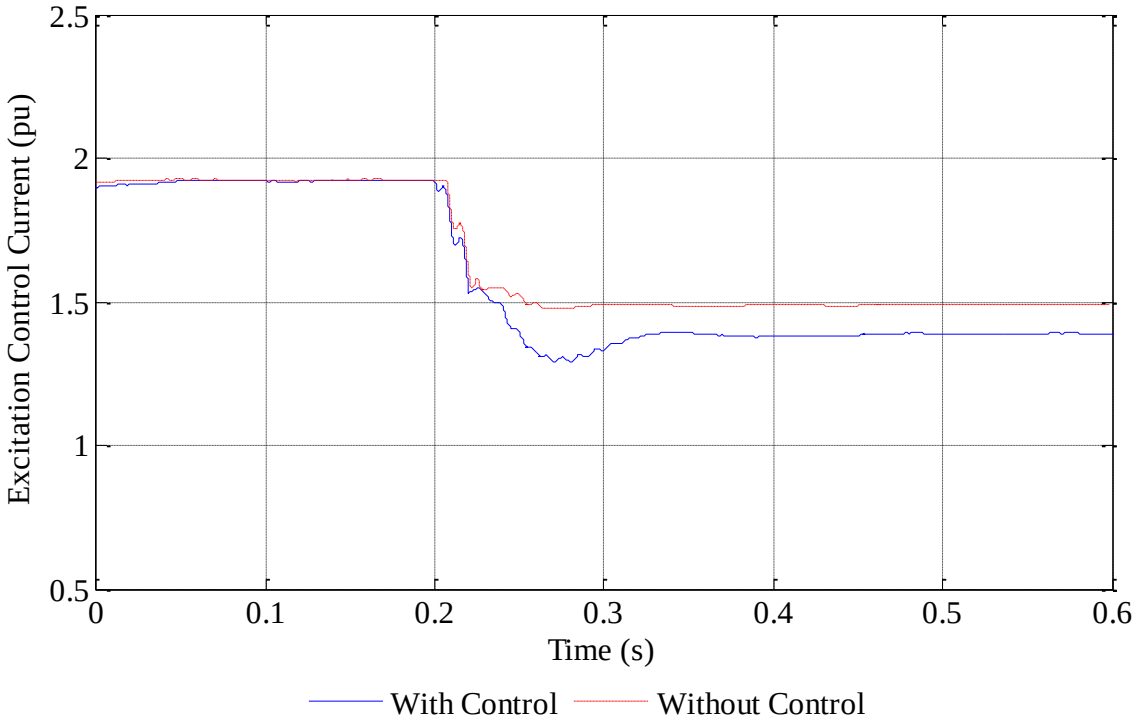

Fig. 7.7.1.12. Variation of excitation control current with and without the feedback controller

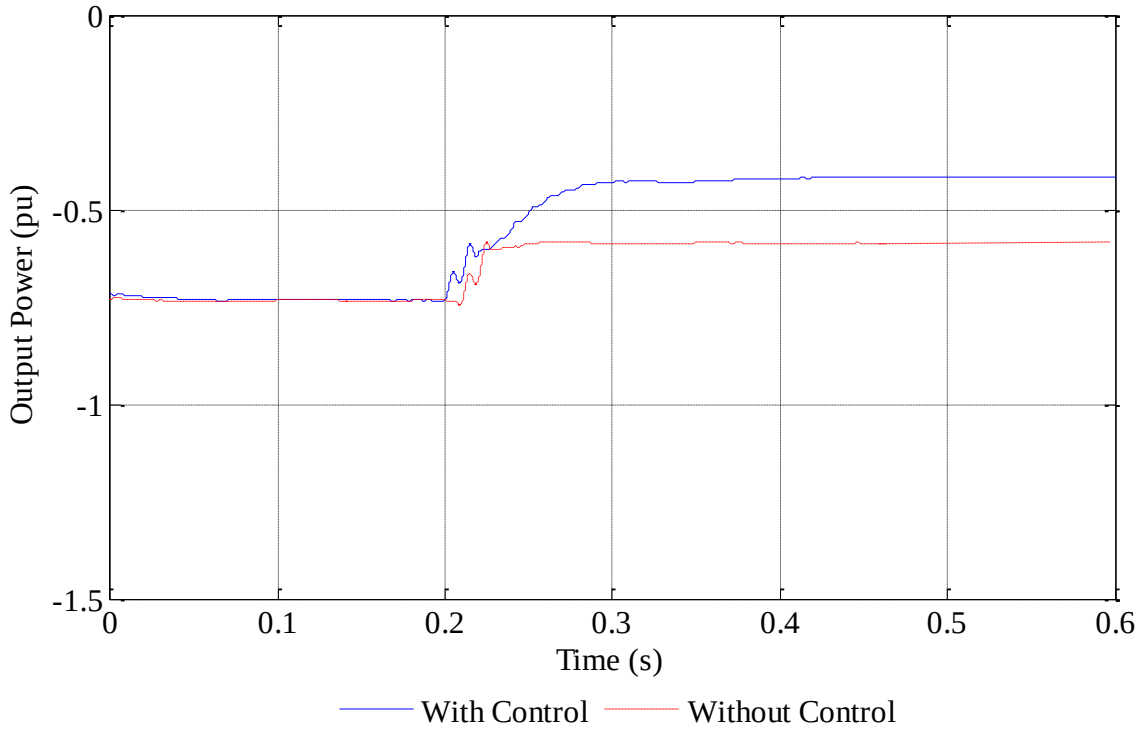

Fig. 7.7.1.13. Variation of output power with and without the feedback controller

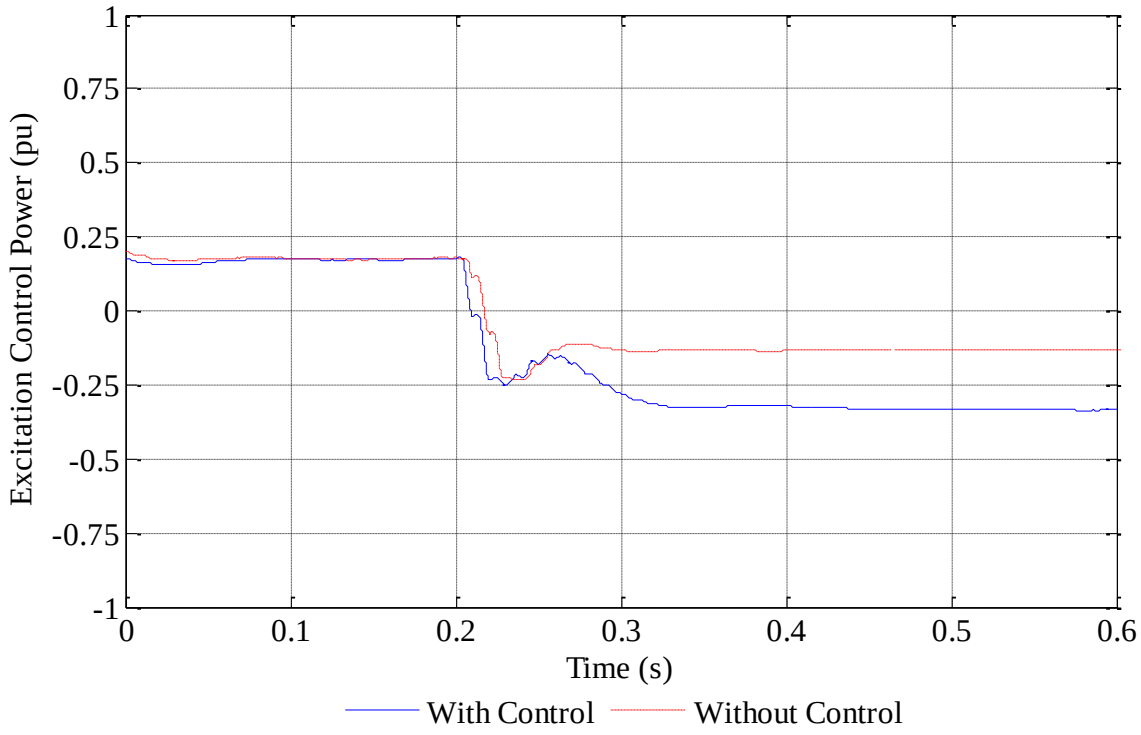

Fig. 7.7.1.14. Variation of excitation control power with and without feedback controller

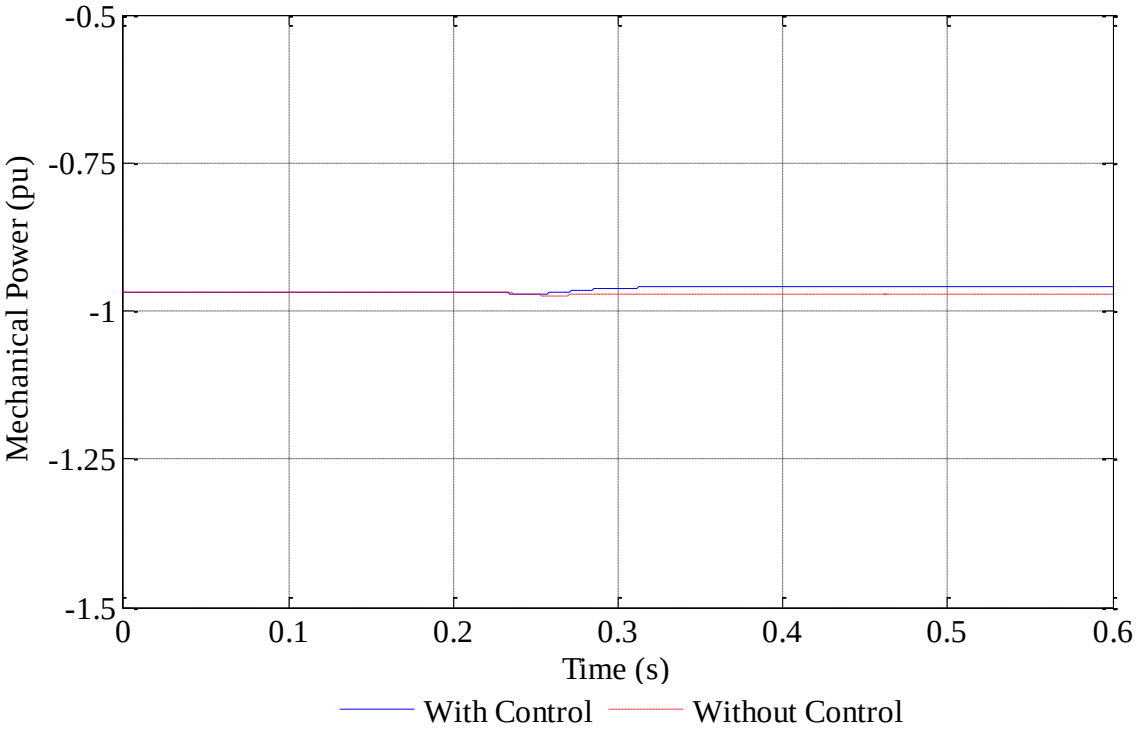

Fig. 7.7.1.15. Variation of mechanical power with and without the feedback controller

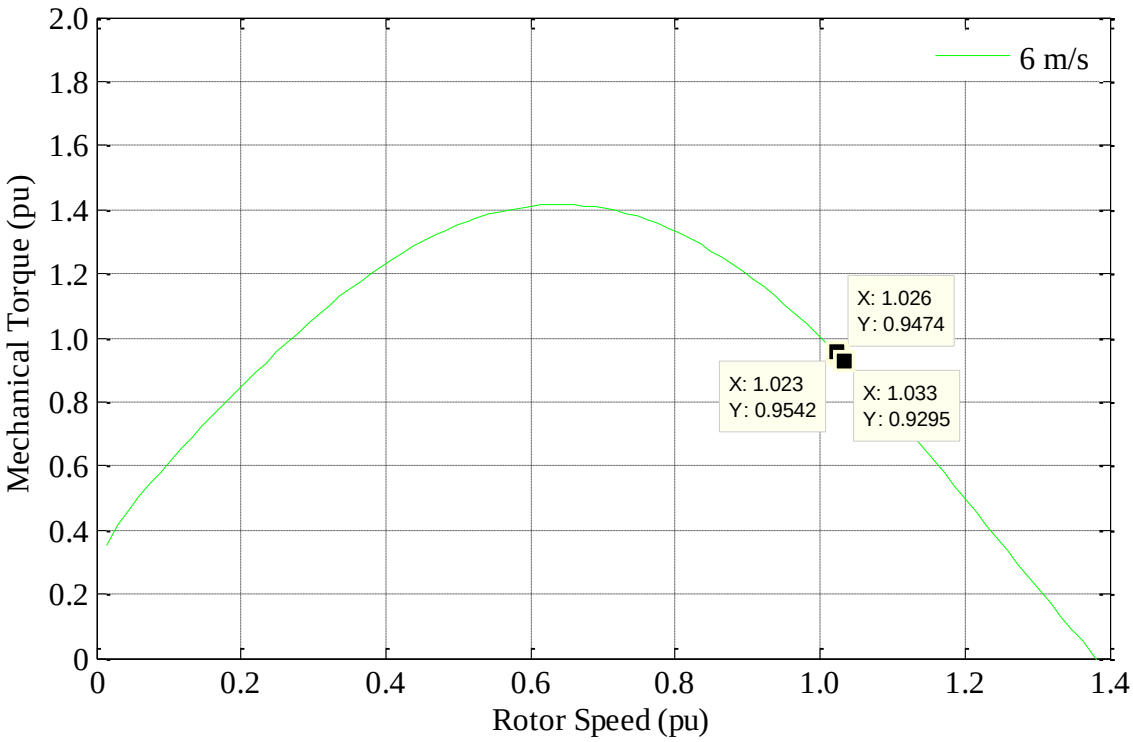

Fig. 7.7.1.16. Torque-speed characteristics of wind turbine at wind speed of 6 m/s

7.7.2. Changes in Fixed Capacitance

Similar to the previous test, the performance of a controlled system is studied for a change in fixed capacitance at time t=0.2 s. First, the generator is operating under a normal operating condition with a consumer load of 0.92 pu (i.e. full-load current at rated voltage) at a wind speed of 6 m/s. Fixed capacitance of 0.54 pu is connected in parallel with the consumer load. In order to apply the disturbance, this capacitance is increased to 0.90 pu at time t=0.2 s. Consumer load and wind speed is kept constant at all the time.

Just after the disturbance, the output voltage increases up to 1.034 pu in both regulated and unregulated systems. However, after a transient period of 0.06 s, the regulated system reaches the original value and becomes stable at the rated voltage as shown by solid line in Fig. 7.7.2.1. In uncontrolled system, output voltage becomes stable at the maximum value reached after the disturbance. This is depicted by the broken line in the same figure.

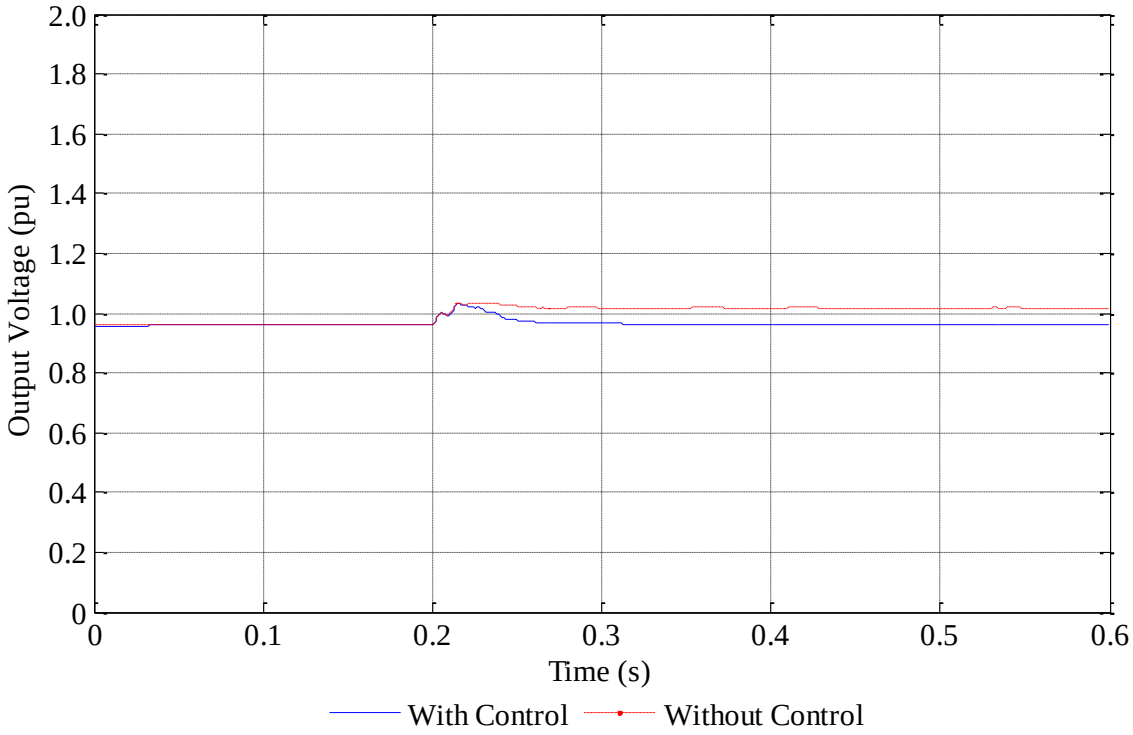

Fig. 7.7.2.1. Variation of output voltage with and without the feedback controller

The variations of output current, excitation control voltage and excitation control current with and without control system is illustrated in Figs. 7.7.2.2 – 7.7.2.4 respectively. With the applied disturbance, the current through the fixed capacitance increases, producing high current in the output winding of the generator. However, after the transient period, the output current in the regulated system decreases to achieve the rated voltage at the output. Due to the increased output voltage in the unregulated system, output current is also stable at a value higher than that of regulated system. When the fixed capacitance is increased, the reactive power in the generator system increases. In order to maintain the power balance, reactive power supplement of the excitation control winding is required to be decreased. Thus, both the voltage and current in excitation control winding decrease with the increasing fixed capacitance. In unregulated generator system, excitation control voltage remains unchanged since the modulation index of PWM inverter is kept constant at all the time. However, excitation control winding decreases to maintain the reactive power balance similar to the regulated system. Similar to the previous analysis, the variations of regulated system variables are shown by solid lines, whereas variations of unregulated system variables are shown by broken lines.

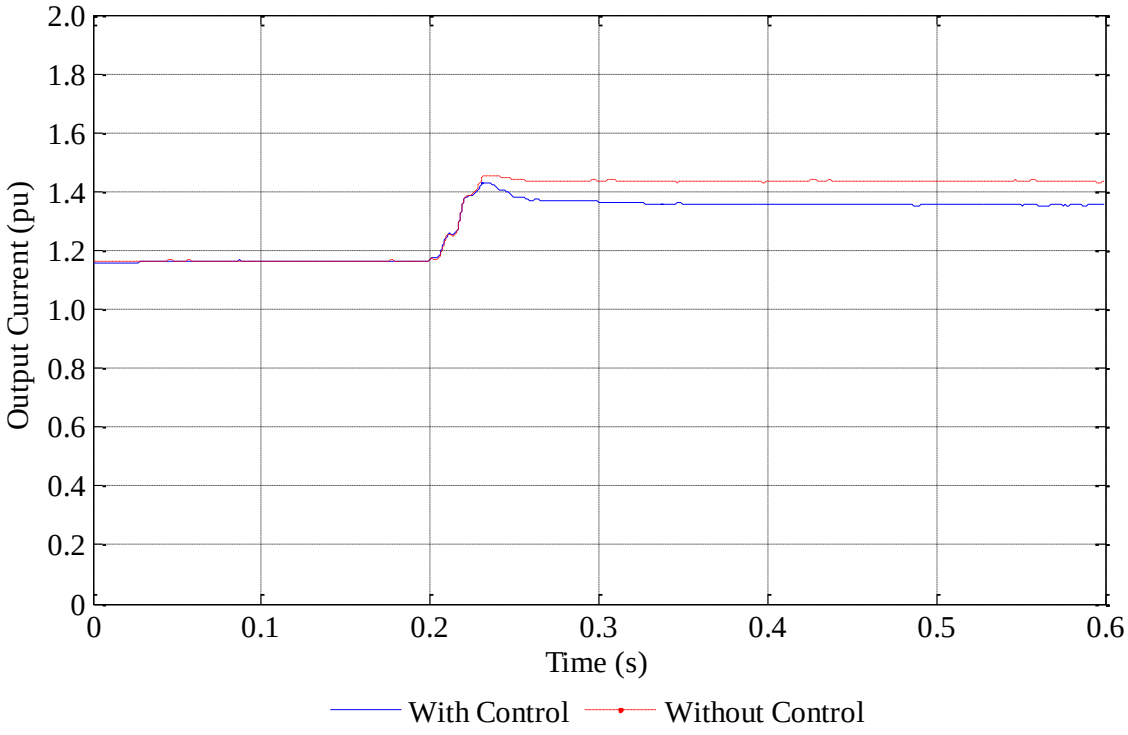

Fig. 7.7.2.2. Variation of output current with and without the feedback controller

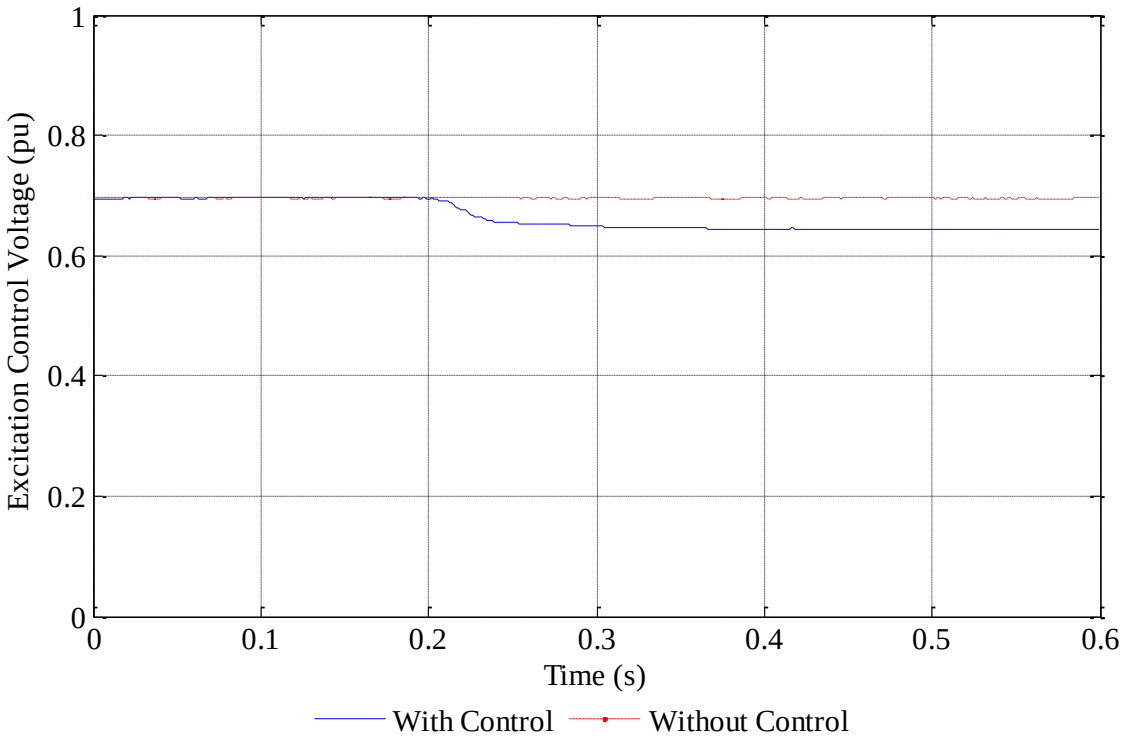

Fig. 7.7.2.3. Variation of excitation control voltage with and without the feedback controller

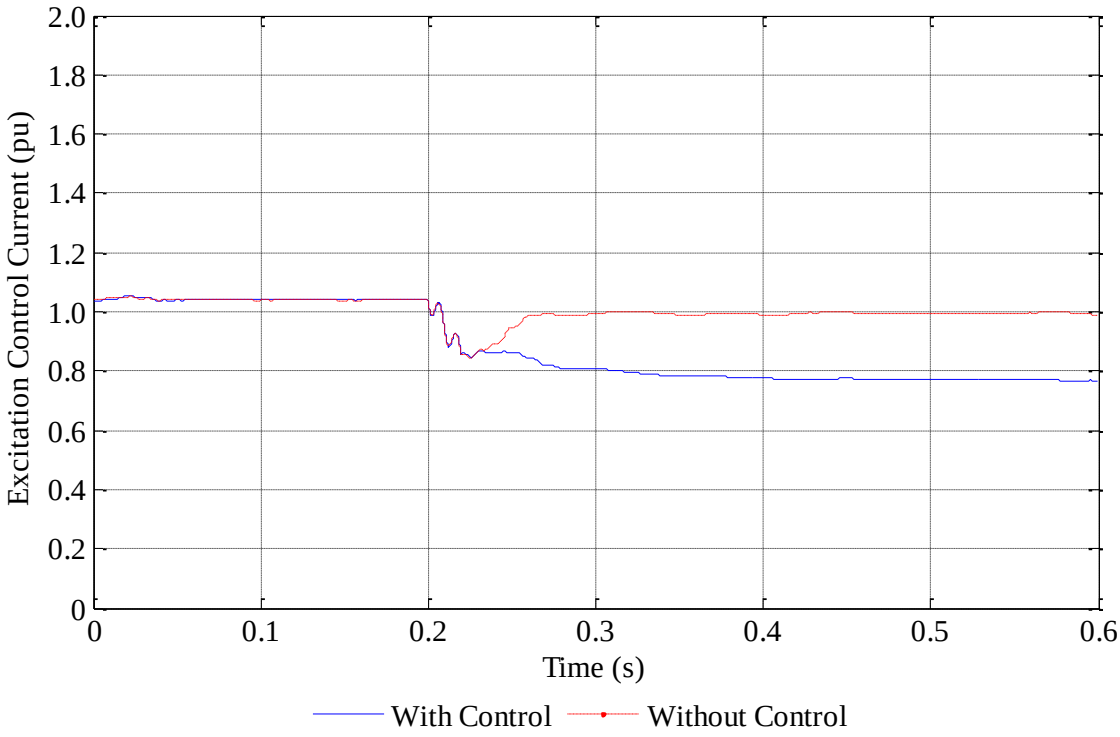

Fig. 7.7.2.4. Variation of excitation control current with and without feedback controller

The variations of real power in output winding, excitation control winding and mechanical system due to the changing fixed capacitance are depicted in Figs. 7.7.2.5 – 7.7.2.7 respectively. In the regulated system, the output power of the generator remains unchanged. However, due to the increase of output voltage, the output power of the unregulated system increases even at a fixed consumer load. This power balance is achieved by increasing both the mechanical power supplied by the prime mover and the deficit power supplied by the ESS. In the regulated system, mechanical power slightly decreases. In order to balance the resistive losses due to the high current in output winding, real power supplied by the ESS increases with the increasing fixed capacitance. In general, real power consumption of the regulated system is less than that of the unregulated system.

The effects of variations in mechanical torque on the torque-speed characteristics curve of a wind turbine are depicted in Fig. 7.7.2.8. In the regulated system, since the mechanical power decreases, mechanical torque is decreased by increasing the speed of the prime mover as shown by the solid arrow in Fig. 7.7.2.8. In the unregulated generator system, in order to increase the input mechanical power, mechanical torque

increases by decreasing the speed of the prime mover as shown by the broken arrow in the same figure.

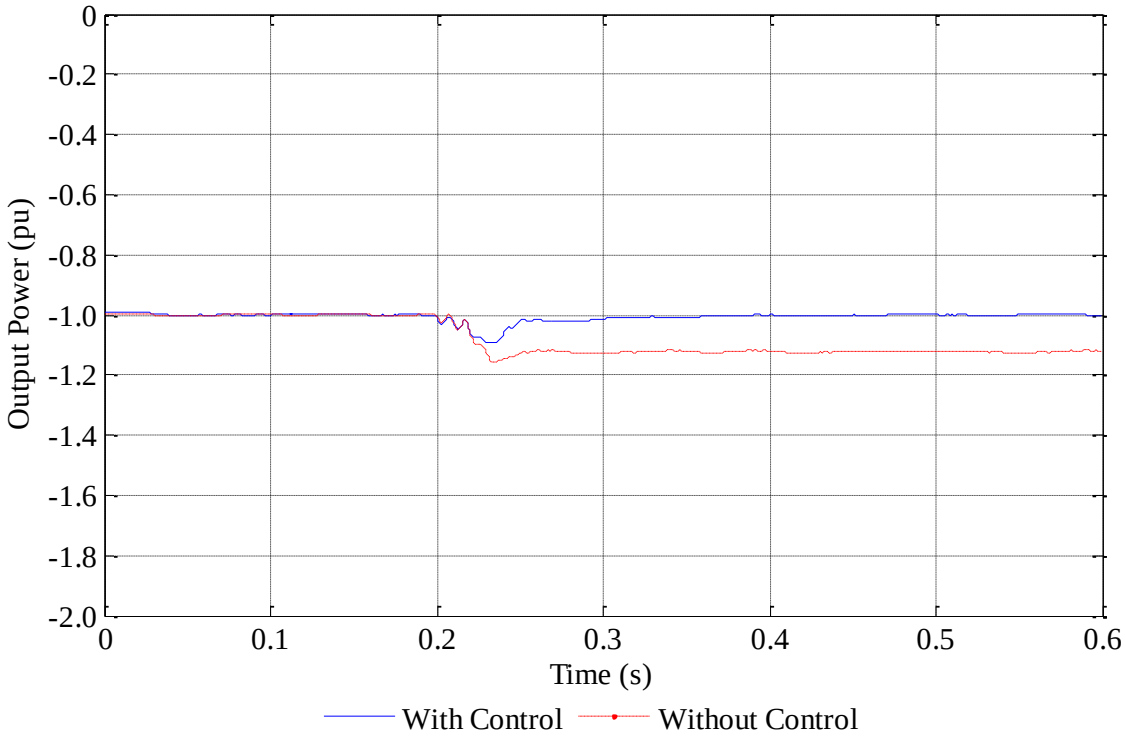

Fig. 7.7.2.5. Variation of output power with and without the feedback controller

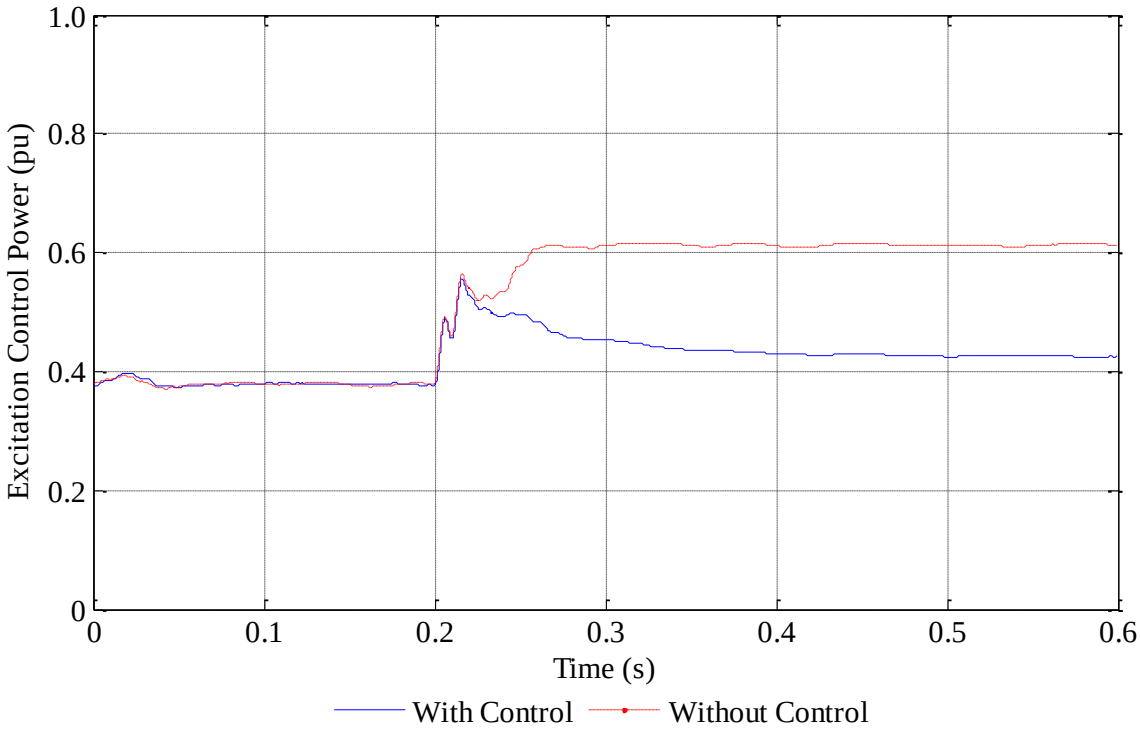

Fig. 7.7.2.6. Variation of excitation control power with and without the feedback controller

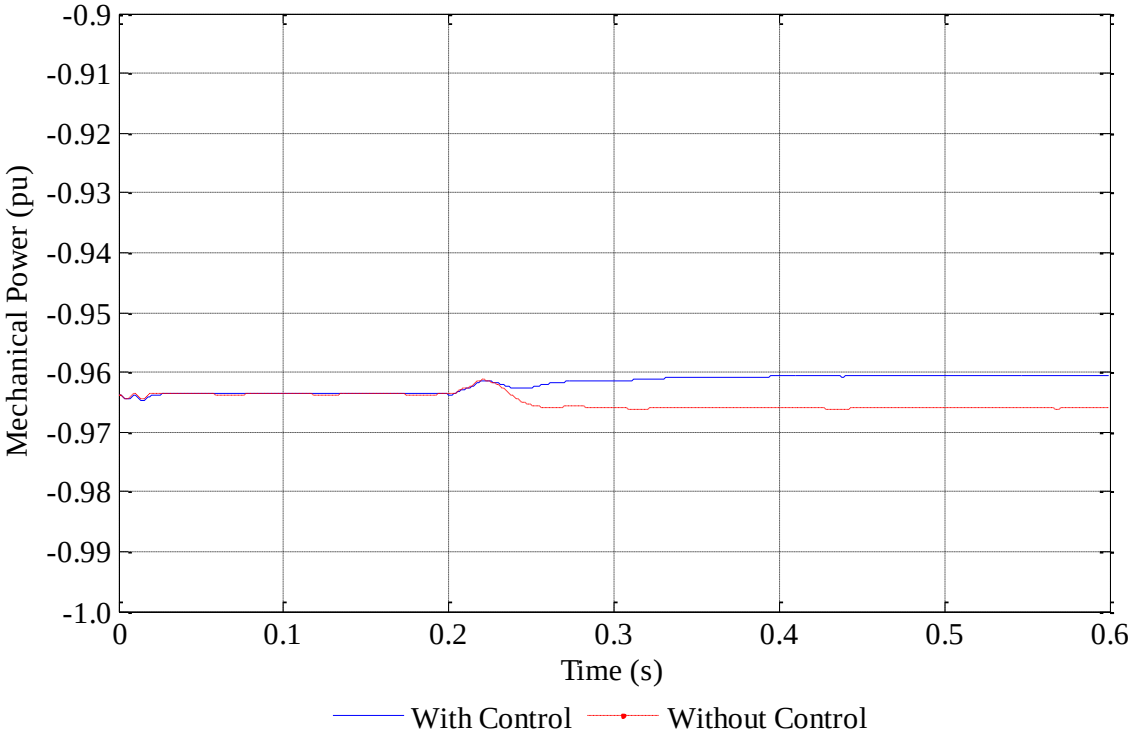

Fig. 7.7.2.7. Variation of mechanical power with and without the feedback controller

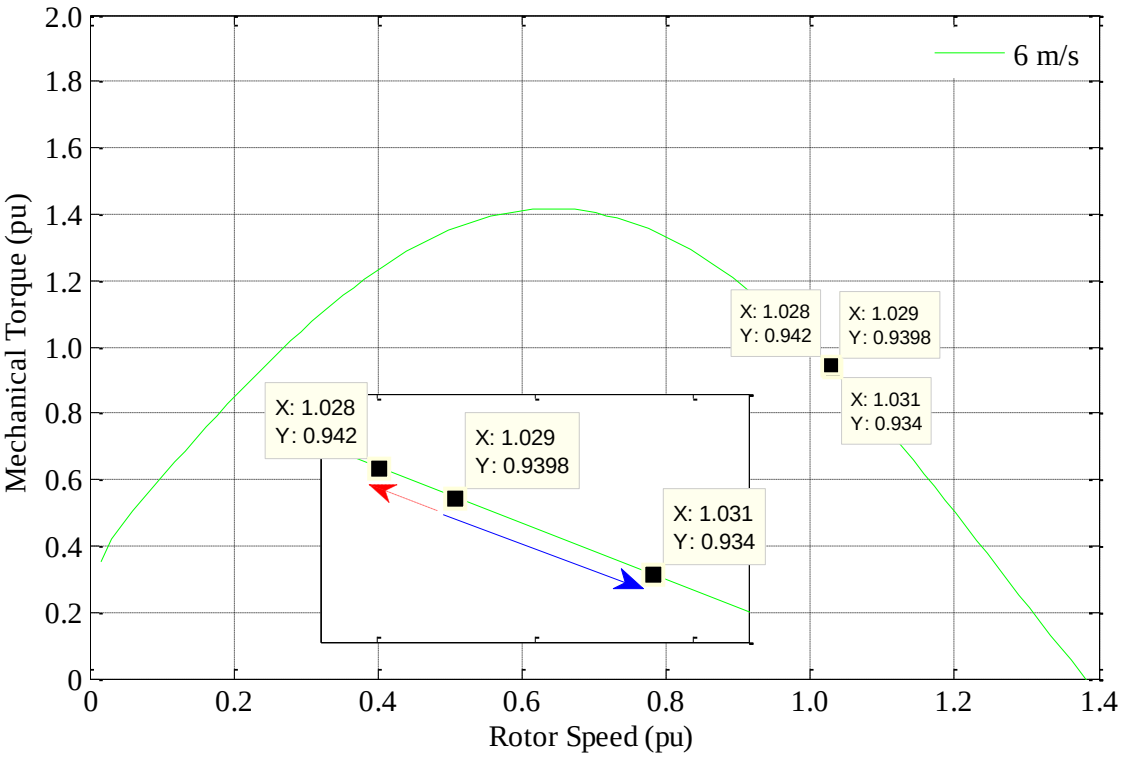

Fig. 7.7.2.8. Torque-speed characteristics of wind turbine at wind speed of 6 m/s

For the convenience of the comparison, the numerical values of system variables with and without the control system are given in Table 7.7.2.1.

Table 7.7.2.1
Values of System Variables

Parameter		V_{so} (pu)	V_{se} (pu)	I_{so} (pu)	I_{se} (pu)	Rotor Speed (pu)
Before disturbance		0.96	0.70	1.16	1.04	1.029
After Disturbance	Regulated System	0.96	0.64	1.36	0.78	1.031
	Unregulated System	1.02	0.7	1.44	0.99	1.028

7.7.3. Changes in Wind Speed

This test is conducted to examine the performance of the controlled system when there is a change in the wind speed. At the beginning, the generator is operating under a normal operating condition with a consumer load of 0.92 pu (i.e. full-load current at rated voltage) connected in parallel with a fixed capacitance of 0.54 pu at the wind speed of 6 m/s. In order to study the system performance when there is a change in the renewable source, the wind speed was increased up to 7 m/s at time t=0.2 s while all other operating parameters remain unchanged.

When this change is applied to both controlled and uncontrolled systems, there are variations of output voltages as illustrated in Fig. 7.7.3.1. The output voltage of controlled and uncontrolled systems increases with the increasing wind speed up to 1.025 pu and 1.04 respectively. However, in a regulated system, this voltage becomes stable at the rated value after experiencing a transient period as shown by the solid line in Fig. 7.7.3.1. When the same change is applied to the uncontrolled system, the output voltage becomes stable at the value 1.033 pu. This is illustrated by the broken line in the same figure. With the increasing wind speed, input mechanical power increases. Since the consumer load demand remains unchanged, the additional power supplied by the prime mover increases the voltage at the output of the unregulated generator system.

Figs. 7.7.3.2 – 7.7.3.4 show the variations of output current, excitation control voltage and excitation control current due to the changing wind speed respectively.

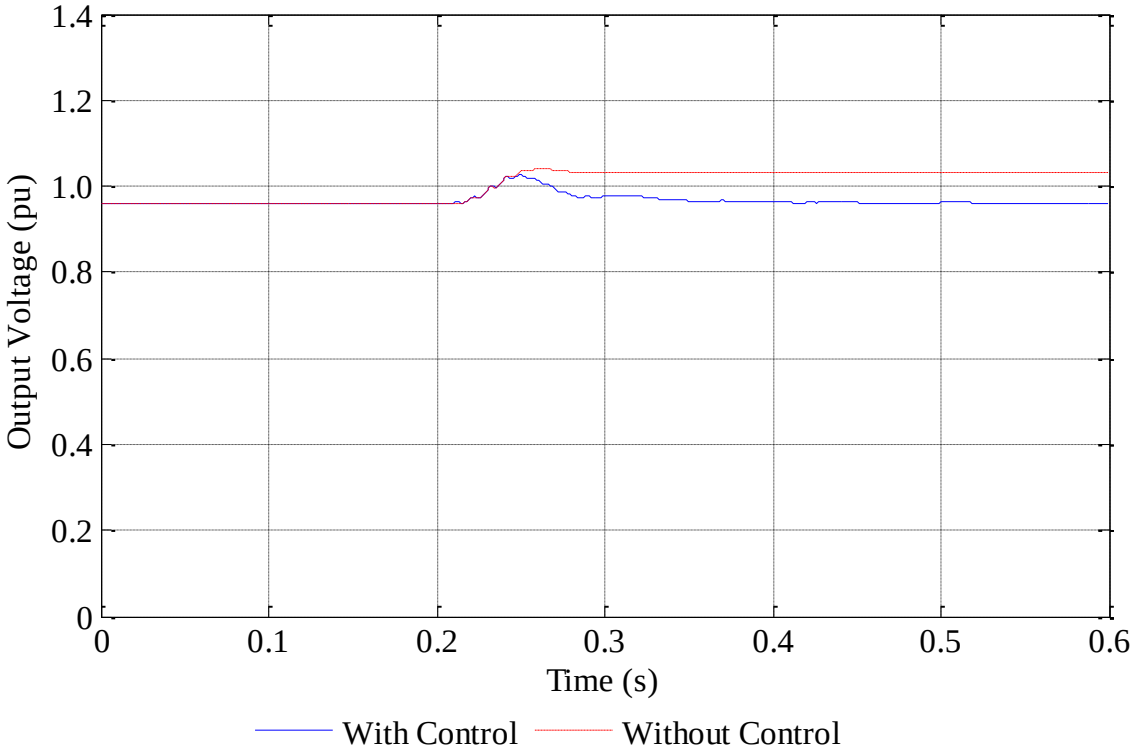

Fig. 7.7.3.1. Variation of output voltage with and without the feedback controller

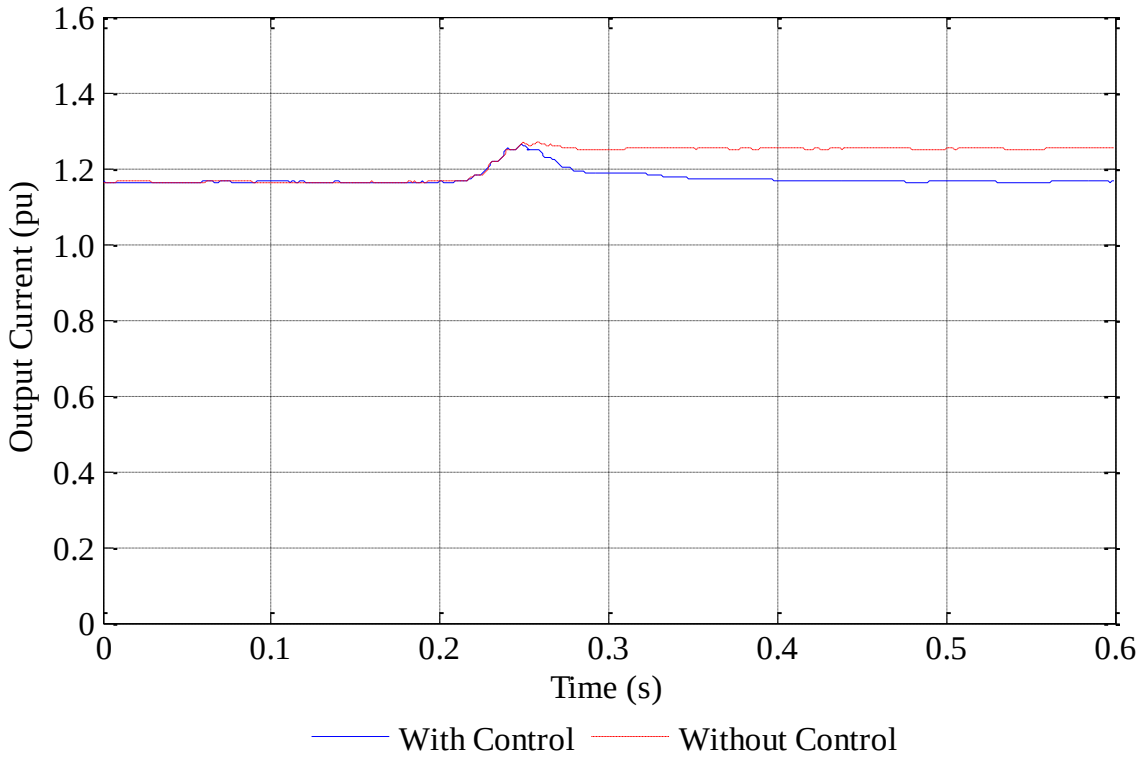

Fig. 7.7.3.2. Variation of output current with and without the feedback controller

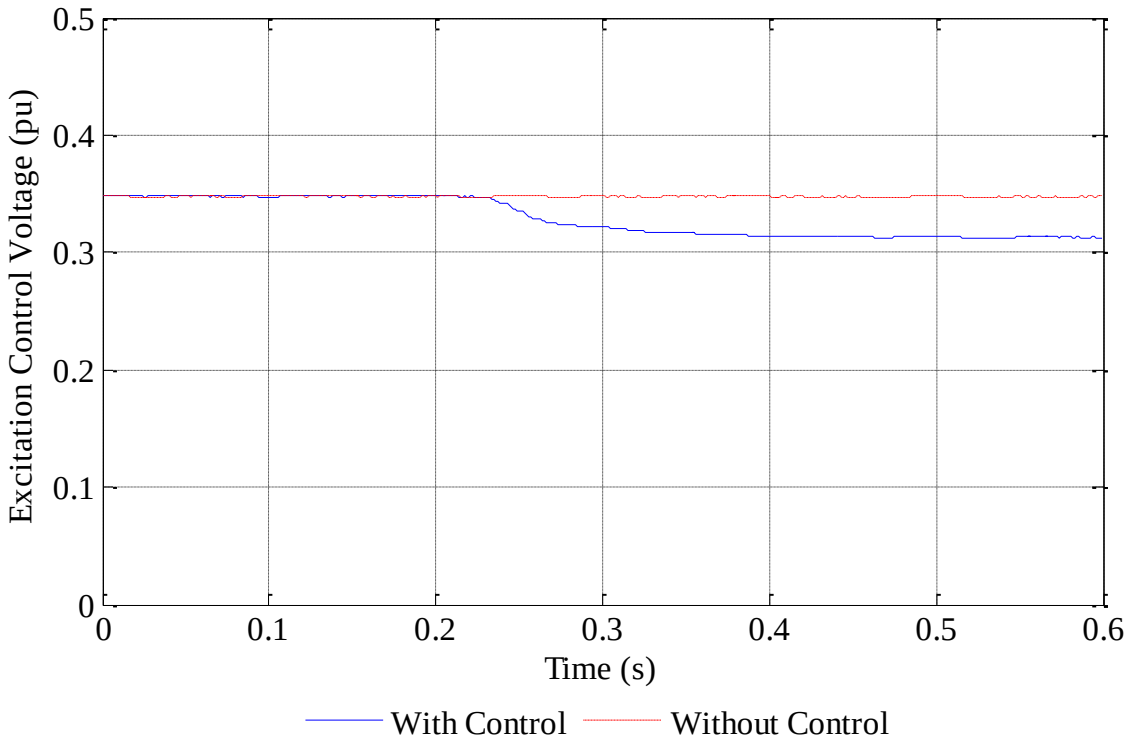

Fig. 7.7.3.3. Variation of excitation control voltage with and without feedback controller

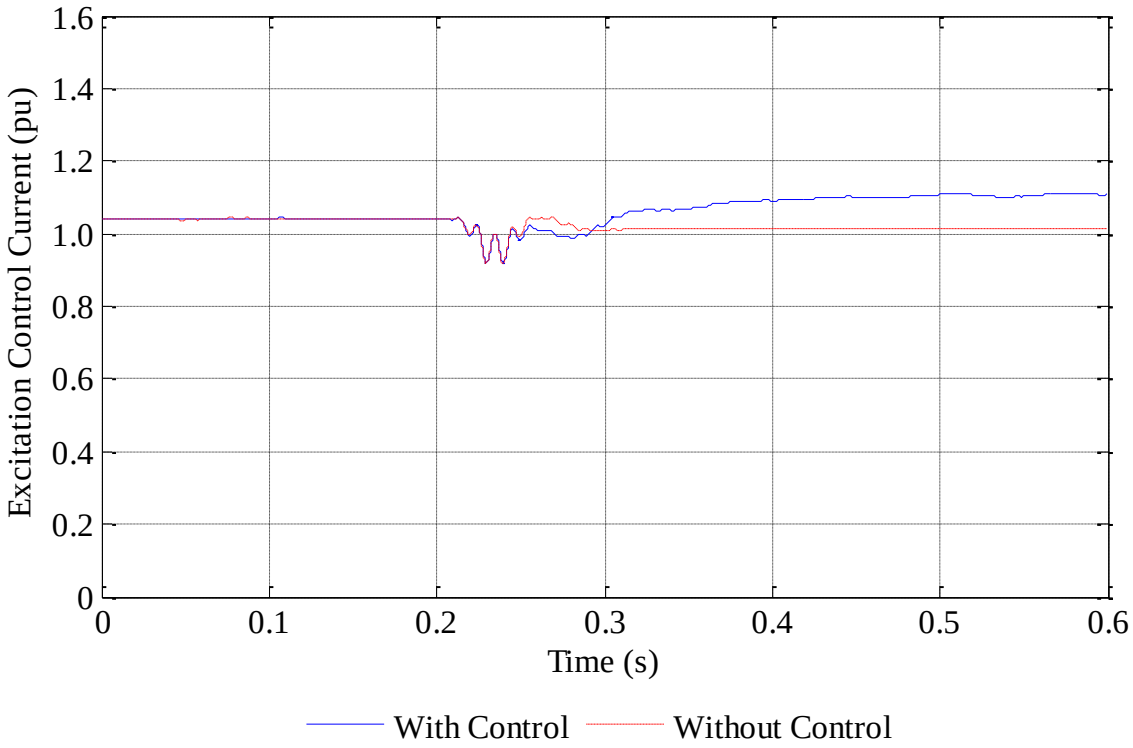

Fig. 7.7.3.4. Variation of excitation control current with and without the feedback controller

The variations of regulated system variables are shown by solid lines, whereas the variations of unregulated system variables are shown by broken lines as given in the legend in each figure. Due to the voltage increase, output current of unregulated system increases with the increasing wind speed. In the regulated system, this current is almost the same as that before the disturbance is applied. In the excitation control winding related variables, voltage decreases and current increases with the applied disturbance to maintain the constant voltage at the output in the regulated generator system. In the unregulated system, the excitation control winding voltage remains the same before and after the disturbance. The excitation control winding current in the same system slightly decreases with the increasing wind speed as shown in Fig. 7.7.3.4.

In order to further understand the variations in system variables due to the increasing wind speed, active power in output winding, excitation control winding and mechanical system are depicted in Fig. 7.7.3.5 – 7.7.3.7 respectively. Increasing wind speed increases the input mechanical power of the generator system. Therefore, the additional power supplied by the prime mover increases the output power and decreases the real power supplied by the ESS of the unregulated generator.

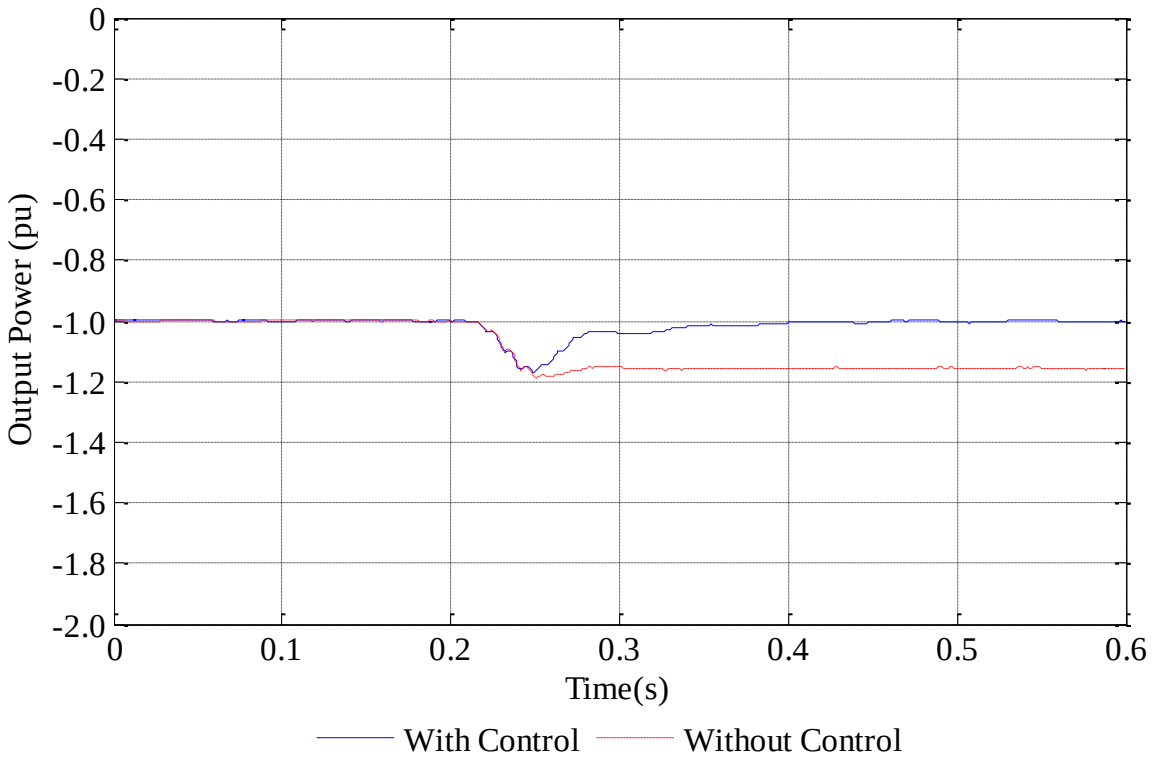

Fig. 7.7.3.5. Variation of output power with and without the feedback controller

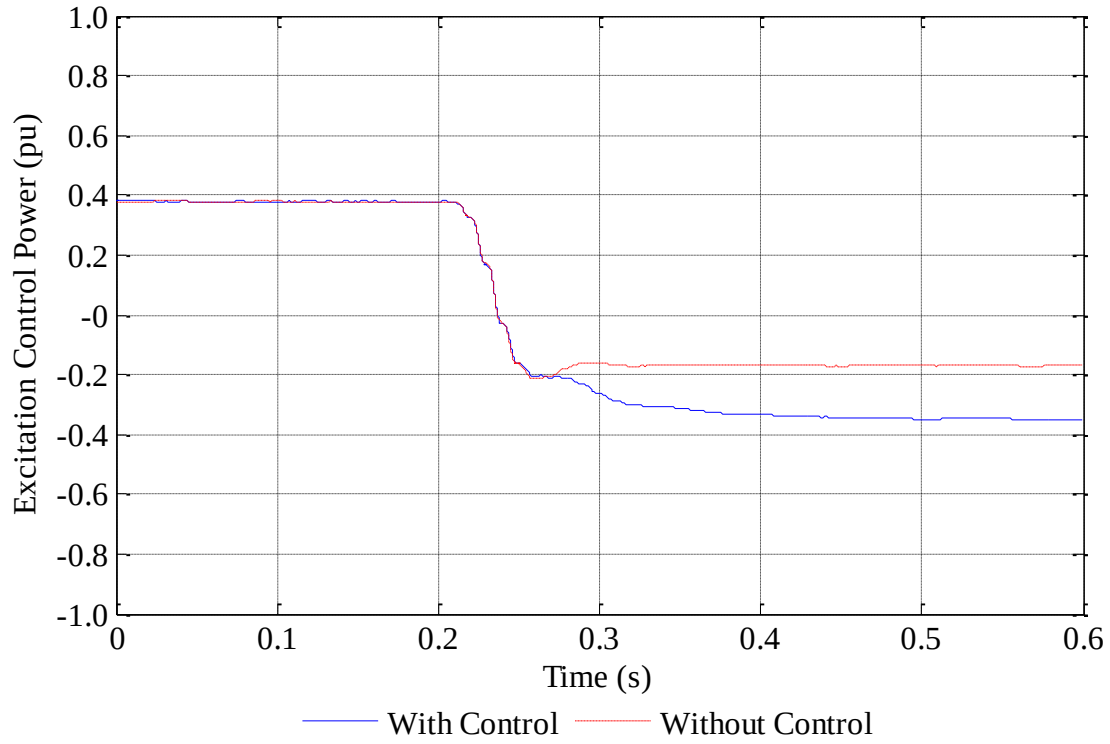

Fig. 7.7.3.6. Variation of excitation control power with and without feedback controller

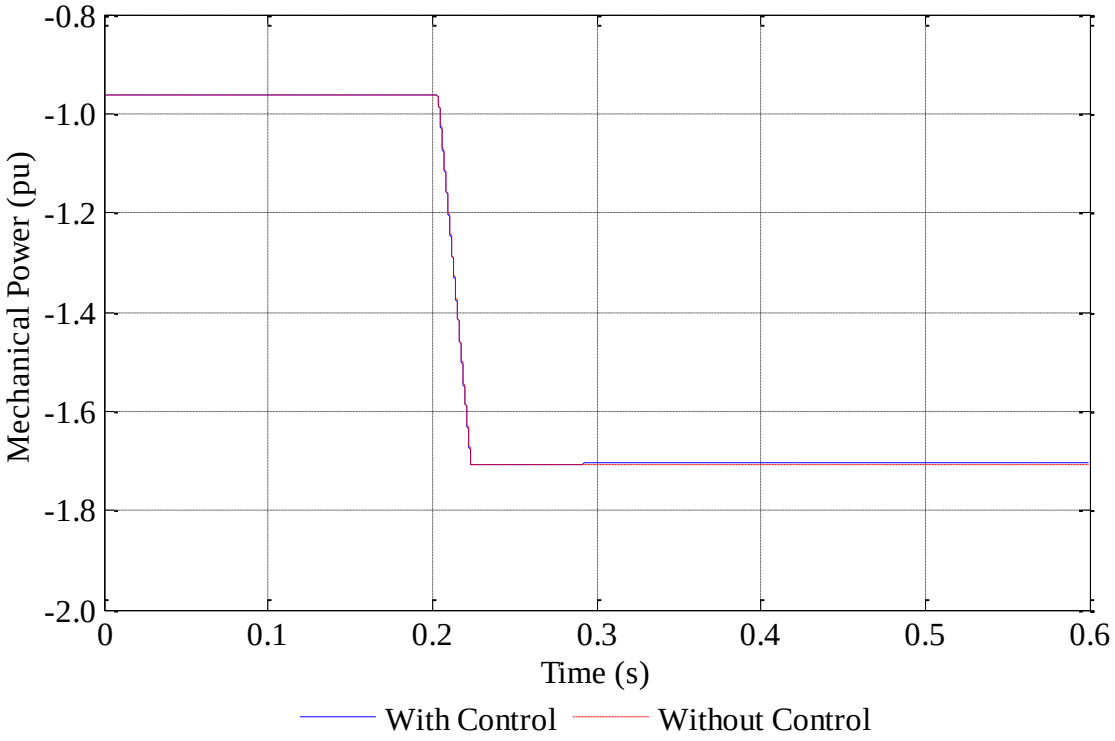

Fig. 7.7.3.7. Variation of mechanical power with and without the feedback controller

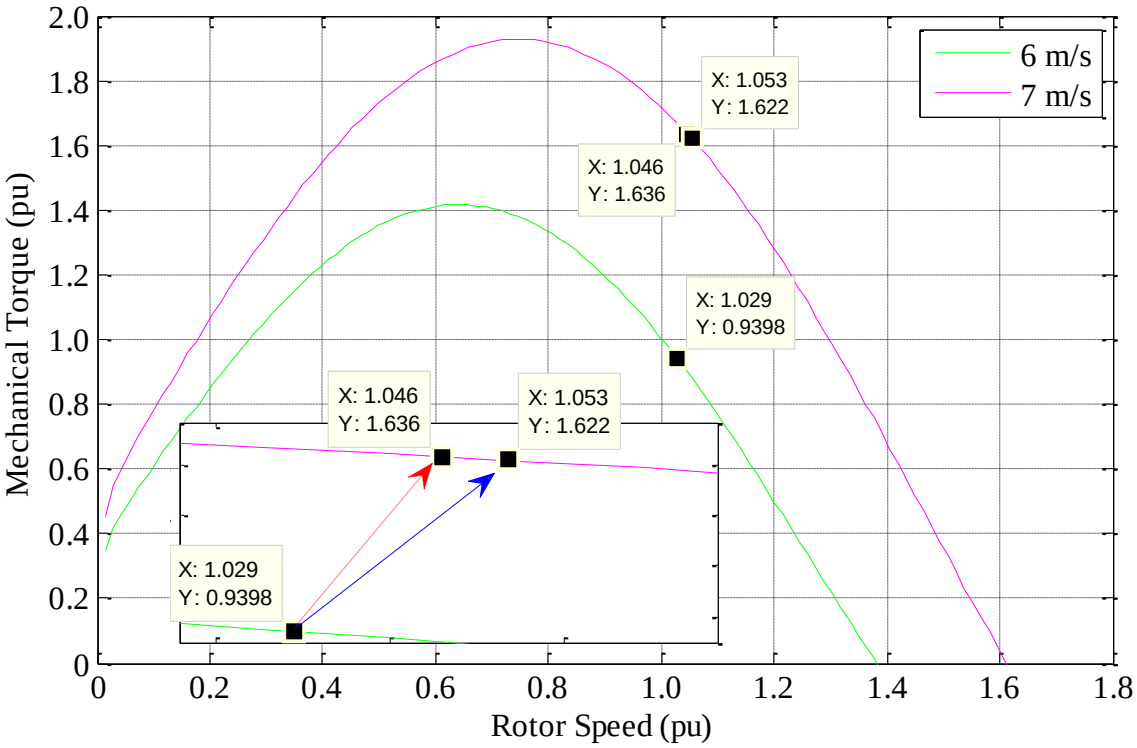

Fig. 7.7.3.8. Torque-speed characteristics of wind turbine at wind speed of 6 m/s and 7 m/s

However, in the regulated system, output power remains constant as the load demand is unchanged. Thus, the additional power is absorbed by the excitation control winding as shown in Fig. 7.7.3.5.

The variation of mechanical torque due to the applied disturbance is depicted on the torque-speed characteristics curve of wind turbine in Fig. 7.7.3.8. Since the mechanical power increases with the increasing wind speed, mechanical torque also increases in both regulated and unregulated systems. The variation of mechanical torque in a regulated system is illustrated using the solid arrow in Fig. 7.7.3.8 and the same variation in an unregulated system is shown by a broken arrow in the same figure.

The numerical values of system variables with and without the control system are given in Table 7.7.3.1.

Table 7.7.3.1
Values of System Variables

Parameter		V_{so} (pu)	V_{se} (pu)	I_{so} (pu)	I_{se} (pu)	Rotor Speed (pu)
Before disturbance		0.96	0.70	1.16	1.04	1.029
After Disturbance	Regulated System	0.96	0.63	1.17	1.11	1.053
	Unregulated System	1.03	0.70	1.25	1.02	1.046

7.7.4. Changes due to Short Circuit Condition

The performance of the designed control system at a short circuit condition is studied in this section. First, the generator is operating under a normal operating condition with a lagging power factor load of 1.15 pu (i.e. 44.8 % of full-load current at rated voltage) at a wind speed of 6 m/s. Fixed capacitance of 0.54 pu is connected in parallel with the consumer load. In order to apply the short circuit condition, at 0.1 s, the fixed capacitance connected at the output winding is short circuited. Within the period of testing, the consumer load and the wind speed are kept constant. Just after the disturbance, the currents in both the windings increase significantly whereas output voltage decreases up to zero. However, due to the equivalent series resistance of the capacitor and the internal resistance of the short circuited winding, the output voltage in uncontrolled system will not remain at zero for a long time. It gradually increases and after 0.5 s becomes steady at 0.17 pu. The output voltage in the controlled system continues at zero. The output winding current in controlled system also becomes steady at 0 pu while, after the heavy transients, output winding current in uncontrolled system reaches to steady condition at 2.69 pu which is 6 times the original current. Output voltage and current are illustrated in Fig. 7.7.4.1 and 7.7.4.2 respectively.

In both the systems, the excitation control winding currents behave similar to the corresponding output winding currents in different magnitude. In uncontrolled system, after the short circuit fault, the steady state value of the excitation control winding current is 2.8 times the its original value. In uncontrolled system, the

excitation control winding voltage remains unchanged whereas in controlled system, it becomes zero after the short circuit condition is applied.

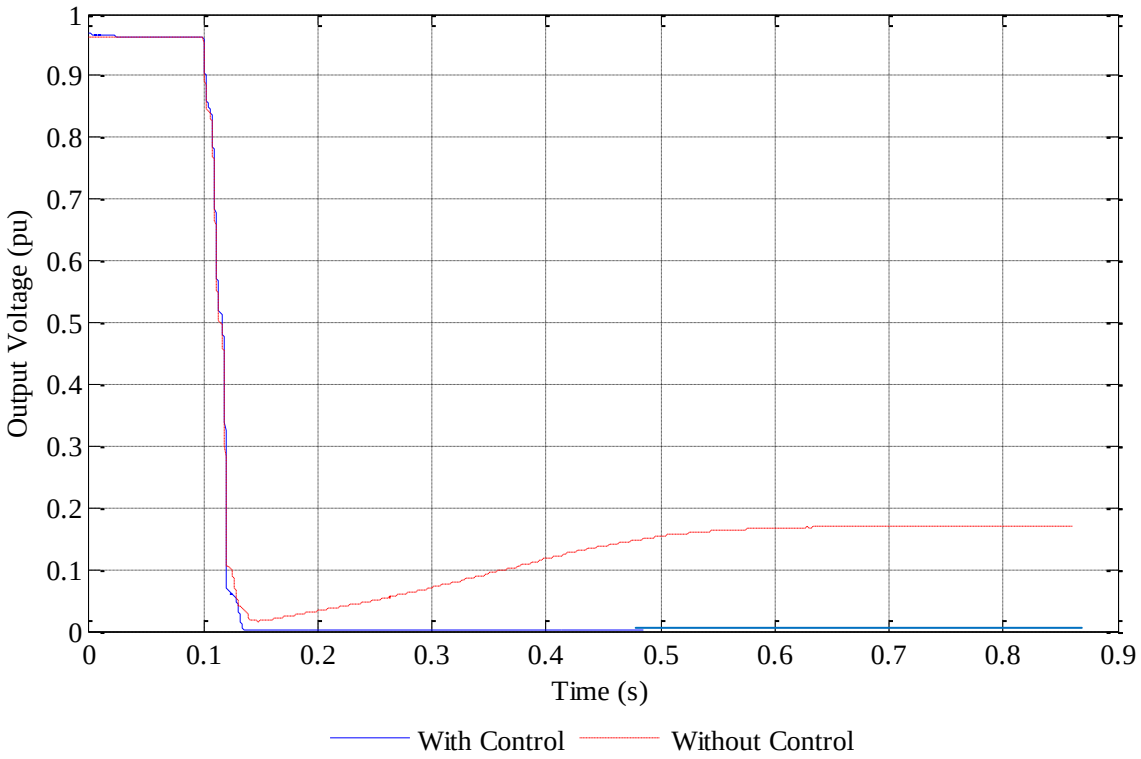

Fig. 7.7.4.1. Variation of output voltage with and without the feedback controller

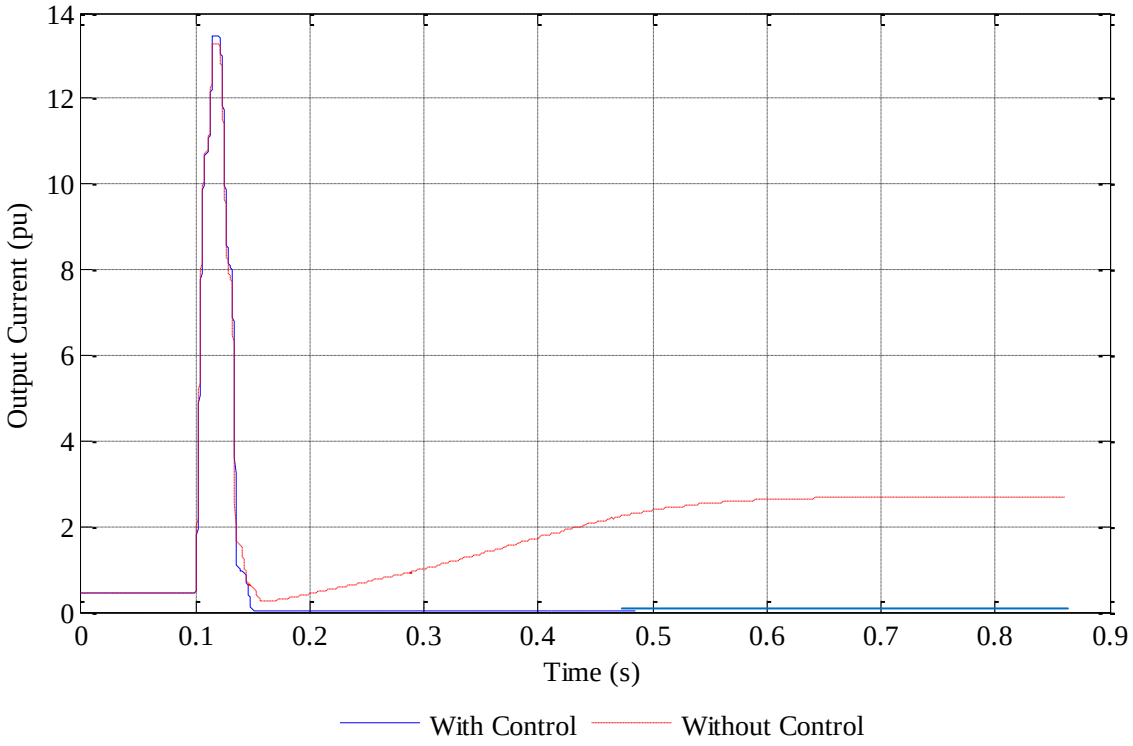

Fig. 7.7.4.2. Variation of output current with and without the feedback controller

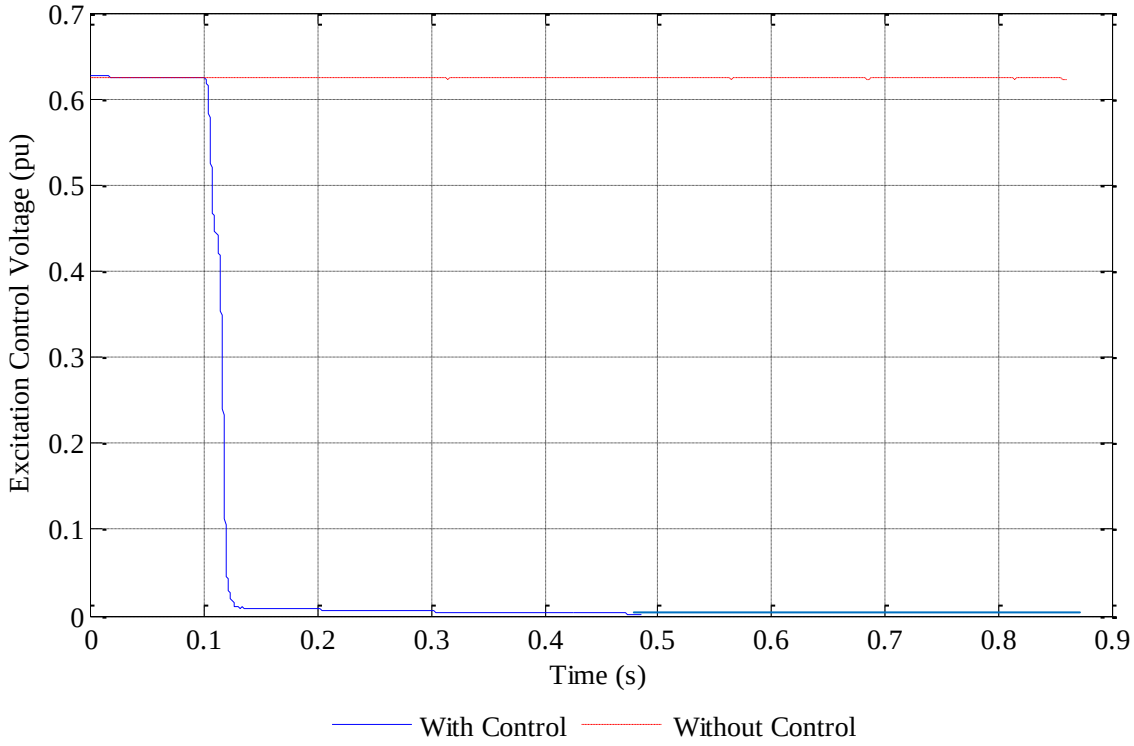

Fig. 7.7.4.3. Variation of excitation control winding voltage with and without the feedback controller

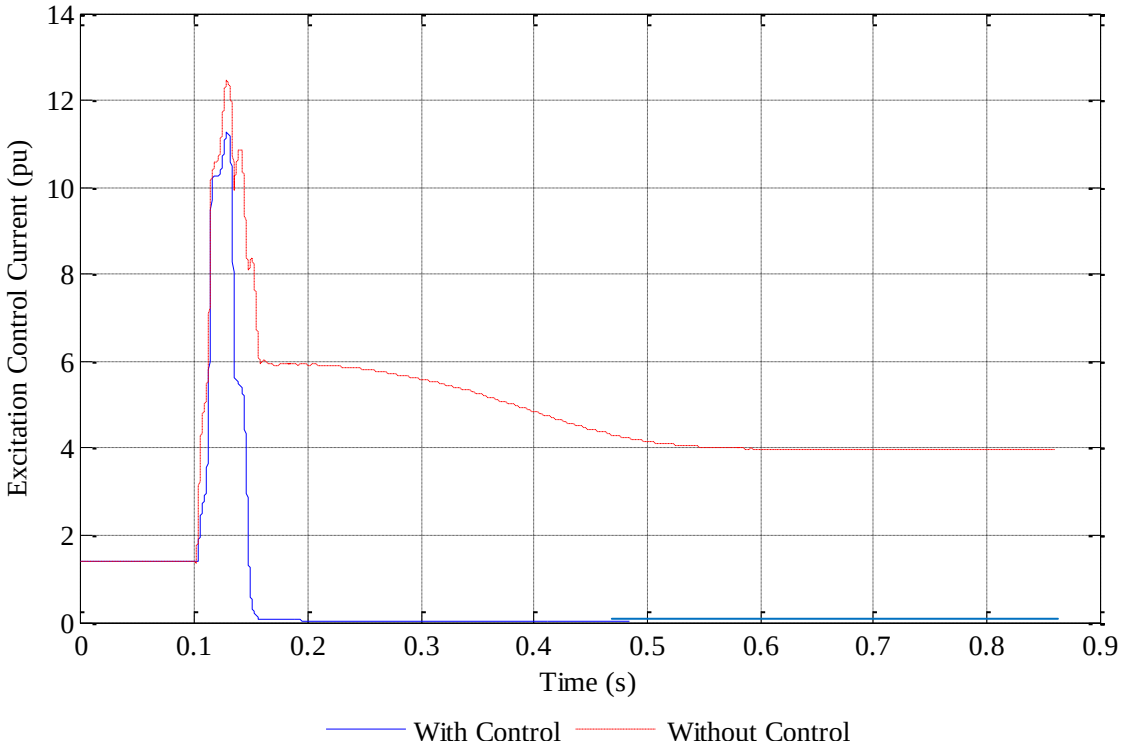

Fig. 7.7.4.4. Variation of excitation control winding current with and without the feedback controller

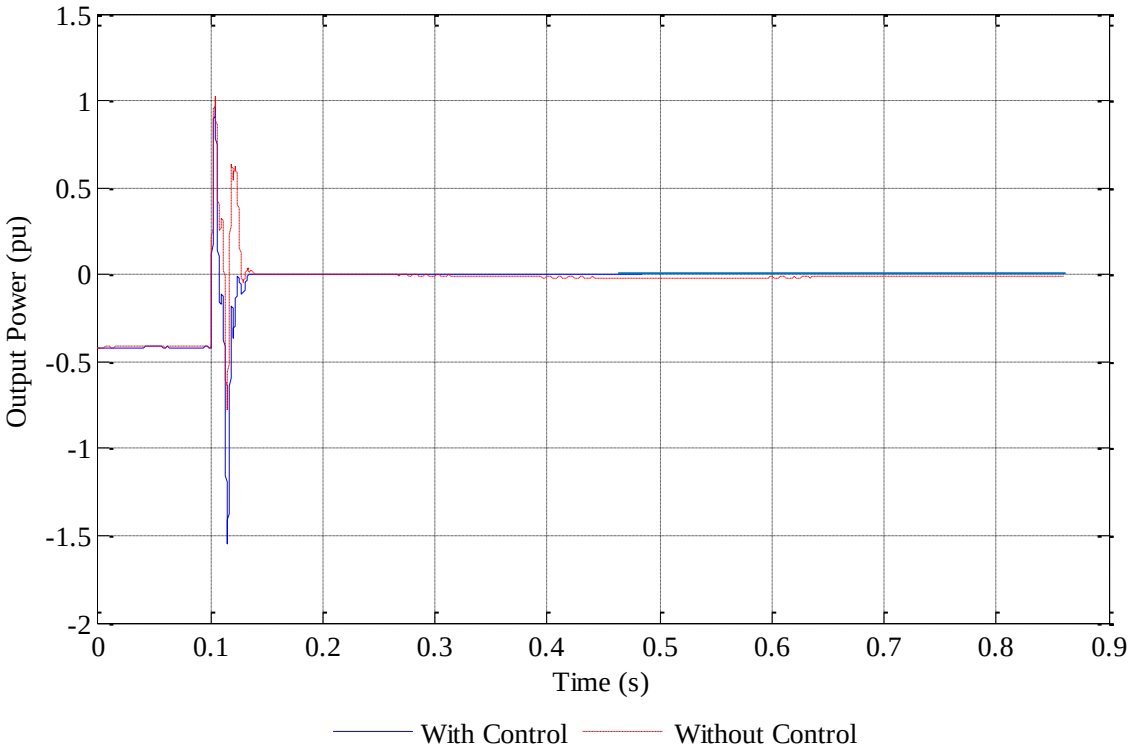

Fig. 7.7.4.5. Variation of output power with and without the feedback controller

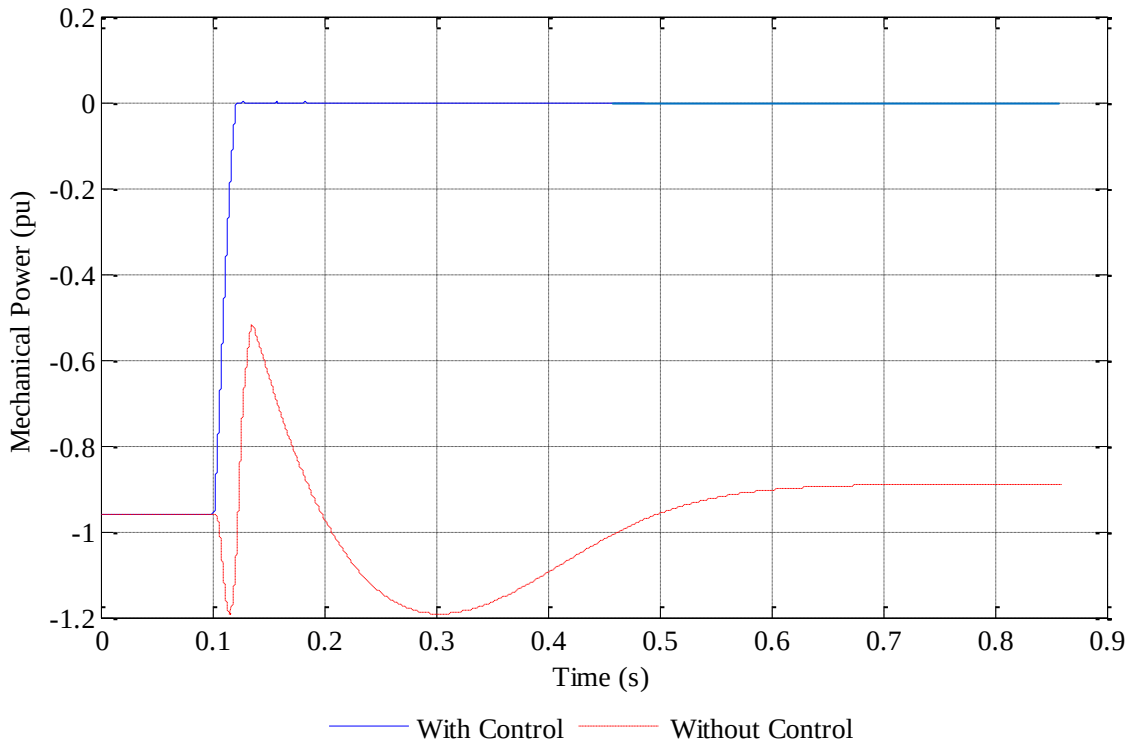

Fig. 7.7.4.6. Variation of mechanical power with and without the feedback controller

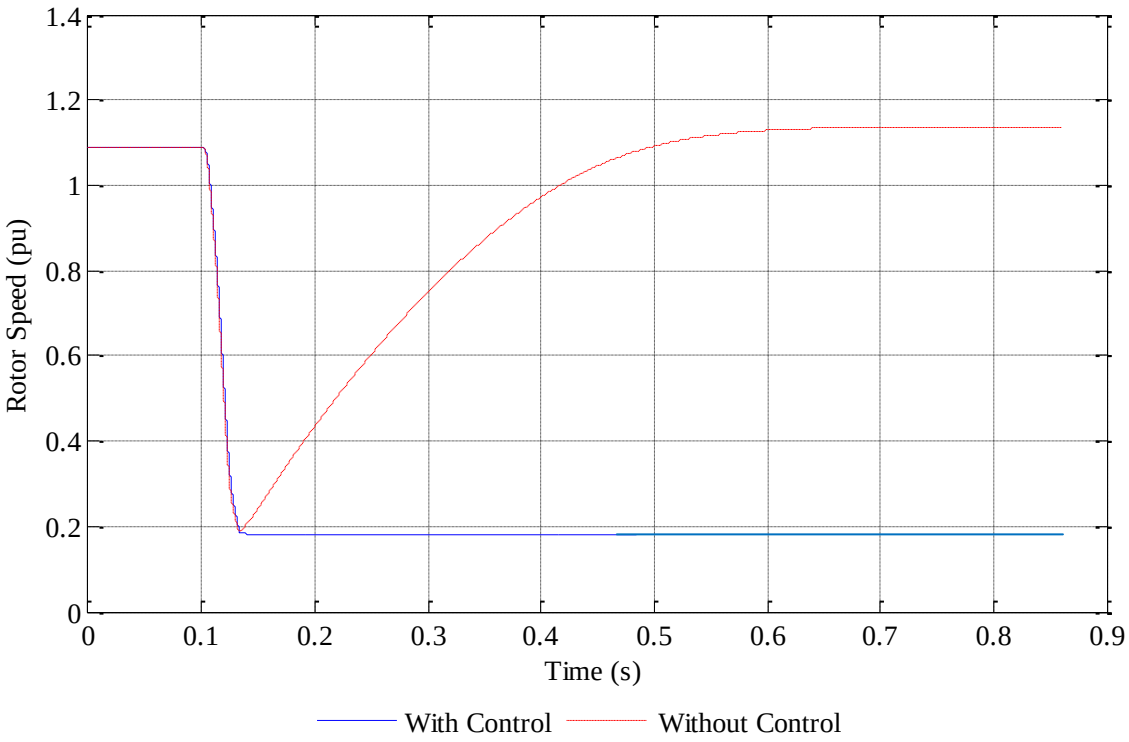

Fig. 7.7.4.7. Variation of rotor speed with and without the feedback controller

The changes in excitation control winding voltage and current are shown in Fig. 7.7.4.3 and 7.7.4.4 respectively. Due to the short circuit condition, since the load at the output winding reduces significantly, the output power becomes almost zero in both controlled and uncontrolled systems. However, in uncontrolled system, as the losses in the generator increases with the increasing currents in both the windings, the mechanical power is still needed to supply for the power balance in the system. Mechanical power of -0.96 pu and -0.89 pu are supplied by the prime mover before and after the disturbance respectively. The variations in output power and mechanical power due to the short circuit fault are depicted in Fig. 7.7.4.5 and 7.7.4.6 respectively. Figure 7.7.4.7 shows the changes in rotor speed due to the short circuit condition occurs at 0.1 s. Just after the disturbance, the rotor speed reduces to 0.2 pu and remains at the same value in controlled system while it increases up to 1.14 pu in uncontrolled system.

In order to evaluate the overall performance of the single-phase generator, the efficiency was calculated for different output power levels when employing a fixed capacitance of 30 µF. The power-efficiency curves are illustrated in Fig. 7.7.1. At the highest output power of 1400 W, the maximum efficiency is obtained as 75% of

the total electrical power of 2000 W. The maximum efficiency of the single-phase generator is more than 80% for an output power below 1000 W.

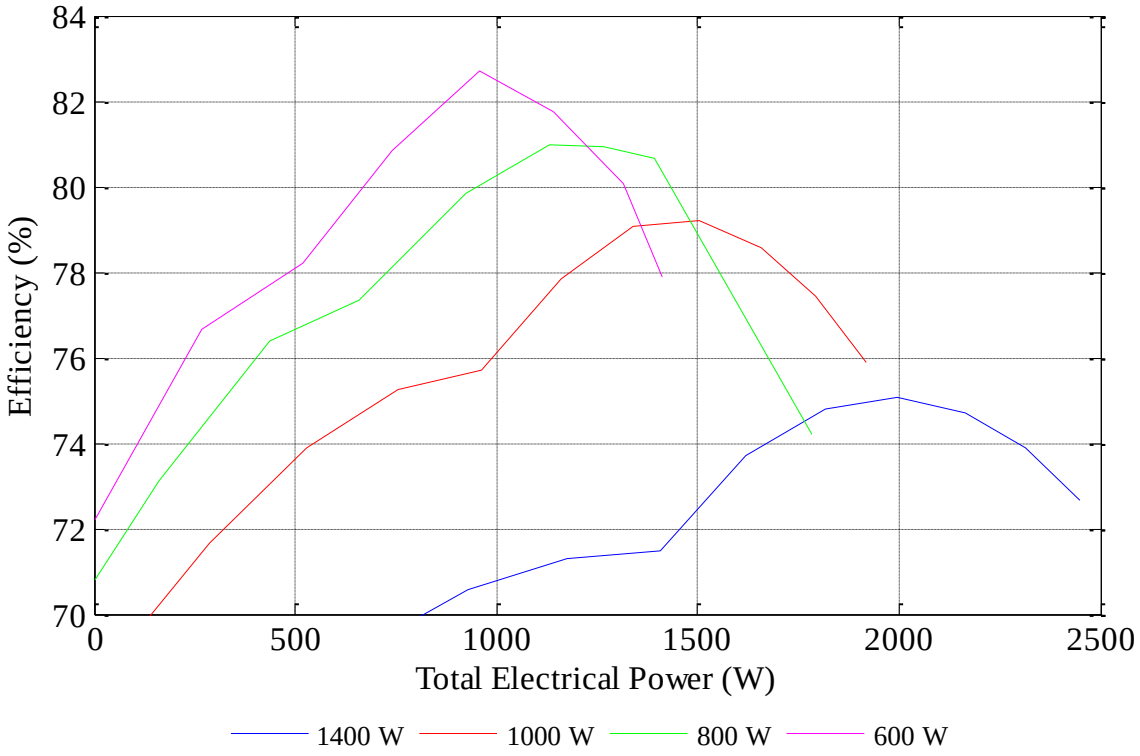

Fig. 7.7.1. Efficiency of single-phase induction generator

7.8 Chapter Conclusions

The designing of energy generation system including battery energy storage system, bi-directional dc-ac inverter and selecting of wind turbine characteristics suitable for small scale electricity generation plant is described in the first part of this chapter. Then the control system which is capable of maintaining a constant voltage and frequency at the output was designed using the mathematical model developed in the synchronous reference frame. The simulation results of the performance of entire system were presented in the later part of the chapter. With the Change of one system variable at a time, the designed control system is capable of supplying a constant output to the consumer. Also the performance of control system at a short circuit condition is presented in this chapter.

CHAPTER 8- CONCLUSIONS

8.1. Summary

In this thesis, mathematical modelling and closed-loop control of the output voltage and frequency of a single-phase induction generator based on a three-phase cage rotor machine suitable for renewable energy generation schemes such as wind or hydro power plants, have been presented. Since these techniques are not reported in the literature, the new methods developed to achieve the expected outcome of this thesis are summarized below.

In Chapter 3, in order to study the dynamic behavior of the novel single-phase induction generator, a comprehensive dynamic model was developed in the stationary 'αβ' reference frame to take into account the core loss resistance and the non-linearity of the magnetizing reactance in the saturated region. The model of consumer load and fixed capacitance of the generator system was developed for the first time in the literature. Furthermore, the equivalent circuit of the comprehensive dynamic model in α-axis and β-axis comprising of the generator, prime mover, excitation capacitors and the consumer loads has been given in this chapter.

The steady-state model in stationary 'αβ' reference frame was developed using the harmonic balance technique. This model and the resulting steady-state equivalent circuit in α–axis and β-axis were presented in the latter part of the Chapter 3.

In Chapter 4, in order to study the system performance in steady-state, using the derived steady-state equations, a computational technique was developed to calculate the values of system variables in steady-state for a given set of operating parameters in two different scenarios. First, the rotor speed is considered as known constant and secondly it is considered as a load-dependent variable. This technique is important to calculate the steady-state results of the novel single-phase generator.

In addition, a technique for calculating the operating parameters for a given set of system variables was developed in Chapter 4. Knowledge of the operational range of the operating parameters is important not only for the steady-state analysis, but also

for the safe operation of a practical renewable energy generation scheme.

Using the equations developed in Chapter 3, a comprehensive analysis of the dynamic behavior of the single-phase induction generator was performed in Chapter 5. Since the consumer load, fixed capacitance and speed of the prime mover are the operating parameters, the effects of changing one of these parameters on the system variables were studied by means of separate tests performed using Matlab software. The accuracy of the developed dynamic model was verified experimentally by comparing the simulation results with the corresponding experimental results obtained using a small three-phase induction machine employed in the laboratory experimental set-up. Furthermore, the voltage build-up process is studied analyzing the transient period of output winding voltage and current as it is important for the off-grid operation of the generator system. In order to validate the model under short circuit condition, the transients of the system variables were observed using the Matlab simulation results.

In the first part of Chapter 6, in order to achieve the voltage and current balance in the two-phase system, the operational ranges of the operating parameters were obtained from both simulations and experiments. Secondly, a comprehensive steady-state analysis of the uncontrolled generator was performed using the developed computational techniques. Considering the output voltage and the frequency are at desired rated values, the system variables were calculated for the change of each operating parameter while other operating parameters remain unchanged. Simulated results were experimentally verified to prove the accuracy of the developed techniques. The effect of changing the lagging power factor load on the system variables is also studied using Matlab simulations and presented in this chapter.

In both dynamic and steady-state analyses, the magnetizing inductance of the generator is considered as a non-linear variable. Linear and non-linear regions of the measured magnetizing characteristics of the machine were approximated by separate curves and the non-linearity of magnetizing inductance in a saturated region was taken into account.

Using the knowledge of steady-state behaviour of the single-phase induction generator, a control system is proposed to regulate the voltage and the frequency at the output winding. According to the proposed system, the generator is operated

using a variable speed prime mover. The regulation of voltage and frequency is achieved controlling the voltage and the frequency of the excitation control winding. Thus, a closed-loop control system was proposed to regulate the voltage and the frequency at the output of the generator. The computational procedure of designing the closed-loop control system is described in Chapter 7 of this thesis.

In the first part of Chapter 7, the computational procedure and the sizing of the energy storage system (ESS) were described. Since the battery energy storage system (BESS) connected at the terminals of the excitation control winding should be capable of supplying a constant voltage and constant frequency at the output of the generator regardless of the fluctuations in renewable energy source, it was designed to supply the load demand for a continuous three days in a situation where the availability of renewable energy source is extremely low.

Secondly, the bi-directional inverter was designed to transfer both real and reactive power through the excitation control winding. Among the available types of the bi-directional inverters, the standard full-bridge PWM single-phase DC-AC inverter connected to a step-up voltage transformer at the ac side was selected due to its simplicity and low cost. The components of the bi-directional inverter were selected based on the ratings of the BESS and the excitation control winding.

Considering this single-phase induction generator is going to be employed in a wind energy generation scheme, the wind turbine was selected to supply the rated power of the generator throughout the year. The power coefficient of the wind turbine was approximated using a fifth order polynomial of the Tip-Speed-Ratio. After using an appropriate gear ratio, the torque-speed and the power-speed characteristics curves of the prime mover were presented in the latter part of Chapter 7.

The ultimate objective of this research was to develop the closed-loop control system to regulate the voltage and the frequency at the consumer point. In order to design the control system, the dynamic model of a single-phase induction generator was developed in a synchronous reference frame. The equivalent circuit of the generator in a synchronous reference frame was presented in Chapter 7.

In order to develop the closed-loop transfer function of the generator system, first, the open-loop transfer function was developed using the derived dynamic equations

in a synchronous reference frame. In order to regulate the output voltage at the desired value, the modulation index of the bi-directional inverter was adjusted using a PI controller. The proportional and integral gains of the PI controller were calculated using the Ziegler–Nichols method. The stability of the proposed control system was verified by means of the Routh-array of the closed-loop transfer function. The frequency of the output voltage is controlled by the frequency of the switching signal of the PWM generator.

In addition, battery charging and discharging must be controlled to ensure the safety of the energy generation system and lifespan of the ESS. During the discharging, when the battery reached the maximum depth of discharge, the whole ESS was isolated from the generator system. On the other hand, during the charging, when the battery was fully charged, the additional power was dissipated through a variable resistor.

The proposed control system was simulated in Matlab Simulink using "user defined function" blocks. The wind turbine was assumed to be operated on the after peak of the torque-speed characteristics curve. In the simulations, this region was approximated by a straight line with a negative slope. The performance of the proposed system was extensively tested for any sudden variation in consumer load, fixed capacitance, wind speed and short circuit conditions. The predicted results can be achieved by the excellent performance of the proposed control system.

8.2. Main contributions of the thesis

The main contributions of this thesis are:

1. Development of a comprehensive dynamic model in stationary 'αβ' reference frame taking into account the core loss resistance and non-linearity of the magnetizing characteristics in the saturated region and the resulting dynamic equivalent circuit for the novel single-phase operation of a three-phase cage rotor induction machine.
2. Development of a steady-state model in stationary 'αβ' reference frame and steady-state equivalent circuit in α–axis and β–axis.
3. Development of a computational technique to calculate the values of system variables in steady-state for a given set of operating parameters at both known

and load-dependent speeds of the prime mover. Furthermore, the development of an analytical technique to calculate operating parameters in order to obtain the given set of generator system variables.

4. Determined both the dynamic and the steady-state performances of the novel single-phase induction generator driven by an unregulated prime mover.
5. Sizing of the proposed battery energy storage system and design of the single-phase bi-directional inverter to transfer both real and reactive power through the control winding.
6. The selection of the prime mover characteristics suitable for a small scale renewable energy generation scheme employs this novel single-phase induction generator.
7. Development of a dynamic model of a single-phase induction generator in synchronous reference frame, proposal of simple closed-loop control system to regulate the charging and discharging of the energy storage system and to maintain a constant voltage and frequency at the output of the generator and analysis of the performance of the proposed control system.

8.3. Future research directions

The work carried out in this thesis has opened several other research areas as listed below.

1. **Hardware prototype of the excitation circuit**: In order to obtain the experimental results presented in this thesis, the ESS and the bi-directional inverter was replaced by an auto transformer connected to the excitation control winding. Since the sizing of the ESS has been calculated in this thesis, a practical system with the same capacity should be selected for experimental purposes. Also, using the values calculated in the designing process, the hardware prototype of bi-directional inverter should be built with the appropriate size of each component available in the market. Replacing the auto transformer by the hardware prototype of ESS and bi-directional inverter, it is suggested that a small scale energy generation scheme be built.
2. **Verification of theoretical results for lagging power factor load:** Due to the limited access to the laboratory equipment, the experimental verifications of both dynamic and steady-state analysis of this generator presented in Chapter 5

and 6 respectively are limited to the consumer load with a unity power factor. Since in a practical system, the average consumer load has a lagging power factor close to unity, some of the steady-state results have been obtained for RL load using Matlab simulations. It is suggested that both dynamic and steady-state analysis of this generator system be undertaken both theoretically and experimentally for an RL load.

3. **Analysis of alternative TSCAOI configuration:** In the two series-connected winding and one isolated winding configuration of the induction machine, alternatively, two series-connected winding can be used for excitation control purposes while the isolated winding is used as the output winding. Using the mathematical equations presented in this thesis, dynamic and steady-state models of alternative generator configuration can be developed. Also the behaviour of the alternative configuration can be analysed. Furthermore, the advantages or the disadvantages of this configuration can be compared with those of the generator used in this thesis.
4. **Implement the energy generation system in the real world:** It is suggested that the proposed control system to be implemented in the real environment with small-scale wind or hydro turbine. Output of the practical energy generation system can be controlled through the bi-directional inverter connected to the excitation control winding. Finally, this energy conversion system can be implemented in both remote and urban areas in order to provide reliable electricity supply at a low unit cost in economical friendly manner.

BIBLIOGRAPHY

[1]. P.J. Musgrove, "Wind energy conversion," *Proc. IEE Phys. Rev.*, vol. 130, pp. 506–516, 1983.

[2]. G. James, W. Peng, K. Deng, "Managing household wind-energy generation," *IEEE Trans. Intelligent Systems*, vol. 23, no. 5, pp. 9-12, 2008.

[3]. M. Lu, C. Chang, W. Lee, L. Wang, "Combining the wind power generation system with energy storage equipment", *IEEE Trans. Industry Applications*, vol. 45, no. 6, pp. 2109-2115 , Nov/ Dec. 2009.

[4]. K. Rahbar, J. Xu, R. Zhang, "Real-time energy storage management for renewable integration in microgrid: an off-line optimization approach", *IEEE Trans. Smart Grid*, vol. 6, no. 1, pp. 124-134, Jan. 2015.

[5]. M. Mohibullah, A. M. Radzi, M.I.A. Hakim, "Basic design aspects of micro hydro power plant and its potential development in Malaysia," in *Proc. PECON*, 2004, pp. 220-223.

[6]. R. Karshi, P. Hu, R. Billinton, "A simplified wind power generation model for reliability evaluation", *IEEE Trans. Energy Conversion*, vol. 21, no. 2, pp. 553-540 , Jun. 2006.

[7]. S.R. Bull, "Renewable energy today and tomorrow", *Proc. IEEE*, vol. 89, no. 8, pp. 1216-1226, Aug. 2001.

[8]. *Dollars from Sense: The economic benefits of renewable energy*. Available: http://www.nrel.gov/docs/legosti/fy97/20505.pdf

[9]. L. Hirth, "Market value of solar power: Is photovoltaics cost-competitive?", *IET Renewable Power Generation*, vol. 9, no.1, pp. 37-45, 2015.

[10]. J. Wu, K. Wu, H. Jou, S. Chang, "Small-capacity grid-connected solar power generation system", *IET Power Electronics*, vol. 7, no. 11, pp. 2717-2725, 2014.

[11]. *Renewables 2010 global status report.* Available: http://www.ren21.net/Portals/0/documents/activities/gsr/REN21_GSR_2010_full_revised%20Sept2010.pdf

[12]. *Clean energy Australia report 2014.* Available: http://www.cleanenergycouncil.org.au/dam/cec/policy-and-advocacy/reports/2015/Clean-Energy-Australia-Report-2014.pdf

[13]. J. Gutierrez-Vera, “Use of renewable sources of energy in Mexico case: San Antonio Agua Bendita”, *IEEE Trans. Energy Conversion,* vol. 9, no. 3, pp. 442-450, Sep. 1994.

[14]. B. Thomsen, J. M. Guerrero, P.B. Thogersen, “Faroe islands wind-powered space heating microgrid using self-excited 220-kW induction generator”, *IEEE Trans. Sustainable Energy,* vol. 5, no. 4, pp. 1361-1366, Oct. 2014.

[15]. A. Y. Saber, G. K. Venayagamoorthy, “Plug-in vehicles and renewable energy sources for cost and emission reductions”, *IEEE Trans. Industrial Electronics,* vol. 58, no. 4, pp. 1229-1238 , Apr. 2011.

[16]. E. S. Rigas, S. D. Ramchurn, N. Bassiliades, “Managing electric vehicles in the smart grid using artificial intelligence: A survey”, *IEEE Trans. Intelligent Transportation Systems,* vol. 16, no. 4, pp. 1619-1635, Aug. 2015.

[17]. P. Hu, R. Karki, R. Billinton, “Reliability evaluation of generating systems containing wind power and energy storage”, *IET Generation, Transmission and Distribution,* vol. 3, no. 8, pp. 783-791, 2009.

[18]. N. Aparicio, I. MacGill, J. R. Abbad and H. Beltran, “Comparison of wind energy support policy and electricity market design in Europe, the United States, and Australia”, *IEEE Trans. Sustainable Energy,* vol. 3, no. 4, pp. 809-818, Oct. 2012.

[19]. E. Lerch, “Storage of fluctuating wind energy”, *in Conf. Power Electronics and Applications,* 2007, pp. 1-8.

[20]. S. Szewczuk, “Review of the strategic wind energy activities in South Africa”, *in Proc. ICUE,* 2012, pp. 1-8.

[21]. V. Akhmatov, P. B. Eriksen, “A large wind power system in almost island operatio – A Danish case study”, *IEEE Trans. Power Systems,* vol. 22, no. 3, pp. 937-943, Aug. 2007.

[22]. A. Izadian, N. Girrens, P. Khayyer, “Renewable energy policies: A brief review of the latest U.S. and E.U. policies ”, *IEEE Trans. Industrial Electronics Magazine,* vol. 7, no. 3, pp. 21-34, Sep. 2013.

[23]. N. H. Radzi, R.C. Bansal, Z. Y. Dong, K. N. Hasan, Z. Lu, “Overview of the Australian national electricity market transmission use of system charges for integrating renewable generation to existing grid”, *IET Generation, Transmission and Distribution,* vol. 6, no. 9, pp. 863-873, Apr. 2012.

[24]. A. S. Satpathy, N. K. Kishore, D. Kastha, N. C. Sahoo, “Control scheme for a stand-alone wind energy conversion system”, *IEEE Trans. Energy Conversion,* vol. 29, no. 2, pp. 418-425, Jun. 2014.

[25]. R. R. Chilipi, B. Singh, S. S. Murthy, S. Madishetti, G. Bhuvaneswari, “Design and implementation of dynamic electronic load controller for three-phase self-excited induction generator in remote small-hydro power generation”, *IET Renewable Power Generation,* vol. 8, no. 3, pp. 269-280, 2014.

[26]. K. Kim, T. L. Van, D. Lee, “Maximum output power tracking control in variable-speed wind turbine systems considering rotor inertial power”, *IEEE Trans. Industrial Electronics,* vol. 60, no. 8, pp. 3207-3217, Aug. 2013.

[27]. H. Li, Z. Chen, “Overview of different wind generator systems and their comparisons”, *IET Renewable Power Generation,* vol. 2, no. 2, pp. 123-138, 2008.

[28]. M. Liserre, R. Cardenas, M. Molinas, J. Rodriguez, “Overview of multi-MW wind turbines and wind parks”, *IEEE Trans. Industrial Electronics,* vol. 58, no. 4, pp. 1081-1095, Apr. 2011.

[29]. P. K. Goel, B. Singh, S. S. Murthy, N. Kishore, “Isolated wind-hydro hybrid system using cage generators and battery storage”, *IEEE Trans. Industrial Electronics,* vol. 58, no. 4, pp. 1141-1153, Apr. 2011.

[30]. T. Thiringer, J. Linders, “Control by variable rotor speed of a fixed-pitch wind turbine operating in a wide speed range”, *IEEE Trans. Energy Conversion,* vol. 8, no. 3, pp. 520-526, Sep. 1993.

[31]. L. Wang, R. Deng, “Transient performance of an isolated induction generator under unbalanced excitation capacitors”, *IEEE Trans. Energy Conversion,* vol. 14, no. 4, pp. 887-893, Dec. 1999.

[32]. S. Hazra, P. S. Sensarma, “Self-excitation and control of an induction generator in a stand-alone wind energy conversion system”, *IET Renewable Power Generation,* vol. 4, no. 4, pp. 383-393, 2010.

[33]. S. Hazra, P. Sensarma, “Vector approach for self-excitation and control of induction machine in stand-alone wind power generation”, *IET Renewable Power Generation,* vol. 5, no. 5, pp. 397-405, 2011.

[34]. A.Kh. Al Jabri, A. I. Alolah, “Limits on the performance of the three-phase self-excited induction generators”, *IEEE Trans. Energy Conversion,* vol. 5, no. 2, pp. 350-356, Jun. 1990.

[35]. J. B. Ekanayake, “Induction generators for small hydro schemes”, *IET Power Engineering,* vol. 16, no. 2, pp. 61-67, 2002.

[36]. R. C. Bansal, “Three-phase self-excited induction generators: An Overview”, *IEEE Trans. Energy Conversion,* vol. 20, no. 2, pp. 292-299, Jun. 2005.

[37]. K. Idjdarene, D. Rekioua, T. Rekioua, A. Tounzi, “Performance of an isolated induction generator under unbalanced loads”, *IEEE Trans. Energy Conversion,* vol. 25, no. 2, pp. 303-311, Jun. 2010.

[38]. M. Kabalan, B. Anabaraonye, “Solar photovoltaic versus micro-hydroelectricity: A framework for assessing the sustainability of community-run rural electrification projects”, *in Conf. Global Humanitarian Technology,* 2014, pp. 6-13.

[39]. M. F. Alkababjie, W. H. Hamdon, “Feasibility and environmental effects study of adding micro hydro power plant, converter and batteries to diesel generators using in electrification a remote Iraqi village”, *in Conf. Engineering Sciences,* 2012, pp. 1-6.

[40]. S. K. Pawar, Y. V. Aaher, A. C. Chaudhari, Y. B. Jadhav, “Modelling and simulation of hybrid solar-wind-grid power generation system for electrification”, *in Conf. Advances in Eng. And Tech.,* 2014, pp. 1-6.

[41]. J. P. Murenzi, T. S. Ustun, “The case for microgrids in electrifying sub-Saharan Africa”, *in Conf. Renewable Energy Congress,* 2015, pp. 1-6.

[42]. O. M. Longe, K. Ouahada, H. C. Ferreira, S. Chinnappen, “Renewable energy sources midrogrid design for rural area in South Africa”, *in Conf. ISGT,* 2014, pp. 1-5.

[43]. S. N. Mahato, S. P. Singh, M. P. Sharma, “Capacitors required for maximum power of a self-excited single-phase induction generator using a three-phase machine”, *IEEE Trans. Energy Conversion,* vol. 23, no. 2, pp. 372-381, Jun. 2008.

[44]. T. F. Chan, “Performance analysis of a three-phase induction generator connected to a single-phase power system”, *IEEE Trans. Energy Conversion,* vol. 13, no.3, pp. 205-211, Sep. 1998.

[45]. T. F. Chan, L. L. Lai, "A novel excitation scheme for a stand-alone three-phase induction generator supplying single-phase loads", *IEEE Trans. Energy Conversion,* vol. 19, no. 1, pp. 136-143, Mar. 2004.

[46]. T. F. Chan, L .L. Lai, "Steady-state analysis and performance of a single-phase self-regulated self-excited induction generator", *Proc. IET Generation, Transmission and Distribution,* vol. 149, no. 2, pp. 233-241, 2002.

[47]. S. S. Murthy, B. Singh, S. Gupta, B. M. Gulati, "General steady-state analysis of three-phase self-excited induction generator feeding three-phase unbalanced load/ single-phase load for stand-alone applications", *Proc. IET Generation, Transmission and Distribution,* vol. 150, no. 1, pp. 49-55, 2003.

[48]. J. L. Bhattacharya, J. L. Woodward, "Excitation balancing of a self-excited induction generator for maximum power output", *Proc. IET Generation, Transmission and Distribution,* vol. 135, no. 2, pp. 88-97, Mar. 1988.

[49]. A. H. Al-Bahrani, N .H. Malik, "Steady-state analysis and performance characteristics of a three-phase induction generator self excited with a single capacitor", *IEEE Trans. Energy Conversion,* vol. 5, no. 4, pp. 725-732, Dec. 1990.

[50]. Y. H. A. Rahim, "Excitation of isolated three-phase induction generator by a single capacitor", *Proc. IET Electric Power Applications,* vol. 140, no. 1, pp. 44-50, 1993.

[51]. T. Fukami, Y. Kaburaki, S. Kawahara, T. Miyamoto, "Performance analysis of a self-regulated self-excited single-phase induction generator using a three-phase machine", *IEEE Trans. Energy Conversion,* vol. 14, no. 3, pp. 622-627, Sep. 1999.

[52]. T. F. Chan, L. L. Lai, "A novel single-phase self-regulated self-excited induction generator using a three-phase machine", *IEEE Trans. Energy Conversion,* vol. 16, no. 2, Jun. 2001.

[53]. T. F. Chan, L. L. Lai, "single-phase operation of a three-phase induction motor with the Smith connection", *in Conf. PESS,* 2000, pp. 2453-2458.

[54]. T. F. Chan, L. L. Lai, "Single-phase operation of a three-phase induction generator using a novel line current injection method", *IEEE Trans. Energy Conversion,* vol. 20, no. 2, pp. 308-315, Jun. 2005.

[55]. U. K. Madawala, T. Geyer, J. B. Bradshaw, D. M. Vilathgamuwa, “Modeling and analysis of a novel variable-speed cage induction generator”, *IEEE Trans. Industrial Electronics,* vol. 59, no. 2, pp. 1020-1028, Feb. 2012.

[56]. S. M. Muyeen, R. Takahashi, T. Murata, J. Tamura, “Integration of an energy capacitor system with a variable-speed wind generator”, *IEEE Trans. Energy Conversion,* vol. 24, no. 3, pp. 740-749, Sep.2009.

[57]. W. Chen, Y. Hsu, “Controller design for an induction generator driven by a variable-speed wind turbine”, *IEEE Trans. Energy Conversion,* vol. 21, no. 3, pp. 625-635, Sep. 2006.

[58]. E. Byon, Y. Choe and N. Yampikulsakul, “Adaptive learning in time-variant processes with application to wind power systems”, *IEEE Trans. Automation Science and Engineering,* vol. PP, no. 99, pp. 1-11, 2015.

[59]. L. Lin, F. Sun, Y. Yang and Q. Li, “Comparison of reactive power compensation strategy of wind farm based on optislip wind turbines”, *in Conf. SUPERGEN,* 2009, pp. 1-6.

[60]. J. G. Slootweg, H. Polinder and W. L. Kling, “Initialization of wind turbine models in power system dynamics simulations”, *in Conf. PTC,* Portugal, Sep. 2001, pp. 6.

[61]. N. Mendis, K. M. Muttaqi, S. Sayeef and S. Perera, “Standalone operation of wind turbine-based variab;e speed generators with maximum power extraction capability”, *IEEE Trans. Energy Conversion,* vol. 27, no. 4, pp. 822-834, Dec. 2012.

[62]. A. Tani, M. B. Camara and B. Dakyo, “Energy management in the decentralized generation systems based on renewable energy-ultracapacitors and battery to compensate the wind/load power fluctuations”, *IEEE Trans. Industry Applications,* vol. 51, no. 2, pp. 1817-1827 , Mar./Apr. 2015.

[63]. G. Mandic, A. Nasiri, E. Ghotbi and E. Muljadi, “Lithium-Ion capacitor energy storage integrated with variable speed wind turbines for power smoothing”, *IEEE Journal Emerging and Selected Topics in Power Electronics,* vol. 1, no. 4, pp. 287-295, Dec. 2013.

[64]. J. P. Barton and D. G. Infield, “Energy storage and its use with intermittent renewable energy”, *IEEE Trans. Energy Conversion,* vol. 19, no. 2, pp. 441-448, Jun. 2004.

[65]. B. C. Ummels, E. Pelgrum and W. L. Kling, “Integration of large-scale wind power and use of energy storage in the Netherlands’ electricity supply”, *IET Renewable Power Generation,* vol. 2, no. 1, pp. 34-46, 2008.

[66]. R. Cardenas, R. Pena, G. Asher and J. Clare, “Power smoothing in wind generation systems using a sensorless vector controlled induction machine driving a flywheel”, *IEEE Trans. Energy Conversion,* vol. 19, no. 1, pp. 206-216, Mar. 2004.

[67]. S. Nomura, Y. Ohata, T. Hagita, H. Tsutsui, S. Tsuji-Iio and R. Shimada, “Wind farms linked by SMES systems”, *IEEE Trans. Applied Superconductivity,* vol. 15, no. 2, pp. 1951-1954, Jun. 2005.

[68]. M. Lu, C. Chang, W. Lee and L. Wang, “Combining the wind power generation system with energy storage equipment”, *IEEE Trans. Industry Applications,* vol. 45, no. 6, pp. 2109-2115, Nov./Dec. 2009.

[69]. M. T. Lawder, B. Suthar, P. W. C. Northrop, S. De, C. M. Hoff, O. Leitermann, M. L. Crow, S. Santhanagopalan and V. R. Subramanian, “Battery energy storage system (BESS) and battery management system (BMS) for grid-scale applications”, *Proc. IEEE,* vol. 102, no. 6, pp. 1014-1030, 2014.

[70]. A. Nagarajan and R. Ayyanar, “Design and strategy for the deployment of energy storage systems in a distribution feeder with penetration of renewable resources”, *IEEE Trans. Sustainable Energy,* vol. 6, no. 3, pp. 1085-1092, Jul. 2015.

[71]. K. W. Wee, S. S. Choi and D. M. Vilathgamuwa, “Design of a least-cost battery-supercapacitor energy storage system for realizing dispatchable wind power”, *IEEE Trans. Sustainable Energy,* vol. 4, no. 3, pp. 786-796, Jul. 2013.

[72]. M. Kleinberg, N. S. Mirhosseini, F. Farzan, J. Hansell, A. Abrams, W. Katzenstein, J. Harrison and M. A. Jafari, “Energy storage valuation under different storage forms and functions in transmission and distribution applications”, *Proc. IEEE,* vol. 102, no. 7, pp. 1073-1083, 2014.

[73]. L. F. Cabeza, C. Sole, A. Castell, E. Oro and A. Gil, “Review of solar thermal storage techniques and associated heat transfer technologies”, *Proc. IEEE,* vol. 100, no. 2, pp. 525-538, 2012.

[74]. B. Daryanian and R. E. Bohn, “Sizing of electric thermal storage under real time pricing”, *IEEE Trans. Power Systems,* vol. 8, no. 1, pp. 35-43, Feb. 1993.

[75]. L. Chen, Y. Liu, A. B. Arsoy, P. F. Ribeiro, M. Steurer and M. R. Iravani, "Detailed modeling of superconducting magnetic enery storage (SMES) system", *IEEE Trans. Power Delivery,* vol. 21, no. 2, pp. 699-710, Apr. 2006.

[76]. J. Lee, S. Joeng, Y. H. Han and B. J. Park, "Concept of cold energy storage for superconducting flywheel energy storage system", *IEEE Trans. Applied Superconductivity,* vol. 21, no. 3, pp. 2221-2224, Jun. 2011.

[77]. S. Vazquez, S. M. Lukic, E. Galvan, L. G. Franquelo and J. M. Carrasco, "Energy storage systems for transport and grid applications", *IEEE Trans. Industrial Electronics,* vol. 57, no. 12, pp. 3881-3895, Dec. 2010.

[78]. J. Rajasekharan and V. Koivunen, "Optimal energy consumption model for smart grid households with energy storage", *IEEE Journal Selected Topics in Signal Processing,* vol. 8, no. 6, pp. 1154-1166, Dec. 2014.

[79]. A. O. Converse, "Seasonal energy storage in a renewable energy system", *Proc. IEEE,* vol. 100, no. 2, pp. 401-409, 2012.

[80]. O. Z. Olaofe and K. A. Folly, "Energy storage technologies for small scale wind conversion system", *in Conf. PEMWA,* 2012, pp. 1-5.

[81]. M. S. Whittingham, "History, evolution, and future status of energy storage", *Proc. IEEE,* vol. 100, no. special centennial, pp. 1518-1534, 2012.

[82]. S. Samineni, B. K. Johnson, H. L. Hess and J.D. Law, "Modelling and analysis of a flywheel energy storage system for voltage sag correction", *IEEE Trans. Industry Applications,* vol. 42, no. 1, pp. 42-52, Jan./Feb. 2006.

[83]. I. Papic, "Simulation model for discharging a Lead-acid battery energy storage system for load leveling", *IEEE Trans. Energy Conversion,* vol. 21, no. 2, pp. 608-615, Jun. 2006.

[84]. V. Agarwal, K. Uthaichana and R. A. DeCarlo, "Development and validation of a battery model useful for discharging and charging power control and lifetime estimation", *IEEE Trans. Energy Conversion,* vol. 25, no. 3, pp. 821-835, Sep. 2010.

[85]. A. S. Satpathy, N. K. Kishore, D. Kastha and N. C. Sahoo, "Control scheme for a stand-alone wind energy conversion system", *IEEE Trans. Energy Conversion,* vol. 29, no. 2, pp. 418-425, Jun. 2014.

[86]. D. Pavkovic, M. Lobrovic, M. Hrgetic, A. Komljenovic and V. Smetko, "Battery current and voltage control system design with charging application", *in Conf. CCA,* 2014, pp. 1133-1138.

[87]. S. Zheng, L. Wang, “Research on charging control for battery in photovoltaic system”, *in Conf. ICIEA,* 2011, pp. 2321-2325.

[88]. R. Karthigaivel, N. Kumaresan and M. Subbiah, “Analysis and control of self-excited induction generator-converter systems for battery charging applications”, *IET Electric Power Applications,* vol. 5, no. 2, pp. 247-257, 2011.

[89]. M. Khamar and J. Askari, “A charging method for Lithium-ion battery using min-max optimal control”, *in Conf. IranianCEE,* 2014, pp. 1239-1243.

[90]. Z. Miao, L. Xu, V. R. Disfani and L. Fan, “An SOC-based battery management system for microgrids”, *IEEE Trans. Smart Grid,* vol. 5, no. 2, pp. 966-973, Mar.2014.

[91]. B.Lin, D. Chen and H. Tsay, “Bi-directional AC/ DC converter based on neutral point clamped”, *in Conf. ISIE,* 2001, pp. 619-624.

[92]. Y. Liao, “A novel reduced switching loss bidirectional AC/ DC converter PWM strategy with feedforward control for grid-tied microgrid systems”, *IEEE Trans. Power Electronics,* vol. 29, no. 3, pp.1500-1513, Mar. 2014.

[93]. D. C. Erb, O. C. Onar and A. Khaligh, “Bi-directional charging topologies for plug-in hybrid electric vehicles”, *in Conf. APEC,* 2010, pp. 2066-2072.

[94]. N. Kroutikova, C. A. Hernandez-Aramburo and T. C. Green, “State-space model of grid-connected inverters under current control mode”, *IET Electric Power Applications,* vol. 1, no. 3, pp. 329-338, 2007.

[95]. K. Natarajan, A.M. Sharaf, S. Sivakumar and S. Naganathan, “Modeling and control design for wind energy power conversion scheme using self-excited induction generator”, *IEEE Trans. Energy Conversion,* vol. EC-2, no. 3, pp. 506-512, Sep.1987.

[96]. S. S. Khorramabadi and A. Bakhshai, “Critic-based self-tuning PI structure for active and reactive power control of VSCs in microgrid systems”, *IEEE Trans. Smart Grid,* vol. 6, no. 1, pp. 92-103, Jan.2015.

[97]. *Missing*

[98]. S. Thomsen, N. Hoffmann and F. Wilhelm, “PI control, PI-basedstate space control, and model-based predictive control for drive systems with elastically coupled loads-a comparative study”, *IEEE Trans. Industrial Electronics,* vol. 58, no. 8, pp. 3647-3657, Aug. 2011.

[99]. M. S. Tavazoei, “From traditional to fractional PI Control: A key for generalization”, *IEEE Trans. Industrial Electronics Magazine,* vol. 6, no. 3, pp. 41-51, 2012.

[100]. N. C. Batista, R. Melicio, J. C. O. Matias and J. P. S. Catalao, “New blade profile for Darrieus wind turbines capable to self-start”, *in IET Conf. Renewable Power Generation,* 2011, pp. 1-5.

[101]. A. Causo, G. Dall’Aglio, G. Sala and A. Salati, “Power converter for vertical axis micro-wind generators”, *in Conf. Clean Electrical Power,* 2011, pp. 304-307.

[102]. L. E. Richartz, L. Huijie and G. Yi, “A new super-productive VAWT”, *in Conf. APPEEC,* 2009, pp. 1-3.

[103]. A. Ahmed, L. Ran and J. R. Bumby, “New constant electrical power soft-stalling control for small-scale VAWTs”, *IEEE Trans. Energy Conversion,* vol. 25, no. 4, pp. 1152-1161, Dec. 2010.

[104]. A. Ahamed, L. Ran and J. R. Bumby, “Stalling region instability compensation for constant power soft stalling control”, *in Conf. PEMD,* 2010, pp. 1-6.

[105]. W. E. Leithead and M. C. M. Rogers, “A comparison of the performance of constant speed HAWTs”, *in IET Conf. Renewable Energy- Clean Power 2001,* 1993, pp. 165-170.

[106]. D. J. Leith and W. E. Leithead, “Application of nonlinear control to a HAWT”, *in Conf. Control Applications,* 1994, pp. 245-250.

[107]. C. Ke, W. Zhongwei, H. Yanchen and Y. Guangjing, “The comparison of theoretical potential application of two types wind turbines in Nothern Shaanxi”, *in Conf. APPEEC,* 2012, pp. 1-4.

[108]. G. Ofualagba and E. U. Ubeku, “Wind energy conversion system-sind turbine modeling”, *in Conf. PES,* 2008, pp.1-8.

[109]. M. Ragheb and A. M. Ragheb, “Wind turbines theory- The Betz equation and optimal rotor tip speed ratio”, University of Illinois, USA. Available: http://cdn.intechopen.com/pdfs-wm/16242.pdf

[110]. S. Brusca, R. Lanzafame and M. Messina, “Design of a vertical axis wind turbine: how the aspect ratio affects the turbine’s performance”, *Int. J. Energy Environ. Eng.,* pp. 333-340. Available: http://link.springer.com/article/10.1007%2Fs40095-014-0129-x#page-1

[111]. C. Balasundar, S. Sudharshanan and R. Elakkiyavendan, "Design of an optimal tip speed ratio control MPPT algorithm for standalone WECS", *Int. J. Research in Applied Science and Engineering Technology*, vol.3, no. 5, May 2015. Available: http://www.ijraset.com/fileserve.php?FID=2435

[112]. Office of Energy Efficiency & Renewable Energy. Available: http://energy.gov/eere/water/types-hydropower-turbines

[113]. E. J. Lerner, "Power/ energy: Low-head hydro power: Small may be beautiful but, so far the economics for small-scale hydroelectric sites cloud a bright potential", *IEEE Spectrum,* vol. 17, no. 11, pp. 37-39, Nov. 1980.

[114]. C. L. T. Borges and R. J. Pinto, "Small hydro power plants energy availability modeling for generation reliability evaluation", *IEEE Trans. Power Systems,* vol. 23, no. 3, pp. 1125-1135, Aug. 2008.

[115]. Renewable energy consultancy agency, corp, "Mini-hydro power". Available: http://reca-corp.com/files/57897502.pdf

[116]. O. Ojo, "The transient and qualitative performance of a self-excited single-phase induction generator", *IEEE Trans. Energy Conversion,* vol. 10, no. 3, pp. 493-501, Sep. 1995.

[117]. S. N. Mahato, S. P. Singh and M. P. Sharma, "Transient performance of a three-phase self-excited induction generator supplying single phase load with electronic load controller", *in Conf. ESARS,* 2010, pp. 1-6.

[118]. C. Grantham, D. Sutanto and B. Mismail, "Stead-state and transient analysis of self-excited induction generators", *IET Journal Electric Power Applications,*vol. 136, no. 2, pp. 61-68, 1989.

[119]. C. Lee and L. Wang, "A novel analysis of parallel operated self-excited induction generators", *IEEE Trans. Energy Conversion,* vol. 13, no. 2, pp. 117-123, Jun. 1998.

[120]. L. Wang and C. Lee, "A novel analysis on the performance of an isolated self-excited induction generator", *IEEE Trans. Energy Conversion,* vol. 12, no. 2, pp. 109-117, Jun. 1997.

[121]. G. Quinonez-Varela and A. Cruden, "Modelling and validation of a squirrel cage induction generator wind turbine during connection to the local grid", *IET Journal Generation, Transmission and Distribution,* vol. 2, no. 2, pp. 301-309, 2008.

[122]. S. C. Kuo and L. Wang, “Analysis of isolated self-excited induction generator feeding a rectifier load”, *IET Journal Generation, Transmission and Distribution,* vol. 149, no. 1, pp. 90-97, 2002.

[123]. K. E. Hallenius, P. Vas and J. E. Brown, “The analysis of a saturated self-excited asynchronous generator”, *IEEE Trans. Energy Conversion,* vol. 6, no. 2, pp. 336-345, Jun. 1991.

[124]. D. Liyange and S. Rajakaruna, “Steady-state analysis of a novel single-phase induction generator for renewable energy conversion”, *in Conf. AUPEC,* 2014, pp. 1-7.

[125]. S. M. Alghuwainem, “Steady-state analysis of an isolated self-excited induction generator driven by regulated and unregulated turbine”, *IEEE Trans. Energy Conversion,* vol. 14, no. 3, pp. 718-723, Sep. 1999.

[126]. N. H. Malik and S. E. Haque, “Steady-state analysis and performance of on isolated self-excited induction generator”, *IEEE Trans. Energy Conversion,* vol. EC-1, no. 3, pp. 134-139, Sep. 1986.

[127]. A. K. Tandon, S. S. Murthy and G. J. Berg, “Steady-state analysis of capacitor self-excited induction generators”, *IEEE Trans. Power Apparatus and Systems,* vol. PAS-103, no. 3, pp. 612-618, Mar. 1984.

[128]. S. Rajakaruna and R. Bonert, “A technique for the steady-state analysis of a self-excited induction generator with variable speed”, *IEEE Trans. Energy Conversion,* vol. 8, no. 4, pp. 757-761, Dec. 1993.

[129]. Z. M. Salameh and L. F. Kazda, “Analysis of the steady-state performance of the double output induction generator”, *IEEE Trans. Energy Conversion,* vol. EC-1, no. 1, pp. 26-32, Mar. 1986.

[130]. S. N. Mahato, S. P. Singh and M. P. Sharma, “Analysis of transient performance of a single-phase self-regulated self-induction generator using a three-phase machine”, *in Conf. ICIT,* 2006, pp. 2709-2714.

[131]. S. S. Murthy, G. J. Berg, B. Singh, C. S. Jha and B. P. Singh, “Transient analysis of a three phase induction motor with single phase supply”, *IEEE Trans. Power Apparatus and Systems,* vol. PAS-102, no. 1, pp. 28-37, Jan. 1983.

[132]. S. N. Mahato, M. P. Sharma and S. P. Singh, “Transient analysis of a single-phase self-excited induction generator using a three-phase machine feeding dynamic load”, *in Conf. PEDES,* 2006, pp. 1-6.

[133]. L. Shridhar, B. Singh and C. S. Jha, “Transient performance of the self regulated short shunt self excited induction generator”, *IEEE Trans. Energy Conversion,* vol. 10, no. 2, pp. 261-267, Jun. 1995.

[134]. D. Liyanage and S. Rajakaruna, “Transient analysis of a single-phase variable speed cage induction generator with active excitation control”, *in Conf. AUPEC,* 2013, pp. 1-6.

[135]. L. Shridhar, B. Singh, C. S. Jha, B. P. Singh and S. S. Murthy, “Selection of capacitors for the self regulated short shunt self excited induction generator”, *IEEE Trans. Energy Conversion,* vol.10, no. 1, pp. 10-16, Mar. 1995.

[136]. L. Shridhar, B. Singh and C.S. Jha, “A step towards improvements in the characteristics of self excited induction generator”, *IEEE Trans. Energy Conversion,* vol. 8, no. 1, pp. 40-46, Mar. 1993.

[137]. D. Seyoum, C. Grantham and M. F. Rahman, “The dynamic characteristics of an isolated self-excited induction generator driven by a wind turbine”, *IEEE Trans. Industry Applications,* vol. 39, no. 4, pp. 936-944, Jul./Aug. 2003.

[138]. S. S. Murthy, O.P. Malik and A. K. Tandon, “Analysis of self-excited induction generators”, *IET Journal Generation, Transmission and Distribution,* vol. 129, no. 6, pp. 260-265, 1982.

[139]. S. Devabhaktuni and S.V.J. Kumar, “Design of excitation capacitance for self-excited induction generator”, *Int. J. Computer Science and Communication Networks,* vol. 1, no. 3, pp. 264-269. Available: http://www.ijcscn.com/Documents/Volumes/vol1issue3/ijcscn2011010311.pdf

[140]. S. S. Murthy and S. Acharya, “MATLAB based steady-state analysis of self-excited induction generator”, *in Conf. PEDS,* 2003, pp. 749-753.

[141]. V. Sandeep, S. S. Murthy and B. Singh, “A comparative study on approaches to curve fitting of magnetization characteristics for induction generators”, *in Conf. PEDES,* India, 2012, pp. 1-6.

[142]. B. K. Debta, K. B. Mohanty, “Analysis, voltage control and experiments on a self excited induction generator”, *in Conf. ICREPQ,* 2011.

[143]. P. Rasilo, An Belahcen and A. Arkkio, “Importance of Ion-loss medeling in simulation of wound-field synchronous machines”, *IEEE Trans. Magnetics,* vol. 48, no. 9, pp. 2495-2504, Sep. 2012.

[144]. D. Liayange and S. Rajakaruna, “An improved dynamic model for a single-phase generator based on three-phase cage rotor induction machine”, *in Conf. PEDS*, Sydney, 2015, pp. 934-939.

[145]. F. M. Fayez, El-Sousy and A. Kh. Al-Asmari, “Wavelet–Neural–Network Control for Maximization of Energy Capture in Grid Connected Variable Speed Wind Driven Self-Excited Induction Generator System”, Salman bin Abdulaziz University, Saudi Arabia. Available: http://cdn.intechopen.com/pdfs-wm/38418.pdf

[146]. O. Ojo, B. Gohoh, “The operation of a stand-alone, single-phase induction generator using a single-phase, pulse-width modulated inverter with a battery supply”, *IEEE Trans. Energy Conversion*, vol. 14, no. 3, pp. 526-531, Sep. 1999.

[147]. O. Ojo, “The transient and qualitative performance of a self-excited single-phase induction generator”, *IEEE Trans. Energy Conversion*, vol. 10, no. 3, pp. 493-501, Sep. 1995.

[148]. L.L. Lai and T.F. Chan, “Distributed Generation: Induction and Permanent Magnet Generators”, John Wiley & Sons Ltd, 2007, Ch. 5, pp. 111-160.

[149]. Lead-Acid battery state of charge vs voltage. Available: https://pssurvival.com/PS/Batteries/Lead_Acid/Lead-Acid_Battery_State_Of_Charge_Vs_Voltage_1993.pdf

[150]. G. M. Masters, “Renewable and efficient electric power systems”, Wiley, 2004, Ch. 9, pp. 562-572.

[151]. O. C. Onar, J. Kobayashi, D. C. Erb and A. Khaligh, “A bidirectional high-power-quality grid interface with a novel bidirectional noninverted buck-boost converter for PHEVs”, *IEEE Trans. Vehicular Technology*, vol. 61, no. 5, pp. 2018-2032, Jun. 2012.

[152]. Office of Environment and Heritage, NSW, “NSW small wind turbine consumer guide”. Available: http://www.environment.nsw.gov.au/resources/communities/110449-small-wind-turbine.pdf

[153]. Bureau of Meteorology, Australia, “Climate statistics for Australia locations”. Available: http://www.bom.gov.au/climate/averages/tables/cw_009789.shtml

[154]. Cheung, University of Kentucky, “EE 422G Notes: Chapter 6-Routh Array”. Available: http://www.vis.uky.edu/~cheung/courses/ee422g/lecture9.pdf

Every reasonable effort has been made to acknowledge the owners of copyright material. I would be pleased to hear from any copyright owner who has been omitted or incorrectly acknowledged.

APPENDIX A

DYNAMIC MODEL OF THE GENERATOR

Using (3.1.19), excitation control winding voltage and output winding voltage of single-phase induction generator can be written as

$$\begin{bmatrix} V_{se} \\ V_{so} \end{bmatrix} = \begin{bmatrix} R_s & 0 \\ 0 & 2R_s \end{bmatrix} \begin{bmatrix} i_{se} \\ i_{so} \end{bmatrix} + \omega_r L_{ms} \begin{bmatrix} -\sin\varphi_r & -\sin(\varphi_r + 2\pi/3) & -\sin(\varphi_r - 2\pi/3) \\ \sqrt{3}\cos\varphi_r & \sqrt{3}\cos(\varphi_r + 2\pi/3) & \sqrt{3}\cos(\varphi_r - 2\pi/3) \end{bmatrix} \begin{bmatrix} i_{ra} \\ i_{rb} \\ i_{rc} \end{bmatrix} + \begin{bmatrix} (L_{ls} + L_{ms}) & 0 \\ 0 & 2\left(L_{ls} + \frac{3}{2}L_{ms}\right) \end{bmatrix} \frac{d}{dt} \begin{bmatrix} i_{se} \\ i_{so} \end{bmatrix} +$$

$$L_{ms} \begin{bmatrix} \cos\varphi_r & \cos(\varphi_r + 2\pi/3) & \cos(\varphi_r - 2\pi/3) \\ \sqrt{3}\sin\varphi_r & \sqrt{3}\sin(\varphi_r + 2\pi/3) & \sqrt{3}\sin(\varphi_r - 2\pi/3) \end{bmatrix} \frac{d}{dt} \begin{bmatrix} i_{ra} \\ i_{rb} \\ i_{rc} \end{bmatrix} \quad \text{(A.1)}$$

Substituting for the rotor currents in (A.1) from (3.1.18), stator voltages can be re-written as

$$\begin{bmatrix} V_{se} \\ V_{so} \end{bmatrix} = \begin{bmatrix} R_s & 0 \\ 0 & 2R_s \end{bmatrix} \begin{bmatrix} i_{se} \\ i_{so} \end{bmatrix} + \omega_r L_{ms} \begin{bmatrix} -\sin\varphi_r & -\sin(\varphi_r + 2\pi/3) & -\sin(\varphi_r - 2\pi/3) \\ \sqrt{3}\cos\varphi_r & \sqrt{3}\cos(\varphi_r + 2\pi/3) & \sqrt{3}\cos(\varphi_r - 2\pi/3) \end{bmatrix} \begin{bmatrix} \cos\varphi_r & \sin\varphi_r \\ \cos\left(\varphi_r + \left(\frac{2\pi}{3}\right)\right) & \sin\left(\varphi_r + \left(\frac{2\pi}{3}\right)\right) \\ \cos\left(\varphi_r - \left(\frac{2\pi}{3}\right)\right) & \sin\left(\varphi_r - \left(\frac{2\pi}{3}\right)\right) \end{bmatrix} \begin{bmatrix} i_{r\alpha} \\ i_{r\beta} \end{bmatrix} +$$

$$\begin{bmatrix} (L_{ls} + L_{ms}) & 0 \\ 0 & 2\left(L_{ls} + \frac{3}{2}L_{ms}\right) \end{bmatrix} \frac{d}{dt} \begin{bmatrix} i_{se} \\ i_{so} \end{bmatrix} + L_{ms} \begin{bmatrix} \cos\varphi_r & \cos(\varphi_r + 2\pi/3) & \cos(\varphi_r - 2\pi/3) \\ \sqrt{3}\sin\varphi_r & \sqrt{3}\sin(\varphi_r + 2\pi/3) & \sqrt{3}\sin(\varphi_r - 2\pi/3) \end{bmatrix} \frac{d}{dt} \left\{ \begin{bmatrix} \cos\varphi_r & \sin\varphi_r \\ \cos\left(\varphi_r + \left(\frac{2\pi}{3}\right)\right) & \sin\left(\varphi_r + \left(\frac{2\pi}{3}\right)\right) \\ \cos\left(\varphi_r - \left(\frac{2\pi}{3}\right)\right) & \sin\left(\varphi_r - \left(\frac{2\pi}{3}\right)\right) \end{bmatrix} \begin{bmatrix} i_{r\alpha} \\ i_{r\beta} \end{bmatrix} \right\} \quad \text{(A.2)}$$

The derivative part of the rotor current in (A.2) can be written as

$$L_{ms} \begin{bmatrix} \cos\varphi_r & \cos(\varphi_r + 2\pi/3) & \cos(\varphi_r - 2\pi/3) \\ \sqrt{3}\sin\varphi_r & \sqrt{3}\sin(\varphi_r + 2\pi/3) & \sqrt{3}\sin(\varphi_r - 2\pi/3) \end{bmatrix} \left\{ \begin{bmatrix} \cos\varphi_r & \sin\varphi_r \\ \cos\left(\varphi_r + \left(\frac{2\pi}{3}\right)\right) & \sin\left(\varphi_r + \left(\frac{2\pi}{3}\right)\right) \\ \cos\left(\varphi_r - \left(\frac{2\pi}{3}\right)\right) & \sin\left(\varphi_r - \left(\frac{2\pi}{3}\right)\right) \end{bmatrix} \frac{d}{dt} \begin{bmatrix} i_{r\alpha} \\ i_{r\beta} \end{bmatrix} + \omega_r \begin{bmatrix} -\sin\varphi_r & \cos\varphi_r \\ -\sin\left(\varphi_r + \left(\frac{2\pi}{3}\right)\right) & \cos\left(\varphi_r + \left(\frac{2\pi}{3}\right)\right) \\ -\sin\left(\varphi_r - \left(\frac{2\pi}{3}\right)\right) & \cos\left(\varphi_r - \left(\frac{2\pi}{3}\right)\right) \end{bmatrix} \begin{bmatrix} i_{r\alpha} \\ i_{r\beta} \end{bmatrix} \right\} \quad \text{(A.3)}$$

Using (A.2) and (A.3), stator voltages in excitation control winding and output winding can be derived as

$$\begin{bmatrix} V_{se} \\ V_{so} \end{bmatrix} = \begin{bmatrix} R_s & 0 \\ 0 & 2R_s \end{bmatrix} \begin{bmatrix} i_{se} \\ i_{so} \end{bmatrix} + \begin{bmatrix} (L_{ls} + L_{ms}) & 0 \\ 0 & 2\left(L_{ls} + \frac{3}{2}L_{ms}\right) \end{bmatrix} \frac{d}{dt} \begin{bmatrix} i_{se} \\ i_{so} \end{bmatrix} + \frac{3}{2} L_{ms} \begin{bmatrix} 1 & 0 \\ 0 & \sqrt{3} \end{bmatrix} \frac{d}{dt} \begin{bmatrix} i_{r\alpha} \\ r_{r\beta} \end{bmatrix} \tag{A.4}$$

Using (3.1.20), the rotor voltages in stationary 'abc' reference frame can be written as

$$\begin{bmatrix} 0 \\ 0 \\ 0 \end{bmatrix} = \begin{bmatrix} R_r & 0 & 0 \\ 0 & R_r & 0 \\ 0 & 0 & R_r \end{bmatrix} \begin{bmatrix} i_{ra} \\ i_{rb} \\ i_{rc} \end{bmatrix} + \omega_r L_{ms} \begin{bmatrix} -\sin\varphi_r & \sqrt{3}\cos\varphi_r \\ -\sin(\varphi_r + 2\pi/3) & \sqrt{3}\cos(\varphi_r + 2\pi/3) \\ -\sin(\varphi_r - 2\pi/3) & \sqrt{3}\cos(\varphi_r - 2\pi/3) \end{bmatrix} \begin{bmatrix} i_{se} \\ i_{so} \end{bmatrix} + \begin{bmatrix} (L_{lr} + L_{mr}) & -\frac{1}{2}L_{mr} & -\frac{1}{2}L_{mr} \\ -\frac{1}{2}L_{mr} & (L_{lr} + L_{mr}) & -\frac{1}{2}L_{mr} \\ -\frac{1}{2}L_{mr} & -\frac{1}{2}L_{mr} & (L_{lr} + L_{mr}) \end{bmatrix} \frac{d}{dt} \begin{bmatrix} i_{ra} \\ i_{rb} \\ i_{rc} \end{bmatrix} +$$

$$L_{ms} \begin{bmatrix} \cos\varphi_r & \sqrt{3}\sin\varphi_r \\ \cos(\varphi_r + 2\pi/3) & \sqrt{3}\sin(\varphi_r + 2\pi/3) \\ \cos(\varphi_r - 2\pi/3) & \sqrt{3}\sin(\varphi_r + 2\pi/3) \end{bmatrix} \frac{d}{dt} \begin{bmatrix} i_{se} \\ i_{so} \end{bmatrix} \tag{A.5}$$

Substituting for the rotor voltages and currents from the inverse of Park transformation in (3.1.18), rotor voltages in stationary 'abc' reference frame can be transferred to stationary 'αβ' reference frame as

$$\begin{bmatrix} \cos\varphi_r & \sin\varphi_r \\ \cos\left(\varphi_r + \left(\frac{2\pi}{3}\right)\right) & \sin\left(\varphi_r + \left(\frac{2\pi}{3}\right)\right) \\ \cos\left(\varphi_r - \left(\frac{2\pi}{3}\right)\right) & \sin\left(\varphi_r - \left(\frac{2\pi}{3}\right)\right) \end{bmatrix} \begin{bmatrix} 0 \\ 0 \end{bmatrix} = \begin{bmatrix} R_r & 0 & 0 \\ 0 & R_r & 0 \\ 0 & 0 & R_r \end{bmatrix} \begin{bmatrix} \cos\varphi_r & \sin\varphi_r \\ \cos\left(\varphi_r + \left(\frac{2\pi}{3}\right)\right) & \sin\left(\varphi_r + \left(\frac{2\pi}{3}\right)\right) \\ \cos\left(\varphi_r - \left(\frac{2\pi}{3}\right)\right) & \sin\left(\varphi_r - \left(\frac{2\pi}{3}\right)\right) \end{bmatrix} \begin{bmatrix} i_{r\alpha} \\ i_{r\beta} \end{bmatrix} + \omega_r L_{ms} \begin{bmatrix} -\sin\varphi_r & \sqrt{3}\cos\varphi_r \\ -\sin(\varphi_r + 2\pi/3) & \sqrt{3}\cos(\varphi_r + 2\pi/3) \\ -\sin(\varphi_r - 2\pi/3) & \sqrt{3}\cos(\varphi_r - 2\pi/3) \end{bmatrix} \begin{bmatrix} i_{se} \\ i_{so} \end{bmatrix} +$$

$$\begin{bmatrix} (L_{lr} + L_{mr}) & -\frac{1}{2}L_{mr} & -\frac{1}{2}L_{mr} \\ -\frac{1}{2}L_{mr} & (L_{lr} + L_{mr}) & -\frac{1}{2}L_{mr} \\ -\frac{1}{2}L_{mr} & -\frac{1}{2}L_{mr} & (L_{lr} + L_{mr}) \end{bmatrix} \frac{d}{dt} \left\{ \begin{bmatrix} \cos\varphi_r & \sin\varphi_r \\ \cos\left(\varphi_r + \left(\frac{2\pi}{3}\right)\right) & \sin\left(\varphi_r + \left(\frac{2\pi}{3}\right)\right) \\ \cos\left(\varphi_r - \left(\frac{2\pi}{3}\right)\right) & \sin\left(\varphi_r - \left(\frac{2\pi}{3}\right)\right) \end{bmatrix} \begin{bmatrix} i_{r\alpha} \\ i_{r\beta} \end{bmatrix} \right\} + L_{ms} \begin{bmatrix} \cos\varphi_r & \sqrt{3}\sin\varphi_r \\ \cos(\varphi_r + 2\pi/3) & \sqrt{3}\sin(\varphi_r + 2\pi/3) \\ \cos(\varphi_r - 2\pi/3) & \sqrt{3}\sin(\varphi_r + 2\pi/3) \end{bmatrix} \frac{d}{dt} \begin{bmatrix} i_{se} \\ i_{so} \end{bmatrix} \tag{A.6}$$

After matrix multiplication, rotor voltages in stationary 'αβ' reference frame can be obtained as

$$\begin{bmatrix}0\\0\end{bmatrix} = \omega_r L_{ms}\begin{bmatrix}0 & \sqrt{3}\\ -1 & 0\end{bmatrix}\begin{bmatrix}i_{se}\\ i_{so}\end{bmatrix} + L_{ms}\begin{bmatrix}1 & 0\\ 0 & \sqrt{3}\end{bmatrix}\frac{d}{dt}\begin{bmatrix}i_{se}\\ i_{so}\end{bmatrix} + \begin{bmatrix}R_r & 0\\ 0 & R_r\end{bmatrix}\begin{bmatrix}i_{r\alpha}\\ r_{r\beta}\end{bmatrix} + \omega_r\left(L_{lr}+\tfrac{3}{2}L_{ms}\right)\begin{bmatrix}0 & 1\\ -1 & 0\end{bmatrix}\begin{bmatrix}i_{r\alpha}\\ r_{r\beta}\end{bmatrix} + \left(L_{lr}+\tfrac{3}{2}L_{ms}\right)\begin{bmatrix}1 & 0\\ 0 & 1\end{bmatrix}\frac{d}{dt}\begin{bmatrix}i_{r\alpha}\\ r_{r\beta}\end{bmatrix} \quad \text{(A.7)}$$

Stator and rotor voltages in (A.4) and (A.7) can be combined to form one matrix as

$$\begin{bmatrix}V_{se}\\ V_{so}\\ 0\\ 0\end{bmatrix} = \begin{bmatrix}R_s & 0 & 0 & 0\\ 0 & 2R_s & 0 & 0\\ 0 & \sqrt{3}L_{ms}\omega_r & R_r & \omega_r\left(L_{lr}+\frac{3L_{ms}}{2}\right)\\ -L_{ms}\omega_r & 0 & -\omega_r\left(L_{lr}+\frac{3L_{ms}}{2}\right) & R_r\end{bmatrix}\begin{bmatrix}i_{se}\\ i_{so}\\ i_{r\alpha}\\ i_{r\beta}\end{bmatrix} + \begin{bmatrix}(L_{ls}+L_{ms}) & 0 & \frac{3L_{ms}}{2} & 0\\ 0 & (2L_{ls}+3L_{ms}) & 0 & \frac{3\sqrt{3}L_{ms}}{2}\\ L_{ms} & 0 & \left(L_{lr}+\frac{3L_{ms}}{2}\right) & 0\\ 0 & \sqrt{3}L_{ms} & 0 & \left(L_{lr}+\frac{3L_{ms}}{2}\right)\end{bmatrix}\frac{d}{dt}\begin{bmatrix}i_{se}\\ i_{so}\\ i_{r\alpha}\\ i_{r\beta}\end{bmatrix} \quad \text{(A.8)}$$

Considering $[i_{se} \quad i_{so} \quad i_{r\alpha} \quad i_{r\beta}]^T$ is as the state vector, the state space model can be given as

$$\frac{d}{dt}\begin{bmatrix}i_{se}\\ i_{so}\\ i_{r\alpha}\\ i_{r\beta}\end{bmatrix} = \begin{bmatrix}(L_{ls}+L_{ms}) & 0 & \frac{3L_{ms}}{2} & 0\\ 0 & (2L_{ls}+3L_{ms}) & 0 & \frac{3\sqrt{3}L_{ms}}{2}\\ L_{ms} & 0 & \left(L_{lr}+\frac{3L_{ms}}{2}\right) & 0\\ 0 & \sqrt{3}L_{ms} & 0 & \left(L_{lr}+\frac{3L_{ms}}{2}\right)\end{bmatrix}^{-1}\left\{\begin{bmatrix}V_{se}\\ V_{so}\\ 0\\ 0\end{bmatrix} - \begin{bmatrix}R_s & 0 & 0 & 0\\ 0 & 2R_s & 0 & 0\\ 0 & \sqrt{3}L_{ms}\omega_r & R_r & \omega_r\left(L_{lr}+\frac{3L_{ms}}{2}\right)\\ -L_{ms}\omega_r & 0 & -\omega_r\left(L_{lr}+\frac{3L_{ms}}{2}\right) & R_r\end{bmatrix}\begin{bmatrix}i_{se}\\ i_{so}\\ i_{r\alpha}\\ i_{r\beta}\end{bmatrix}\right\} \quad \text{(A.9)}$$

Substituting for $L_m = \frac{3}{2}L_{ms}$, $L_{ss} = L_{ls} + \frac{3}{2}L_{ms}$ and $L_{rr} = L_{lr} + \frac{3}{2}L_{ms}$ in (A.9) and after matrix manipulations, state space model can be re-written as in (A.10).

Substituting $D = L_{ss}L_{rr} - {L_m}^2$ and $D_1 = L_{ls}L_{rr} + \frac{2}{3}L_{lr}L_m$ in (A.10), the simplified state space model can be given in (A.11).

$$\frac{d}{dt}\begin{bmatrix} i_{se} \\ i_{so} \\ i_{r\alpha} \\ i_{r\beta} \end{bmatrix} = \begin{bmatrix} \left(\frac{-3L_{rr}}{-3L_{rr}L_{sl}-2L_mL_{rr}+2{L_m}^2}\right) & 0 & \left(\frac{3L_m}{-3L_{rr}L_{sl}-2L_mL_{rr}+2{L_m}^2}\right) & 0 \\ 0 & \left(\frac{-L_{rr}/2}{{L_m}^2-L_{ss}L_{rr}}\right) & 0 & \left(\frac{\sqrt{3}L_m/2}{{L_m}^2-L_{ss}L_{rr}}\right) \\ \left(\frac{2L_m}{-3L_{rr}L_{sl}-2L_mL_{rr}+2{L_m}^2}\right) & 0 & \left(\frac{-(3L_{sl}+2L_m)}{-3L_{rr}L_{sl}-2L_mL_{rr}+2{L_m}^2}\right) & 0 \\ 0 & \left(\frac{L_m/\sqrt{3}}{{L_m}^2-L_{ss}L_{rr}}\right) & 0 & \left(\frac{-L_{ss}}{{L_m}^2-L_{ss}L_{rr}}\right) \end{bmatrix} \begin{bmatrix} V_{se} \\ V_{so} \\ 0 \\ 0 \end{bmatrix} +$$

$$\begin{bmatrix} \frac{3L_{rr}R_s}{-3L_{rr}L_{sl}-2L_mL_{rr}+2{L_m}^2} & \frac{-2\sqrt{3}{L_m}^2\omega_r}{-3L_{rr}L_{sl}-2L_mL_{rr}+2{L_m}^2} & \frac{-3L_mR_r}{-3L_{rr}L_{sl}-2L_mL_{rr}+2{L_m}^2} & \frac{-3L_m\omega_rL_{rr}}{-3L_{rr}L_{sl}-2L_mL_{rr}+2{L_m}^2} \\ \frac{{L_m}^2\omega_r/\sqrt{3}}{{L_m}^2-L_{ss}L_{rr}} & \frac{L_{rr}R_s}{{L_m}^2-L_{ss}L_{rr}} & \frac{\sqrt{3}L_m\omega_rL_{rr}/2}{{L_m}^2-L_{ss}L_{rr}} & \frac{-\sqrt{3}L_mR_r/2}{{L_m}^2-L_{ss}L_{rr}} \\ \frac{-2L_mR_s}{-3L_{rr}L_{sl}-2L_mL_{rr}+2{L_m}^2} & \frac{2L_m\omega_r(3L_{sl}+2L_m)/\sqrt{3}}{-3L_{rr}L_{sl}-2L_mL_{rr}+2{L_m}^2} & \frac{(3L_{sl}+2L_m)R_r}{-3L_{rr}L_{sl}-2L_mL_{rr}+2{L_m}^2} & \frac{L_{rr}\omega_r(3L_{sl}+2L_m)}{-3L_{rr}L_{sl}-2L_mL_{rr}+2{L_m}^2} \\ \frac{-2L_{ss}L_m\omega_r/3}{{L_m}^2-L_{ss}L_{rr}} & \frac{-2L_mR_s/\sqrt{3}}{{L_m}^2-L_{ss}L_{rr}} & \frac{-L_{ss}\omega_rL_{rr}}{{L_m}^2-L_{ss}L_{rr}} & \frac{L_{ss}R_r}{{L_m}^2-L_{ss}L_{rr}} \end{bmatrix} \begin{bmatrix} i_{se} \\ i_{so} \\ i_{r\alpha} \\ i_{r\beta} \end{bmatrix} \quad \text{(A.10)}$$

$$\frac{d}{dt}\begin{bmatrix} i_{se} \\ i_{so} \\ i_{r\alpha} \\ i_{r\beta} \end{bmatrix} = \begin{bmatrix} \left(\frac{L_{rr}}{D_1}\right) & 0 & \left(\frac{-L_m}{D_1}\right) & 0 \\ 0 & \left(\frac{L_{rr}}{2D}\right) & 0 & \left(\frac{-\sqrt{3}L_m}{2D}\right) \\ \left(\frac{-2L_m}{3D_1}\right) & 0 & \left(\frac{L_{ls}+\frac{2}{3}L_m}{D_1}\right) & 0 \\ 0 & \left(\frac{-L_m}{\sqrt{3}D}\right) & 0 & \left(\frac{L_{ss}}{D}\right) \end{bmatrix} \begin{bmatrix} V_{se} \\ V_{so} \\ 0 \\ 0 \end{bmatrix}$$

$$+ \begin{bmatrix} \left(\frac{-L_{rr}R_s}{D_1}\right) & \left(\frac{2{L_m}^2\omega_r}{\sqrt{3}D_1}\right) & \left(\frac{L_mR_r}{D_1}\right) & \left(\frac{L_m\omega_rL_{rr}}{D_1}\right) \\ \left(\frac{-{L_m}^2\omega_r}{\sqrt{3}D}\right) & \left(\frac{-L_{rr}R_s}{D}\right) & \left(\frac{-\sqrt{3}L_m\omega_rL_{rr}}{2D}\right) & \left(\frac{\sqrt{3}L_mR_r}{2D}\right) \\ \left(\frac{2L_mR_s}{3D_1}\right) & \left(\frac{-2L_m\omega_r(L_{ls}+2L_m/3)}{\sqrt{3}D_1}\right) & \left(\frac{-(L_{ls}+2L_m/3)R_r}{D_1}\right) & \left(\frac{-L_{rr}\omega_r(L_{ls}+2L_m/3)}{D_1}\right) \\ \left(\frac{2L_{ss}L_m\omega_r}{3D}\right) & \left(\frac{2L_mR_s}{\sqrt{3}D}\right) & \left(\frac{L_{ss}\omega_rL_{rr}}{D}\right) & \left(\frac{-L_{ss}R_r}{D}\right) \end{bmatrix} \begin{bmatrix} i_{se} \\ i_{so} \\ i_{r\alpha} \\ i_{r\beta} \end{bmatrix} \quad \text{(A.11)}$$

The instantaneous electromagnetic torque of an electrical machine can be defined in terms of vector quantities as

$$T_e = \left(\frac{P}{2}\right)\frac{3}{2}\, imag\,(\boldsymbol{\psi}_s{}^*.\boldsymbol{i}_s) \quad \text{(A.12)}$$

State vector of linked fluxes $\boldsymbol{\psi}_s$ can be defined as the sum of the state vectors of leakage fluxes $\boldsymbol{\psi}_{ls}$ and magnetizing fluxes $\boldsymbol{\psi}_{ms}$ of the machine.

$$\boldsymbol{\psi}_s = \boldsymbol{\psi}_{ls} + \boldsymbol{\psi}_{ms} \quad \text{(A.13)}$$

Considering the stator phase 'a' of a three-phase electrical machine is as the real axis, the state vector of linked fluxes can be given

$$\boldsymbol{\varphi}_s = \frac{2}{3}\left(\psi_{lsa} + (-\frac{1}{2} + j\,\frac{\sqrt{3}}{2}).\,\psi_{lsb} + (-\frac{1}{2} - j\,\frac{\sqrt{3}}{2}).\psi_{lsc}\right) + \frac{2}{3}\left(\psi_{msa} + (-\frac{1}{2} + j\,\frac{\sqrt{3}}{2}).\,\psi_{msb} + (-\frac{1}{2} - j\,\frac{\sqrt{3}}{2}).\psi_{msc}\right) \quad \text{(A.14)}$$

When the effect of core loss resistance is taken into account, instantaneous current through the leakage inductance differs than that through the magnetizing inductance. The state vector of the current related to the leakage fluxes can be defined as

$$\boldsymbol{i}_{ls} = \frac{2}{3}\left(i_{sa} + (-\frac{1}{2} + j\,\frac{\sqrt{3}}{2}).\,i_{sb} + (-\frac{1}{2} - j\,\frac{\sqrt{3}}{2}).\,i_{sc}\right) \quad \text{(A.15)}$$

Similarly, the state vector of the current related to the magnetizing fluxes can be given as

$$\boldsymbol{i}_{ms} = \frac{2}{3}\left(i_{sa} + \left(-\frac{1}{2} + j\frac{\sqrt{3}}{2}\right).i_{sb} + \left(-\frac{1}{2} - j\frac{\sqrt{3}}{2}\right).i_{sc}\right) - \frac{2}{3}\left(i_{ca} + \left(-\frac{1}{2} + j\frac{\sqrt{3}}{2}\right).i_{cb} + \left(-\frac{1}{2} - j\frac{\sqrt{3}}{2}\right).i_{cc}\right) \quad \text{(A.16)}$$

In terms of real and imaginary components, the electromagnetic torque in (A.12) can be re-written as

$$T_e = \left(\frac{P}{2}\right)\frac{3}{2}\, imag\left((\boldsymbol{\psi}_{sR} + j\boldsymbol{\psi}_{sI})^*.(\boldsymbol{i}_{sR} + j\boldsymbol{i}_{sI})\right) = \left(\frac{P}{2}\right)\frac{3}{2}\,\left(\boldsymbol{\psi}_{sR}\boldsymbol{i}_{sI} - \boldsymbol{\psi}_{sI}\boldsymbol{i}_{sR}\right) \quad \text{(A.17)}$$

Considering core loss resistance, the electromagnetic torque can be given as

$$T_e = \left(\frac{P}{2}\right)\frac{3}{2}\left((\boldsymbol{\psi}_{lsR}\boldsymbol{i}_{lsI} - \boldsymbol{\psi}_{lsI}\boldsymbol{i}_{lsR}) + (\boldsymbol{\psi}_{msR}\boldsymbol{i}_{msI} - \boldsymbol{\psi}_{msI}\boldsymbol{i}_{msR})\right) \quad \text{(A.18)}$$

Using (A.15) and (A.16), real and imaginary components of leakage and mutual current vectors of single-phase induction generator can be given as

$$\boldsymbol{i}_{lsR} = \frac{2}{3}\left(i_{lsa} - \frac{1}{2}i_{lsb} - \frac{1}{2}i_{lsc}\right) = \frac{2}{3}i_{se} \quad \text{(A.19)}$$

$$\boldsymbol{i}_{lsI} = \frac{2}{3}\left(\frac{\sqrt{3}}{2}\, i_{lsb} - \frac{\sqrt{3}}{2}i_{lsc}\right) = \frac{2}{\sqrt{3}}i_{so} \quad \text{(A.20)}$$

$$\boldsymbol{i}_{msR} = \frac{2}{3}\left(\left(i_{sa} - \frac{1}{2}i_{sb} - \frac{1}{2}i_{sc}\right) - \left(i_{ca} - \frac{1}{2}i_{cb} - \frac{1}{2}i_{cc}\right)\right) = \frac{2}{3}(i_{se} - i_{c1}) \quad \text{(A.21)}$$

$$\boldsymbol{i}_{msI} = \frac{2}{3}\left(\left(\frac{\sqrt{3}}{2}\, i_{sb} - \frac{\sqrt{3}}{2}i_{sc}\right) - \left(\frac{\sqrt{3}}{2}\, i_{cb} - \frac{\sqrt{3}}{2}i_{cc}\right)\right) = \frac{2}{\sqrt{3}}(i_{so} - i_{c2}) \quad \text{(A.22)}$$

Using (3.1.4) and Park transformation, linked fluxes in three phases of the stator can be written as a sum of leakage fluxes and mutual fluxes as given in (A.23).

$$\begin{bmatrix}\psi_{sa}\\ \psi_{sb}\\ \psi_{sc}\end{bmatrix} = L_{ls}\begin{bmatrix}1 & 0\\ 0 & 1\\ 0 & -1\end{bmatrix}\begin{bmatrix}i_{se}\\ i_{so}\end{bmatrix} + \begin{bmatrix}L_{m1} & 0\\ -\frac{1}{2}L_{m1} & \frac{1}{2}L_{m2}\\ -\frac{1}{2}L_{m1} & -\frac{1}{2}L_{m2}\end{bmatrix}\left\{\begin{bmatrix}i_{se}\\ i_{so}\end{bmatrix} + \begin{bmatrix}i_{r\alpha}{}'\\ r_{r\beta}{}'\end{bmatrix} - \begin{bmatrix}i_{c1}\\ i_{c2}\end{bmatrix}\right\} \quad \text{(A.23)}$$

Using (A.14) and (A.23), real and imaginary components of linked flux vectors of single-phase induction generator can be given as

$$\boldsymbol{\psi}_{lsR} = \frac{2}{3}\left(\psi_{lsa} - \frac{1}{2}\psi_{lsb} - \frac{1}{2}\psi_{lsc}\right) = \frac{2}{3}L_{ls}i_{se} \quad \text{(A.24)}$$

$$\boldsymbol{\psi}_{lsI} = \frac{2}{3}\left(\frac{\sqrt{3}}{2}\, \psi_{lsb} - \frac{\sqrt{3}}{2}\psi_{lsc}\right) = \frac{2}{\sqrt{3}}L_{ls}i_{so} \quad \text{(A.25)}$$

$$\boldsymbol{\psi}_{msR} = \frac{2}{3}\left(\psi_{msa} - \frac{1}{2}\psi_{msb} - \frac{1}{2}\psi_{msc}\right) = L_{m1}(i_{se} + i_{r\alpha}{}' - i_{c1}) \quad \text{(A.26)}$$

$$\boldsymbol{\psi}_{msI} = \frac{2}{3}\left(\frac{\sqrt{3}}{2}\,\psi_{msb} - \frac{\sqrt{3}}{2}\psi_{msc}\right) = \frac{1}{\sqrt{3}}L_{m2}\left(i_{so} + i_{r\beta}{}' - i_{c2}\right) \quad \text{(A.27)}$$

Substituting from (A.19)-(A.22) and (A.24) - (A.27) in (A.18), instantaneous electromagnetic torque of the single-phase induction generator can be given as

$$T_e = \left(\frac{P}{2}\right)\sqrt{3}\left(L_{m1}\left(i_{mo} - i_{r\beta}{}'\right)i_{me} - \frac{1}{3}L_{m2}(i_{me} - i_{r\alpha}{}')i_{mo}\right) \quad \text{(A.28)}$$

APPENDIX B

DETAILS OF THE EXPERIMENTAL INDUCTION MACHINE

Name-plate data of the three-phase induction machine used for the experiments of this thesis is given in Table B.1.

Table B.1
Name plate data of induction machine

Winding Configuration	Star
Rated Voltage	415 V (line-to-line, rms)
Rated Current	6.4 A (phase)
Rated Frequency	50 Hz
Rated Speed	1420 rpm
Rated Power Factor	0.82
Rated Power	3 kW
Number of Poles	4

Induction machine parameters measured using dc test, blocked rotor test and synchronous test are given in Table B.2.

Table B.2
Measured parameters of the three-phase induction machine

Parameter	Value
Stator resistance (R_s)	2.85 Ω
Rotor resistance (R_r)	2.1 Ω
Core loss resistance (R_c)	980.0281 Ω
Stator leakage inductance (L_{ls})	0.0077 H
Rotor leakage inductance (L_{lr})	0.0077 H
Inertia (J)	0.03 kg.m^2

A measured magnetizing characteristic of the three-phase induction machine is approximated by three equations. First linear region is approximated by

$$\psi_m = K_{lo} * i_m \qquad 0 \leq i_m \leq i_{mo} \qquad \text{(B.1)}$$

Second linear region is approximated by

$$\psi_m = (K_l * i_m - C) \qquad i_{mo} < i_m \leq i_{mo1} \qquad \text{(B.2)}$$

And the non linear region is approximated by

$$\psi_m = (K_l * i_{mo1} - C) + \left(\frac{k_l}{b}\right) tan^{-1}\left(b * (i_m - i_{mo1})\right) \qquad i_{mo1} < i_m \qquad \text{(B.3)}$$

where constants $C, i_{mo}, i_{mo1}, K_{lo}, K_l$ and b are determined by fitting the curve to the measured characteristic curve. Figure B.1 shows the measured and approximated magnetizing characteristics of the three-phase induction machine. The approximated magnetizing characteristics are corresponding to the constant given below.

$$C = -0.0257, i_{mo} = 0.3, i_{mo1} = 0.8, K_{lo} = 0.1856, K_l = 0.2712, b = 0.4$$

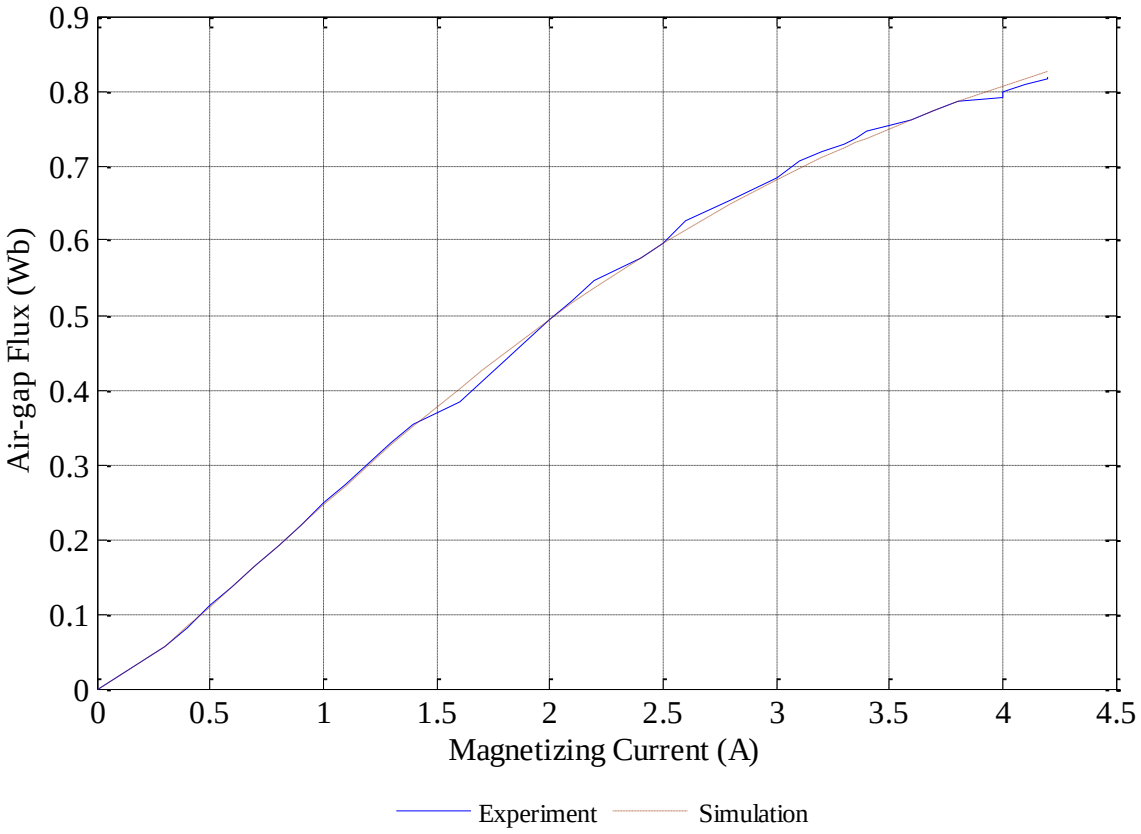

Fig. B.1. Measured and approximated magnetizing characteristics of the three-phase induction machine

The calculated parameters of the α-axis and the β-axis of the single phase induction machine are given in Table B.3.

Table B.3
Calculated parameters of the single-phase induction machine

Parameter	α-axis	β-axis
Stator resistance	R_s =2.85 Ω	$2R_s$ =5.7 Ω
Rotor resistance	$\frac{2}{3}R_r = 1.4$ Ω	$2R_r = 4.2$ Ω
Core loss resistance	$R_c = 980.0281$ Ω	$2R_c = 1960.0562$ Ω
Stator leakage inductance	$L_{ls} = 0.0077$ Ω	$2L_{ls} = 0.0154$ Ω
Rotor leakage inductance	$\frac{2}{3}L_{lr} = 0.0051$ Ω	$2L_{lr} = 0.0154$ Ω

Magnetizing inductance in α–axis $L_{m1}$and β-axis L_{m2} are equal to L_{ms} and $3L_{ms}$ respectively. The magnetizing characteristic curves of α–axis and β-axis can be obtained using the measured magnetizing characteristics of the three-phase induction machine. These are shown by the solid curves in Fig. B.2. Using the same equations in (B.1) – (B.3), magnetizing characteristics of α–axis and β-axis are approximated with the following substitutions.

The magnetizing characteristics of α-axis is obtained by substituting for $\psi_m = \frac{V_{m1}}{\omega}$, $i_m = i_{me}$, $C = -0.0257, i_{mo} = 0.45, i_{mo1} = 1.2, K_{lo} = 0.1237, K_l = 0.1808$ and $b = 0.265$

Similarly the magnetizing characteristics of β-axis can be obtained by substituting for $\psi_m = \frac{V_{m2}}{\omega}$, $i_m = i_{mo}$, $C = -0.0522, i_{mo} = 0.3, i_{mo1} = 0.5, K_{lo} = 0.3713, K_l = 0.5455$ and $b = 0.334$

The approximated characteristics are presented by the dashed curves in Fig. B.2.

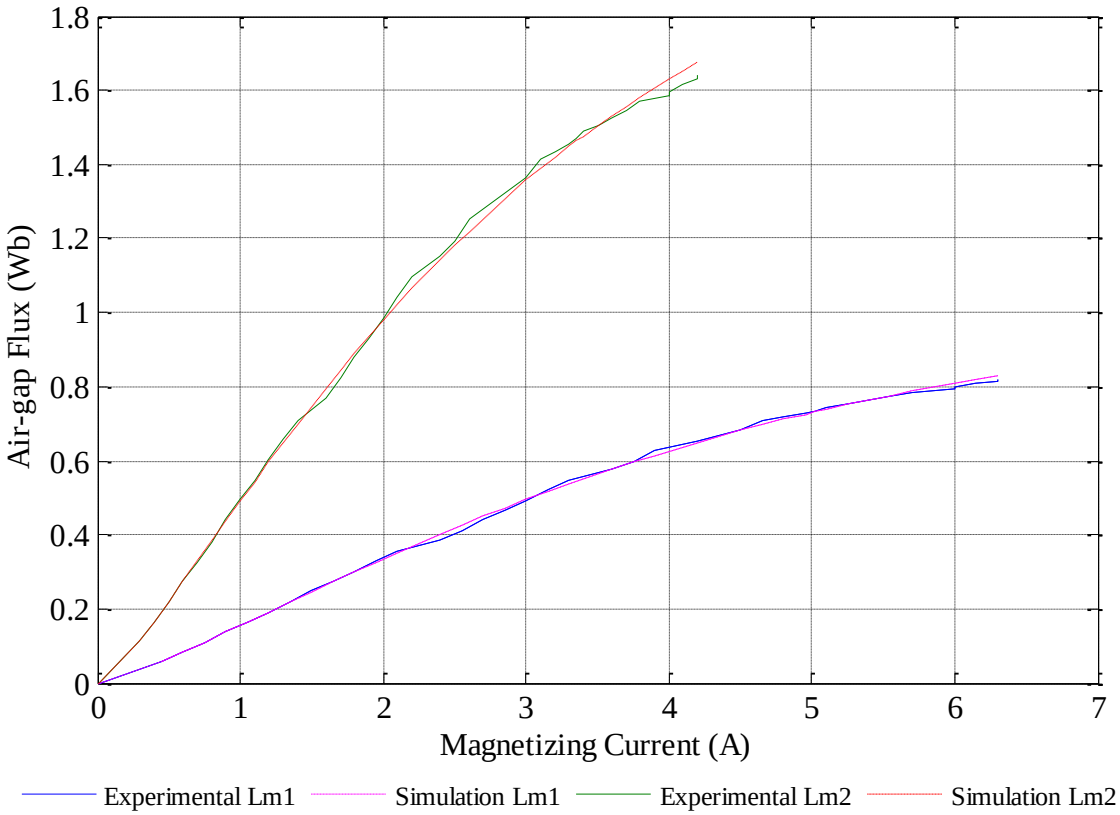

Fig. B.2. Calculated and approximated magnetizing characteristics of the single-phase induction machine

APPENDIX C

TORQUE-SPEED CHARACTERISITICS OF THE WIND TURINE

Parameters of (4.2.58) related to the wind turbine used for the Matlab simulations are given below.

```
if 0 <= Vw && Vw < 5
    T1=0;
    T2=0;
    Om1=168;
    Om2=158;
    T0=0;

elseif 5 <= Vw && Vw < 6
    T1=-1.1826;
    T2=-2.1251;
    Om1=168;
    Om2=158;
    T0=-2.211;

elseif 6 <= Vw && Vw < 7
    T1=-5.371;
    T2=-6.313;
    Om1=168;
    Om2=158;
    T0=-6.394;

elseif 7 <= Vw && Vw < 8
    T1=-10.1197;
    T2=-10.8716;
    Om1=168;
    Om2=158;
    T0=-10.9333;

elseif 8 <= Vw && Vw < 9
    T1=-15.0499;
    T2=-15.5411;
    Om1=168;
    Om2=158;
    T0=-15.578;

elseif 9 <= Vw && Vw < 10
    T1=-20.0375;
    T2=-20.2444;
    Om1=168;
    Om2=158;
    T0=-20.2549;

elseif 10 <= Vw && Vw < 10.6
    T1=-25.0346;
    T2=-24.9658;
    Om1=164;
    Om2=158;
    T0=-24.9498;
```

```
else
    T1=-28.2007;
    T2=-28.0464;
    Om1=163;
    Om2=158;
    T0=-28.0135;

end

m=(T1-T2)/(Om1-Om2);

Om0=pi*50;
```

APPENDIX D

FLOW CHART OF TRANSIENT-STATE PROGRAM

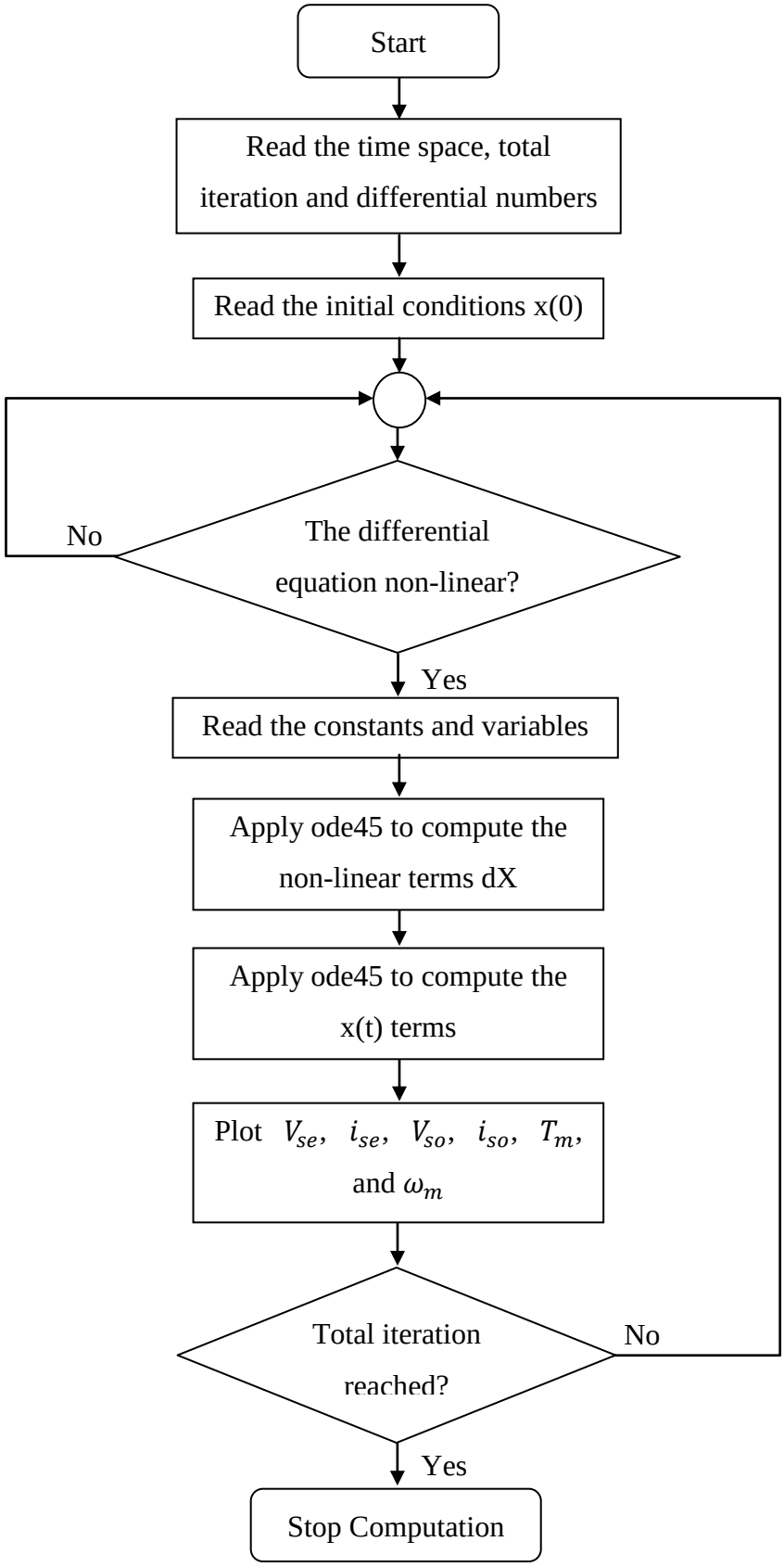

APPENDIX E
OPEN-LOOP TRANSFER FUNCTION

Open-loop transfer function of the single-phase induction generator is defined as

$$G(s) = \frac{K_a s}{s^7 + K_b s^6 + K_c s^5 + K_d s^4 + K_e s^3 + K_f s^2 + K_g s + K_h} \quad \text{(E.1)}$$

The constants of the open-loop transfer function are given below.

$$K_a = \frac{1}{L_{ls} * K_{25}} \quad \text{(E.2)}$$

$$K_b = \frac{(R_s * K_{25}) + (L_{ls} * K_{26}) + (L_{m1} * K_{19})}{L_{ls} * K_{25}} \quad \text{(E.3)}$$

$$K_c = \frac{(R_s * K_{26}) + (L_{ls} * K_{27}) + (L_{m1} * K_{20})}{L_{ls} * K_{25}} \quad \text{(E.4)}$$

$$K_d = \frac{(R_s * K_{27}) + (L_{ls} * K_{28}) + (L_{m1} * K_{21})}{L_{ls} * K_{25}} \quad \text{(E.5)}$$

$$K_e = \frac{(R_s * K_{28}) + (L_{ls} * K_{29}) + (L_{m1} * K_{22})}{L_{ls} * K_{25}} \quad \text{(E.6)}$$

$$K_f = \frac{(R_s * K_{29}) + (L_{ls} * K_{30}) + (L_{m1} * K_{23})}{L_{ls} * K_{25}} \quad \text{(E.7)}$$

$$K_g = \frac{(R_s * K_{30}) + (L_{ls} * K_{31}) + (L_{m1} * K_{24})}{L_{ls} * K_{25}} \quad \text{(E.8)}$$

$$K_h = \frac{R_s * K_{31}}{L_{ls} * K_{25}} \quad \text{(E.9)}$$

$$K_1 = 2 C_o L_{ls} \quad \text{(E.10)}$$

$$K_2 = 2\left((R_s C_o) + \left(\frac{L_{ls}}{R_o}\right)\right) \quad \text{(E.11)}$$

$$K_3 = \left(1 + \left(\frac{2R_s}{R_o}\right)\right) \quad \text{(E.12)}$$

$$K_4 = \frac{K_1}{2R_c} \quad \text{(E.13)}$$

$$K_5 = \frac{K_2}{2R_c} + \frac{K_1}{L_{m2}} + C_o \quad \text{(E.14)}$$

$$K_6 = \frac{K_3}{2R_c} + \frac{K_2}{L_{m2}} + \frac{1}{R_o} \quad \text{(E.15)}$$

$$K_7 = \frac{K_3}{L_{m2}} \quad \text{(E.16)}$$

$$K_8 = \frac{(2K_4L_{lr})}{\sqrt{3}\omega_r} \quad \text{(E.17)}$$

$$K_9 = \frac{\left((2K_4R_r)+(2K_5L_{lr})+K_1\right)}{\sqrt{3}\omega_r} \quad \text{(E.18)}$$

$$K_{10} = \frac{\left((2K_5R_r)+(2K_6L_{lr})+K_2\right)}{\sqrt{3}\omega_r} \quad \text{(E.19)}$$

$$K_{11} = \frac{\left((2K_6R_r)+(2K_7L_{lr})+K_3\right)}{\sqrt{3}\omega_r} \quad \text{(E.20)}$$

$$K_{12} = \frac{(2K_7R_r)}{\sqrt{3}\omega_r} \quad \text{(E.21)}$$

$$K_{13} = -\frac{3K_8}{2R_r} \quad \text{(E.22)}$$

$$K_{14} = -\frac{3K_9}{2R_r} \quad \text{(E.23)}$$

$$K_{15} = -\left(\frac{3}{2Rr}\right) * \left(K_{10} + \left(\frac{2\omega_r L_{lr} K_4}{\sqrt{3}}\right)\right) \quad \text{(E.24)}$$

$$K_{16} = -\left(\frac{3}{2Rr}\right) * \left(K_{11} + \left(\frac{\omega_r(K_1+2L_{lr}K_5)}{\sqrt{3}}\right)\right) \quad \text{(E.25)}$$

$$K_{17} = -\left(\frac{3}{2Rr}\right) * \left(K_{12} + \left(\frac{\omega_r(K_2+2L_{lr}K_6)}{\sqrt{3}}\right)\right) \quad \text{(E.26)}$$

$$K_{18} = -\left(\frac{3}{2Rr}\right) * \left(\frac{\omega_r(K_3+2L_{lr}K_7)}{\sqrt{3}}\right) \quad \text{(E.27)}$$

$$K_{19} = -\frac{2L_{lr}K_{13}}{(3L_{m1})} \quad \text{(E.28)}$$

$$K_{20} = \frac{(K_8-(2L_{lr}K_{14}/3))}{L_{m1}} \quad \text{(E.29)}$$

$$K_{21} = \frac{(K_9-(2L_{lr}K_{15}/3))}{L_{m1}} \quad \text{(E.30)}$$

$$K_{22} = \frac{(K_{10}-(2L_{lr}K_{16}/3))}{L_{m1}} \quad \text{(E.31)}$$

$$K_{23} = \frac{(K_{11} - (2L_{lr}K_{17}/3))}{L_{m1}} \quad \text{(E.32)}$$

$$K_{24} = \frac{(K_{12} - (2L_{lr}K_{18}/3))}{L_{m1}} \quad \text{(E.33)}$$

$$K_{25} = L_{m1} * \frac{K_{19}}{R_c} \quad \text{(E.34)}$$

$$K_{26} = K_{19} - K_{13} + \frac{(L_{m1} * K_{20})}{R_c} \quad \text{(E.35)}$$

$$K_{27} = K_{20} - K_{14} + \frac{(L_{m1} * K_{21})}{R_c} \quad \text{(E.36)}$$

$$K_{28} = K_{21} - K_{15} + \frac{(L_{m1} * K_{22})}{R_c} \quad \text{(E.37)}$$

$$K_{29} = K_{22} - K_{16} + \frac{(L_{m1} * K_{23})}{R_c} \quad \text{(E.38)}$$

$$K_{30} = K_{23} - K_{17} + \frac{(L_{m1} * K_{24})}{R_c} \quad \text{(E.39)}$$

$$K_{31} = K_{24} - K_{18} \quad \text{(E.40)}$$

APPENDIX F

SIMULATION BLOCK DIAGRAM

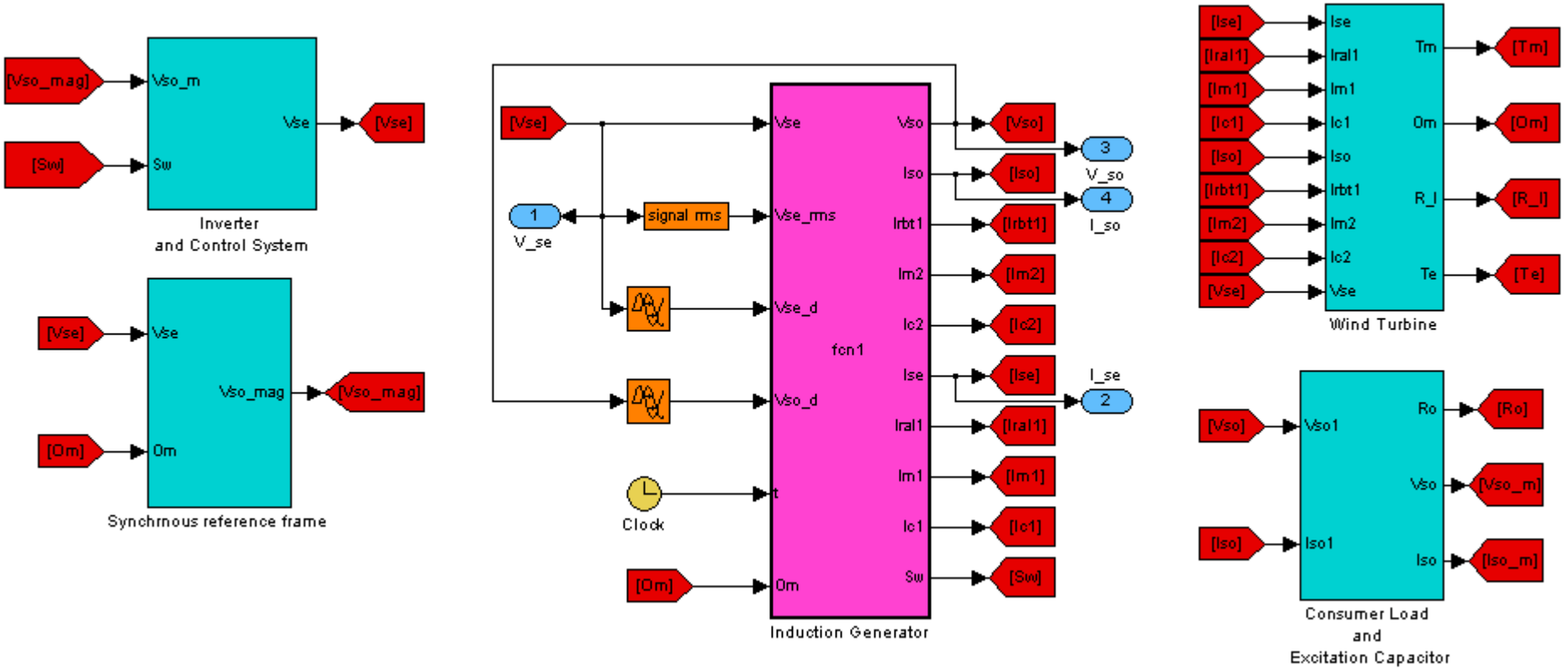

Fig. F.1. Simulation Block Diagram

APPENDIX G
PER UNIT VALUES

Due to easier comparison of regulated and unregulated behaviour of the generator system, the results in Chapter 7 are presented by per unit values. The rated values of voltage, power and frequency are selected as the base values of the corresponding system variables. Since the rated voltage is 415 V, (415/√3) V is selected as the base value of the voltage. Base values of other system variables are derived using the relationships of the selected base values.

Selected base values:

Voltage $V_B = 239.6\,V$

Power $P_B = 1000\,W$

Frequency $f_B = 50\,/s$

Electrical speed $\omega_B = 2\pi * f_B = 314.16\,rad/s$

Derived base values:

Resistance $R_B = {V_B}^2/P_B = \ 57.4\,\Omega$

Current $I_B = V_B/R_B = \ 4.17\,A$

Inductance $L_B = V_B/\omega_B I_B = 0.1829\,H$

Capacitance $C_B = I_B/\omega_B V_B = 55.4 * 10^{-6}\,F$

Time $T_B = 2\pi/\omega_B = 0.02\,s$

Flux $\psi_B = V_B/\omega_B = 0.763\,Wb$

Mechanical Speed $\Omega_B = \omega_B/P_p = 157.08\,rad/s$

; where P_p is the number of pole pairs

Torque $\tau_B = P_B P_p/\omega_B = \ 6.37\,Nm$

Inertia $J_B = 2\pi\, P_B {P_p}^2 / {\omega_B}^3 = \ 8.11 * \ 10^{-4}\ kg.m^2$

APPENDIX H

EXPERIMENTAL SET-UP

Laboratory set-up used for the experimental purposes is shown in Figs. H.1-H.3.

Fig. H.1. Name plate data of the three-phase induction machine

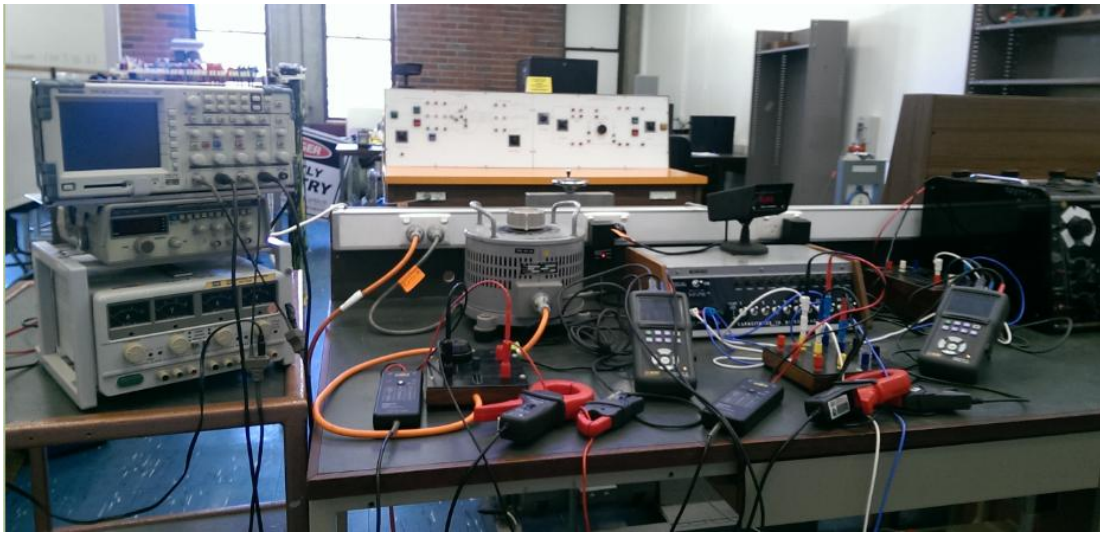

Fig. H.2. Auto transformer connected at the excitation control winding

Fig. H.3. Fixed capacitor, resistive load and variable speed drive